THÈSE

présentée à

L'UNIVERSITÉ DE PAU ET DES PAYS DE L'ADOUR

ÉCOLE DOCTORALE DES SCIENCES EXACTES ET DE LEURS APPLICATIONS

par **Hai HOANG**

POUR OBTENIR LE GRADE DE

DOCTEUR

SPÉCIALITÉ: **Physique**

MODELING OF SIMPLE FLUIDS CONFINED IN SLIT NANOPORES: TRANSPORT AND POROMECHANICS

Soutenue le : 12 Mars 2013

Après avis de:

M. FILLOT Nicolas	MC-HDR, INSA de Lyon	**Rapporteur**
M. ROTENBERG Benjamin	CR-HDR CNRS, Université Pierre et Marie Curie	**Rapporteur**

Devant la Commission d'examen formée de:

M. JOLY Laurent	MC, Université Lyon 1	**Examinateur**
M. PIJAUDIER-CABOT Gilles	PR, Université de Pau et des Pays de l'Adour	**Examinateur**
M. WÜRGER Aloïs	PR, Université Bordeaux 1	**Examinateur**
M. GALLIERO Guillaume	PR, Université de Pau et des Pays de l'Adour	**Directeur**

Acknowledgement

First of all, I would like to thank Prof. Guillaume GALLIERO for giving me the opportunity to pursue the Phd study in the field of the molecular dynamics simulations as my desire after graduating the MSc study. During more three years of doing the Phd study under his enthusiastic guidance, I have achieved not only a lot of knowledge of the specific research topic but also ways to conduct a new project and to adapt to a new study environment. In addition, Prof. Galliero has always made me feel confident in myself that I can do research for which I seemingly did not have previously. These have been helping me to mature in the study and research. I certainly believe that I could not have found a better professor to follow the Phd study. I am also grateful to Prof. Gilles PIJAUDIER-CABOT for his valuable help and suggestions and particularly that he is the leader of the “FAILFLOW” project funded by an advanced grant from the European Research Council that has supported funding to my Phd study.

I am indebted to Prof. Yong Kweon Suh, my MSc supervisor, for his valuable guidance during the MSc study that has helped my Phd study not little. Particularly, Prof. Suh firstly introduced the subject of the molecular dynamics simulations to me, which has opened a new direction in my research.

Moreover, I would like to thank the members of unit of “Propriétés de Transport” in Laboratoire des Fluides Complexes et leurs Reservoirs, Dr. Rachid HANNAOUI, Dr. Djilali AMEUR, Dr. Brahim Khalil BENAZZOUZ, Dr. Romain VERMOREL and Mr. Julien COLLEL, for their interesting and valuable help, suggestions, discussions and sharing the documents and papers. I am also grateful to all the members of Laboratoire des Fluides Complexes et leurs Reservoirs who have given me a comfortable research environment and

stimulating encouragement. I would like to thank Ms. Véronique GIANCOLA and Ms. Catherin URREA for their kindness help in my missions of the conference.

I am grateful for the computational facilities of the cluster UPPA, TREELE and MCIA. I would like to thank Dr. Stephanie DELAGE for his valuable help in the parallel computing.

I would like to thank all of my friends and the Vietnamese students in Pau for their encouragement, support and wonderful help in past years. In particular, I am very grateful Ms. Le Van Anh NGUYEN for her encouragement and support in my study and valuable helps in life, without her I would not have enjoyed and known much the life in not only Pau but also in France and Europe.

Finally, I would like to thank my family for encouraging and guiding me in the right part since childhood. In particular, I am indebted my mother for her sacrifice for my study.

CONTENTS

Chapter 1

Introduction

Fluid transfer and storage in porous medium and the mechanical response of the porous solid to them are central in a variety of contexts both from the fundamental and the industrial point of view: oil and gas production, CO2 storage in petroleum engineering, chromatography, membrane science, lubrication in chemical engineering processes, cement paste and tight rocks in civil engineering, etc. [1-5]. This work aims at providing fundamental information on some points of such a problematic through the numerical and theoretical analysis of the transport properties and the poromechanics of simple fluids confined in slit nanopores. This work is a part of a more global project named “Failflow” (ERC Advanced Grant leaded by Pr. Gilles Pijaudier-Cabot) that focuses on fluid flow in low permeability porous materials with evolving microstructure in the context of geo-mechanics and civil engineering applications.

In general, to deal with physical problems involving a fluid in a porous medium, the first requirement is to determine the behavior (static and dynamic) at the pore-scale, and then using up-scaling techniques (analytically or numerically) to arrive to a macroscopic formulation, see Fig. 1.1 [1-2, 6-10]. For porous medium in which pores are sufficiently large, i.e. typically pore diameters greater than 50nm (much greater than the characteristic distance of intermolecular interaction) and so-called macro-pores [10], the characteristics of the fluid in the pores are assumed to be the one in the bulk. In addition, the fluid-solid interactions are neglected [1-2] apart from low density conditions where such effects are usually represented by a “modified” boundary condition through a slip length [4]. This assumption is reasonable because in macro-pores the surface effects induced by the solid-fluid interaction on the fluid is much weaker that those from the fluid-fluid interaction (volume) itself [3, 5].

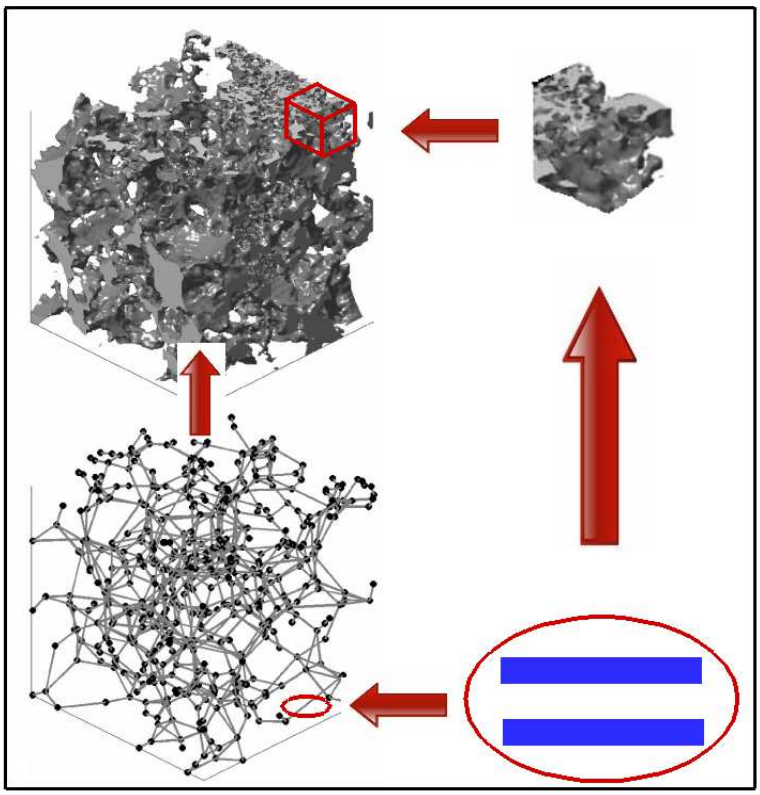

Figure 1.1: Usual up-scaling schemes to describe the fluid in a porous medium from the characteristics at the pore-scale [6-10].

When the size of the pores decreases, in particular for pores diameter smaller than 2nm called micro-pores, the situation becomes more complex. This is because in such narrow pores the ratio of the surface to the volume is very high, and so surface effects on the fluid become dominant over the volume ones [3, 5]. Hence, the surface effects at the pore scale must be elucidated before trying to build an up-scaled scheme dedicated to the poromechanics of microporous materials.

Sensitive microscopic experiments [the surface force apparatus (SFA), atomic force microscopy (AFM), and friction force microscopy (FFM)] on a fluid between solid surfaces have shown that the effective shear viscosity and the normal pressure of the fluid are strongly dependent on the distance between the solid surfaces, see Figs. 1.2a and 1.2b [11]. This may lead for instance to macroscopically observable phenomena such as the swelling of some

micro-porous materials, see Fig. 1.2c. Such observations can physically be understood because in a region close to the solid surfaces the fluid molecules have a tendency to organize themselves into layered structures parallel to the solid-fluid interface due to physical adsorption and molecular packing, [3, 5]. Because of such surface effects at the pore-scale, the behaviors of micro-porous medium are very different from those predicted from the macroscopic theories developed to deal with usual macroporous medium [6-10, 12-13].

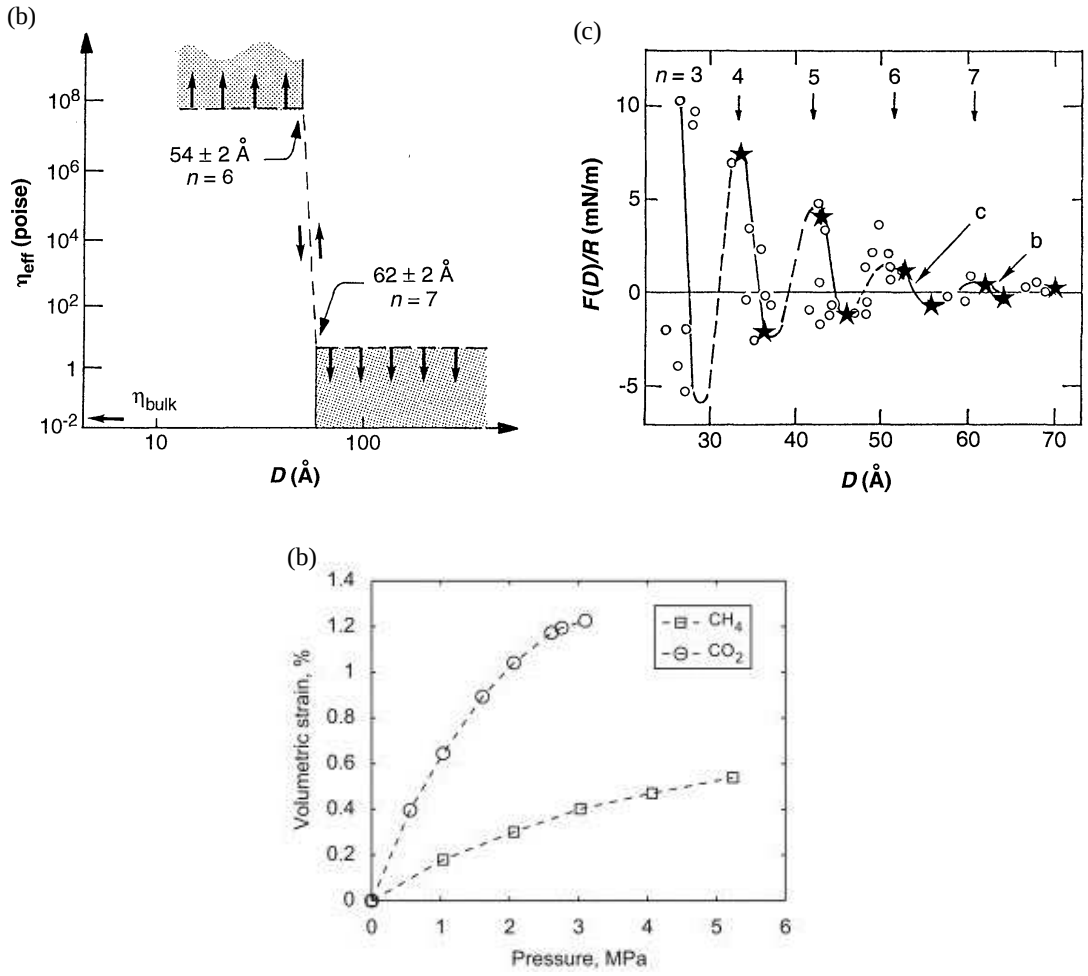

Figure 1.2: (a) Variation with film thickness of the effective mean viscosity of OMCTS confined between mica sheets (SFA experiments) [11]. (b) Normal force-distance profile between mica sheets immersed in OMCTS is (SFA experiments) [11]. (c) Volumetric strain versus pore pressure in a CO_2-injected coal and in a CH_4-injected coal [8, 13].

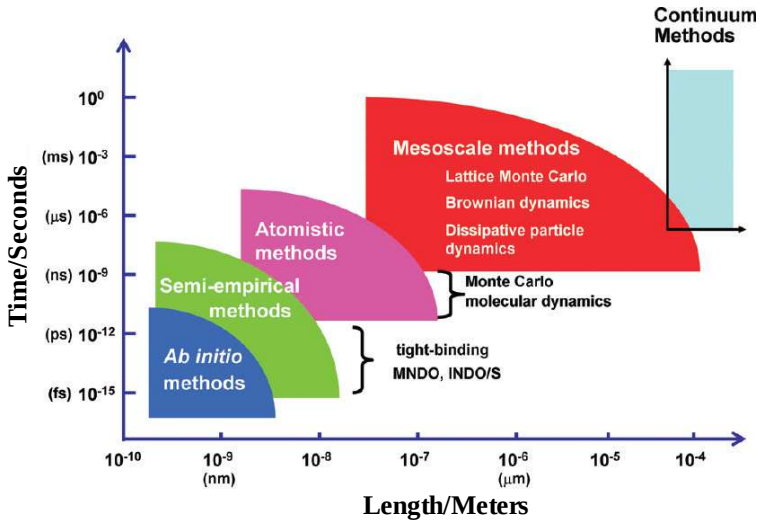

Figure 1.3: Simulations techniques range of applicability [15].

Although experiments on a fluid confined in narrow pores can provide the "apparent/effective" pictures, there exists no experimental method that can provide yet the full picture which is compulsory to test deeply the proposed theories. Thus, alternative methods have been proposed to deal with such problems which often rely on numerical simulations at a molecular scale [14] ranging from quantum like approaches to mesoscale techniques, see Fig. 1.3. These methods have shown to be valuable tools (and associated to limited costs) to reproduce quantitatively the apparent properties, but also to predict the behavior for extreme/dangerous situations which cannot be resolved by experiments easily [3-5]. In such numerical methods, the main difficulty is to be able to design "molecular" model at the appropriate scale to encompass the key characteristics/behaviors of the real system while keeping a sufficient simplicity to be tractable and computable in a reasonable time.

In this work, we have employed atomistic methods which are based on a classical representation of the system simulated at the molecular scale, i.e. the system is represented by a set of atoms interacting through effective potential. More precisely, we have employed the Molecular Dynamics (MD) technique that consists in following over time the trajectories of

all atoms simulated using simply the classical Newton equations. One of the main interests of such a numerical approach is that the (collective) physical phenomena that may emerge are not postulated a priori and are a consequence of the molecular description only (which is so central in the approach). Thus, this approach can provide “exactly” all information on the physical properties of a given modeled system and allows developing/testing molecular models and molecular based theories following the classical picture shown in Fig. 1.4 [14, 15].

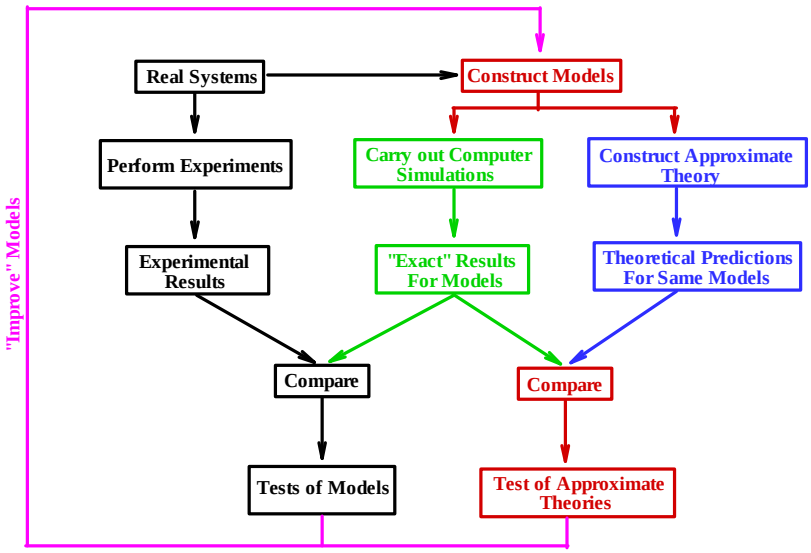

Figure 1.4: The connection between experiment, theory and computer simulation [14].

In what follows, is provided a brief overview of the existing theories and simulations results obtained in the literature on some specific physical properties of highly confined fluids. Details on the molecular simulation techniques are presented in the next chapter.

1.1. On the Apparent and Local Density of Confined Fluid

Confirming what known experimentally [3], results obtained from the molecular simulations (Monte Carlo and Molecular Dynamics) in the Grand Canonical ensemble have shown that the average density of a simple fluid confined in slit pores can vary appreciably

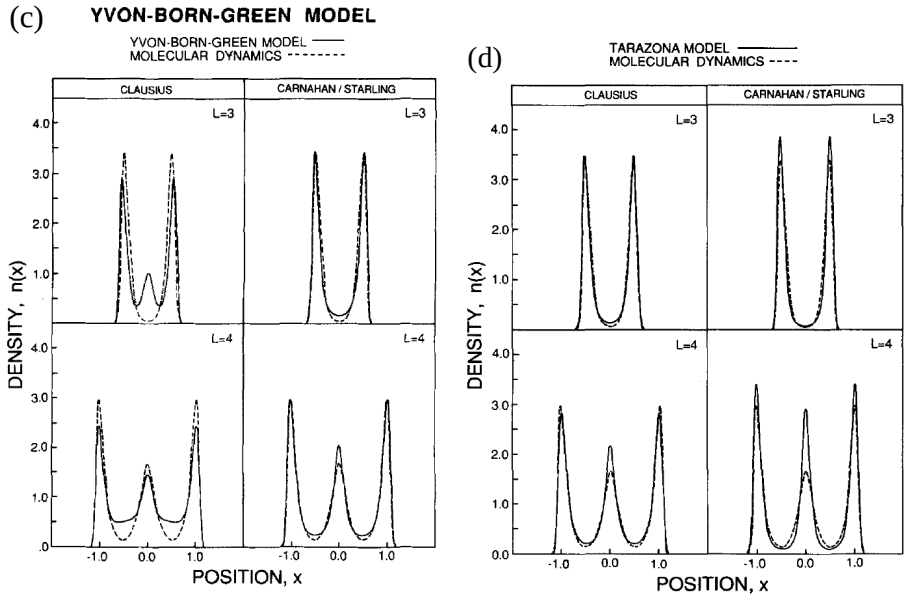

Figure 1.5: Density of fluids confined between solid surfaces separated by a distance obtained from the molecular simulations and theories. (a) Density profiles obtained from the MD simulations and the YBG theory [18]. (b) Density profiles obtained from the MD simulations and the DFT using the Tarazona model [18].

with the size of the pore for width of the order of a few nanometers (i.e., micro and mesopores) [3, 5, 16-17]. This reflects the inhomogeneity of the fluid in the pores due to physical adsorption and molecular packing, see Fig. 1.5. It has been found that such behaviors depend on the type of the fluid, the solid-fluid interaction and the thermodynamic operating conditions [3, 16-17].

Beside molecular simulations, theoretical methods have been developed in which the density profile is provided by numerically solving integral equations that are obtained from the statistical mechanics [5, 16, 18-19]. Usually these integral equations are derived from:

- The distribution function theory: in this approach the Liouville's equation is integrated over all coordinates and momentum of the fluid particles. The use of the Kirkwood's superposition approximation leads to the Born-Green-Yvon (BGY) equation that relates the local density and the pair correlation function. To determine the local

density from the BGY equation, the pair correlation function is usually taken as that of a homogeneous fluid at some average density computed by spatial coarse graining.

- The density functional theory (DFT): in this approach the integral equations are obtained from differentiation of the grand potential of the fluid in pores with respect to the local density. This requires specifying the intrinsic free energy per atom or volume at a given position. The usual approach consists to assume it equal to the one of a homogenous fluid at a bulk state corresponding to a locally averaged density around the given position. Various definitions of the locally averaged density (using different weight functions) specify different forms of the DFT.

Results obtained from such theories all have shown that the local density noticeably varies with the position, see Fig. 1.5 [5, 16, 18-19]. However, the theoretical results are not always in a qualitative agreement with the simulation ones, particularly for dense fluids. The DFT with adequate assumptions on the weight function usually provides results in better agreement with the simulation ones compared to those obtained from the distribution function theory, see Fig. 1.5 [5, 16, 18-19].

1.2. Effective and Local Transport Properties

As found experimentally [3], apparent/effective transport coefficients (shear viscosity and mass diffusion) of strongly confined fluids, calculated during MD simulations using different procedures have shown to vary appreciably with the pore size, see Fig. 1.6 [3-4, 20-25]. In most systems studied in the literature, the effective shear viscosity and the diffusion coefficient of fluid in pore are higher and smaller than the ones of the bulk fluid, respectively, these effects increasing when the pore size decreases. The trend of the noted variations is often correlated to the one of variation in the average density. However, the use of the average density cannot explain a dramatic increase of the effective shear viscosity of fluid in very

narrow pores observed in some non-equilibrium MD simulations. In fact, the simulation results have shown that the confined fluid may exhibit different responses when the size of pore changes, e.g. going from a liquid-like response to a solid-like response, [3, 20].

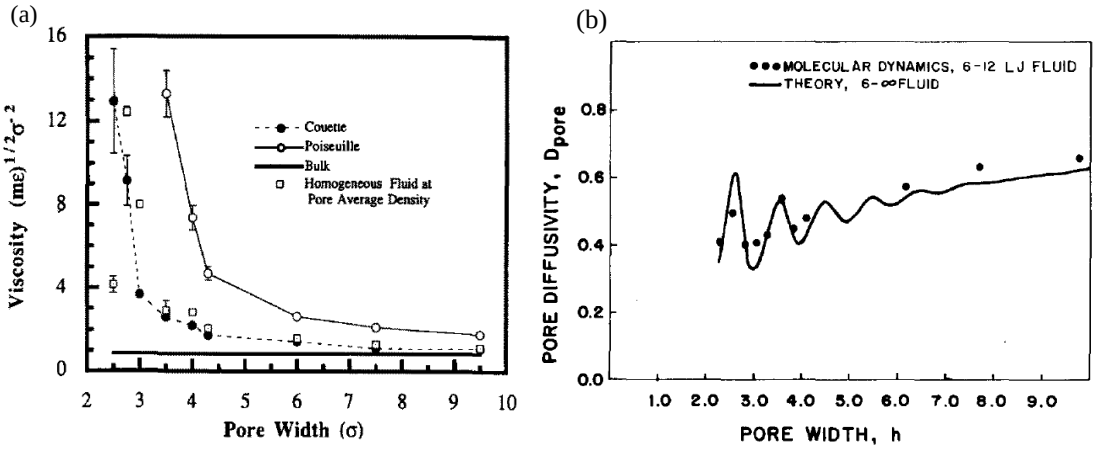

Figure 1.6: Effective transport properties of a confined fluid between solid surfaces obtained from the MD simulations and theories. (a) Variation in the effective shear viscosity with the pore width [30]. (b) Variation in the effective diffusion coefficient with the pore width [43].

Local transport coefficients (mass diffusion and shear viscosity) have also been studied using MD simulations [22-23, 26-29]. Results have shown that the local transport coefficients appreciably vary with the position with variations strongly correlated to the local density ones, see Fig. 1.7. However the definition itself of a local transport property may sometimes leads to inconsistencies. Thus, in some cases, the local shear viscosity computed from non-equilibrium MD simulations using the classical Newton's law of viscosity can correspond to unphysical (negative) values [29]. This is due to the fact that the inhomogeneity of the fluid in pores may result to rapid variations in the strain rate over a length typical of intermolecular correlations. In such circumstances, the Newton's law must be generalized by a nonlocal constitutive equation [30].

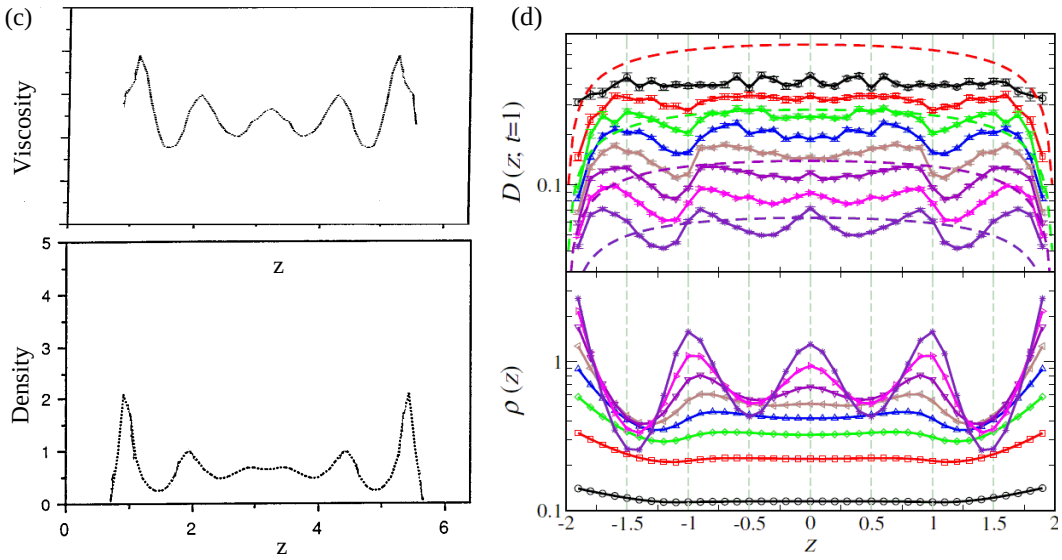

Figure 1.7: Local transport coefficients of fluids confined between solid surfaces. (a) The viscosity and density profiles [26]. (b) The diffusion and density profiles [23].

Most of the theoretical works for determining the transport coefficients of a strongly confined fluid are based on the generalized Enskog's kinetic theory [26-28, 31]. This theory requires determining the pair correlation function which can be done by using the spatially coarse grained model as in the distribution function theory. There also exists another theory in which the main idea employed is similar to the DFT one, i.e. the local transport coefficients at a given position are heuristically assumed to be equal to those of a homogeneous fluid at a bulk state corresponding to a locally averaged density around the given position [32-33]. This approach is called the local average density model (LADM).

The transport coefficients obtained from these theories exhibit characteristics similar to what observed in the MD simulations, i.e. the effective and local transport coefficients that varies appreciably with the pore size and the position respectively, see Fig. 1.7 [26-28, 31-33]. However, comparisons between the MD simulation and theoretical results have indicated that such theories cannot always predict quantitatively the transport coefficients for different fluids and different states. In addition, the use of such theories are not able to deal with the dramatic

increase of the effective shear viscosity of fluid in very narrow pores as obtained in some non-equilibrium MD simulations.

The effective and local transport coefficients of fluid confined slit narrow pores are so correlated to the effective and local densities (but not only) which are strongly influenced by the fluid-solid interaction [3, 16, 20]. This means that for a given fluid the characteristics of the solid surface have a significant effect on the transport coefficients [3-4, 34-35]. In fact, other “apparent” quantities related to the transport such as the slip length and the friction force, are also strongly affected by the characteristics of the solid surface [3-4, 35-36].

1.3. Swelling/Shrinkage

To better understand the well known swelling/shrinkage of some porous media (clay minerals, coal seams, porous glass, etc.) due to the presence of fluids as observed experimentally [1-2, 37], molecular simulations have been used to provide a microscopic picture of such systems [37-43]. Results obtained from the molecular simulations at the micropore scale have shown that the normal pressure and the free energy of the fluid in pores appreciably vary with the pore size, the fluid type and fluid-solid interactions, see Fig. 1.8 [1, 8-10, 37-38, 41-42]. In fact, such behaviors are an indirect consequence of the inhomogeneity of the fluid in pores due to physical adsorption and molecular packing. In other words, the swelling/shrinkage of such micro-porous medium is induced by the physical adsorption and molecular packing at the pore-scale (in uncharged systems).

The modeling of the swelling/shrinkage of porous medium requires thus in a first step an accurate description of the thermodynamics of the confined fluid [5, 40]. For mesoporous medium, the thermodynamics of the fluid in pores is mainly influenced by the physical adsorption and can so be estimated thanks to the help of a usual theory of adsorption [8, 44-

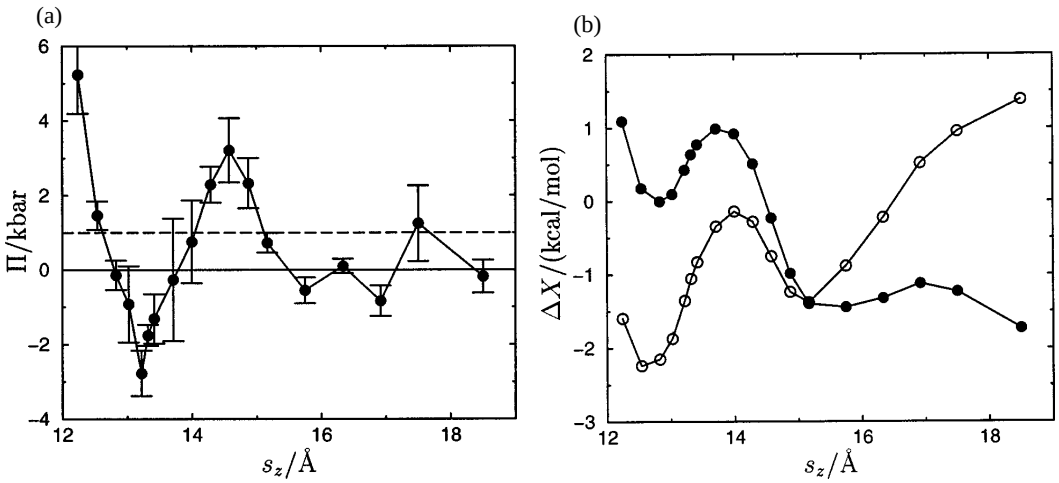

Figure 1.8: Swelling of clay minerals obtained from the MD simulations. (a) Variation in the disjoining pressure with the size of the clay layer spacing [38]. (b) Variations in clay swelling free energy for different external pressures with the size of the clay layer spacing [38].

45]. In micro-porous medium, the thermodynamics can be well described by using the distribution function theory or the DFT as mentioned above for simple fluids in simple pores, however such approaches are not as efficient to deal with more complex systems involving association, charges, etc. The second step is to take into account the influence of the modification on the fluid thermodynamic to deal with the porous medium. To do so, among possible approaches, modified poromechanics constitutive equations have been derived [1, 8-10, 42]. They include additional quantities/variables to take into account explicitly the modifications in the apparent fluid and the fluid-solid interactions and they seem able to lead to reasonable results in relatively simple situations, see Fig. 1.9.

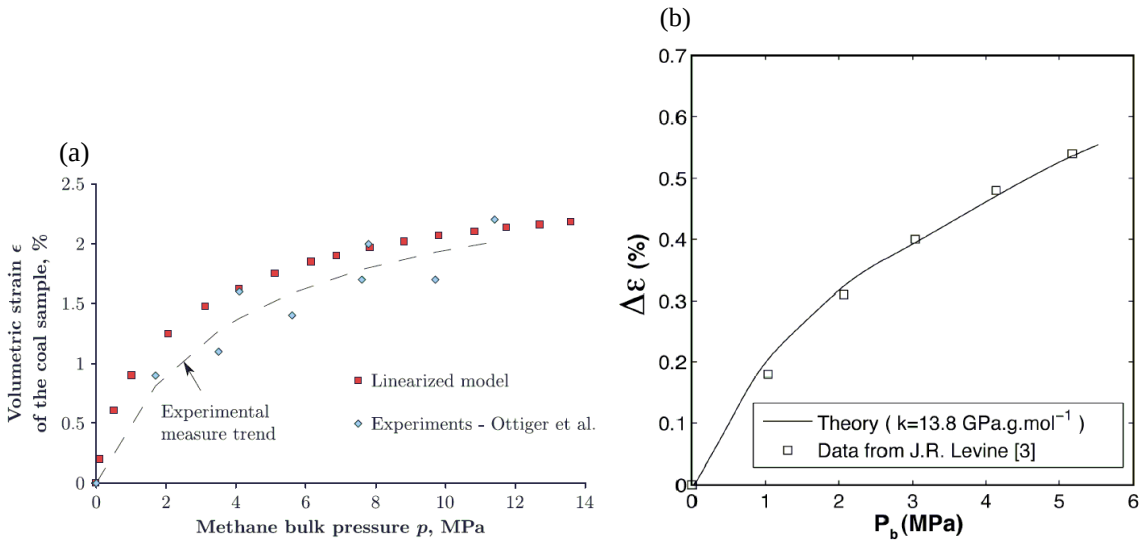

Figure 1.9: Evolution of the volumetric strain with the bulk pressure obtained from experiments and extended poromechanics. (a) A coal sample immersed in methane using Brochard *et al.*'s derived constitutive equations [10]. (b) An Illinois charcoal in methane using Pijaudier-Cabot *et al.*'s derived constitutive equations [9].

1.4. Organization of the Dissertation

The body of the dissertation is divided into 6 chapters.

In chapter 2, a brief description of the theories to model the fluid dynamics and the poromechanics at the continuum scale are first introduced. Then, some details of the molecular simulation methods developed in the literature are presented and discussed.

In chapter 3, two grand canonical-like molecular dynamics approaches are first presented. Then, the transient behavior of the diffusion process associated with the migration of one fluid into another one confined between parallel solid walls is studied.

In chapter 4, the local shear viscosity of strongly inhomogeneous fluids (from the hard-sphere to Lennard-Jones fluids) at different fluid states is first studied by using the molecular simulations. Then a tractable theory is developed to predict the viscosity profile in such conditions from the density one.

In chapter 5, different molecular dynamics schemes used in the literature to study the shear behavior of a confined thin film are presented and discussed. The influence of the choice of the molecular dynamics scheme of the shear properties (viscosity, friction, etc.) of such thin film is then analyzed.

In chapter 6, the volumetric deformation (swelling/shrinkage) of a simple saturated (by a liquid) slit pore induced by solid displacement in the direction parallel to the solid-fluid interface is studied by non equilibrium molecular simulations.

In chapter 7, the main results are summarized and perspectives associated to each chapter are then provided.

References

[1] O. Coussy, Mechanics and Physics of Porous Solids, John Wiley & Sons, Chichester (2010)

[2] O. Coussy, Poromechanics, John Wiley & Sons, Chichester (2004)

[3] J. Israelachvili, *Intermolecular and Surface Forces*, Academic Press, Third Edition (2010)

[4] G. Karniadakis, A. Beskok and N. Aluru, Microflows and Nanoflows, Springer (2004)

[5] J. Hansen and I. R. McDonald: Theory of simple liquid, Third Edition, Elsevier, (2006)

[6] M. J. Blunt, M. D. Jackson, M. Piri, P. H. Valvatne, Advances Water Res. 25, 1069 (2002).

[7] Q. Cai, A. Buts, N.A. Seaton, M.J. Biggs, Chem. Eng. Sci. 63, 3319 (2008)

[8] M. Vandamme, L. Brochard, B. Lecampion and O. Coussy, J. Mech. Phys. Solids 58, 1489 (2010)

[9] G. Pijaudier-Cabot, R. Vermorel, C. Miqueu and B. Mendiboure, C. R. Mecanique 339, 770 (2010)

[10] L. Brochard, M. Vandamme and R. J. M. Pellenq, J. Mech. Phys. Solids 60, 606 (2012)

[11] J. Klein and E. Kumacheva, Science 269, 816 (1995)

[12] H. Kajiro, A. Kondo, K. Kaneko and H. Kanoh, Int. J. Mol. Sci. 11, 3803 (2010)

[13] J. R. Levine, Geological Society, London, Special Publication 109, 197 (1996)

[14] M.P. Allen and D.J. Tildesley, Computer Simulation of Liquids, Oxford University Press (1989)

[15] K. E. Gubbins and J. D. Moore, Ind. Eng. Chem. Res. 49, 3026 (2010)

[16] M. Schoen, Computer simulation of condensed phases in complex geometries, New series m: monographs, Lecture note in physics, m17 (1993)

[17] J. Gao, W. D. Luedtke and U. Landman, J. Chem. Phys., 106, 4309 (1997)

[18] T. K. Vanderlick, L. E. Scriven and H. T. Davis, J. Chem. Phys. 90(4), 2422 (1988)

[19] P. Tarazona, J. A. Cuesta and Y. Martínez-Ratón, Density functional theories of hard particle systems, Lecture note in physics, 753, (Springer-Verlag, Berlin–Heidelberg, 2008).

[20] M. H. Muser, M. Urbakh and M. O. Robbins, Adv. Chem. Phys. 126, 188 (2003)

[21] I. Bitsanis, S. A. Somers, H. T. Davis and M. Tirrell, J. Chem. Phys. 93, 3427 (1990)

[22] J. J. Magda, M. Tirrell and H. T. Davis, J. Chem. Phys. 83, 1888 (1985)

[23] J. Mittal, T. M. Truskett, J. R. Errington and G. Hummer, Phys. Rev. Lett. 100, 145901 (2008)

[24] J. Gao, W. D. Luedtke and U. Landman, Phys. Rev. Let. 79, 705 (1997)

[25] J. Gao, W. D. Luedtke, D. Gourdon, M. Ruths, J. N. Israelachvili and U. Landman, J. Phys. Chem. B 108, 3410 (2004)

[26] X. D. Din and E. E. Michaelides, Phys. Fluids 9, 3915 (1997)

[27] E. Akhmatskaya, B. D. Todd, P. J. Daivis, D. J. Evans, K. E. Gubbins and L. A. Pozhar, J. Chem. Phys. 106, 4684 (1997)

[28] L. A. Pozhar, Phys. Rev. E 61, 1432 (2000)

[29] K. P. Travis and K. E. Gubbins, J. Chem. Phys. 112, 1984 (2000)

[30] B. D. Todd, J. S. Hansen and P. J. Daivis, Phys. Rev. Lett. 100, 195901 (2008)

[31] T. K. Vanderlick and H. T. Davis, J. Chem. Phys. 87, 1791 (1987)

[32] I. Bitsanis, T.K Vanderlick, M. Tirell and H.T. Davis, J. Chem. Phys. 87, 1733 (1987)

[33] I. Bitsanis, T.K Vanderlick, M. Tirell and H.T. Davis, J. Chem. Phys. 89, 3152 (1988)

[34] A. Saugey, L. Joly, C. Ybert, J. L. Barrat and L. Bocquet, J. Phys.: Condens. Matter 17, S4075 (2005)

[35] H. Berro, Phd thesis: A molecular dynamics approach to nano-scale lubrication. Institut National des Sciences Appliquées de Lyon (2010)

[36] Bocquet and J.L. Barrat, Soft Matter 3, 685 (2007)

[37] E. J. M. Hensen, B. Smit, J. Phys. Chem. B 106, 126664 (2002)

[38] R. M. Shroll and D. E. Smith, J. Chem. Phys. 111, 9025 (1999)

[39] D. D. Do, D. Nicholson, H.D. Do, J. Phys. Chem. C 112, 14075 (2008).

[40] M. Jeffroy, A.H. Fuchs, A. Boutin, Chemical Communications 28, 3275 (2008)

[41] A. Botan, Phd thesis: Modélisation moléculaire d'argile en contact avec un réservoir de CO_2. UNIVERSITÉ PARIS 6 (2011)

[42] L. Brochard, M. Vandamme, R. Pellenq, T. Feng-Chong, Langmuir 28, 2659 (2012)

[43] V.T. Nguyen, D.D. Do, D. Nicholson, Journal of Colloid and Interface Science 388, 209 (2012)

[44] G. Y. Gor and A. V. Neimark, Langmuir 26, 13027 (2010)

[45] G. Y. Gor and A. V. Neimark, Langmuir 27, 6926 (2011)

Chapter 2

Theory and Simulation

This chapter presents the theories and the simulations method which forms the basics to determine the properties/behavior of a fluid and a porous medium. The first two parts are brief descriptions of the classical equations used to deal with the fluid dynamics and poremechanics at the continuum scale. The subsequent parts detail the molecular dynamics simulations approaches for exploring the properties of a fluid at the molecular scale.

2.1. Conservation Equations

At the macroscopic scale, a fluid is assumed to be a continuum, i.e. it can be subdivided into infinitesimal fluid elements [1]. However, the fluid element should be large enough to contain a huge number of fluid molecules so that it can be viewed as a continuous medium. This means that the length scale of the fluid element should be much larger than the mean free path of the molecules composing the fluid. In this approximation, all physical properties that characterize a fluid (i.e. density, pressure, temperature, velocity etc.) are well defined at any point in the fluid and at any time.

In that frame, to determine the behavior of the fluid, one solves the ***conservation equations*** associated to mass, momentum and energy conservation and subject to the ***constitutive equations*** governing mass diffusion (Fick's Law), momentum transfer (Newton's Law), energy (Fourier's Law), etc. , together with a thermodynamic equation of state [1].

So, in this section, we briefly introduce the conservation equations and the constitutive equations which are generally employed to study the behavior of a fluid at the ***continuum scale***.

2.1.1. The Continuity Equation

The conservation equation for mass states that the time rate of decrease of the mass inside a finite control volume V fixed in space is equal to the net mass flow out of the control volume through surface S, see Fig. 2.1 [2]. From this statement, by evaluating the variation of the mass in the fluid control volume, it is possible to deduce the differential equation associated to the local mass conservation as [2]:

$$\frac{\partial \rho}{\partial t} + \nabla \cdot \left(\rho \vec{V} + M \vec{J} \right) = 0 \tag{2.1}$$

or

$$\frac{D\rho}{Dt} + \rho \nabla \cdot \vec{V} + M \nabla \cdot \vec{J} = 0 \tag{2.2}$$

where ρ is the density of the fluid, $\vec{V}$ is the streaming velocity, $\vec{J}$ is the diffusive flux per unit time per unit area due to mass diffusion and M is the molar mass. Eqs. (2.1) and (2.2) are the ***continuity equations*** in which the former is in the *conservative form* and the latter is in the *non-conservative* form [2].

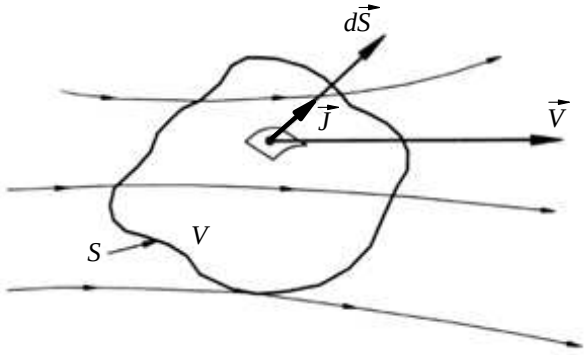

Figure 2.1: Finite control volume fixed in space [2].

2.1.2. The Momentum Equation

The conservation equation for momentum states that the deformation of a fluid element submitted to a stress is governed by the Newton's 2nd law [2]. By analyzing the

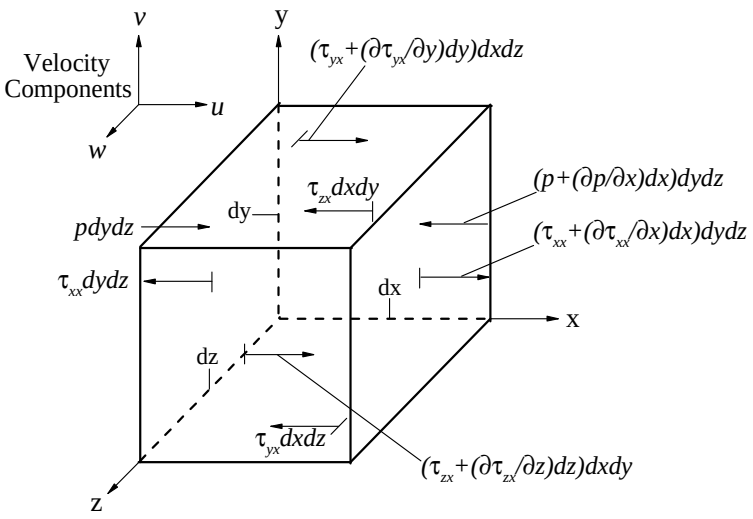

Figure 2.2: Infinitesimally small, evolving fluid element. Only the forces in the *x* direction are shown [2].

evolution of a cuboidal fluid element as shown in Fig. 2.2, the differential equations on the local velocity can be written as [2]:

$$\rho\frac{Du}{Dt}=\left(-\frac{\partial p}{\partial x}+\frac{\partial\tau_{xx}}{\partial x}+\frac{\partial\tau_{yx}}{\partial y}+\frac{\partial\tau_{zx}}{\partial z}\right)+\rho f_x \tag{2.3a}$$

$$\rho\frac{Dv}{Dt}=\left(-\frac{\partial p}{\partial y}+\frac{\partial\tau_{xy}}{\partial x}+\frac{\partial\tau_{yy}}{\partial y}+\frac{\partial\tau_{zy}}{\partial z}\right)+\rho f_y \tag{2.3b}$$

$$\rho\frac{Dw}{Dt}=\left(-\frac{\partial p}{\partial z}+\frac{\partial\tau_{xz}}{\partial x}+\frac{\partial\tau_{yz}}{\partial y}+\frac{\partial\tau_{zz}}{\partial z}\right)+\rho f_z \tag{2.3c}$$

or

$$\frac{\partial(\rho u)}{\partial t}+\nabla\cdot\left(\rho u\vec{V}\right)=\left(-\frac{\partial p}{\partial x}+\frac{\partial\tau_{xx}}{\partial x}+\frac{\partial\tau_{yx}}{\partial y}+\frac{\partial\tau_{zx}}{\partial z}\right)+\rho f_x \tag{2.4a}$$

$$\frac{\partial(\rho v)}{\partial t}+\nabla\cdot\left(\rho v\vec{V}\right)=\left(-\frac{\partial p}{\partial y}+\frac{\partial\tau_{xy}}{\partial x}+\frac{\partial\tau_{yy}}{\partial y}+\frac{\partial\tau_{zy}}{\partial z}\right)+\rho f_y \tag{2.4b}$$

$$\frac{\partial(\rho w)}{\partial t}+\nabla\cdot\left(\rho w\vec{V}\right)=\left(-\frac{\partial p}{\partial z}+\frac{\partial\tau_{xz}}{\partial x}+\frac{\partial\tau_{yz}}{\partial y}+\frac{\partial\tau_{zz}}{\partial z}\right)+\rho f_z \tag{2.4c}$$

where u, v, w are the components of $\vec{V}$ in the x, y, z directions respectively, p is the pressure, $\tau_{\alpha\beta}$ is the stress in the β direction exerted on a plane perpendicular to the α axis, and f_α is the body force per unit mass acting on the fluid element in the α direction. Eqs. (2.3) and (2.4) are the ***momentum equations***, in which the former is in the *non-conservative* form and the latter is in the *conservative* form [2].

2.1.3. The Energy Equation

The conservation equation for energy states that the rate of change of energy inside a fluid element is equal to the net flux of heat into the fluid element plus the rate of work done on the fluid element [2]. Considering the variation in the energy of the fluid element having a cuboidal geometry, as shown in Fig. 2.3, the differential equation of the internal energy per unit mass can be obtained as [2]:

$$\begin{aligned}\rho\frac{D}{Dt}\left(e+\frac{V^2}{2}\right)=&\left[\rho q^{'}-\left(\frac{\partial q_x^{'}}{\partial x}+\frac{\partial q_y^{'}}{\partial y}+\frac{\partial q_z^{'}}{\partial z}\right)\right]+\rho\vec{f}\cdot\vec{V}+\left[-\left(\frac{\partial(up)}{\partial x}+\frac{\partial(vp)}{\partial y}+\frac{\partial(wp)}{\partial z}\right)\right.\\&+\left(\frac{\partial(u\tau_{xx})}{\partial x}+\frac{\partial(u\tau_{yx})}{\partial y}+\frac{\partial(u\tau_{zx})}{\partial z}\right)+\left(\frac{\partial(v\tau_{xy})}{\partial x}+\frac{\partial(v\tau_{yy})}{\partial y}+\frac{\partial(v\tau_{zy})}{\partial z}\right)\\&\left.+\left(\frac{\partial(w\tau_{xz})}{\partial x}+\frac{\partial(w\tau_{yz})}{\partial y}+\frac{\partial(w\tau_{zz})}{\partial z}\right)\right]\end{aligned}\tag{2.5}$$

or

$$\begin{aligned}&\frac{\partial}{\partial t}\left[\rho\left(e+\frac{V^2}{2}\right)\right]+\nabla\left[\rho\left(e+\frac{V^2}{2}\right)\cdot\vec{V}\right]=\\&=\left[\rho q^{'}-\left(\frac{\partial q_x^{'}}{\partial x}+\frac{\partial q_y^{'}}{\partial y}+\frac{\partial q_z^{'}}{\partial z}\right)\right]+\rho\vec{f}\cdot\vec{V}+\left[-\left(\frac{\partial(up)}{\partial x}+\frac{\partial(vp)}{\partial y}+\frac{\partial(wp)}{\partial z}\right)\right.\\&+\left(\frac{\partial(u\tau_{xx})}{\partial x}+\frac{\partial(u\tau_{yx})}{\partial y}+\frac{\partial(u\tau_{zx})}{\partial z}\right)+\left(\frac{\partial(v\tau_{xy})}{\partial x}+\frac{\partial(v\tau_{yy})}{\partial y}+\frac{\partial(v\tau_{zy})}{\partial z}\right)\\&\left.+\left(\frac{\partial(w\tau_{xz})}{\partial x}+\frac{\partial(w\tau_{yz})}{\partial y}+\frac{\partial(w\tau_{zz})}{\partial z}\right)\right]\end{aligned}\tag{2.6}$$

where e is the internal energy per unit mass, $\vec{f} = f_x\vec{e}_x + f_y\vec{e}_y + f_z\vec{e}_z$ in which $\vec{e}_\alpha$ is the unit vector in the α direction, q' is the rate of volumetric heat addition per unit mass and q'_α is the heat transferred in the α direction per unit time per unit area by the thermal conduction. Eqs. (2.5) and (2.6) are the ***energy equations***, in which the former is in the *non-conservative* form and the latter is in the *conservative* form [2].

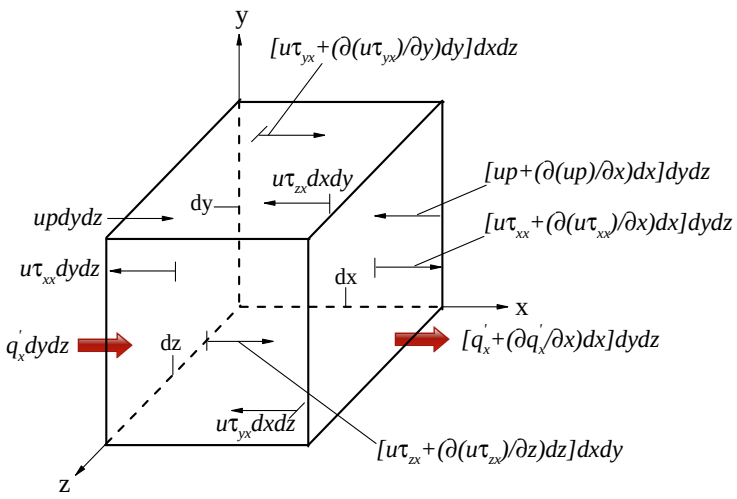

Figure 2.3: Energy fluxes associated with an infinitesimally small, evolving fluid element. For simplicity, only the fluxes in the *x* direction are shown [2].

2.1.4. The Constitutive Equation

The different properties: density, pressure, temperature and velocity, of a fluid can be completely determined by solving these conservation equations (+ an equation of states) if the diffusive fluxes (mass, momentum and energy) are specified.

We briefly present in what follows the usual constitutive equations that describe the diffusive fluxes in a pure fluid.

2.1.4.1. Fick's Law

The Fick's law for mass diffusion states that the diffusive flux per unit time per unit area due to mass diffusion is proportional to the opposite of the gradient in density [2]:

$$\vec{J} = -D\nabla\left(\frac{\rho}{M}\right) \tag{2.7}$$

2.1.4.2. Newton's Law

The Newton's law states that the shear stress in a fluid is proportional to the time-rate-of-strain, i.e. the velocity gradients. From this statement, Stokes obtained [2]:

$$\tau_{xx} = \lambda\nabla\cdot\vec{V} + 2\mu\frac{\partial u}{\partial x} \tag{2.8a}$$

$$\tau_{yy} = \lambda\nabla\cdot\vec{V} + 2\mu\frac{\partial v}{\partial y} \tag{2.8b}$$

$$\tau_{zz} = \lambda\nabla\cdot\vec{V} + 2\mu\frac{\partial w}{\partial z} \tag{2.8c}$$

$$\tau_{xy} = \tau_{yx} = \mu\left(\frac{\partial v}{\partial x} + \frac{\partial u}{\partial y}\right) \tag{2.8d}$$

$$\tau_{xz} = \tau_{zx} = \mu\left(\frac{\partial u}{\partial z} + \frac{\partial w}{\partial x}\right) \tag{2.8e}$$

$$\tau_{yz} = \tau_{zy} = \mu\left(\frac{\partial w}{\partial y} + \frac{\partial v}{\partial z}\right) \tag{2.8f}$$

where μ is the shear viscosity coefficient and λ is the bulk viscosity coefficient. Stokes proposed the hypothesis that [2]:

$$\lambda = -\frac{2}{3}\mu \tag{2.9}$$

which is usually used in literature.

2.1.4.3. Fourier's Law

The Fourier's law for heat diffusion/conduction states that the time rate of heat transfer per unit area through a material is proportional to the opposite of the gradient in temperature [2]:

$$q_x^{'} = -k\frac{\partial T}{\partial x} \tag{2.10a}$$

$$q_y^{'} = -k\frac{\partial T}{\partial y} \tag{2.10b}$$

$$q_z^{'} = -k\frac{\partial T}{\partial z} \tag{2.10c}$$

where k is the thermal conductivity of the fluid element.

2.2. Poromechanics

Similar to what have been presented for a pure fluid, to determine the behavior of a porous medium (composed of the solid phase and the fluid phases) at the macroscopic scale, i.e. the ***poromechanics*** of the studied system, requires:

- To construct differential equations associated to the porous medium as a whole.
- To establish constitutive equations [3-4].

To derive the differential equations, the porous medium is assumed to be a continuum [3-4]. By doing so, the porous medium can be subdivided into infinitesimal elements for which the hypothesis of continuity and homogeneity are valid, i.e. the heterogeneities at the microscopic scale (in an element) are ignored. Consider a cuboidal porous element as shown in Fig. 2.4, the ***mechanical equilibrium*** conditions leads to [3-4]:

$$\frac{\partial \tau_{xx}}{\partial x} + \frac{\partial \tau_{yx}}{\partial y} + \frac{\partial \tau_{zx}}{\partial z} = 0 \tag{2.11a}$$

$$\frac{\partial \tau_{xy}}{\partial x} + \frac{\partial \tau_{yy}}{\partial y} + \frac{\partial \tau_{zy}}{\partial z} = 0 \tag{2.11b}$$

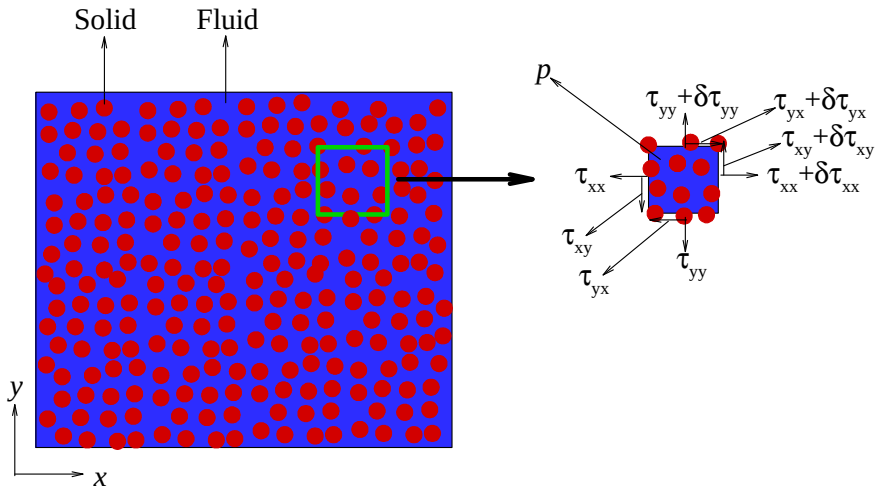

Figure 2.4: 2D view of porous medium. The red dots represent the solid phase. The blue domain is the fluid phase.

$$\frac{\partial \tau_{xy}}{\partial x}+\frac{\partial \tau_{yy}}{\partial y}+\frac{\partial \tau_{zy}}{\partial z}=0 \qquad (2.11c)$$

where $\tau_{\alpha\beta}$ is the stress on the surfaces of this element.

These stresses are composed of two parts: one which is caused by the hydrostatic pressure p of the fluid filling the pores, and the other by the average stress in the solid phase [3-4]. It should be mentioned that the classical definition of p is inappropriate when the pore size is very small or the order of the size of the fluid molecule (this quantity is affected by the porous medium itself) [5]. However, in this part, for simplicity the equations introduced corresponds to a porous medium in which the pore size is sufficiently large (macropores) so that the definition of the hydrostatic pressure is held and the fluid can be treated as a continuum.

To describe completely the behavior of a porous medium at the macroscopic scale requires specifying the relations between the stresses and the deformation of the porous medium, i.e. the constitutive equations. In this part, we present the constitutive equations for a

porous medium that possesses the following basic properties : (1) isotropy of the material, (2) reversibility of stress-strain relations under final equilibrium, (3) linearity of stress-strain relations, (4) small strains, (5) the fluid contained in the pores is incompressible, (6) the fluid flows through the porous medium according to Darcy's law [3-4]. In that frame, the ***constitutive equations*** are given as [3-4]:

$$\tau_{xx} = 2G\left(\xi_{xx} + \frac{\nu\xi}{1-2\nu}\right) - \alpha p \tag{2.12a}$$

$$\tau_{yy} = 2G\left(\xi_{yy} + \frac{\nu\xi}{1-2\nu}\right) - \alpha p \tag{2.12b}$$

$$\tau_{zz} = 2G\left(\xi_{zz} + \frac{\nu\xi}{1-2\nu}\right) - \alpha p \tag{2.12c}$$

$$\tau_{xy} = \tau_{yx} = G\gamma_{xy} \tag{2.12d}$$

$$\tau_{yz} = \tau_{zy} = G\gamma_{yz} \tag{2.12e}$$

$$\tau_{zx} = \tau_{xz} = G\gamma_{zx} \tag{2.12f}$$

$$\varphi = \alpha\xi + \frac{p}{N} \tag{2.12g}$$

where, G, υ, N and α are the shear modulus and Poisson's ratio, the Biot modulus and Biot coefficient respectively, and φ is the increment of fluid volume per unit volume of the porous medium, or a porosity. The strain components of the deformation are defined as [3-4]:

$$\xi_{xx} = \frac{\partial\bar{u}}{\partial x} \tag{2.13a}$$

$$\xi_{yy} = \frac{\partial\bar{v}}{\partial y} \tag{2.13b}$$

$$\xi_{zz} = \frac{\partial\bar{w}}{\partial z} \tag{2.13c}$$

$$\xi = \xi_{xx} + \xi_{yy} + \xi_{zz} \tag{2.13d}$$

$$\gamma_{xy} = \frac{\partial \bar{v}}{\partial x} + \frac{\partial \bar{u}}{\partial y} \tag{2.13e}$$

$$\gamma_{yz} = \frac{\partial \bar{w}}{\partial y} + \frac{\partial \bar{v}}{\partial z} \tag{2.13f}$$

$$\gamma_{zx} = \frac{\partial \bar{w}}{\partial x} + \frac{\partial \bar{u}}{\partial z} \tag{2.13g}$$

where, $\bar{u}$, $\bar{v}$ and $\bar{w}$ are the components of the displacement of the porous medium in the x, y and z directions respectively.

Substituting Eqs. (2.12) and (2.13) into Eq. (2.11), leads to three equations for four unknowns $\bar{u}$, $\bar{v}$, $\bar{w}$ and φ. Therefore, an additional differential equation has to be introduced to have a closed system. To do so, using a continuity-like equation, one can obtain [3-4]:

$$\frac{\partial \varphi}{\partial t} = -\frac{\partial u}{\partial x} - \frac{\partial v}{\partial y} - \frac{\partial w}{\partial z} \tag{2.14}$$

where the velocity components u, v and w are determined from the classical ***Darcy's law*** as [3-4]:

$$u = -k\frac{\partial \varphi}{\partial x} \tag{2.15a}$$

$$v = -k\frac{\partial \varphi}{\partial y} \tag{2.15b}$$

$$w = -k\frac{\partial \varphi}{\partial z} \tag{2.15c}$$

where k is called the coefficient of permeability of the porous medium.

2.3. Molecular Dynamics Simulations

When one is dealing with a fluid element whose length scales are comparable to the size of the molecules composing the fluid, then the previous equations used at the continuum scale are no longer always adequate. This is because that the fluid cannot be subdivided into

infinitesimal fluid element that can be viewed as continuous medium, e.g. the fluid transport properties are not precisely defined at any point in the fluid and at any instant time (because of fluctuations). In such situations, the fluid must be treated as discontinuous, composed of atoms, and obeys the equations of the statistical mechanics [1, 6-9]. However, most properties of realistic fluids (in particular transport properties) at the molecular scale cannot be determined by analytically solving the equations of the statistical mechanics [1, 6-9]. In such situations, molecular simulations have shown to be a valuable tool to circumvent numerically that difficulty.

The basic idea of the molecular simulation is to solve numerically the equations of the statistical mechanics to sample efficiently the integrals of the configurations of a system composed of atoms by either the ***Monte-Carlo*** (MC) or the ***Molecular Dynamics*** (MD) approach [1, 6-9]. In other words, the molecular simulations approaches allow exploring numerically the possible configurations of the system using two different approaches (they are "equivalent" if ergodicity is respected) as shown on Fig 2.5:

- By following a stochastic process obeying probability distribution laws of the statistical mechanics for the MC method,
- By solving the deterministic equations of motion of all atoms in the system for the MD method.

Although the MC method requires usually less CPU time than the MD method, the MD method is the most widely used among the two to study the behavior of the fluids [1, 6-9]. This is because the states/configurations transition in the MC method is completely stochastic, i.e. the dynamics of the systems is not explicitly described. Whereas the MD method describes these transitions that are governed by the classical equations of motion of all the atoms and so gives access to the dynamic of the system. In fact, the MC approach is

very efficient when dealing with static properties of relatively large and complex systems at equilibrium.

In the following parts are introduced some details of the MD methods that are usually used to study the properties of a fluid at the molecular scale.

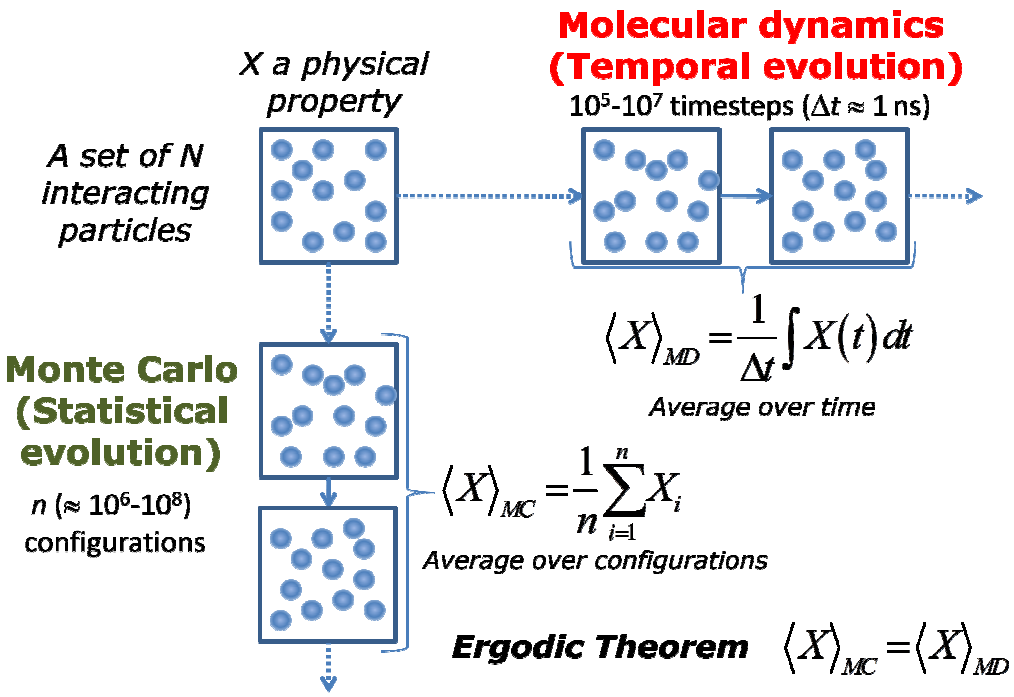

Figure 2.5: The two usual molecular simulation approaches

2.3.1. Equations of Motion

First, let start considering an isolated fluid system composed of N atoms interacting via a total potential U, in which the coordinate of atom i is denoted by $\mathbf{r}_i$ and the configuration is denoted by $\mathbf{r}^N = \{\mathbf{r}_1, \mathbf{r}_2, \ldots, \mathbf{r}_N\}$ [6].

The ***Lagrangian*** of the system L which allows describing the dynamics of the N interacting atoms depends on $\mathbf{r}^N$ and $\mathbf{r}'^N$ where:

$$\mathbf{r}'^N = \frac{\partial \mathbf{r}^N}{\partial t} = \left\{\frac{\partial \mathbf{r}_1}{\partial t}, \frac{\partial \mathbf{r}_2}{\partial t}, \ldots, \frac{\partial \mathbf{r}_N}{\partial t}\right\} = \{\mathbf{r}'_1, \mathbf{r}'_2, \ldots, \mathbf{r}'_N\} \tag{2.16}$$

More precisely, the Lagrangian form of the equation of motion of an atom i in the system is:

$$\frac{d}{dt}\left(\partial L/\partial \mathbf{r}_i'\right)-\left(\partial L/\partial \mathbf{r}_i\right)=0 \tag{2.17}$$

The generalized momentum $\mathbf{p}_i$ conjugate to $\mathbf{r}_i$ is defined as:

$$\mathbf{p}_i=\frac{\partial L\left(\mathbf{r}^N,\mathbf{r}'^N\right)}{\partial \mathbf{r}_i'} \tag{2.18}$$

The ***Hamiltonian*** is defined as:

$$H\left(\mathbf{p}^N,\mathbf{r}^N\right)=\sum_i \mathbf{r}_i'\cdot\mathbf{p}_i-L\left(\mathbf{r}^N,\mathbf{r}'^N\right) \tag{2.19}$$

and the Hamiltonian form of equations of motion of an atom i in the system is given by:

$$\mathbf{r}_i'=\frac{\partial H\left(\mathbf{p}^N,\mathbf{r}^N\right)}{\partial \mathbf{p}_i} \tag{2.20a}$$

$$\mathbf{p}_i'=-\frac{\partial H\left(\mathbf{p}^N,\mathbf{r}^N\right)}{\partial \mathbf{r}_i} \tag{2.20b}$$

If $\mathbf{r}_i$ represents the Cartesian coordinate of atom i, the Lagrangian of the system is simply:

$$L\left(\mathbf{r}^N,\mathbf{r}'^N\right)=\sum_{i=1}^{N}\sum_{\alpha}\frac{1}{2}m_i r_{i\alpha}'^2-U\left(\mathbf{r}^N\right) \tag{2.21}$$

where m_i is the atomic mass of atom i, and the index α runs over the different (x,y,z) components.

Substituting Eq. (2.21) into Eq. (2.17), leads to (Lagragian form):

$$m_i\mathbf{r}_i''=-\nabla_{\mathbf{r}_i}U \tag{2.22}$$

and substituting Eq. (2.21) into Eqs. (2.19) and (2.20) leads to (Hamiltonian form):

$$\mathbf{r}_i'=\frac{\mathbf{p}_i}{m_i} \tag{2.23a}$$

$$\mathbf{p}_i'=-\nabla_{\mathbf{r}_i}U \tag{2.23b}$$

It is worthy to notice that the Lagrangian and Hamiltonian equations of motion are fully equivalent. From the mathematical point of view, the difference between the Lagrangian and the Hamiltonian equations of motion is that the former is composed of 3*N* second-order differential equations while the latter is composed of 6*N* first-order differential equations. From the mechanical point of view, solving the Lagrangian equation of motion, i.e. Eq. (2.22), allows to obtain the evolution of the coordinates of the atoms with the time only, while the Hamiltonian one, i.e. Eq. (2.23), provides not only the coordinates but also of the momentum over time. In fact, from the evolution of the coordinates with the time obtained from the Lagrangian equation of motion, one can deduce the momentum of the atoms.

2.3.2. Ensembles

From the information at the microscopic level, i.e. atomic coordinates and velocities, so-called ***microstates***, the fluid macroscopic thermodynamics, i.e. internal energy, pressure, temperature etc., can be fully determined [6-9]. A collection of microstates in each of which the same macroscopic thermodynamic restrictions are imposed, is defined as a ***microscopic ensemble*** [6-7]. An ensemble is so specified by the choice of a set of constrained macroscopic thermodynamic variables.

During MD simulations, if the microstates of a fluid are generated from Eqs. (2.22) or (2.23), both density and the total energy (E) are maintained. This situation corresponds to the ***micro canonical ensemble*** (NVE). However, to directly compare results of MD simulations to experiments, one has to use an adequate ensemble, i.e. constrain the same macroscopic thermodynamics variables during MD simulations as the ones imposed in an experiment [6-7, 10].

For comparison with experiments, the ensembles that are widely employed in the MD simulations consist of the ***canonical ensemble*** (NVT), the ***isothermal-isobaric ensemble***

(NPT) and the ***grand canonical ensemble*** (μVT). The first corresponds to a constant number of atoms N, volume V, and temperature T during simulations. In the second, N, pressure P, and T are held constant. In the last the chemical potential μ, V and T are kept constant [6-7].

The canonical ensemble is the most widely used among these ensembles, which is probably due to its easy implementation compared to other ensemble and because often the properties of the fluids are described as a function of temperature and density. When dealing with fluids in which it is desired to constrain the temperature and pressure, as it is generally the case in experiments, the MD simulations must be performed in the isothermal-isobaric ensemble. This ensemble is usually used to elucidate experimental behavior or to predict some results that are difficult to obtain by experiments. The MD simulations in the grand canonical ensemble are suitable to investigate an "open" fluid that is in equilibrium with a reservoir. In the laboratory, such situation usually corresponds to studies on a fluid in contact with a solid surface or confined in a porous medium.

In what follows are briefly introduced the way the "natural" equations of motion are modified such that some macroscopic thermodynamics are constrained.

2.3.2.1. Constant Temperature

To maintain ***the temperature*** of a system one needs a ***thermostat***. Before describing thermostats that are usually used in the MD simulations, it is worthy to mention that for a system of a fluid confined between solid surfaces as studied in this work, to dissipate any heat generated in the fluid, for example by the viscous dissipation, thermostat can be applied on the fluid or the solid (or on both). In fact, the latter, usually named ***boundary thermostat*** [11], is probably more realistic. However, to do so, one needs to consider the realistic motions of the solid atoms, which is CPU time consuming. Furthermore, it seems that the approach based

on a thermostat applied on the fluid only provides results similar to those obtained from the boundary thermostat when the shear rate is not so high [11-13]. Thus, in this work we have employed the thermostat on the fluid particles only to maintain the temperature around a constant value.

The average temperature of a fluid $\overline{T}$ is related to the average kinetic energy of the fluid $\overline{K}$ as [6]:

$$\overline{K} = \langle K \rangle = \frac{1}{2} k_B N_f \overline{T} \tag{2.24}$$

where N_f is the number of degrees of freedom, k_B is the Boltzmann constant, $\langle . \rangle$ denotes the average value, and K is the instantaneous kinetic energy that is defined as:

$$K = \frac{1}{2} \sum_{i=1}^{N} m_i \mathbf{r}_i'^2 \tag{2.25}$$

Substituting Eq. (2.25) into Eq. (2.24), we obtain the average temperature:

$$\overline{T} = \left\langle \frac{1}{N_f k_B} \sum_{i=1}^{N} m_i \mathbf{r}_i'^2 \right\rangle \tag{2.26}$$

while the instantaneous temperature is defined as:

$$T = \frac{1}{N_f k_B} \sum_{i=1}^{N} m_i \mathbf{r}_i'^2 \tag{2.27}$$

Since the temperature of a fluid is directly related to the velocity of the atoms, maintaining the temperature constant during MD simulations requires imposing some modifications on the equation of the velocity (i.e. the kinetic energy) compared to the classical one, i.e. Eq. (2.23b). To do so, the fluid is generally assumed to be in “contact” with a heat bath at the target temperature, T_0. Different thermostats describe different “contacts” between the fluid and the heat bath, i.e. different descriptions of the kinetic energy exchanges between the fluid and the heat bath [14].

From Eq. (2.26), it is possible to maintain the temperature constant by constraining the instantaneous temperature T at the value of the desired one T_0. However, thermostats using this idea usually generate an unrealistic dynamic of the fluid [14]. To improve the description of the dynamics, other strategies to maintain $\overline{T}$ have been proposed that correspond to constrain an average temperature over a timescale to be equal to T_0, i.e. the instantaneous temperature is allowed to fluctuate around T_0 [14]. It should be noted that the timescale chosen should be smaller than the time of the MD simulations, but longer than the time separating atomic collisions.

In this part, we briefly describe some thermostats that are usually employed when performing MD simulations.

Instantaneous thermostats

In the instantaneous thermostats, the idea is to maintain the instantaneous temperature T equal to the desirable temperature, T_0. From Eq. (2.27), we have:

$$T = \frac{1}{N_f k_B} \sum_{i=1}^{N} m_i \mathbf{r}_i'^2 = T_0 \tag{2.28}$$

Making derivative with time for this equation, one can obtain:

$$\frac{\partial T}{\partial t} = \frac{\partial}{\partial t}\left(\frac{1}{N_f k_B} \sum_{i=1}^{N} m_i \mathbf{r}_i'^2 \right) = 0 \tag{2.29a}$$

$$T(t=0) = T_0 \tag{2.29b}$$

The Hamiltonian equations of motion for the instantaneous thermostats are generally written as:

$$\mathbf{r}_i' = \frac{\mathbf{p}_i}{m_i} \tag{2.30a}$$

$$\mathbf{p}_i' = -\nabla_{\mathbf{r}_i} U + \alpha_T \mathbf{p}_i \tag{2.30b}$$

where α_T is a parameter that is determined from the constraints imposed by Eq. (2.28) or (2.29). These types of thermostats generate a change in the momentum that is smooth, deterministic and time-reversible [14].

Combining Eq. (2.28) with Eq. (2.30), we obtain:

$$\alpha_T = -\frac{\sum_{i=1}^{N} \nabla_{\mathbf{r}_i} U \cdot \mathbf{p}_i}{N_f k_B T_0} \tag{2.31}$$

This is usually referred to as the ***Woodcock thermostat*** [15]. This thermostat rigorously maintains the instantaneous temperature and produces correctly the distribution of configurations of a fluid at a constant temperature, but does not provide the correct momentum. Additionally, the dynamic of the fluid obtained from this thermostat are unrealistic [14].

When the constraint of Eq. (2.29) is employed, we can deduce that:

$$\alpha_T = -\frac{\sum_{i=1}^{N} \nabla_{\mathbf{r}_i} U \cdot \mathbf{p}_i}{\sum_{i=1}^{N} \mathbf{p}_i^2 / m_i} \tag{2.32}$$

This thermostat is called the ***Hoover-Evans thermostat*** [16]. The distribution of configurations of a fluid generated from the Hoover-Evans thermostat is correct, but it is not the case for the momentum. Furthermore, because T_0 does not appear explicitly in the equation of α_T, the temperature actually drifts during simulation due to the numerical inaccuracies. In addition, this thermostat may provide unrealistic dynamics of the fluid [14].

Average thermostats

In contrast to the instantaneous thermostats, the instantaneous temperature in the average thermostats is allowed to fluctuate, but it requires that its average over a timescale of τ_T is equal to the target temperature, i.e.:

$$\overline{T}_{\tau_T} = \langle T \rangle_{\tau_T} = \left\langle \frac{1}{N_f k_B} \sum_{i=1}^{N} m_i \mathbf{r}_i'^2 \right\rangle_{\tau_T} = T_0 \tag{2.33}$$

To constrain the average temperature over a timescale, Andersen [17] proposed that the atoms of a fluid are conditionally stochastically colliding with a heat bath such that:

- First the momentum of an atom after the stochastic collision is chosen from the Maxwell-Boltzmann distribution
- Second the stochastic collisions suffered by an atom occur accordingly to a Poisson process
- Third the times at which different atoms experience the stochastic collisions are statistically uncorrelated.

In this thermostat, usually referred to as the ***Andersen thermostat*** or the ***stochastic coupling thermostat***, the Hamiltonian equations of motion can be written as:

$$\mathbf{r}_i' = \frac{\mathbf{p}_i}{m_i} \tag{2.34a}$$

$$\mathbf{p}_i' = -\nabla_{\mathbf{r}_i} U + \sum_{n=1}^{\infty} \delta\left(t - \sum_{m=1}^{n} t_{i,m} \right) \left[\mathbf{p}_{i,n}^{*} - \mathbf{p}_i \right] \tag{2.34b}$$

where $\left\{ t_{i,n} \middle| n = 1,2,\ldots \right\}$ is the series of intervals without stochastic collisions for atom i, and $\mathbf{p}_{i,n}^{*}$ is the momentum after the stochastic collision at the n^{th} interval. The fluid evolves so in accord with the classical Newtonian motions, interrupted by small energy jumps corresponding to each stochastic collision. The Andersen thermostat leads to a non-deterministic and time-irreversible change in momentum. Moreover, it has the disadvantage that the momentum of an atom is not-smooth when the stochastic collision occurs, which may interfere with the natural dynamics of the fluid. However, the Andersen thermostat with an adequate stochastic collision frequency can generate correctly the distribution of configurations and momentum of a fluid at a constant temperature [14].

To constrain the average temperature over a timescale, each atom of a fluid can be assumed to be stochastically colliding (without correlation) with light atoms composing the heat bath [18]. So, the motions of atoms are governed by the following Hamilton equations of motion:

$$\mathbf{r}_i' = \frac{\mathbf{p}_i}{m_i} \tag{2.35a}$$

$$\mathbf{p}_i' = -\nabla_{\mathbf{r}_i} U - \gamma_i \mathbf{p}_i + \mathbf{R}_i \tag{2.35b}$$

where γ_i is the atomic friction coefficient and $\mathbf{R}_i$ is the stochastic force. This thermostat is referred to as the ***Langevin thermostat*** [18]. Clearly, in this thermostat the fluid is not only globally coupled to the heat bath, but is also locally coupled to the heat bath, i.e. not only the global temperature is maintained, but the local one also. The change in the momentum obtained from this thermostat is smooth, non-deterministic and time-irreversible. However, this thermostat with an adequate atomic friction coefficient can generate correctly the distribution of configurations and momentum of a fluid at the temperature constant and provide realistic dynamics of the fluid [14].

From the Langevin thermostat it is possible to impose a global coupling on the fluid with minimal local disturbances induced by the stochastic coupling, instead of imposing the local coupling [19]. By doing so, the temperature of the entire of the fluid can be maintained, but not the local temperature. This prescription leads to the following Hamiltonian equations of motion:

$$\mathbf{r}_i' = \frac{\mathbf{p}_i}{m_i} \tag{2.36a}$$

$$\mathbf{p}_i' = -\nabla_{\mathbf{r}_i} U + \alpha_T \mathbf{p}_i \tag{2.36b}$$

$$\alpha_T = \gamma_i \left(\frac{T_0}{T} - 1 \right) = \frac{1}{2\tau_T} \left(\frac{T_0}{T} - 1 \right) \tag{2.36c}$$

where $\tau_T = (2\gamma_i)^{-1}$. This thermostat proposed by Berendsen *et al.* [19], is referred to as the ***Berendsen thermostat***. The change in the momentum generated from this thermostat is smooth, deterministic and time-irreversible. In addition, this thermostat produces realistic dynamics of the fluid. However, the distribution of configurations and momentum generated from this thermostat is not rigorously demonstrated to be correct [14].

As long as the temperature of a fluid is proportional to the square momentum of the atoms, it is possible to control the temperature by adjusting the rate of the heat flow between the fluid and the heat bath during the evolution of the simulation. The rate of the heat flow should be adjusted so that the distribution of configurations and momentum generated is kept correct [7]. To achieve this prescription, Nosé proposed an extended system that consists of the fluid and an external system, in which the latter is characterized by a degree of freedom s to control the rate of the heat flow (the conjugate momentum of s is p_s) [20-21]. More precisely, the additional variable $s$plays a role to rescale the time unit so as to control the rate. To do so, Nosé introduced a virtual time variable $\hat{t}$ that is related to the real one t through s as:

$$d\hat{t} = sdt \tag{2.37}$$

The Hamiltonian equations of motion in this virtual time are written as:

$$\frac{d\mathbf{r}_i}{d\hat{t}} = \frac{\mathbf{p}_i}{m_i s^2} \tag{2.38a}$$

$$\frac{d\mathbf{p}_i}{d\hat{t}} = -\nabla_{\mathbf{r}_i} U \tag{2.38b}$$

$$\frac{ds}{d\hat{t}} = \frac{p_s}{Q} \tag{2.38c}$$

$$\frac{dp_s}{d\hat{t}} = \frac{\left(\sum_{i=1}^{N} \frac{\mathbf{p}_i^2}{m_i s^2} - (N_f + 1) k_B T_0 \right)}{s} \tag{2.38d}$$

where Q is a parameter of dimension $\text{Energy}\times\text{time}^2$ and behaves as a mass for the motion of s. It should be noted that the dynamical quantities of the fluid is explicitly related to $\hat{\mathbf{p}}_i = \mathbf{p}_i / s$, not to $\mathbf{p}_i$. Nosé demonstrated that the distribution of configurations and $\hat{\mathbf{p}}^N$ generated from Eq. (2.38) is correct [20-21]. This thermostat is usually referred to as the ***Nosé thermostat*** or the ***extended-System thermostat***. The change in the momentum generated from Eq. (2.38) is smooth, deterministic and time-reversible. However, the use of the virtual time is not very intuitive, and the sampling at uneven real time intervals is rather impractical for the investigation of the dynamical quantities of the fluid. To avoid this problem, Hoover reformulated these Hamiltonian equations of motion in terms of the real variables as [22]:

$$\mathbf{r}_i' = \frac{\mathbf{p}_i}{m_i} \tag{2.39a}$$

$$\mathbf{p}_i' = -\nabla_{\mathbf{r}_i} U - p_\xi \mathbf{p}_i \tag{2.39b}$$

$$p_\xi' = \frac{\left[\sum_{i=1}^{N} \frac{\mathbf{p}_i^2}{m_i} - N_f k_B T_0\right]}{Q} \tag{2.39c}$$

This thermostat is usually referred to as the ***Nosé-Hoover thermostat***. It should be mentioned that in these real variables dynamical quantities of the fluid are explicitly related to $\mathbf{p}_i$.

In summary, we have briefly described some thermostats that are commonly used in MD simulations. In fact, the Hamiltonian equations of motion of these thermostats can be reformulated to reduce the disadvantages. For instance, to improve the conservations in the Langevin thermostat, the ***Dissipative-Particle-Dynamic thermostat*** has been proposed [23]. The ***Nosé-Hoover chain thermostat*** [24] and the ***Nosé-Poincaré thermostat*** [25] have been given for improving the ergodic behavior in the Nosé-Hoover thermostat for special fluids. However, these thermostats are usually developed for some peculiar MD simulations and their implementations are rather complicated, so they are not widely employed in MD simulations.

More generally, the choice of a thermostat should depend on the characteristics and the quantities of fluid that we want to explore and the level of accuracies required.

2.3.2.2. Constant Pressure

The way to maintain the ***pressure*** of a system is called a ***barostat***. Before introducing barostats that are usually employed in MD simulations, one should mention that for a fluid confined between solid surfaces it is sometimes required to control the normal pressure exerted on the solid surface due to inter-atomic forces between the fluid and the solid atoms [12-13]. To do so, the solid surface is commonly assumed to possess a mass, and is allowed to move accordingly to the forces due to the fluid-solid interaction for a given constant external pressure. This barostat is usually referred to as the ***fluctuating wall barostat*** [26]. In fact, since the pressure in the fluid in the direction normal to the solid surface is equal the one acting on the solid surface due to inter-atomic forces between the fluid and the solid atoms, it is possible to maintain the normal pressure exerted on the solid surface by controlling the pressure in the fluid [5, 27].

The average pressure of a fluid $\overline{P}$ can be derived from the virial theorem and then defined thanks to the temperature $\overline{T}$ and the internal virial $\overline{W}$ as [6]:

$$\overline{P} = N_f k_B \overline{T} + \overline{W} \tag{2.40}$$

In which, the internal virial is written as:

$$\overline{W} = \langle W \rangle = \left\langle \frac{1}{3} \mathbf{r}_{ij} \cdot \left(-\nabla_{\mathbf{r}_{ij}} U \right) \right\rangle \tag{2.41}$$

where, $\mathbf{r}_{ij} = \mathbf{r}_i - \mathbf{r}_j$. From Eqs. (2.40) and (2.41), it is consistent to define the instantaneous pressure as [6]:

$$P = \frac{1}{V} \left[N_f k_B T + \sum_{i=1}^{N-1} \sum_{j>i}^{N} \frac{1}{3} \mathbf{r}_{ij} \cdot \left(-\nabla_{\mathbf{r}_{ij}} U \right) \right] \tag{2.42a}$$

or

$$P = \frac{1}{V}\left[N_f k_B T + \sum_{i=1}^{N-1} \sum_{j>i}^{N} \frac{1}{3} \omega(r_{ij}) \right] \tag{2.42b}$$

where V is the volume of the fluid and $\omega(r_{ij}) = r_{ij}\, dU / dr_{ij}$.

From Eqs. (2.40) and (2.42), it appears that to control the pressure of a fluid it is possible to impose a variation in the number of atoms if the volume is constant or in contrast a variation of the volume if the number of atoms is constant. Clearly, to employ the former requires the insertion/depletion of the atoms into/out of the fluid, which is not suitable to deal with dense fluid and to calculate the dynamical and transport properties. So, the choice of volume changes is usually employed in MD simulations. This requires imposing some modifications on the equation of coordinates compared to the conventional one, Eq. (2.23).

Similarly to what has been described in the thermostat section, the pressure of a fluid can be maintained by constraining the instantaneous pressure or the average pressure over a timescale. So in what follows, we briefly introduce the barostats in the same manner as for the thermostats.

Instantaneous barostats

In the instantaneous barostats, the instantaneous pressure *P* is constrained to be equal to the target pressure P_0. From Eq. (2.42), we can obtain:

$$PV = P_0 V = \left[N_f k_B T + \sum_{i=1}^{N-1} \sum_{j>j}^{N} \frac{1}{3} \omega(r_{ij}) \right] \tag{2.43}$$

This equation can be rewritten as:

$$P_0 V' = \left[N_f k_B T' + \sum_{i=1}^{N-1} \sum_{j>i}^{N} \frac{d\omega(r_{ij})}{dr_{ij}} r'_{ij} \right] \tag{2.44}$$

The Hamiltonian equations of motion for the instantaneous barostats are generally written as [6, 28-29]:

$$\mathbf{r}_i' = \frac{\mathbf{p}_i}{m_i} + \alpha_P \mathbf{r}_i \tag{2.45a}$$

$$\mathbf{p}_i' = -\nabla_{\mathbf{r}_i} U - \alpha_P \mathbf{p}_i \tag{2.45b}$$

$$V' = 3V\alpha_P \tag{2.45c}$$

where α_P is deduced from the constraint of Eqs. (2.43) and (2.44) as:

$$\alpha_P = \frac{\sum_{i=1}^{N} 2\mathbf{p}_i \nabla_{\mathbf{r}_i} U / m_i - \sum_{i=1}^{N-1} (1/m_i) \sum_{j \succ i}^{N} (\mathbf{r}_{ij} \mathbf{p}_{ij}) \Omega(r_{ij}) / r_{ij}^2}{\sum_{i=1}^{N} 2\mathbf{p}_i^2 / m_i + \sum_{i=1}^{N-1} \sum_{j \succ i}^{N} \Omega(r_{ij}) + 9P_0 V} \tag{2.45d}$$

where $\Omega(r) = r\, d\omega / dr$. This barostat was first proposed by Evans and Morris [28-29] and is called the ***constraint barostat***. The change in the volume and coordinates generated from this barostat is smooth, deterministic and time-reversible. However, this barostat generate incorrectly the distribution of configurations, and constraining the instantaneous pressure may lead to an inadequate description of the dynamic [6, 28-29].

Average barostats

Before introducing the average barostats that are used in MD simulations, it is interesting to mention that no ***stochastic coupling barostat*** seems to have been proposed in the literature. This is probably due to the fact that the temperature is a function of the individual properties of one atom, whereas the pressure is a function of the collective properties of all atoms. So, the development of the stochastic barostat may be more complicated than the ones for the temperature. However, similar to the idea that has been employed to develop the stochastic coupling thermostats, it is probably feasible to propose that at intervals the volume is stochastically changed in accord with a probability distribution function that is derived from the theory of the associated statistical mechanism.

In the average barostats, the average pressure over a timescale τ_P is constrained to be equal the desirable pressure P_0, i.e.

$$\overline{P}_{\tau_P} = \langle P \rangle_{\tau_P} = \left\langle \frac{1}{V}\left[N_f k_B T + \sum_{i=1}^{N-1}\sum_{j>i}^{N} \frac{1}{3}\omega(r_{ij}) \right] \right\rangle_{\tau_P} = P_0 \tag{2.46}$$

Based on the idea similar to the Langevin thermostat, first Kolb *et al.* [30] developed a ***Langevin barostat***, in which the variation in the deformation of volume of the fluid with the time is governed by the Langevin dynamics in the extended Andersen system [30]. Later, Quigley *et al.* [31] reformulated the Hamiltonian equations of motion based on Martyna et al.'s correction on the Hoover equations of the extended Andersen system as [31]:

$$\mathbf{r}_i' = \frac{\mathbf{p}_i}{m_i} + \frac{p_\chi}{\Lambda}\mathbf{r}_i \tag{2.47a}$$

$$\mathbf{p}_i' = -\nabla_{\mathbf{r}_i} U - \left(1 + \frac{3}{N_f}\right)\frac{p_\chi}{\Lambda}\mathbf{p}_i \tag{2.47b}$$

$$V' = \frac{3p_\chi}{\Lambda}V \tag{2.47c}$$

$$p_\chi' = 3V(P - P_0) + \frac{3}{N_f}\left(\sum_{i=1}^{N}\frac{\mathbf{p}_i^2}{m_i}\right) - \gamma_P p_\chi + R_P \tag{2.47d}$$

where γ_P is a "barostat" friction coefficient and R_P is a stochastic "force" which acts on the barostat. This barostat is smooth, non-deterministic and time-irreversible. However, Quigley and Probert [31] demonstrated that this barostat generates correctly the distribution of configurations.

Similar to what has been developed for maintaining the temperature, to introduce a constraint on the pressure, Berendsen *et al.* [19] supposed that the fluid is coupled to a constant pressure bath at P_0. This leads to the following Hamiltonian equations of motion:

$$\mathbf{r}_i' = \frac{\mathbf{p}_i}{m_i} + \alpha_P \mathbf{r}_i \tag{2.48a}$$

$$\mathbf{p}_i' = -\nabla_{\mathbf{r}_i} U \tag{2.48b}$$

$$V' = 3\alpha_P V \tag{2.48c}$$

$$\alpha_P = -\beta\left(\frac{P_0 - P}{3\tau_P}\right) \tag{2.48d}$$

where β is the isothermal compressibility. This barostat is usually referred to as the ***Berendsen barostat*** [19]. The change in the volume and coordinates generated from this thermostat is smooth and deterministic. However, this barostat is not time-reversible and has not rigorously been proven to provide correctly the distribution of configurations [19].

Similar to the extended-system thermostat, an extended system barostat is introduced to constrain the pressure of a fluid. It is composed of the fluid and a piston, in which the fluid is assumed to be compressed by a piston that is acted by an external pressure equal to the target pressure P_0 [6-7, 17]. The coordinate of the piston plays a role to scale the coordinates of the atoms, and is represented by the volume of the fluid V, i.e. the coordinates of atoms $\mathbf{r}_i$ are replaced by scaled coordinates $\hat{\mathbf{r}}_i$ as:

$$\hat{\mathbf{r}}_i = \frac{\mathbf{r}_i}{V^{1/3}} \tag{2.49}$$

The Hamiltonian equations of motion in this scaled coordinate are written as:

$$\hat{\mathbf{r}}_i' = \frac{\hat{\mathbf{p}}_i}{m_i V^{2/3}} \tag{2.50a}$$

$$\hat{\mathbf{p}}_i' = -V^{1/3}\left(\sum_{j(\neq i)=1}^{N} \frac{\hat{\mathbf{r}}_{ij}}{\hat{r}_{ij}} \frac{dU\left(V^{1/3}\hat{r}_{ij}\right)}{d\hat{r}_{ij}}\right) \tag{2.50b}$$

$$V' = \frac{p_V}{\Lambda} \tag{2.50c}$$

$$p_V' = -\frac{1}{3V}\left[\frac{2}{V^{2/3}}\sum_{i=1}^{N}\frac{\hat{\mathbf{p}}_i^2}{2m_i} + V^{1/3}\sum_{i=1}^{N-1}\sum_{j>i}^{N}\hat{\mathbf{r}}_{ij}\frac{dU\left(V^{1/3}\hat{r}_{ij}\right)}{dr_{ij}} + 3P_0V\right] \tag{2.50d}$$

where Λ is a parameter of dimension $\text{mass}\times\text{length}^{-4}$ and behaves as the mass of the piston. It is worthy to note that the dynamical quantities of the fluid is explicitly related to $\hat{\mathbf{p}}_i/V^{1/3}$, and not to $\hat{\mathbf{p}}_i$. This barostat was originally proposed by Andersen [17] and called ***the***

extended-system barostat or ***Andersen barostat***. Andersen proved that this barostat produces correctly the distribution of configurations [17]. The change in the volume and coordinates generated from Eq. (2.50) are smooth, deterministic and time-reversible. However, the equations of motion are written in term of the scaled variables, so it can be inconvenient to calculate the properties. To circumvent this problem, Hoover reformulated these equations in terms of the real variables as [32]:

$$\mathbf{r}_i' = \frac{\mathbf{p}_i}{m_i} + \frac{p_\chi}{\Lambda}\mathbf{r}_i \tag{2.51a}$$

$$\mathbf{p}_i' = -\nabla_{\mathbf{r}_i} U - \frac{p_\chi}{\Lambda}\mathbf{p}_i \tag{2.51b}$$

$$V' = \frac{3p_\chi}{\Lambda}V \tag{2.51c}$$

$$p_\chi' = 3V\left(P - P_0\right) \tag{2.51d}$$

However, when this barostat is coupled to the thermostats to constrain both the temperature and the pressure of a fluid in NPT ensemble, it fails to correctly generate the NPT ensemble [33]. To overcome this problem, first Melchionna *et al.* [33] modified these equations. Nevertheless, the modified equations have not been widely employed due to the fact that they involve constraining the center of mass of the fluid. Hence, Martyna *et al.* [34] proposed the Hamiltonian equations of motion:

$$\mathbf{r}_i' = \frac{\mathbf{p}_i}{m_i} + \frac{p_\chi}{\Lambda}\mathbf{r}_i \tag{2.52a}$$

$$\mathbf{p}_i' = -\nabla_{\mathbf{r}_i} U - \left(1 + \frac{3}{N_f}\right)\frac{p_\chi}{\Lambda}\mathbf{p}_i \tag{2.52b}$$

$$V' = \frac{3p_\chi}{\Lambda}V \tag{2.52c}$$

$$p_\chi' = 3V\left(P - P_0\right) + \frac{3}{N_f}\left(\sum_{i=1}^{N}\frac{\mathbf{p}_i^2}{m_i}\right) \tag{2.52d}$$

Martyna *et al.* demonstrated that these equations generate correctly the phase-space, and when they are coupled to the thermostat provide correctly the NPT ensemble [34]. This barostat is usually referred to as the ***Hoover barostat*** [34]. However, this barostat is applicable to simulation boxes that have cubic form and isotropic volume fluctuations. To overcome this problem, the scaled coordinates of atoms are defined as [35]:

$$\hat{\mathbf{r}}_i = \mathbf{h}^{-1}\mathbf{r}_i \tag{2.53}$$

where $\mathbf{h}$ is a 3×3 matrix and is formed from the edges vectors $(\mathbf{a},\mathbf{b},\mathbf{c})$, i.e. $\mathbf{h}=(\mathbf{a},\mathbf{b},\mathbf{c})$. The volume V is given by $V=\mathbf{c}\times\mathbf{b}\cdot\mathbf{a}=\det(\mathbf{h})$. Similar to what have been developed for a fluid of the cubic form and isotropic fluctuations, the Hamiltonian equations of motion are derived as [34]:

$$\mathbf{r}_i' = \frac{\mathbf{p}_i}{m_i} + \frac{\mathbf{p}_\chi}{\Lambda}\mathbf{r}_i \tag{2.54a}$$

$$\mathbf{p}_i' = -\nabla_{\mathbf{r}_i}U - \frac{\mathbf{p}_\chi}{\Lambda}\mathbf{p}_i - \frac{1}{N_f}\frac{\mathrm{Tr}(\mathbf{p}_\chi)}{\Lambda}\mathbf{p}_i \tag{2.54b}$$

$$\mathbf{h}' = \frac{\mathbf{p}_\chi}{\Lambda}\mathbf{h} \tag{2.54c}$$

$$\mathbf{p}_\chi' = V(\mathbf{P}-P_0\mathbf{I}) + \left(\frac{1}{N_f}\sum_{i=1}^{N}\frac{\mathbf{p}_i^2}{m_i}\right)\mathbf{I} \tag{2.54d}$$

where $\mathbf{I}$ is the 3×3 identity matrix, $\mathbf{P}$ is the stress tensor, $\mathbf{p}_\chi$ is a 3×3 matrix, and $\mathrm{tr}(\mathbf{A})$ is the trace of the matrix $\mathbf{A}$. The main idea of this barostat was originally proposed by Parrinello and Rahman, so it is called the ***Parrinello and Rahman barostat*** or the ***changing box-shape barostat*** [35].

All these barostats rely on separating the descriptions of the equations of the coordinates of the atoms and the variation in the volume with the time. In fact, there exist some alternative barostats in which the volume is expressed in accord with the coordinates

[36-37]. However, these barostats cannot be combined with periodic boundary conditions, so they are not commonly used.

2.3.2.3. Constant Chemical Potential

In contrast to the temperature and the pressure that can be directly determined from the evolution over time of the coordinates and the momentum of atoms, i.e. the phase-space trajectory, the chemical potential is related to its integrals, i.e. the phase-space volume [6, 8]. So, to maintain the chemical potential requires imposing some modifications on the phase-space volume. To do so in pure fluids, the number of atoms of a fluid can be allowed to vary with the time when the volume of the fluid is fixed, or the volume can be varied when the number of atoms is fixed. Usually the former is employed since the MD simulations with a constant chemical potential are carried out to explore the phenomena where interface are present which makes desirable to fix the volume.

The change in the number of atoms of a fluid means that the fluid is coupled to a matter reservoir. MD simulations at a constant chemical potential can so be performed using two approaches, one including the matter reservoir explicitly and the other one including it implicitly. The variation in the number of atoms leads to the fact that it requires introducing an equation associated to the evolution of the number of atoms. This equation is directly obtained in the explicit approach and needs to be derived in the implicit one. In what follows, we first present the methods using the former followed by the ones using the latter.

Explicit matter reservoir

The idea of these methods consists in simulating explicitly the fluid in contact with a matter reservoir maintained at a constant chemical potential, i.e. the simulation box contains both the fluid and the reservoir [38-43]. So, the essence of these methods is to transfer the

constraint of the chemical potential of a complex system, e.g. a confined fluid, to the one of a simple system, i.e. the matter reservoir. Since the thermodynamics of the matter reservoir behaves as bulk one, i.e. the chemical potential can be deduced from the pressure or density for a pure fluid, it is possible to constrain the chemical potential of the reservoir by controlling it rigorously or through other thermodynamics properties. To maintain the chemical potential, grand canonical MC simulations in the reservoir can be employed, which is usually referred to as the ***control volume grand canonical molecular dynamics (CV-GCMD)*** [38-41]. Otherwise, to maintain other thermodynamics properties of the matter reservoir, e.g. pressure, the methods that we have described above can be used [42-43]. These methods are called the ***Gao GCMD***.

These methods introducing explicitly a matter reservoir are convenient to explore the properties of dense fluids, the transient behaviors and the non-equilibrium properties. However, because it needs simulating the matter reservoir, such MD simulations are usually very CPU time demanding [38-43].

Implicit matter reservoir

The chemical potential of a fluid is defined as [6, 8]:

$$\bar{\mu} = -k_B \bar{T} \ln\left[\frac{1}{\left(\bar{N}/V\right)\Xi^3 \left\langle k_B T \right\rangle^{3/2}} \left\langle \left(k_B T\right)^{3/2} \exp\left(-\frac{U}{N k_B T} \right) \right\rangle \right] \tag{2.55}$$

where Ξ is the thermal de Broglie wavelength.

Instantaneous chemical potential

To obtain the equation of the number of atoms from the constraint of an instantaneous chemical potential requires defining the instantaneous chemical potential in terms of the instantaneous number of atoms. One of the difficulties is that the number of atoms is regarded as integer value and so it is impossible to determine the derivative of the “instantaneous”

chemical potential with respect to the number to obtain the equation of variation in the number of atoms. However, if the number of atoms is considered as a real value, as mentioned later, it is perhaps possible to obtain the equation of variation in the number of atoms. This suggestion is left as a future work.

Average chemical potential constant

From the idea that has been used to propose the ***stochastic coupling*** thermostat, it is consistent to assume that the change in the number of atoms can be obtained by stochastically coupling the matter reservoir, i.e. atom creation/depletion attempts are accepted with a probability that is deduced from the classical theory of statistical mechanism. Using this idea, two methods to constrain the chemical potential have been proposed. In the first, the number of atoms is an integer value, which leads to the fact that the variation in it is discontinuous. This method is usually referred to as the method of Lupkowski and van Swol [44]. Because of the discretisation of the variation of the number of atoms, it may lead to an unrealistic dynamics of the fluid. As an improvement to this method, Boinepalli and Attard proposed a continuous variation in the number of atoms [45]. To do so, the number of atoms in a fluid is characterized as a real variable $\tilde{N}$, in which its integer part is the actual number of atom in the fluid N and its fractional part ϑ is assumed as an "additional" atom [45]. The meaning of the presence of this additional atom is that when $\vartheta = 0$ the number of the actual atoms is unchanged, and when $\vartheta = 1$ it increases by one. The physical presence of this additional atom is described by a peculiar interaction potential ϕ between it and actual atoms and mass m_f. According to this convention, it is clear that when $\vartheta = 1$, ϕ is the same as the interaction potential between actual atoms and m_f is the same as the mass of actual atom, otherwise when $\vartheta = 0$, both ϕ and m_f are zero. The fractional part is randomly changed by the trial/move attempts in which the acceptance or rejection is followed by a condition deduced from the theory of the statistical mechanics. These methods are non-smooth, non-

deterministic and time-irreversible. However, similar to what is demonstrated for the thermostats, they can generate correctly the distribution of configurations of fluid at a constant chemical potential [45].

The idea of the ***Langevin dynamics*** has been used to propose methods for constraining the temperature and pressure [18, 30], but ***no method*** using this idea has been developed for the chemical potential. From the extended-system methods proposed by Cagin and Pettitt [46-47] for the chemical potential that will be introduced latter, we think that it is feasible to propose a ***Langevin method*** for the chemical potential. In the Langevin form, the Lagrangian equations of motion of the fluid containing the actual atoms and the additional atom could be written as:

$$m_i \mathbf{r}_i'' = -\nabla_{\mathbf{r}_i} U - \nabla_{\mathbf{r}_i} \phi \tag{2.56a}$$

$$m_f \mathbf{r}_f'' = -\nabla_{\mathbf{r}_f} \Phi - \frac{\partial m_f}{\partial t} \mathbf{r}_f' \tag{2.56b}$$

$$Z \vartheta'' = -\frac{\partial \phi}{\partial \vartheta} + \frac{1}{2} \frac{\partial m_f}{\partial \vartheta} \mathbf{r}_f'^2 - \frac{\partial \psi}{\partial \vartheta} - \gamma_\mu \vartheta' + R_\mu \tag{2.56c}$$

where Φ is the total potential energy due to interactions between the additional atom and the actual atoms, i.e. $\Phi = \sum_{i=1}^{N} \phi_{if}$, $\mathbf{r}_f$ is the coordinate of the additional atom, Z is a parameter and behaves as a mass for the motion of ϑ, ψ is a potential function related to the desired chemical potential μ_0, γ_μ is "chemical potential" friction coefficient and R_μ is a stochastic "force" which acts on the chemical potential. The main problems of this method at the time being are to specify γ_μ and R_μ, are left as a future work. This method would be smooth, non-deterministic and time-irreversible in the variation of number of atoms. However, it could provide correctly the distribution of configurations of the fluid at a constant chemical potential.

Although the thermostat and barostat using the idea proposed ***Berendsen et al***. are widely used [19], ***no method*** using this idea for the chemical potential has been proposed in the literature. We think that it is probably feasible to develop such a method. In the Berendsen form, the fractional part of the equation of variation could be written as:

$$\vartheta' = \sum_k A_k \left[\mu\left(\mathbf{r}^N, \mathbf{r}'^N, \mathbf{r}_f, \mathbf{r}'_f, \vartheta\right) - \mu_0\right]^k \tag{2.57}$$

where A_k is a constant and μ is an unknown function of $\left(\mathbf{r}^N, \mathbf{r}'^N, \mathbf{r}_f, \mathbf{r}'_f, \vartheta\right)$ that can be interpreted as an "instantaneous chemical potential". The Langrangian equations of motion of the actual and additional atoms are given by Eqs. (2.56a) and (2.56b). The main problems of this method at the present time are to specify A_k and μ, which is left as a future work. Similarly to the Berendsen thermostat and barostat [19], this method would be smooth, deterministic and time-irreversible.

From the idea used in the ***extended-system methods*** proposed for the temperature and the pressure, Cagin and Pettitt first developed one approach for constraining the chemical potential [46-48]. The extended system consists of the fluid and an additional atom, in which the latter represents the coupling of the fluid to the matter reservoir. The presence of this additional atom is represented by the fractional part ϑ as mentioned above.

During the simulations, ϑ varies with the time and is governed by an equation that is derived from the Langrangian of the extended system:

$$m_i \mathbf{r}''_i = -\nabla_{\mathbf{r}_i} U - \nabla_{\mathbf{r}_i} \Phi \tag{2.58a}$$

$$m_f \mathbf{r}''_f = -\nabla_{\mathbf{r}_f} \Phi - \frac{\partial m_f}{\partial t} \mathbf{r}'_f \tag{2.58b}$$

$$Z \vartheta'' = -\frac{\partial \phi}{\partial \vartheta} + \frac{1}{2} \frac{\partial m_f}{\partial \vartheta} \mathbf{r}'^2_f - \frac{\partial \psi}{\partial \vartheta} \tag{2.58c}$$

The problems of this method are to define Φ, m_f and ψ and to insert/delete an actual atom when $\vartheta = 1$ or 0. In the original study, Cagin and Pettitt [46-47] defined these variables as:

$$\phi = \vartheta u \tag{2.59a}$$

$$m_f = \vartheta m_1 = \ldots = \vartheta m_N \tag{2.59b}$$

$$\psi = \vartheta \mu_0 \tag{2.59c}$$

where u is the potential between actual atoms. When $\vartheta = 1$ the current additional atom is considered as a actual atom, and a new additional atom is inserted to the fluid at the position where the local density of the fluid is minimal, otherwise when $\vartheta = 0$ the current additional atom is deleted, and a current actual atom whose kinetic and potential are the closest the ones of the additional atom is switched to a new additional atom. In more recent works, Lynch and Pettitt [49] reformulated the definition of ψ to include the ideal gas behavior and various partitioning of ideal and excess chemical potentials in order to correctly incorporate this method with thermostats. This method is smooth, deterministic and time-reversible. Cagin and Pettitt rigorously demonstrated that this method generates correctly the distribution of configurations [47].

The subsequent studies have used the same Lagrangian equations of motion with modifications on the definitions of Φ, m_f and ψ, and on insertion/deletion in order to improve the applicability of the method [50] or to remove the local density-bias search [51]. In particular, Shroll and Smith [52] reformulated the Lagrangian equations of motion to include umbrella sampling. By doing so, the efficiency of the atom insertion/deletion is improved.

It is clear that implementations of the conventional MD simulation with a constant number of atoms, e.g. the MD simulations using thermostats or barostats, are simpler than those with a dynamically variable number of atoms as in the previously described methods. Based on this advantage, some methods for controlling the chemical potential have been proposed, in which MD simulations with a constant number of atoms are performed [53-54].

For instance, for investigating properties of a fluid confined between solid surfaces and in equilibrium with a reservoir, i.e. the chemical potential of atoms of the confined fluid is equal to that of the reservoir, Wang and Fichthorn [53] assumed that the parallel pressure of the confined fluid is equal to the one of the reservoir. So instead of constraining the chemical potential, they constrain the parallel pressure using a barostat [53]. However, in the present work we have found that the parallel pressure of a confined fluid is not equal to the bulk one when the separation between the solid surfaces is small.

Another alternative is to perform parallel sets of conventional MD simulations corresponding to different numbers of atoms of the fluid. Then, an adequate combination of chains of configurations generated from these classical MD simulations is selected according to the prescription of a probability distribution to obtain the fluid at a constant chemical potential [54]. This method has a certain disadvantage: many classical MD simulations corresponding to different numbers of atoms are requested to reflect correctly the change in the number of atoms of a fluid at a constant chemical potential.

2.3.2.4. Equations of Motion in Ensembles

The methods to constrain the temperature, pressure and chemical potential separately have been introduced. The equations of motion of MD simulations in the ***canonical ensemble*** are the ones presented in subsection 2.3.2.2. To obtain the equations of motion of the MD simulations in the ***isothermal-isobaric ensemble*** and the ***grand canonical ensemble*** one has to combine the ones constraining different macroscopic thermodynamic variables. Here we present some combined equations of motion in the ensembles that have commonly been used in MD simulations.

The isothermal-isobaric ensemble

In the Berendsen form [19], the equations of motion are combined as:

$$\mathbf{r}_i' = \frac{\mathbf{p}_i}{m_i} + \alpha_P \mathbf{r}_i \tag{2.60a}$$

$$\mathbf{p}_i' = -\nabla_{\mathbf{r}_i} U + \alpha_T \mathbf{p}_i \tag{2.60b}$$

$$V' = 3\alpha_P V \tag{2.60c}$$

$$\alpha_T = \frac{m}{2\tau_T}\left(\frac{T_0}{T} - 1\right) \tag{2.60d}$$

$$\alpha_P = -\beta\left(\frac{P_0 - P}{3\tau_P}\right) \tag{2.60e}$$

In the extended-system form [34], we can obtain the equations of motion as:

$$\mathbf{r}_i' = \frac{\mathbf{p}_i}{m_i} + \frac{p_\chi}{\Lambda}\mathbf{r}_i \tag{2.61a}$$

$$\mathbf{p}_i' = -\nabla_{\mathbf{r}_i} U - \left(1 + \frac{3}{N_f}\right)\frac{p_\chi}{\Lambda}\mathbf{p}_i - \frac{p_\xi}{Q}\mathbf{p}_i \tag{2.61b}$$

$$V' = \frac{3p_\chi}{\Lambda} V \tag{2.61c}$$

$$p_\xi' = \sum_{i=1}^{N}\frac{\mathbf{p}_i^2}{m_i} + \frac{p_\xi^2}{\Lambda} - \left(N_f + 1\right)k_B T_0 \tag{2.61d}$$

$$p_\chi' = 3V\left(P - P_0\right) + \frac{3}{N_f}\left(\sum_{i=1}^{N}\frac{\mathbf{p}_i^2}{m_i}\right) - \frac{p_\xi}{Q}p_\chi \tag{2.61e}$$

The grand canonical ensemble

In the extended-system form [47], the equations of motion are combined as:

$$m_i \mathbf{r}_i'' = \frac{1}{s^2}\left[-\nabla_{\mathbf{r}_i} U - \nabla_{\mathbf{r}_i}\Phi\right] - 2m_i\frac{s'}{s}\mathbf{r}_i' \tag{2.62a}$$

$$m_f \mathbf{r}_f'' = \frac{1}{s^2}\left[-\nabla_{\mathbf{r}_f}\Phi\right] - \frac{\partial m_f}{\partial t}\mathbf{r}_f' - 2m_f\frac{s'}{s}\mathbf{r}_f' \tag{2.62b}$$

$$Qs'' = \sum_{i=1}^{N} m_i s\mathbf{r}_i'^2 + m_f s\mathbf{r}_f'^2 - \frac{N_f + 1}{s}k_B T_0 \tag{2.62c}$$

$$Z\vartheta'' = -\frac{\partial \phi}{\partial \vartheta} + \frac{1}{2}\frac{\partial m_f}{\partial \vartheta}\mathbf{r}_f'^2 - \frac{\partial \psi}{\partial \vartheta} \tag{2.62d}$$

As introduced and discussed previously, the choice of a method for constraining the macroscopic properties depends on many factors. In this work, since most of results focus on the dynamic of various systems, for simplicity in implementation we have used the Berendsen thermostat and barostat [19] in the MD simulations in the canonical and the isothermal-isobaric ensembles. In addition, we have employed the method of the explicit matter reservoir to deal with the grand canonical ensemble using the Gao approach [42-43].

2.3.3. Finite Different Methods

As mention previously, in MD simulations, the macroscopic properties of a fluid are determined from its microstates that are obtained by solving the classical equations of motion of atoms. The finite different methods are usually employed to obtain solutions of these equations [6-9]. The main idea of the methods is to attempt to determine the microstate at a time $t + \delta t$ from the one at previous time t with a sufficient accuracy [6-9]. By doing so, the microstate is completely specified at any time as long as the initial microstate is given. The choice of δt depends not only on the method used, but also on the typical time taken for an atom to travel over its own length (δt should be decreased when the temperature increases).

There have been many methods proposed and reviewed to solve the equations of motion in MD simulations [6-9]. Here we do not detail the advantages and disadvantages of such methods. However, it is worthy to note that a “successful” method should possess the following characteristics [6-9]:

Mathematical point of view: The method should be stable and accurate, and permit the use of a long time step

Computer point of view: The method requires little memory, is simple in form and easy to implement. In particular, it does not require computing the forces many times at each time step.

Physical point of view: The macroscopic and microscopic properties obtained from the microstates are realistic and satisfy the laws of the thermodynamics.

Here we briefly introduce the methods that are often used in MD simulations [6-9]. For simplicity, only the real coordinate variables of atoms $\mathbf{r}_i$ are provided, other "coordinate" variables of "extended-system", e.g. s and ϑ, can easily be obtained in the same way.

Verlet method

$$\mathbf{r}_i(t+\delta t) = 2\mathbf{r}_i(t) - \mathbf{r}_i(t-\delta t) + \delta t^2 \frac{\partial^2 \mathbf{r}_i}{\partial t^2}(t) \tag{2.63}$$

Leap-Frog method

$$\mathbf{r}_i(t+\delta t) = \mathbf{r}_i(t) + \delta t \frac{\partial \mathbf{r}_i}{\partial t}\left(t+\frac{1}{2}\delta t\right) \tag{2.64a}$$

$$\frac{\partial \mathbf{r}_i}{\partial t}\left(t+\frac{1}{2}\delta t\right) = \frac{\partial \mathbf{r}_i}{\partial t}\left(t-\frac{1}{2}\delta t\right) + \frac{1}{2}\delta t \frac{\partial^2 \mathbf{r}_i}{\partial t^2}(t) \tag{2.64b}$$

$$\frac{\partial \mathbf{r}_i}{\partial t}(t+\delta t) = \frac{1}{2}\left[\frac{\partial \mathbf{r}_i}{\partial t}\left(t-\frac{1}{2}\delta t\right) + \frac{\partial \mathbf{r}_i}{\partial t}\left(t+\frac{1}{2}\delta t\right)\right] \tag{2.64c}$$

Velocity Verlet method

$$\mathbf{r}_i(t+\delta t) = \mathbf{r}_i(t) + \delta t \frac{\partial \mathbf{r}_i}{\partial t}(t) + \frac{1}{2}\delta t^2 \frac{\partial^2 \mathbf{r}_i}{\partial t^2}(t) \tag{2.65a}$$

$$\frac{\partial \mathbf{r}_i}{\partial t}(t+\delta t) = \frac{\partial \mathbf{r}_i}{\partial t}\left(t+\frac{\delta t}{2}\right) + \frac{1}{2}\delta t\left[\frac{\partial^2 \mathbf{r}_i}{\partial t^2}(t) + \frac{\partial^2 \mathbf{r}_i}{\partial t^2}(t+\delta t)\right] \tag{2.65b}$$

Fifth-Order Gear Predictor-Corrector method

The prediction step:

$$\mathbf{r}_i^P(t+\delta t) = \mathbf{r}_i(t) + \delta t \frac{\partial \mathbf{r}_i}{\partial t}(t) + \frac{1}{2!}\delta t^2 \frac{\partial^2 \mathbf{r}_i}{\partial t^2}(t) + \frac{1}{3!}\delta t^3 \frac{\partial^3 \mathbf{r}_i}{\partial t^3}(t) + \frac{1}{4!}\delta t^4 \frac{\partial^4 \mathbf{r}_i}{\partial t^4}(t) + \frac{1}{5!}\delta t^5 \frac{\partial^5 \mathbf{r}_i}{\partial t^5}(t) \tag{2.66a}$$

$$\frac{\partial \mathbf{r}_i^P}{\partial t}(t+\delta t)=\frac{\partial \mathbf{r}_i}{\partial t}(t)+\delta t\frac{\partial^2 \mathbf{r}_i}{\partial t^2}(t)+\frac{1}{2!}\delta t^2\frac{\partial^3 \mathbf{r}_i}{\partial t^3}(t)+\frac{1}{3!}\delta t^3\frac{\partial^4 \mathbf{r}_i}{\partial t^4}(t)+\frac{1}{4!}\delta t^4\frac{\partial^5 \mathbf{r}_i}{\partial t^5}(t) \quad (2.66b)$$

$$\frac{\partial^2 \mathbf{r}_i^P}{\partial t^2}(t+\delta t)=\frac{\partial^2 \mathbf{r}_i}{\partial t^2}(t)+\delta t\frac{\partial^3 \mathbf{r}_i}{\partial t^3}(t)+\frac{1}{2!}\delta t^2\frac{\partial^4 \mathbf{r}_i}{\partial t^4}(t)+\frac{1}{3!}\delta t^3\frac{\partial^5 \mathbf{r}_i}{\partial t^5}(t) \quad (2.66c)$$

$$\frac{\partial^3 \mathbf{r}_i^P}{\partial t^3}(t+\delta t)=\frac{\partial^3 \mathbf{r}_i}{\partial t^3}(t)+\delta t\frac{\partial^4 \mathbf{r}_i}{\partial t^4}(t)+\frac{1}{2!}\delta t^2\frac{\partial^5 \mathbf{r}_i}{\partial t^5}(t) \quad (2.66d)$$

$$\frac{\partial^4 \mathbf{r}_i^P}{\partial t^4}(t+\delta t)=\frac{\partial^4 \mathbf{r}_i}{\partial t^4}(t)+\delta t\frac{\partial^5 \mathbf{r}_i}{\partial t^5}(t) \quad (2.66e)$$

$$\frac{\partial^5 \mathbf{r}_i^P}{\partial t^5}(t+\delta t)=\frac{\partial^5 \mathbf{r}_i}{\partial t^5}(t) \quad (2.66f)$$

The error in the prediction step:

$$\Delta=\frac{\partial^2 \mathbf{r}_i}{\partial t^2}\left[\mathbf{r}_i^P(t+\delta t),\frac{\partial \mathbf{r}_i^P}{\partial t}(t+\delta t)\right]-\frac{\partial^2 \mathbf{r}_i^P}{\partial t^2}(t+\delta t) \quad (2.67)$$

The corrector step:

$$\mathbf{r}_i(t+\delta t)=\mathbf{r}_i^P(t+\delta t)+\alpha_0\frac{\Delta\times\delta t^2}{2!} \quad (2.68a)$$

$$\frac{\partial \mathbf{r}_i}{\partial t}(t+\delta t)\times\delta t=\frac{\partial \mathbf{r}_i^P}{\partial t}(t+\delta t)\times\delta t+\alpha_1\frac{\Delta\times\delta t^2}{2!} \quad (2.68b)$$

$$\frac{1}{2!}\frac{\partial^2 \mathbf{r}_i}{\partial t^2}(t+\delta t)\times\delta t^2=\frac{\partial^2 \mathbf{r}_i^P}{\partial t^2}(t+\delta t)\times\delta t^2+\alpha_2\frac{\Delta\times\delta t^2}{2!} \quad (2.68c)$$

$$\frac{1}{3!}\frac{\partial^3 \mathbf{r}_i}{\partial t^3}(t+\delta t)\times\delta t^3=\frac{\partial^3 \mathbf{r}_i^P}{\partial t^3}(t+\delta t)\times\delta t^3+\alpha_3\frac{\Delta\times\delta t^2}{2!} \quad (2.68d)$$

$$\frac{1}{4!}\frac{\partial^4 \mathbf{r}_i}{\partial t^4}(t+\delta t)\times\delta t^4=\frac{\partial^4 \mathbf{r}_i^P}{\partial t^4}(t+\delta t)\times\delta t^4+\alpha_4\frac{\Delta\times\delta t^2}{2!} \quad (2.68e)$$

$$\frac{1}{5!}\frac{\partial^5 \mathbf{r}_i}{\partial t^5}(t+\delta t)\times\delta t^5=\frac{\partial^5 \mathbf{r}_i^P}{\partial t^5}(t+\delta t)\times\delta t^5+\alpha_5\frac{\Delta\times\delta t^2}{2!} \quad (2.68f)$$

where $\alpha_{i=0\div5}$ are parameter.

In addition, the use of the Verlet method usually requires computing the velocities that can be obtained from [6-9]:

$$\frac{\partial \mathbf{r}_i}{\partial t} = \frac{1}{2 \times \delta t}\left[\mathbf{r}(t+\delta t) - \mathbf{r}(t-\delta t)\right] \tag{2.69}$$

whereas other methods involve the determination of this derivative. The order of this equation is δt^2, and so, when velocity is needed the accuracy of the Verlet method is significantly smaller than the one of the other methods [6-9].

Among the methods having a good accuracy, the Velocity Verlet method provides the velocity in a completely satisfactory manner at $t, t+\delta t, t+2\delta t, \ldots$ not at $t, t+1/2\,\delta t, t+\delta t, t+3/2\,\delta, t+2\delta \ldots$ as in the Leap-Frog method, and is seemingly easier to implement than the Fifth-Order Gear Predictor-Corrector method [6-9]. This method is widely employed in MD simulations and provided realistic results. Therefore, in this work, we have used the Velocity Verlet algorithm to solve the equations of motion.

2.3.4. Periodic Boundary Conditions

Using finite different methods as in section 2.3.3 to solve the equations of motion given in section 2.3.2, the motions of N atoms are completely determined. However, a problem hidden in MD simulations is to impose a requirement on the motions of the atoms crossing the boundaries of the given volume V (finite size) of the simulation box. To do so, first one could imagine that the surfaces of the volume are container walls. Nevertheless, the presence of the container walls has significant effects on the motions of atoms near the surfaces, i.e. so-called the surface effects [10] which are not desirable. To achieve the finite size simulations requirement without walls effect, periodic boundary conditions (PBC) can be employed [6-9] so as to mimic an infinite system using a finite number of atoms.

When the PBC are applied to a system of N atoms contained in a volume V, so-called a primary box, the primary box is replicated throughout space [6-9]. These replicas are called image boxes. By doing so, at any time of the simulation, the positions and momenta of atoms

in the image boxes are exactly the same than those in the primary box. In the course of the simulations, as an atom moves in the primary box, its image in other image boxes moves in exactly the same way. Hence, as an atom leaves the primary box at one boundary, one of its images simultaneously enters through at the opposite boundary, see Fig. 2.6 [6-9]. However, imposing the artificial periodicity into the primary box by the use of the PBC can affect some simulated quantities [6-9]. Usually, to reduce the PBC effects, the primary box should initially be set up to be sufficiently large, which depends on the range of the inter-atomic potential, the state of the substance of interest, the quantity under investigation and the used computer [6-9].

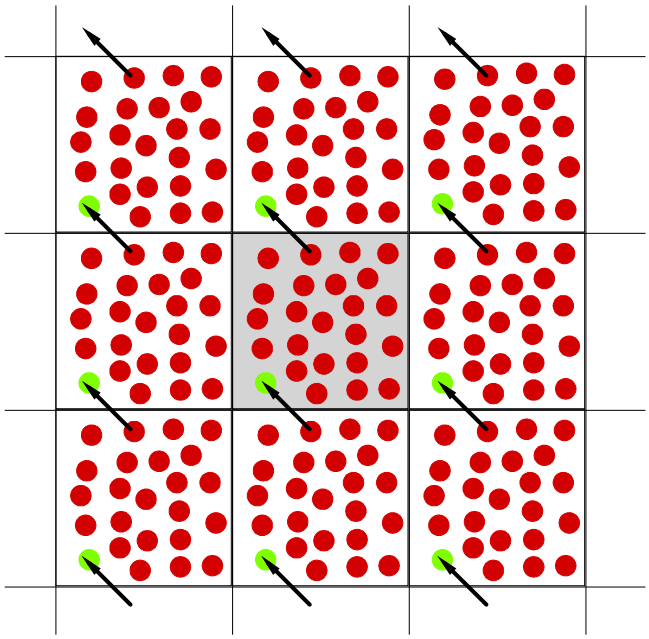

Figure 2.6: A 2D periodic system. Atoms can enter and leave each box across each of four boundaries. The shadowed box is the primary box [6].

2.3.5. Force Evaluation

To solve completely the equations of motion as described previously requires specifying the gradient of the total potential energy of a system $\nabla_{\mathbf{r}_i} U$. Accuracy and reality of

the simulation results crucially depend on the description of the total potential U which represents the interaction between the atoms composing the system.

2.3.5.1. Force Field

Considering a system containing N atoms, the total potential of the system is defined to be the sum of individual interactions each of which is characterized by the coordinates of individual atoms, pairs, triplets etc. [6]:

$$U = \sum_{i=1}^{N} u_1(\mathbf{r}_i) + \sum_{i=1}^{N-1}\sum_{j>i}^{N} u_2(\mathbf{r}_i, \mathbf{r}_j) + \sum_{i=1}^{N-2}\sum_{j>i}^{N-1}\sum_{k>j}^{N} u_3(\mathbf{r}_i, \mathbf{r}_j, \mathbf{r}_k)\ldots \tag{2.70}$$

where $u_1(\mathbf{r}_i)$ represents the effect of an external field and the remaining terms are particle interactions in which $u_2(\mathbf{r}_i, \mathbf{r}_j)$ is the pair potential and $u_3(\mathbf{r}_i, \mathbf{r}_j, \mathbf{r}_k)$ is the triplet potential, etc. In this work, we only focus on studying simple fluids that are composed of spherical atoms without bonds between atoms. The total potential can so be rewritten as:

$$U = \sum_{i=1}^{N} u_1(\mathbf{r}_i) + \sum_{i=1}^{N-1}\sum_{j>i}^{N} u_2(\mathbf{r}_i, \mathbf{r}_j) \tag{2.71}$$

It is worthy to notice that the pair potential depends only on the magnitude of the pair separation $r_{ij} = |\mathbf{r}_i - \mathbf{r}_j|$, i.e. $u_2(\mathbf{r}_i, \mathbf{r}_j) = u_2(r_{ij}) = u(r_{ij})$.

In this work, three simple spherical fluids: Lennard-Jones (LJ) fluid, Weeks-Chandler-Andersen (WCA) fluid and Soft fluid, are considered [6-9]. The three corresponding pair potentials are the followings:

The Lennard-Jones potential:

$$u(r_{ij}) = 4\varepsilon_{ij}\left[\left(\frac{\sigma_{ij}}{r_{ij}}\right)^{12} - \left(\frac{\sigma_{ij}}{r_{ij}}\right)^{6}\right] \tag{2.72}$$

The WCA potential:

$$u(r_{ij}) = \begin{cases} 4\varepsilon_{ij}\left[\left(\frac{\sigma_{ij}}{r_{ij}}\right)^{12} - \left(\frac{\sigma_{ij}}{r_{ij}}\right)^{6}\right] + \varepsilon_{ij} & \text{if } r_{ij} \le 2^{1/6}\sigma_{ij} \\ 0 & \text{if } r_{ij} \succ 2^{1/6}\sigma_{ij} \end{cases} \quad (2.73)$$

The Soft potential:

$$u(r_{ij}) = \varepsilon_{ij}\left(\frac{\sigma_{ij}}{r_{ij}}\right)^{n} \quad (2.74)$$

in which, n is a parameter that determines the potential steepness.

The two "atomic" parameters ε_{ij} and σ_{ij} are defined in term of the diameters and the potential depths of individual atoms as:

$$\sigma_{ij} = \frac{\sigma_i + \sigma_j}{2} \quad (2.75a)$$

$$\varepsilon_{ij} = k_{ij}\sqrt{\varepsilon_i \varepsilon_j} \quad (2.75b)$$

where σ_i and ε_i are the diameter and the potential depth of atom i respectively, and k_{ij} is a classical pre-factor to modulate the cross interaction between different species. It should be note that when $k_{ij} = 1$, Eq. (2.75) is the standard Lorentz-Berthelot combining rules.

2.3.5.2. Efficient Calculation of Forces

When the PBC is applied to a system containing N atoms, an atom in the primary box interacts not only with the $N-1$ remaining atoms in this cell but also with the atoms in the image boxes [6-9]. This leads to a total energy being an infinite sum, which is of course impossible to compute in practice and may induce unphysical self-correlations [6-9]. Fortunately, the pair potentials used in this work are short-range ones. It is so possible to restrict the number of atoms interacting with a given atom by neglecting atoms that are beyond some distance r_c from the given atom. This means setting the pair potential $u(r_{ij})$ to

zero for $r_{ij} \geq r_c$. r_c is called the cutoff radius. This is usually referred to as the method of ***truncation of pair potential*** [6-9].

However, the use of the truncation of pair potential induces two problems. First, the potential and its derivative, i.e. force, are both discontinuous at $r_{ij} = r_c$, which can result in perturbations. Second, the long range contributions are neglected, i.e. the contributions to properties of the system due to interactions between atoms separated by distance greater than r_c are not taken into account. To circumvent these problems, shifted potential and force are sometimes employed [6-9]. However, the use of such an approach may change the properties compared to the ones of the full potential.

In this work, we chose the cutoff radius to be sufficiently large so that the discontinuous of the potential and force at $r_{ij} = r_c$ remains small [6-9]. Additionally, to compensate for the missing long range part of the potential, the properties are corrected by adding long-range terms to the simulated ones, e.g. for the energy $E_{full} = E_{Simulation} + E_{LRC}$ and for the pressure $P_{full} = P_{Simulation} + P_{LRC}$ in which E_{LRC} and E_{LRC} are the long-range terms that are defined as, in the bulk [6-9]:

$$E_{LRC} = 2\pi\rho \int_{r_c}^{\infty} u(r) r^2 dr \tag{2.76a}$$

$$P_{LRC} = -\frac{2}{3}\pi\rho^2 \int_{r_c}^{\infty} r \frac{du(r)}{dr} r^2 dr \tag{2.76b}$$

Since the potentials used are short-range ones, the cutoff radius is usually smaller the size of the primary box that is rather large to restrict the PBC effects, i.e. $r_c \prec \min(L_x, L_y, L_z)$ where (L_x, L_y, L_z) are the dimensions of the primary box in the x, y, z directions respectively. This leads to the fact in the course of the MD simulation an atom in the primary box can

interact only with the $(N-1)$ remaining atoms in this box and their images in the adjacent boxes [6-9], i.e.

$$\nabla_{\mathbf{r}_i} U = -\sum_{\alpha_x=-1}^{1}\sum_{\alpha_y=-1}^{1}\sum_{\alpha_z=-1}^{1}\sum_{j\neq i}^{N}\nabla_{\mathbf{r}_i} u\left(\mathbf{r}_{ij}-\boldsymbol{\alpha}\mathbf{L}\right) \tag{2.77}$$

where $\boldsymbol{\alpha}=(\alpha_x,\alpha_y,\alpha_z)$ and $\mathbf{L}=(L_x,L_y,L_z)$. Eq. (2.77) indicates that the atom i can interact with the atom j in the primary box and its own images in the adjacent boxes (but only one of the 27 terms has a separation $|\mathbf{r}_{ij}-\boldsymbol{\alpha}\mathbf{L}|$ less than $L/2$). Therefore, when $L/2 \succ r_c$, which should be satisfied during MD simulations, Eq. (2.77) can be rewritten as:

$$\nabla_{\mathbf{r}_i} U = -\sum_{j\neq i}^{N}\nabla_{\mathbf{r}_i} u\left(\min\left[\left|\mathbf{r}_{ij}-\boldsymbol{\alpha}\mathbf{L}\right|,\left(\alpha_x=-1\div 1,\alpha_y=-1\div 1,\alpha_z=-1\div 1\right)\right]\right) \tag{2.78}$$

This is usually called the ***minimum image convention***, see Fig. 2.7.

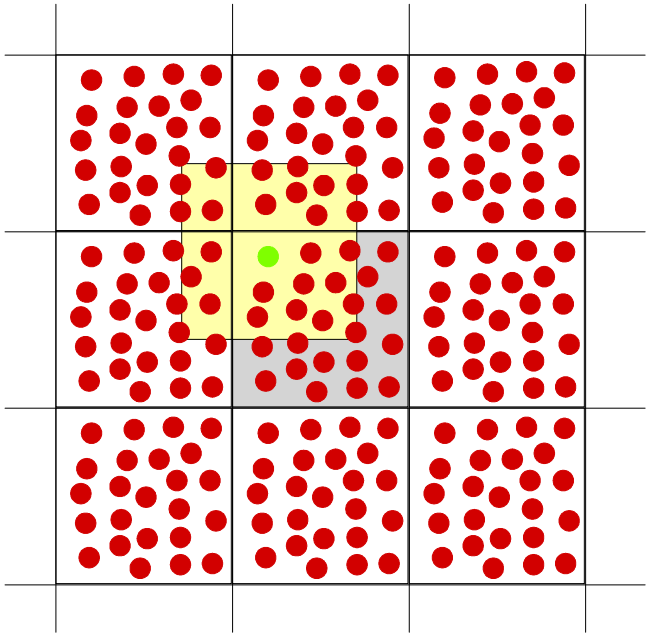

Figure 2.7: The minimum image convention in a 2D system. The yellow box contains atoms that contribute to the forces acting on the green atom.

To determine the force on an atom i using Eq. (2.78), at each time step of the MD simulations, requires computing inter-atomic distances between this atom and the $(N-1)$ remaining atoms, i.e. even taking into account all atoms beyond the cutoff radius r_c from the atom i. This is clearly a lost of CPU time because such atoms do not contribute the force on the atom i. To restrict the number of atoms beyond r_c, Verlet [55] proposed a bookkeeping scheme. In a first step, a list composed of all atoms lying within a distance $r_L \succ r_c$ of the atom i is constructed, where r_L is called the list radius, see Fig. 2.8, [6-9, 55]. The same list is used in the force evaluation over several consecutive time steps. The list will be updated once one of the N atoms has travelled from a distance $(r_L - r_c)/2$ from its position at the time of the last update. This method is usually referred to as the ***Verlet neighbor list*** [6-9, 55].

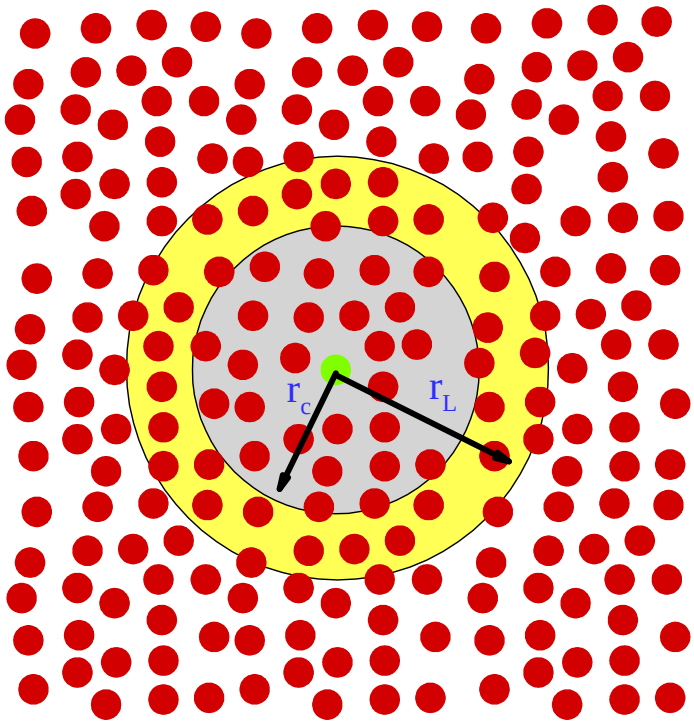

Figure 2.8: The cutoff and the neighbor list spheres around the green atom.

At each timestep the list is updated and the use of the Verlet neighbor list requires examining all the pair distances. This is really inefficient to systems containing many atoms as long as all pair distances larger than the list radius r_L are not necessary to be taken into account. To circumvent this problem, the primary box is divided into a regular lattice of $M_x \times M_y \times M_z$ cells, where M_x, M_y, M_z are the number of lattices in the x, y, z directions respectively, such that $\min\left(L_x/M_x, L_y/M_y, L_z/M_z\right) \succ r_L$, and all the atoms are sorted into their appropriate cells. Therefore, the list of an atom i located in a corresponding cell is reconstructed by searching all atoms only in this cell and its adjacent cells that lie within the list radius of the atom i, instead of in the entire primary box [6-7], see Fig. 2.9. This is called the ***cell sub-division***.

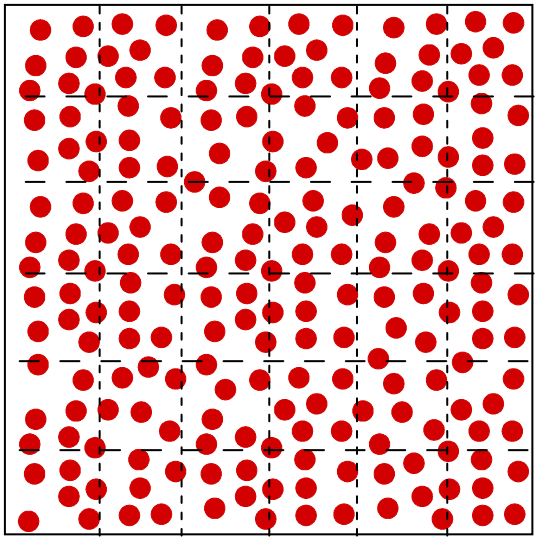

Figure 2.9: The cell list method in 2D. The primary box is divided into $M_x \times M_y$ cells. The size of cells exceeds the list radius r_L

The use of the methods described in this section to determine the forces can save much CPU time, and it is then possible (few days of computation) to perform MD simulations of systems containing a number of atoms around 5000 on only one processor. However, when

dealing with bigger systems the use of only one processor limits the possibilities due to the requirements on the CPU time and memory [7]. To circumvent this problem, the code can be parallelized, i.e. the computation of all the forces on all atoms is divided into several parts which are concurrently carried out on different processors [7, 56-58]. This is called the ***parallel computation***.

To be efficient, an algorithm of parallel computation should possess the following characteristics [7, 56-58]:

- An equilibrated number of calculations and memory needs on every processor,
- A limited amount of information exchanges between the processors

A non-negligible number of algorithms for parallelizing MD simulations have been proposed to achieve such characteristics [57-58]. Here we briefly introduce only the two main basic algorithms that can equally distribute the evaluations of the forces on the processors and that are not too complex to implement: ***Domain Decomposition*** and ***Functional Decomposition***.

In the ***domain decomposition algorithm***, the space of the primary box is equally divided into cells, each of which is assigned to a processor, see Fig. 2.10. Each processor is responsible for computing the forces on its own atoms. Since the neighbor list or at least the truncation of potential are usually used for the force calculations, each processor needs information of atoms from other cells within the list radius or the cutoff radius, see Fig. 2.10. The main advantage of this algorithm is that it does not require all the information of all atoms to be exchanged among all processors. It is so efficient for systems containing a large number of atoms when ran on a large number of processors. However, the implementation of this algorithm is not straightforward in inhomogeneous systems (as in this work) as it is rather complicated to divide the primary cell such that the above requirements of the parallel computation are achieved. Therefore, this algorithm is not used in this work.

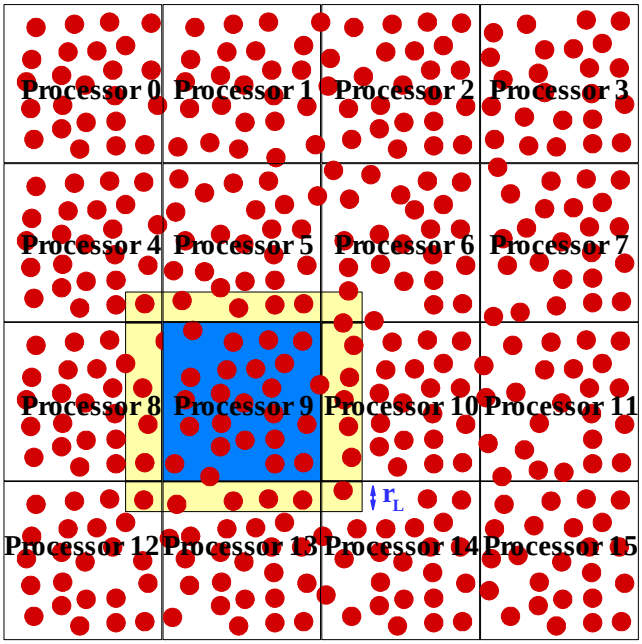

Figure 2.10: The domain decomposition algorithm in 2D. Each processor calculates the forces on its own atoms, i.e. processor 9 is responsible for atoms within the blue cell, but needs information of atoms from other cells within the radius list r_L in yellow, when updating the list.

In the ***functional decomposition algorithm***, as the potentials used in this work are pair ones, it is possible to define a force matrix $(N\times N)$ that is composed of:

$$\mathbf{F}=\begin{pmatrix} 0 & \mathbf{f}_{12} & \mathbf{f}_{13} & \mathbf{f}_{14} & \cdots \\ \mathbf{f}_{21} & 0 & \mathbf{f}_{23} & \mathbf{f}_{24} & \cdots \\ \mathbf{f}_{31} & \mathbf{f}_{32} & 0 & \mathbf{f}_{34} & \cdots \\ \mathbf{f}_{41} & \mathbf{f}_{42} & \mathbf{f}_{43} & 0 & \cdots \\ \vdots & \vdots & \vdots & \vdots & \end{pmatrix} \tag{2.79}$$

where $\mathbf{f}_{ij}=\nabla_{\mathbf{r}_{ij}}u(r_{ij})$ is the force on atom $i$due to atom j. From the third Newton's law: $\mathbf{f}_{ij}=-\mathbf{f}_{ji}$, it is clear that the total force on atom i $\mathbf{f}_i=-\sum_{j\neq i}^{N}\nabla_{\mathbf{r}_i}u(r_{ij})=\sum_{j\neq i}^{N}\mathbf{f}_{ij}$ is completely determined as long as the upper triangular portion of matrix is given. To equilibrate the

charge, the calculations of all $\mathbf{f}_{ij}$ are distributed over the n processors as following: processor 0 is responsible for the determination of the first $N/(2n)$ and the last $N/(2n)$ rows of the upper triangular portion; processor 1 is from row $N/(2n)+1$ to row $2N/(2n)$ and from row $N-2N/(2n)+1$ to row $N-N/(2n)$ and so on.

Although this method requires exchanging the information of all atoms among all processors, i.e. it is inefficient for systems containing a large number of atoms and a lot of processor, it is rather simple to implement and it does not depend of the inhomogeneity of the system. Thus, we have used this algorithm in this work when dealing with systems containing a number of atoms greater than 7000.

2.3.6. Transport Coefficients

In this part, we briefly introduce how to compute the transport coefficients of a system from its information at the microscopic level. Generally, transport coefficients are defined in terms of a (linear) response of a system to a (small) perturbation [6-9]. Hence, to obtain such coefficients, the response of the system to a perturbation is evaluated and compared with the corresponding macroscopic constitutive equation. Using MD simulations there exist two possibilities to deal with that problem [6-9]:

- The perturbation corresponds to the ones already existing due to the natural fluctuations (that may be artificially enhanced) at equilibrium.
- The system is put out of equilibrium by applying a large external perturbation while keeping the system still in the linear response regime (but the transport coefficient can vary with the perturbation).

Thus, transport coefficients can be determined either from the equilibrium state or the non-equilibrium state.

Since a large part of this work focus on momentum transport, only the techniques dedicated to compute the shear viscosity are mentioned in this section. For other transport properties, there exist equivalent techniques [6-9].

2.3.6.1. Equilibrium Molecular Dynamics Simulations

During equilibrium MD simulations, the shear viscosity can be obtained by invoking either the Green-Kubo formula or the Einstein relation as follows [6-9]:

The Green-Kubo formula

$$\mu = \frac{V}{k_B T} \int_{t=0}^{\infty} \left\langle J_{\alpha\beta}(t) J_{\alpha\beta}(0) \right\rangle dt \tag{2.80}$$

where α, β indicate the directions, i.e. x, y, z, $\langle . \rangle$ is the average over different original times and over the directions. The opposite of $J_{\alpha\beta}$ is the element of the stress tensor ($\tau_{\alpha\beta}$) that is given as:

$$J_{\alpha\beta} = \frac{1}{V} \left(\sum_{i=1}^{N} \frac{p_{i\alpha} p_{i\beta}}{m_i} + \sum_{i=1}^{N} r_{i\alpha} f_{i\beta} \right) \tag{2.81a}$$

or

$$J_{\alpha\beta} = \frac{1}{V} \left(\sum_{i=1}^{N} \frac{p_{i\alpha} p_{i\beta}}{m_i} + \sum_{i=1}^{N-1} \sum_{j>i}^{N} r_{ij\alpha} f_{ij\beta} \right) \tag{2.81b}$$

The Einstein relation

$$2t\mu = \frac{V}{k_B T} \left\langle \left(Q_{\alpha\beta}(t) - Q_{\alpha\beta}(0) \right)^2 \right\rangle \tag{2.82}$$

where

$$Q_{\alpha\beta} = \frac{1}{V} \sum_{i=1}^{N} r_{i\alpha} p_{i\beta} \tag{2.83}$$

In fact, Eqs. (2.80) and (2.82) are fully equivalent. The use of such techniques at equilibrium allows avoiding the effects of a large perturbation on the shear viscosity that may be unwanted [59-60]. Nevertheless, as we are interested by local properties in inhomogeneous

systems and by the out of equilibrium behaviors (flows in particular) these techniques have not been employed in this work.

2.3.6.2. Non-Equilibrium Molecular Dynamics Simulations

When an external perturbation is applied to a system, the system is out of equilibrium. The response of the system to the perturbation is then computed and using an appropriate macroscopic constitutive equation, the corresponding transport property can be obtained. For shear viscosity the perturbation can be either the shear rate or the shear stress (and vice-versa for the response) and the constitutive equation is the Newton's equation.

Here we briefly introduce some techniques to apply a convenient perturbation to a system that are widely employed in direct Non-Equilibrium MD simulations.

The boundary driven algorithms

The main idea of the boundary driven algorithms is to impose different velocities to the different boundaries of a given system. This corresponds generally to a Couette like configuration in a parallepipedic simulation box. For a system in which the boundaries are solid walls, it is easy to impose a shear rate by moving the solid walls at the desirable velocities [61]. However, the situation becomes more difficult to manage when the system contains no solid walls at the boundary and employs PBC. In such situations, imposing a velocity at the boundaries of the primary box can be done by moving the adjacent image boxes, see Fig. 2.11. It should be noted that the moving velocities of the adjacent image boxes must be different from the boundary velocities. By doing so, when an atom crosses the boundary of the primary box, its velocity must be modified to be consistent with the boundary velocities. In other words, imposing velocities at different boundaries can be achieved while keeping PBC, which was proposed by Lees and Edwards and is so-called the ***Lees-Edwards PBC*** [6, 62].

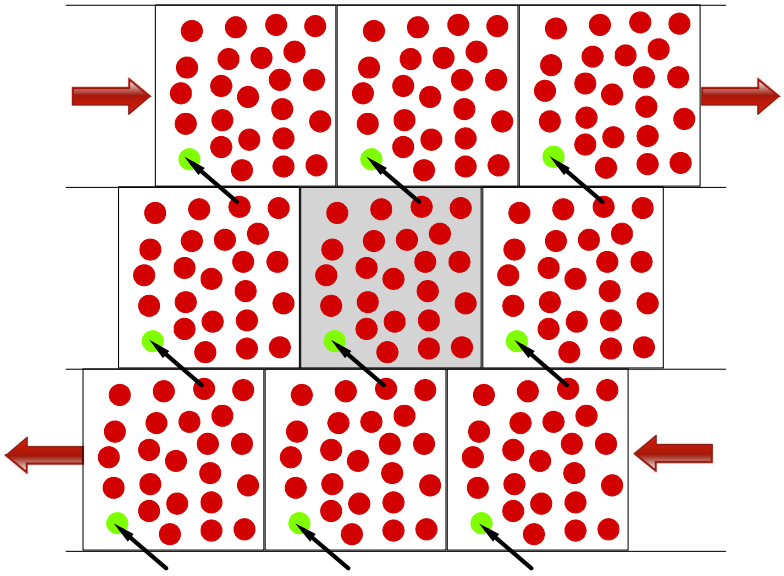

Figure 2.11: Homogeneous shear boundary conditions in 2D.

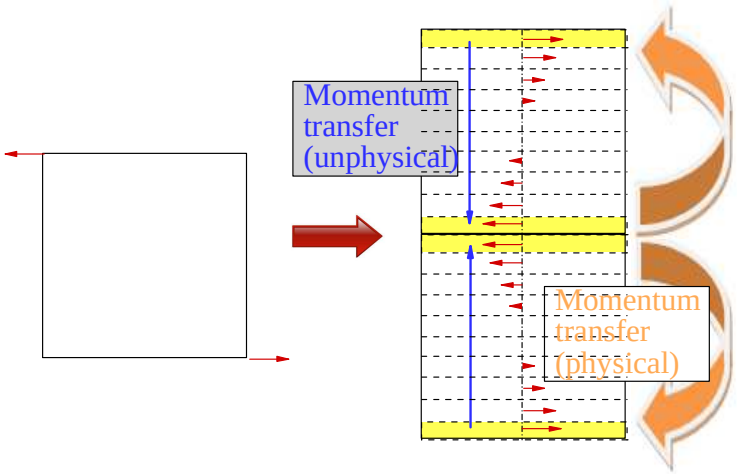

Figure 2.12: A 2D scheme view of the boundary driven algorithm proposed by Müller-Plathe.

An alternative and efficient technique to impose velocities at boundaries was proposed by Müller-Plathe and is called the ***Reverse Non-Equilibrium MD*** [63]. In this approach, first a primary box is duplicated in the direction perpendicular the flow to construct a bi-periodic system, see Fig. 2.12. Then, the boundaries of the primary box are driven by propelling atoms

within a small region adjacent to the boundaries. To do so, the bi-periodic box is divided into N_{Slab} slabs parallel the flow that needs to be generated (in the *x* direction in our example, see Fig. 2.12). Then, at a given number of time-steps (swapping time), the atoms located in the slabs that will induce the shear flow are looked for. In the slabs 1^{th} and N_{Slab}^{th}, the two atoms with the largest momentum component in the $-x$ direction are found. Likewise, in the slabs $(N/2)^{th}$ and $(N/2+1)^{th}$, the two atoms with largest momentum component in the $+x$ direction are found. Finally, the momentum of these atoms in slabs 1^{th} and N^{th} are exchanged with those in slab $(N/2)^{th}$ and $(N/2+1)^{th}$, respectively. By doing so, the boundary velocities depend strongly the interval chosen to perform the momentum exchanges, i.e. using different intervals yields different shear rate. Although the use of this technique requires doubling the primary box, this technique is easy to implement, keep the total energy and momentum of the system and does not require modifying the PBC.

The external force algorithms

The main idea of the external field algorithms is to apply a perturbation on all atoms of a system. By doing so, the equations of motion of the atoms must be modified by adding terms corresponding to the perturbation, which generally makes the system easier to interpret theoretically than what obtained from the boundary driven algorithms [6]. For a system containing solid walls at the boundaries, the perturbation is applied to the system simply by adding a ***uniform "gravitational" force*** on each atom [64], corresponding generally to a Poiseuille like configuration. This technique is widely used to study of the flow/shear viscosity of a fluid confined between solid surfaces. For systems without solid walls at boundaries, to maintain the PBC the velocity field generated from the perturbation must be spatially periodic. This requires applying a ***spatially periodic force*** on each atom which is often chosen to be a spatially sinusoidal function, see Fig. 13 [6, 65-66].

An alternative technique was proposed by Hoover *et al.* [67] and later modified by Evans et al. [68-69], and is called the SLLOD. In this technique, the conventional equations of motion are modified to represent the motions of atoms of a system with a ***linear streaming velocity***. To do so, the "laboratory" velocities of atoms are decomposed into the "peculiar" and streaming ones, in which the latter is initially given and the former is governed by the modified equations of motion. The use of this technique requires the use of Lees-Edwards PBC. Since the streaming velocity is generated by modifying the equations of motion of all atoms, this technique allows speeding up the simulations compared to the boundary driven one using the Lees-Edwards PBC alone.

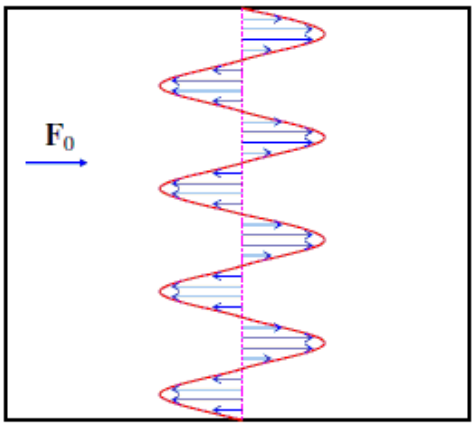

Figure 13: A schematic representation of spatially periodic force applied to the simulation box [6]

Transport coefficients of Inhomogeneous systems

For homogeneous systems, external field algorithms are often more suitable than the boundary driven algorithms due to the more tractable theoretical analysis of the results [6, 68-69]. When dealing with strongly inhomogeneous systems (as in this work) in which the shear viscosity may vary spatially, the computation of the local shear rate may be needed [64]. The

use of the external field algorithms implies the application of a local perturbation and so the local shear viscosity obtained may differ significantly from the “true” ones. The use of the external field algorithms induces variations in the shear rate that result from the inhomogeneity of the system and the local perturbation, whereas it is due to only the former when using the boundary driven algorithms. Furthermore, for systems in which the shear rate varies rapidly over a length typical of intermolecular correlations, the classical local Newton’s law of viscosity must be generalized by a nonlocal constitutive equation, i.e. the local shear viscosity cannot be defined as the ratio between the local shear stress and the local shear rate [70-71]. In fact, these problems could be completely avoided if the streaming velocity is fully linear over the entire system [71]. However, it requires modifying the equations of motion and the boundary conditions, which is obviously more complicated in inhomogeneous systems than that in homogeneous ones.

For all these previous reasons, we have used in this work the boundary driven algorithms to determine the flow properties/local shear viscosity of an inhomogeneous system.

References

[1] K. E. Gubbins and J. D. Moore, Ind. Eng. Chem. Res. 49, 3026 (2010)

[2] J. F. Wendt "Computational Fluid Dynamics" 3rd Edition, Springer-Verlag Berlin Heidelberg (2009)

[3] M. A. Biot, J. Appl. Phys. 12, 155 (1941)

[4] O. Coussy, Poromechanics, John & Sons, Chichester (2004)

[5] F. Varnik, J. Baschnagel and K. Binder, J. Chem. Phys. 113, 4444 (2000)

[6] M. P. Allen and D. J. Tildesley, "Computer Simulation of Liquids", Oxford University Press (1989)

[7] D. C. Rapaport, "The Art of Molecular Dynamics Simulation", Cambridge University Press (1995)

[8] J. M. Haile, "Molecular Dynamics Simulation: Elementary Methods", JOHN WILEY & SONS, INC. (1997)

[9] D. Frenkel, B. Smit, "Understanding Molecular Simulation, From Algorithms to Applications", Academic Press, Second edition (2001)

[10] M. Schoen, "Computer simulation of condensed phases in complex geometries", New series m: monographs, Lecture note in physics, m17 (1993)

[11] R. Khare, J. de Pablo, and A. Yethiraj, J. Chem. Phys. 107, 2589 (1997)

[12] J. Gao, W. D. Luedtke, D. Gourdon, M. Ruths, J. N. Israelachvili and U. Landman, J. Phys. Chem. B 108, 3410 (2004)

[13] L. Zhang, R. Balasundaram and S. H. Gehrke, J. Chem. Phys. 114, 6869 (2001)

[14] P. H. Hunenberger, Adv. Polym. Sci. 173, 105 (2005)

[15] L. V. Woodcock, Chem. Phys. Lett. 10, 257 (1971)

[16] D. J. Evans, W. G. Hoover, B. H. Failor, B. Moran, and A. J. C. Ladd, Phys. Rev. A 28, 1016 (1983)

[17] H. C. Andersen, J. Chem. Phys. 74, 2384 (1980)

[18] T. Schneider and E. Stoll, Phys. Rev. B 17, 1302 (1978)

[19] H. J. C. Berendsen, J. P. M. Postma, W. F. van Gunsteren, A. Dinola and J. R. Haak, J. Chem. Phys. **81**, 3684 (1984).

[20] S. Nosé, Mol. Phys. 53, 255 (1983)

[21] S. Nosé, J. Chem. Phys. 81, 511 (1984)

[22] W. G. Hoover, Phys. Rev. A 31, 1695 (1985)

[23] T. Soddemann, B. Dünweg and K. Kremer, Phys. Rev. E 68, 046702 (2003)

[24] G. J. Martyna, M. L. Klein, and M. Tuckerman, J. Chem. Phys. 97, 2635 (1992)

[25] S. D. Bond, B. J. Leimkuhler and B. B. Lairdb, J. Comput. Phys. 151, 114 (1999)

[26] M. Lupkowski and F. van Swol, J. Chem. Phys. 93, 737 (1990)

[27] B. D. Todd, D. J. Evans and P. J. Daivis, Phys. Rev. E 52, 1627 (1995)

[28] D. J. Evans and G. P. Morris, Chem. Phys. 77, 63 (1983)

[29] D. J. Evans and G. P. Morris, Phys. Lett. 98A, 433 (1983)

[30] A. Kolb and B. Dünweg, J. Chem. Phys. 111, 4453 (1999)

[31] D. Quigley and M. I. J. Probert, J. Chem. Phys. 120, 11432 (2004)

[32] W. G. Hoover, Phys. Rev. A 34, 2499 (1986)

[33] S. Melchionna, G. Ciccotti and B. L. Holian, Mol. Phys. 78, 533 (1993)

[34] G. J. Martyna, D. J. Tobias and M. L. Klein, J. Chem. Phys. 101, 4177 (1994)

[35] M. Parrinello and A. Rahman, J. Appl. Phys. 52, 7182 (1981)

[36] A. I. Landau, J. Chem. Phys., 117, 8607 (2002)

[37] D. Y. Sun and X. G. Gong, J. Phys. Condens. Matter, 14, 487 (2002)

[38] A. Papadopoulou, F. van Swol and U. M. B. Marconi, J. Chem. Phys. 97, 6942 (1992)

[39] A. Papadopoulou, E. D. Becker, M. Lupkowski and Frank van Swol, J. Chem. Phys. 98, 4897 (1993)

[40] A. P. Thompson, D. M. Ford and G. S. Heffelfinger, J. Chem. Phys. 109, 6406 (1998)

[41] A. P. Thompson and G. S. Heffelfinger, J. Chem. Phys. 110, 10693 (1999)

[42] J. Gao, W. D. Luedtke, and U. Landman, J. Chem. Phys. 106, 4309 (1997)

[43] J. Gao, W. D. Luedtke, and U. Landman, J. Phys. Chem. B 101, 4013 (1997)

[44] M. Lupkowski and F. van Swol, J. Chem. Phys. 95, 1995 (1991)

[45] S. Boinepalli and P. Attard, J. Chem. Phys. 119, 12769 (2003)

[46] T. Cagin and B. M. Pettitt, Mol. Phys. 72, 167 (1991)

[47] T. Cagin and B. M. Pettitt, Mol. Simul. 6, 5 (1991)

[48] J. Ji, T. Cagin and B. M. Pettitt, J. Chem. Phys. 96, 1333 (1992)

[49] G. C. Lynch and B. M. Pettitt, J. Chem. Phys. 107, 8594 (1997)

[50] H. Eslami and F. Muller-Plathe, J. Comput. Chem. 28, 1763 (2007)

[51] C. Lo and B. Palmer, J. Chem. Phys. 102, 925 (1995)

[52] R. M. Shroll and D. E. Smith, J. Chem. Phys. 110, 8295 (1999)

[53] J. C. Wang and Kristen A. Fichthorn, J. Chem. Phys. 112, 8252 (2000)

[54] L. F. Vega, K. S. Shing and L. F. Rull, Mol. Phys. 82, 439 (1994)

[55] L. Verlet, Phys. Rev. 159, 98 (1967)

[56] G. Galliero "Thermodiffusion dans les fluides de Lennard-Jones par dynamique moleculaire" Phd Thesis, Univesité Bordeaux I (2003)

[57] Y. Aoyama and J. Nakano "RS/6000 SP: Practical MPI Programming" International Technical Support Organization, IBM (1999)

[58] R. Koradi, M. Billeter and P. Güntert, Comput. Phys. Commun. 124, 139 (2000)

[59] D. M. Heyes, J. Chem. Soc., Faraday Trans. 2, 82, 1365 (1986)

[60] S. Hess, Int. J. Thermophys. 23, 905 (2002)

[61] I. Bitsanis, J. J. Magda, M. Tirrell, and H. T. Davis, J. Chem. Phys. 87, 1733 (1987)

[62] A. W. Lees and S. F. Edwards, J. Phys. C: Solid State Phys. 5 1921 (1972)

[63] F. Muller-Plathe, Phys. Rev. E 59, 4894 (1999)

[64] K. P. Travis and K. E. Gubbins, J. Chem. Phys. 112,1984 (2000)

[65] E. M. Gosling, I. R. McDonald and K. Singer, Mol. Phys. 26, 1475 (1973)

[66] G. Ciccotti, G. Jacucci and I. R. McDonald, Phys. Rev. A 13, 426 (1976)

[67] W. G. Hoover, D. J. Evans, R. B. Hickman, A. J. C. Ladd, W. T. Ashurst and B. Moran, Phys. Rev. A 22, 1690 (1980)

[68] D. J. Evans and O.P. Morriss, Comput. Phys. Rep. 1, 297 (1984)

[69] D. J. Evans and O.P. Morriss, Phys. Rev. A 30, 1528 (1984)

[70] B. D. Todd, J. S. Hansen and P. J. Daivis, Phys. Rev. Lett. 100, 195901 (2008)

[71] B. D. Todd and J. S. Hansen, Phys. Rev. E 78, 051202 (2008)

Chapter 3

Grand-Canonical Like Molecular Dynamics Simulations: Application to Anisotropic Mass Diffusion in a Nanoporous Medium*

* This chapter has been published in J. Chem. Phys. 136, 184702 (2012)

DOI: 10.1063/1.4712139

Abstract:

In this work, we describe two grand canonical-like molecular dynamics approaches to investigate mass diffusion phenomenon of a simple Lennard-Jones fluid confined between solid surfaces and in direct contact with reservoirs. In the first method, the density is used as the controlling variable in the reservoir whereas this is the pressure in the second method. Both methods provide consistent results, however the constant density approach is the most efficient with respect to the computational time and implementation. Then, employing the constant density approach, we have studied the transient behavior of the diffusion process associated with the migration of one fluid into another one confined between parallel solid walls. Results have shown that the evolution of molar fraction of the invading fluid follows roughly a 1D diffusion model when the solid phase is weakly or moderately adsorbent with a characteristic time increasing when the pore width decrease. However, when the adsorption is high and the pore width small (i.e. below ten molecular sizes), the apparent mass diffusion in the adsorbed layer is reduced compared to that in the center of the slit pore. Hence, this mass diffusion process becomes a two-dimension phenomenon that must take into account an effective mass diffusion coefficient varying locally.

3.1. Introduction

Behaviors of fluids in contact with and confined in microscopic spaces by solid surfaces have gained increasing attention recently [1-4]. Such specific behaviors are central in a variety of contexts both from the fundamental and the industrial point of views: lubrication, adhesion, coating, chromatography and membrane. In fact, in region close to the surfaces, the fluid molecules have a general tendency to organize into layered structures parallel to the surfaces [5-6]. Furthermore, in such highly confined systems, the ratio of the surface to the volume is very high, which leads to a strong impact of the layered structures on the global behaviors of the fluids. As a consequence, such effects can induce unusual experimental behaviors of both equilibrium and non-equilibrium effective properties of the fluids e.g. oscillatory solvation forces between confining solid surfaces, transition between liquid-like and solid-like behavior as solid surfaces get closer, effective shear viscosity several orders of magnitude higher than the bulk value, etc. [6-11]. In addition to these experimental approaches, molecular simulations mainly based on a Grand-Canonical Monte Carlo scheme, have shown to be a valuable tool in such confined systems since they can provide a microscopic picture of the confined fluids in conditions mimicking experimental ones [12-18].

When dealing with transport properties, one needs to employ Molecular Dynamics (MD) simulations instead of Monte-Carlo (MC) ones [19]. However, the Grand-Canonical Ensemble (GCE) which is the most suitable in most cases to deal with confined systems, is not easy to implement within a MD scheme even if there have been a non negligible number of algorithms proposed in literature to deal with Grand-Canonical-like MD (GCMD) [15, 17, 20-25]. The algorithms described in Refs. [20, 21, 23] proposed schemes based on extended system Hamiltonians of the confined systems to perform MD simulations at a constant chemical potential. The approaches proposed in Refs. [22, 24] assumes that a constant parallel

component of pressure of the confined systems (equal to bulk pressure) leads to equivalent results to those coming from a GCMD scheme. The approaches proposed in Refs. [15, 17, 25] consists in simulating explicitly the confined systems in contact with reservoirs maintained at a desired state. It is worth noticing that each algorithm has individual advantages and disadvantages. The first algorithms [20, 21, 23] have the advantage that the chemical potential is fixed (GCE), but the disadvantage that the insertion/deletion of particles is not always easy to deal with in dense systems. The second approaches [22, 24] are rather easy to implement and is not computationally demanding, but the assumption that a constant parallel component of pressure for different pore width is equivalent to a GCE is more than questionable. In our opinion the last algorithms [15, 17, 25] are a reasonable compromise even though they require significant CPU time, a disadvantage that is progressively reducing due to advances in high performance computing [19].

In this last family of Grand-Canonical-like Molecular Dynamics algorithm [17], systems are usually simulated at a constant number of particles, N, a constant total temperature, T, and a constant pressure in the reservoir, P_{res}. To control P_{res} they extended a changing box-shape method proposed by Parrinello and Rahman [26], in which the Lagrangian equations were modified in order to include some constraints. In this work, we propose a slightly modified and simpler version of this algorithm in which the thermodynamic state in the reservoir is controlled through a relaxation scheme of the type proposed by Berendsen et al. [27]. More precisely, we present two alternatives to control the thermodynamic state of the reservoir (i.e. the chemical potential), one based on pressure and one based on density.

As mentioned earlier, highly confined fluids has attracted a lot of attention during the last two decades. One of the main aspects is related to the mass diffusion process in such situations which is a problem that is usually difficult to tackle experimentally in dense fluids.

There exist a lot of theoretical studies of such general problem [2, 28-31] indicating a strong impact of both the confinement and the nature of the fluid-solid interactions in micro-pores (< 2nm). However, in our opinion, a perfect model does not exist in dense fluids despite recent progress in the modeling of this phenomenon [32-35].

MD is one of the tools employed to deal with diffusion at the (nano)-pore scale compared to what occurs without confinement. Unfortunately some of the works done are not performed using GCMD (or GCE + MC) approaches which lead to a difficult interpretation of the results obtained. Furthermore most of the studies have been devoted to pure fluids (i.e., self-diffusion) and not mixtures (i.e. mutual diffusion). Among the interesting results using GCMD simulations, it has been noticed that the transport properties are generally not strongly influenced by the confinement in systems with pore width larger than 10 times the size of the molecules [5, 14, 16]. However, to the best of our knowledge there is no study that investigates the transient behavior of mass diffusion of simple binary mixtures confined in slit pore. This is rather surprising as such configuration may enrich the analysis of the mass diffusion process in mixtures compared to what yield by equilibrium or even steady state simulations. Thus, in the present work, using the proposed GCMD scheme we have studied the transient behavior of the mass diffusion process of one fluid into slit pores, of varying adsorptions and widths, filled by a second fluid.

This paper is organized as follows. In Sect. 3.2 the two GCMD scheme proposed are presented. In Sect. 3.3 the methodology and the numerical details associated to both schemes are described. Then, in Sect. 3.4, some results of both GCMD approaches are provided and compared together and with the literature. In Sect. 3.5, some results on the transient mass diffusion in nanopores using the proposed GCMD scheme are presented. Our conclusions are summarized in Sect. 3.6.

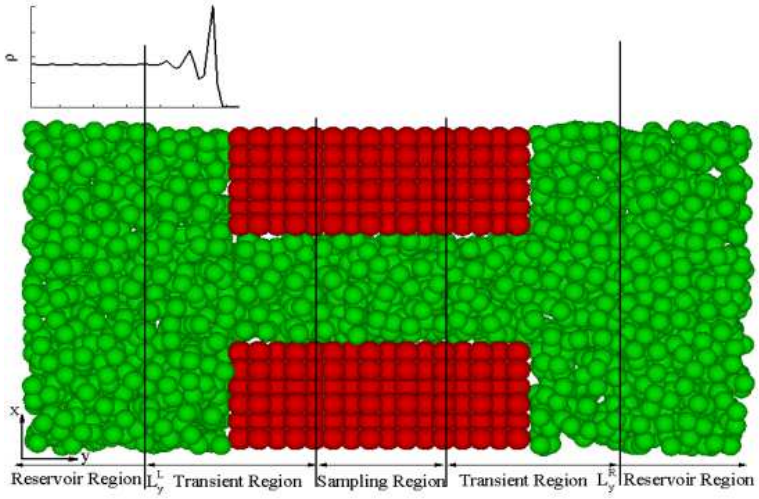

Figure 3.1: Side view of the simulation cell used in the Grand Canonical like Molecular Dynamics proposed in this work.

3.2. Methods

In this section, we present two alternatives to perform grand canonical-like molecular dynamics simulations of a pure fluid confined in a simple porous medium. The presented methods are similar to the ones proposed by Gao et al. [17], i.e. the explicit simulation of a "bulk" fluid reservoir controlled to maintain a given state in direct contact with the porous structure. A typical sketch of the simulation box is shown in Fig. 3.1, it consists of five regions: two reservoir regions, two transient regions and one sampling region.

The control of the thermodynamic state (i.e. the chemical potential) of the reservoirs is achieved by means of the relaxation scheme proposed by Berendsen *et al.* [27]. The first method uses the pressure and the temperature as controlling variable, called in the following "constant pressure GCMD" method, and the second method employs the density and temperature as controlling variables, named "constant density GCMD" method in the following.

For both methods, to maintain the temperature at a target value T_0, we have used the Berendsen thermostat [27]. According to this method, at each time step the velocities are scaled by a quantity:

$$\lambda_T = 1 + \frac{\Delta t}{2\tau_T}\left(\frac{T_0}{T} - 1\right) \tag{3.1}$$

where, Δt is the time step, τ_T is the time constant, and T is the instantaneous temperature.

3.2.1. The Constant Pressure GCMD Method

The pressure of the reservoir is maintained at desirable value by coupling to an external bath with constant pressure, i.e. pressure bath. The change in pressure can be written as:

$$\left(\frac{dP_{res}}{dt}\right)_{bath} = \frac{P_0 - P_{res}}{\tau_P} \tag{3.2}$$

where, P_0 is the target pressure, τ_p the pressure time constant and P_{res} is the instantaneous pressure in the reservoir regions defined as following:

$$P_{res} = \frac{1}{3V_{res}}\left[\sum_{i\in reservoir} m_i \mathbf{v}_i^2 + \frac{1}{2}\sum_{i\in reservoir}\sum_j \mathbf{r}_{ij}\mathbf{f}_{ij}\right] \tag{3.3}$$

where, V_{res} is the total volume of the reservoirs, m_i is the mass of i^{th} particle, $\mathbf{v}_i$ is the velocity of i^{th} particle, r_{ij} is the distance between particles i and j, $\mathbf{f}_{ij}$ is interaction force between i^{th} and j^{th} particles. The pressure change can be accomplished by varying the virial through a concomitant scaling of the interparticle distances in the y direction and the volume of the reservoirs. As described Berendsen et al. [27], the y coordinates of the particles in the reservoirs and the L_y lengths of the reservoir in the y direction are scaled by the quantity:

$$\lambda_P = 1 - \beta\Delta t\frac{(P_0 - P_{res})}{\tau_P} \tag{3.4}$$

where, β is the isothermal compressibility.

3.2.2. A Constant Density GCMD Method

The reservoirs could be maintained at a given thermodynamic state by controlling their instantaneous density (and temperature), instead of their instantaneous pressure (and temperature) of one. Hence, we propose a second approach in which the density of the reservoirs is maintained using the Berendsen et al. (1984) scheme [27], i.e. the reservoirs are supposed to be in contact with a controlling bath with constant density, i.e. density bath. For that purpose, we define the density change as:

$$\left(\frac{d\rho_{res}}{dt}\right)_{bath} = \frac{\rho_0 - \rho_{res}}{\tau_\rho} \tag{3.5}$$

where, ρ_{res} is the instantaneous density in reservoir regions, ρ_0 is the target density, and τ_ρ is the density time constant. The density change can so be accomplished by concomitantly scaling the dimension of the reservoirs and the coordinate of the fluid molecules in the reservoirs in the *y* direction. Using mathematical substitutions similar to the ones described by Berendsen et al. [27], the density scaling constant can be expressed as:

$$\mu_\rho = 1 - \frac{\Delta t}{\tau_\rho}\frac{\rho_0 - \rho_{res}}{\rho_{res}} \tag{3.6}$$

3.3. Simulation Procedure

From the above descriptions of the GCMD methods proposed in this work, the constant pressure scheme should be more CPU time demanding than the constant density one as long as it needs the determination of the instantaneous pressure which requires more computation than the estimation of the instantaneous density. However, since the time constant has an impact on the fluctuations of some thermodynamic properties, i.e. pressure and density, and on the number of the time steps required to equilibrate the system, we have performed a systematic comparison of the two methods on very simple configurations to obtain further information on the relative advantages of each method.

3.3.1. Particle Modeling

To be as simple as possible, all solid and fluid molecules have been modeled as spherical ones. All interactions are described by a classical truncated Lennard-Jones (LJ) 12-6 potential between pairs of particle:

$$U_{LJ} = \begin{cases} 4\epsilon \left[\left(\frac{\sigma}{r}\right)^{12} - \left(\frac{\sigma}{r}\right)^{6} \right] & \text{if } r \le r_c \\ 0 & \text{if } r > r_c \end{cases} \tag{3.7}$$

where r is the distance between the two particles, ε is the potential depth, σ is the particle diameter, and r_c is the cut-off diameter (=3.5σ in this work). To analyze the impact of the adsorption, the parameters in the interaction between fluid and solid molecules are modulated by using a classical k pre-factor as: $\sigma_{\mathrm{f-s}} = \sigma_{\mathrm{f-f}} = \sigma$ and $\varepsilon_{\mathrm{f-s}} = \varepsilon_{\mathrm{f-f}} = k\varepsilon$.

In the following variables are usually expressed in classical LJ dimensionless units noted with a star as superscript.

3.3.2. Simulation Box

The simulation box, as shown in Fig. 3.1, contains both fluid and solid particles, with periodic boundary conditions extending the system all three directions. The solid molecules are arranged in a faced centered cubic (FCC) lattice with a size of the lattice $a = 1.6\sigma$, i.e. corresponding to a solid density $\rho^*_{Solid} \approx 0.98$, to form two solid walls. The solid blocks are placed at the middle of the simulation cell in the y direction. In the x direction, the blocks are separated by a distance (W^*), defined as the distance between two innermost opposing atomic solid layers, that defines the width of the gap confining the fluid. The solid blocks are of finite size in the x and y directions, whereas, they are extended through the whole cell in the z direction. The remaining space of the simulation cell is filled by the fluid molecules, so-called the fluid space.

To describe the solid walls, each block consists of $3 \times N_{l,y} \times 8$ lattices in the *x*, *y* and *z* direction, respectively. The value used for $N_{l,y}$ depends upon the bulk state and is chosen to get a sufficient statistics on the data collected in the sampling region, i.e. for a dilute fluid $N_{l,y}$ is taken larger than for a dense fluid.

To perform the measurements, the simulation cell is divided into three different types of regions: sampling, transient and reservoir, see Fig. 3.1:

- The reservoir region corresponds to the area where the thermodynamic conditions (*P*, *T* or ρ, *T*) are imposed to the "bulk" fluid.
- The transient regions are regions where the data are not collected as they correspond to regions which are neither "bulk" neither fully confined, i.e. boundaries effect (because of the finite size of the solid walls) are important.
- The sampling region is the one employed to compute the thermodynamic properties of the confined fluid in contact with the reservoirs avoiding effects due to the finite size of the walls.

Thus, the sizes of the sampling and transient region are fixed, whereas the size of the reservoir region is varied dynamically. To do so, during the simulations, the *y* coordinates of the molecules in the reservoir region and the *y* size of this region are scaled at each time step thanks to the two schemes previously described.

To avoid as much as possible the effects due to the finite size of the two solid walls on the sampling region, its dimension has been taken equal to $\left(N_{l,y} - 4\right)a$ on the y direction, i.e. fluids in ending regions of the confined space in the *y* direction that are strongly influenced by the finite pore size effects are discarded. The *y* dimension of each ending region is equal to $2a = 3.2\sigma$, which has been found to be sufficient to obtain that the variation of the fluid density in the *y* direction in the sampling region is not affected by the pore end effects. The positions of boundaries of the reservoirs, i.e. L_y^{Right} and L_y^{Left} see Fig. 3.1, are chosen to be

larger than a "critical" distance defined as the distance from the walls for which the influence of the walls is noticeable on the fluid density (oscillation due to adsorption). This critical distance is of the order of a few times the diameter of the fluid particle [36]. In this work, we have chosen the critical distance to be 4.5σ and 7σ for respectively the supercritical and the liquid states studied in Sect. 3.4. In fact, these values have been determined by testing different distances and their influence on the confined density obtained.

The initial values of the dimensions of the two reservoirs region in the *y* direction have been chosen to be sufficiently large, so that the fluid in the reservoir satisfies the equilibrium hypothesis of the bulk fluid [17, 36] and also system is equilibrated rapidly.

3.3.3. Numerical Details

To perform the MD simulations, we employed a numerical code of our own, already employed to deal with diffusion in confined situations [37-39]. The motion equations of the fluid molecules are solved using the Verlet velocity algorithm with a time step Δt^*=0.002, whereas the solid molecules are fixed at their sites. To compute the force on each fluid molecules effectively, we have combined the periodic boundary conditions (PBC) and the neighbor list [40]. The systems are equilibrated for $10^6 \sim 2 \times 10^6$ time steps followed by a simulation period of $5 \times 10^5 \sim 10^6$ time steps, during which the samplings are carried out.

3.4. Preliminary Results

3.4.1. Comparison of the Two Schemes

To evaluate the impact of the time constant on the results for both GCMD methods, simulations have been performed with different time constants and for two target bulk states in the reservoirs: $\rho^*_{Bulk} = 0.75$, $P^*_{Bulk} = 0.619$, $T^*_{Bulk} = 1$ (a liquid state) and $\rho^*_{Bulk} = 0.3$, $P^*_{Bulk} = 0.524$, $T^*_{Bulk} = 2$ (a supercritical state). The potential depth between the fluid and

solid molecules is $\varepsilon_{\mathrm{f-s}} = \varepsilon_{\mathrm{f-f}} = \varepsilon$. To analyze the transient behavior, we have generated initial configurations such that the density of the fluid is slightly different from the targeted "bulk" density. For the liquid state we have used $\rho_{ini}^{*} = 0.7$ and for the supercritical state $\rho_{ini}^{*} = 0.25$.

Results in Figs. 3.2 and 3.3 show that for both methods and for both states the *y* size of the reservoir, L_y, evolves with time relatively monotonously to its equilibrium value. The corresponding pressure and density evolve to the equilibrium pressure and density respectively with fluctuations that are similar for both schemes and of the order of those at equilibrium. In addition, it can be noticed that the shorter the time constant, the shorter the equilibrium time and the larger the fluctuations on the L_y size of the reservoir [27].

The results in Figs. 3.2 and 3.3 exhibit two interesting additional features. First, the order of the equilibrium time is slightly larger than the order of the time constant, which can be understood from the fact the fluid in the system is only partly coupled with the bath (only the fluid in the reservoir region). Second, the equilibrium times provided by the two methods are very similar, which indicates that the methods are of the same efficiency with respect to the equilibrium time.

The first objective of the methods outlined previously is to estimate the average density of the confined fluids extracted from the sampling region at equilibrium. As can be deduced from Table 3.1, for a time constant (for both GCMD schemes) varying in the range $\tau^{*} = 10{\sim}200$, the results indicate that the average densities are independent upon the time constant within the statistical uncertainty for the studied range of values. The statistical uncertainty represents the standard deviation and is estimated by employing the sub-blocks average method [40]. In addition, the results show that both GCMD methods yield the same average density and uncertainty.

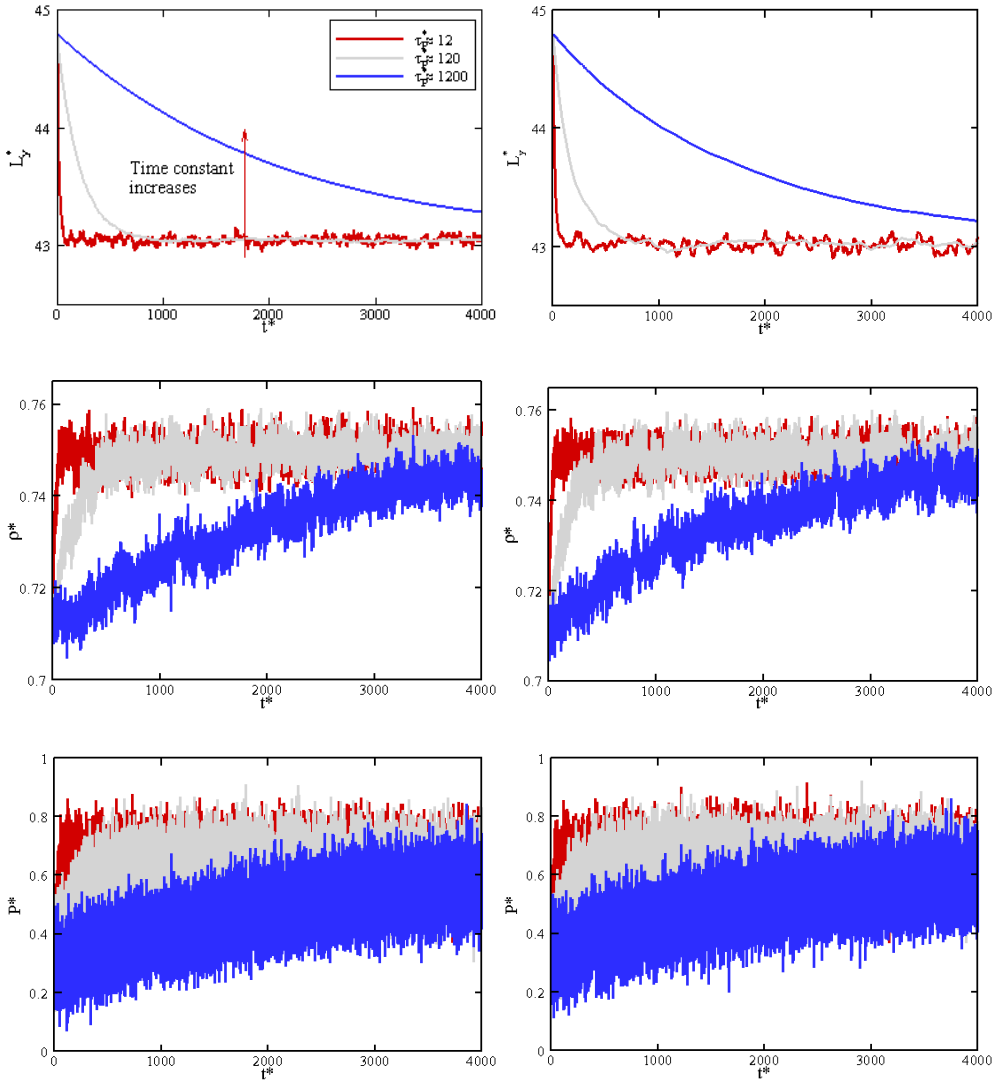

Figure 3.2: Effect of the time constant on the evolution of the system towards the equilibrium for the liquid state, $\rho^*_{Bulk} = 0.75$ and $T^*_{Bulk} = 1$. The left figure corresponds to the constant pressure GCMD method and the right one to the constant density GCMD method.

To confirm further that both methods provide the same static properties of the confined fluids, we have estimated the density profiles for different widths of the gap, using $\tau^* = 100$. As can be deduced from Fig. 3.4, both methods are in excellent agreement (with deviations below 1%) whatever the state and the pore width and provide results consistent with what known for confined LJ fluids [6, 36].

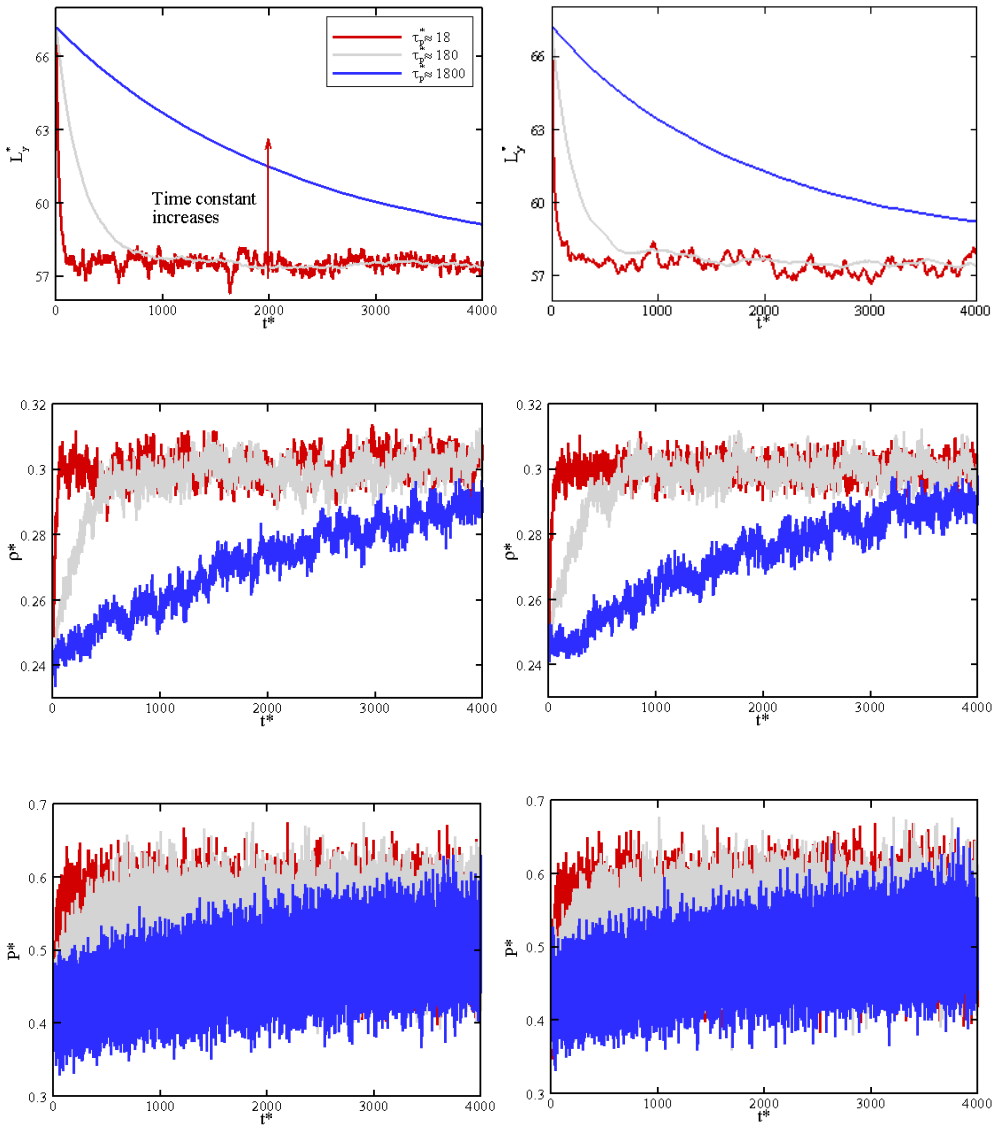

Figure 3.3: Effect of the time constant on the evolution of the system towards the equilibrium for the supercritical state $\rho^*_{Bulk} = 0.3$ and $T^*_{Bulk} = 2$. The left figure corresponds to the constant pressure GCMD method and the right one to the constant density GCMD method.

Thus, taking into account that both methods provide the same results with the same order of uncertainties for a given time constant, considering the CPU time and implementation needed by both approaches, we can conclude that the constant density GCMD proposed in this work is the preferable option among the two.

	Time Constant	Constant P GCMD	Constant ρ GCMD
$\rho^*_{Bulk} = 0.3,\ T^*_{Bulk} = 2$	$\tau^* = 18.0$	$\rho_{Ave} = 0.2951 \pm 0.0021$	$\rho_{Ave} = 0.2985 \pm 0.0021$
	$\tau^* = 180$	$\rho_{Ave} = 0.2991 \pm 0.0021$	$\rho_{Ave} = 0.3002 \pm 0.002$
$\rho^*_{Bulk} = 0.75, T^*_{Bulk} = 1$	$\tau^* = 12.0$	$\rho_{Ave} = 0.6274 \pm 0.0044$	$\rho_{Ave} = 0.6329 \pm 0.0045$
	$\tau^* = 120$	$\rho_{Ave} = 0.6325 \pm 0.0045$	$\rho_{Ave} = 0.6293 \pm 0.0044$

Table 3.1: Effect of the time constant on the average equilibrium density obtained by the two GCMD schemes.

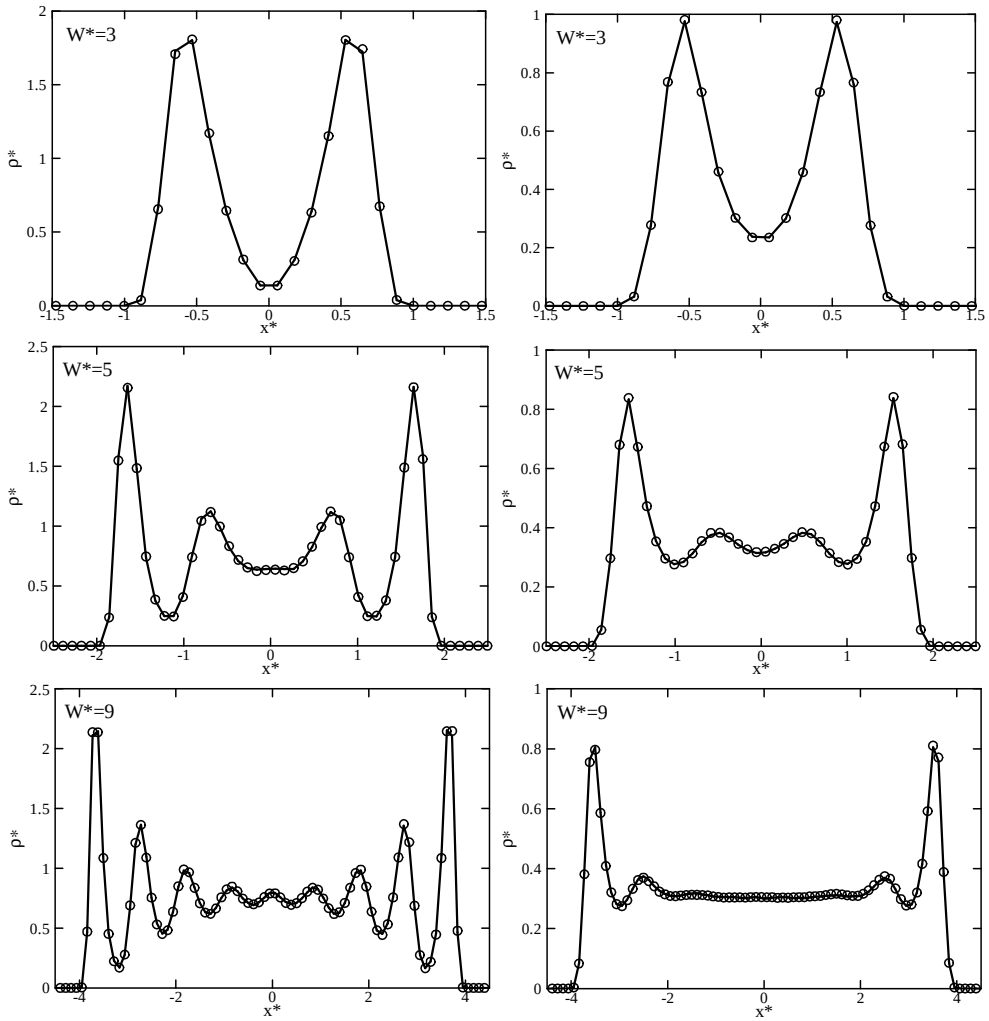

Figure 3.4: Density profiles for different pore width: $W^* = 3;\ 5$ and 9. Left figures: $\rho^*_{Bulk} = 0.75$ and $T^*_{Bulk} = 1$, right figures: $\rho^*_{Bulk} = 0.3$ and $T^*_{Bulk} = 2$. Solid lines correspond to the results provided by the constant pressure GCMD method. Open symbols corresponds to the constant density GCMD results.

3.4.2. Validation vs GCMC Simulations

To further validate the results provided by the methods described previously, we have compared results provided from our constant density GCMD simulations using $\tau_\rho^* = 200$ with some coming from Grand-Canonical Monte Carlo. However this comparison should be even if it is always difficult to compare properly MD and MC simulations of discontinuous potentials (like the truncated LJ potential used in this work) [41-42]. The comparison has been done by choosing the data provided in Schoen *et al.*'s GCMC study [5] corresponding to $\rho_{Bulk}^* \approx 0.6965$, $P_{Bulk}^* = 0$, $T_{Bulk}^* = 1$, $\rho_{Solid}^* \approx 0.98$, and $\varepsilon_{\mathrm{f-s}} = \varepsilon_{\mathrm{f-f}} = \varepsilon$ respectively. Since each solid wall consists of only one atomic layer in their work, instead of using full solid blocks as in Fig. 3.1, only the first layer of the solid atoms in contact with fluid have been included to perform the comparison, as shown in Fig. 3.5(a).

Figure 3.5(b) depicts the variation of the average density of the confined fluid with the distance between the two solid surfaces from the GCMC by Schoen *et al.* [5] and from our simulations. The figure shows that there is rather good agreement between results provided from the GCMC and our method, despite the differences in the methodologies. In particular, our method predicts that a phase transition occurs at $W^* \approx 2.3$ which is the same value as the one that is obtained by Schoen *et al.* Furthermore, the absolute deviation between our results and those of Schoen et al. is below 5 %. Thus, the good agreement with the results provided by a GCMC scheme indicates that the constant density GCMD presented in this work is consistent.

Nevertheless, there are expected slight differences between the results from our study and the one of Schoen *et al.* [5]. These differences are due to two main reasons apart from the fact that the two methodologies are completely different. First, in Schoen's simulation, they employed systems of $8\sigma \times 8\sigma$ in the *y* and *z* directions respectively, whereas in our simulations the sampling region of the confined fluid has dimensions of $6.4\sigma \times 12.8\sigma$ in the *y*

and *z* directions, respectively. Second, and even more important, we have used a truncated LJ force, while Schoen et al. took a truncated LJ potential combined a very simple (but only approximate) long-range corrections (LRC) on the potential.

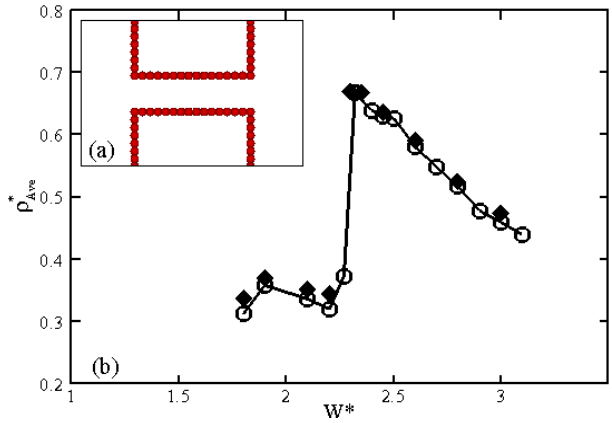

Figure 3.5: A comparison of the constant density GCMD method and the GCMC. a) The configuration of the solid used in simulations. b) Variation of the average density with the distance between solid surfaces. Full symbols: constant density GCMD results, open symbols: GCMC results given in Schoen *et al.* [5]. The solid curve serves as a guide for the eye.

3.5. Transient Mass Diffusion in Nanopores

In this section, we present an application of the constant density GCMD method to the analysis of the transient behavior of the mass diffusion process into a slit nanopore. More precisely is studied the invasion (by mass diffusion) of one fluid, named fluid 2, into a slit pore filled by another fluid, called fluid 1, for different adsorption characteristics and various widths of the pore. For that study the thermodynamic state of the reservoir fluid has been fixed at a supercritical state: $T^* = 2$ and $\rho^* = 0.5$.

To simplify as much as possible the system studied, the molecular parameters of both fluids have been taken equal ($\sigma_1 = \sigma_2 = \sigma$ and $\varepsilon_1 = \varepsilon_2 = \varepsilon$), except their masses which have been chosen to be $m_2 = 10m_1$, i.e. the fluid region is composed of two "isotopes". The main

interest of choosing such a fluid system is that both species are fully equivalent from a thermodynamic point of view, i.e. they have the same phase diagram in reduced units and the same adsorption isotherms in reduced units. This feature allows starting the simulation from an equilibrated situation without any artifacts related to the construction of an initial system composed of two species which differs in size or in energy. More precisely to construct a fully equilibrated initial system as described in Fig. 3.6(a), two steps are needed:

- The system is assumed to contain only one species in the fluid phase, and is equilibrated by using the constant density GCMD method.
- The fluid particles being out of the pore are transformed to become fluid 2, i.e. the mass of these particles out of the pore becomes equal to m_2 and their velocities are rescaled in order to keep the temperature unchanged.

Then, the simulation of the transient mass diffusion process of fluid 2 into fluid 1 can be performed by using the constant density GCMD method.

In the case of a bulk fluid phase with a similar configuration, the evolution of the molar fraction can be described by an approximate (not perfectly valid in the short time limit) solution to a one dimension (1D) diffusion equation as [43-44]:

$$\frac{x_2}{x_{2\_Stat}} = 1 - e^{\left(-t^*/\theta^*\right)} \tag{3.8}$$

where x_2 is the instantaneous molar fraction of the fluid 2 at the time t^*, x_{2_Stat} is the stationary molar fraction of the fluid 2, and θ^* is the mass diffusion characteristic time. When dealing with confined fluids the situation is more complex because:

- The geometric confinement leads to a mass diffusion coefficient which is no longer isotropic [1, 2, 5, 30-31, 45] (diffusion perpendicular to the walls becomes very small) and that may vary with the pore width depending on the nature of the walls [5, 33, 37, 39, 45].

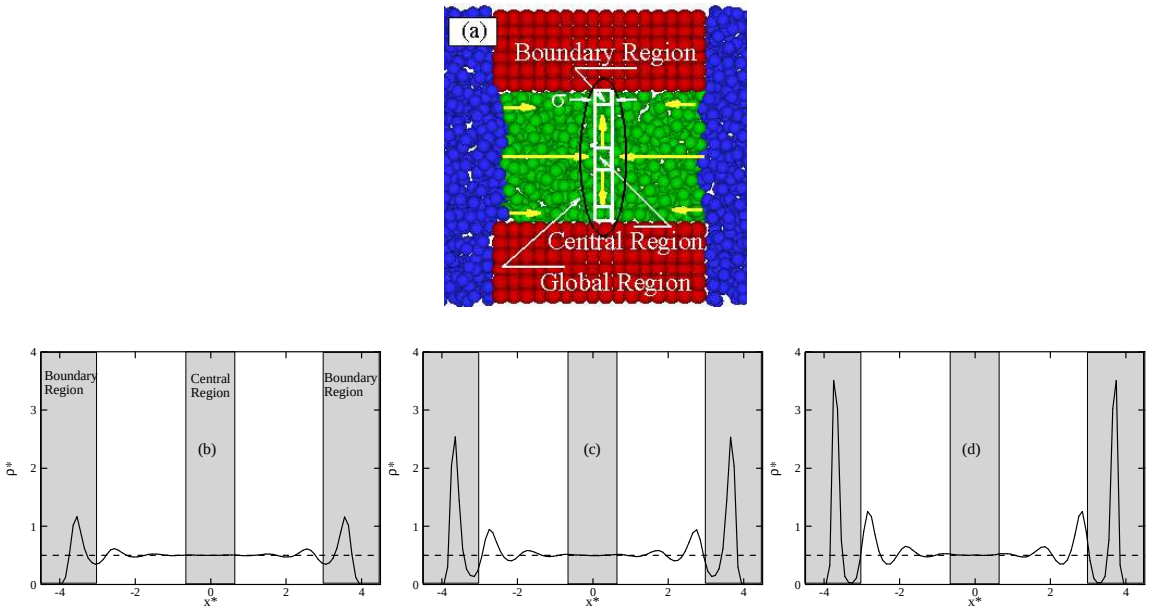

Figure 3.6: (a) Snapshot of the invasion of one fluid (in blue) into the slit pore (in red) filled by another fluid (in green). (b-d) Effect of the fluid-solid interaction on the density profile in the pore. (b) Low fluid-solid interaction. (c) Intermediate fluid-solid interaction. (d) High fluid-solid interaction.

- The physical adsorption and confinement leads to a strongly inhomogeneous fluid close to the walls in the *x* direction which may modify the transport property locally [30, 34-35, 46].

So, to study the impact of the confinement and fluid inhomogeneities on the transient diffusion process described in Fig. 3.6(a), we have estimated the evolutions of x_2 over time (averaged over 100 time step) in two different local regions of the central slab (of a width of one σ) in the *y* direction. One region is adjacent to the solid phase and extent over a distance of 1.5σ from the nearest solid surface which corresponds to the region of the first adsorbed layer. This region is named “boundary region”. The second region is located in the centre of the central slab with dimension of one σ in the *x* direction and named “central region”. In addition we have estimated the evolution of x_2 in the entire central slab, named “global region” in the following.

For a given thermodynamics state of the reservoir, the density inhomogeneities of the confined fluid are influenced by the fluid-solid interaction and width of the gap [5-6]. So, we have investigated the possible effects of density inhomogeneity on the evolutions of x_2 over time by determining them for different fluid-solid interactions and for various pore widths. The behavior at very short time has not been discussed in the following as it may leads to specific problems [47]. In order to reduce the statistical uncertainties, the results provided in the following correspond to an average over 20 different independent runs.

3.5.1. Effect of Fluid-Solid Interaction

The effect of the fluid-solid interaction has been considered by using three different types of solid-fluid interactions: $\varepsilon_{fs} = \varepsilon$, low adsorption, $\varepsilon_{fs} = 2.5\varepsilon$, intermediate adsorption and $\varepsilon_{fs} = 4\varepsilon$, high adsorption. The gap (width of the pore) between the two solid walls, W^*, has been taken equal to 9. Figures 3.6(b)-3.6(d) show the density profiles of the fluid 1 at the equilibrium state for the three solid-fluid interactions. As expected, results indicate that the density vary appreciably with distance from the solid surface for all the interactions with a classical damped oscillation shape [5-6], in which the amplitude is increasing with the solid-fluid interaction.

Figure 3.7 shows the evolutions of x_2 in the three regions analyzed (boundary, central and global, see Fig. 3.6) for different fluid-solid interactions. One interesting result is observed for the low adsorption case, for which the evolutions of x_2 for the three regions are nearly superposed. This is rather surprising since the fluid is noticeably inhomogeneous in the x direction as shown in Fig. 3.6(b). However, this result is consistent with the ones found by previous authors [14, 48-49], which confirms that when both the fluid-solid interaction and the fluid density are not very large, local diffusion coefficient in the plane parallel the solid surface does not vary significantly, even if local density appreciably oscillates. Another

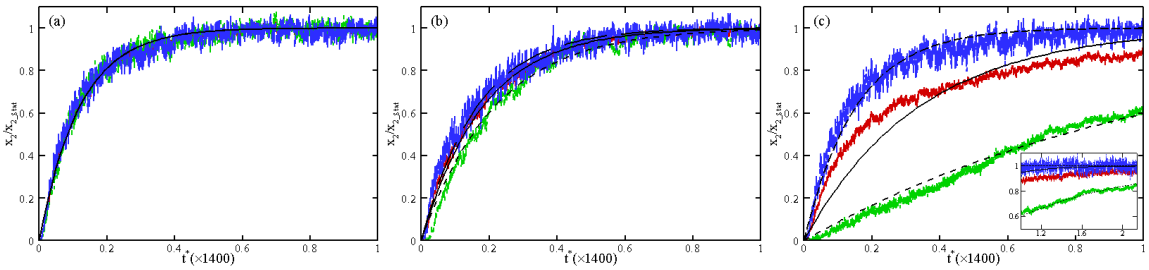

Figure 3.7: Evolution of x_2 in the central fluid layer (perpendicular to the walls) for t^* varying from *0* to*1400*. (a) Low adsorption. (b) Intermediate adsorption. (c) High adsorption: Inset is the evolutions for $t^*=1400 \div 3000$. Solid red curves: global region, dashed green curves: boundary region and long-dashed blue curves: central region. Black curves: fitted curves using Eq. (3.8).

interesting result is that the x_2 profiles obtained for the low adsorption case can be very well fitted by employing Eq. (3.8), see Fig. 3.7(a). This confirms, as assumed in most works, that the evolutions of x_2 in such systems can be well described by a simple 1D diffusion equation with one effective diffusion coefficient despite the density inhomogeneities.

When the fluid-solid interaction increases (intermediate and high adsorption cases), the evolutions of x_2 in the three regions clearly departs from each other, see Figs. 3.7(b) and 3.7(c). Interestingly, the evolution of x_2 in the boundary and central regions can be well described by a simple 1D diffusion equation, see Figs. 3.7(b) and 3.7(c), with an effective diffusion time depending on the position and the fluid-solid interaction, see Table 3.2. More precisely, the evolution in the central region is noticeably faster than that in the boundary region, a trend which is particularly obvious in the high adsorption case, see Fig. 3.7(c). Thus, these results indicate that the effective mass diffusion coefficient in the adsorbed layer is smaller than in the central region and tends to decrease when the fluid-solid interactions increases. It is worth to notice that such trend for the effective mass diffusion coefficient is

Adsorption	Region	$(\theta^*/1400)^{-1}$	R-square
Low	Global	8.304	0.9899
	Central	8.372	0.9714
	Boundary	8.296	0.9813
Intermediate	Global	5.493	0.9937
	Central	6.073	0.9694
	Boundary	4.621	0.9859
High	Global	3.128	0.8824
	Central	6.516	0.9582
	Boundary	0.8972	0.9748

Table 3.2: Mass diffusion characteristic time for the different cases using Eq. (3.8). R-square represents the correlation coefficient of the fit of Eq. (3.8).

sometimes interpreted as a result of the modification of the fluid-solid friction when changing fluid-solid interactions [33].

Another interesting result, see Figs. 3.7(a)-3.7(c), is that the evolutions of x_2 in the central region tends to be slower when the adsorption increases, even if the density in this region is uniform and the same for all adsorption cases, see Figs. 3.6(b)-3.6(d). This can be understood by the mechanism described briefly in Fig. 3.6(a). In fact, the evolution of x_2 in the centre of the pore (parallel to the walls) is faster than that in the region close to the walls which leads to a mass flux (along the x direction) of the fluid 2 from the centre to the boundaries in the pore. So, because of this mass flux, the time need for fluid 2 to reach the central region (perpendicular to the pore walls) will be increased.

Concerning the global region, as clearly shown in Fig. 3.7(c), the evolution of x_2 cannot be described anymore by a simple 1D diffusion equation in the high adsorption case. This not surprising as the characteristic times in the boundary and the central region are so different that the global mass diffusion process in such case cannot be 1D phenomenon anymore.

All these results clearly lead to the conclusion that, when the densities inhomogeneities are large, the mass diffusion varies locally noticeably within the pore width. More precisely its amplitude decreases strongly in the adsorbed layer compared to the centre of the pore (parallel to the wall). Because of these local variations of the mass diffusion coefficient, the diffusion in a slit nanopore in the high adsorption case does not correspond anymore to a one-dimension configuration and should be described by a 2D mass diffusion equation including a mass diffusion coefficient position dependent (in the *x* direction), a problem that cannot be solved analytically.

In order to confirm these findings visually, we have measured the relative local density of the fluid 2, i.e. ρ_2^*/ρ^*, over the simulation box at various time. Figure 3.8 shows the distribution of the relative local density at several instants for the three fluid-solid interactions. Two interesting features can be noticed on these figures. First, the invading surface of the fluid 2 is roughly a plane for the low fluid-solid interaction, which means that the evolution at any position is a 1D diffusion process. Second, for the intermediate and high fluid-solid interaction the invading surface has roughly a parabolic form in early stages. This shape of the diffusion front is consistent with the above explanations and the mechanism described in Fig. 3.6(a).

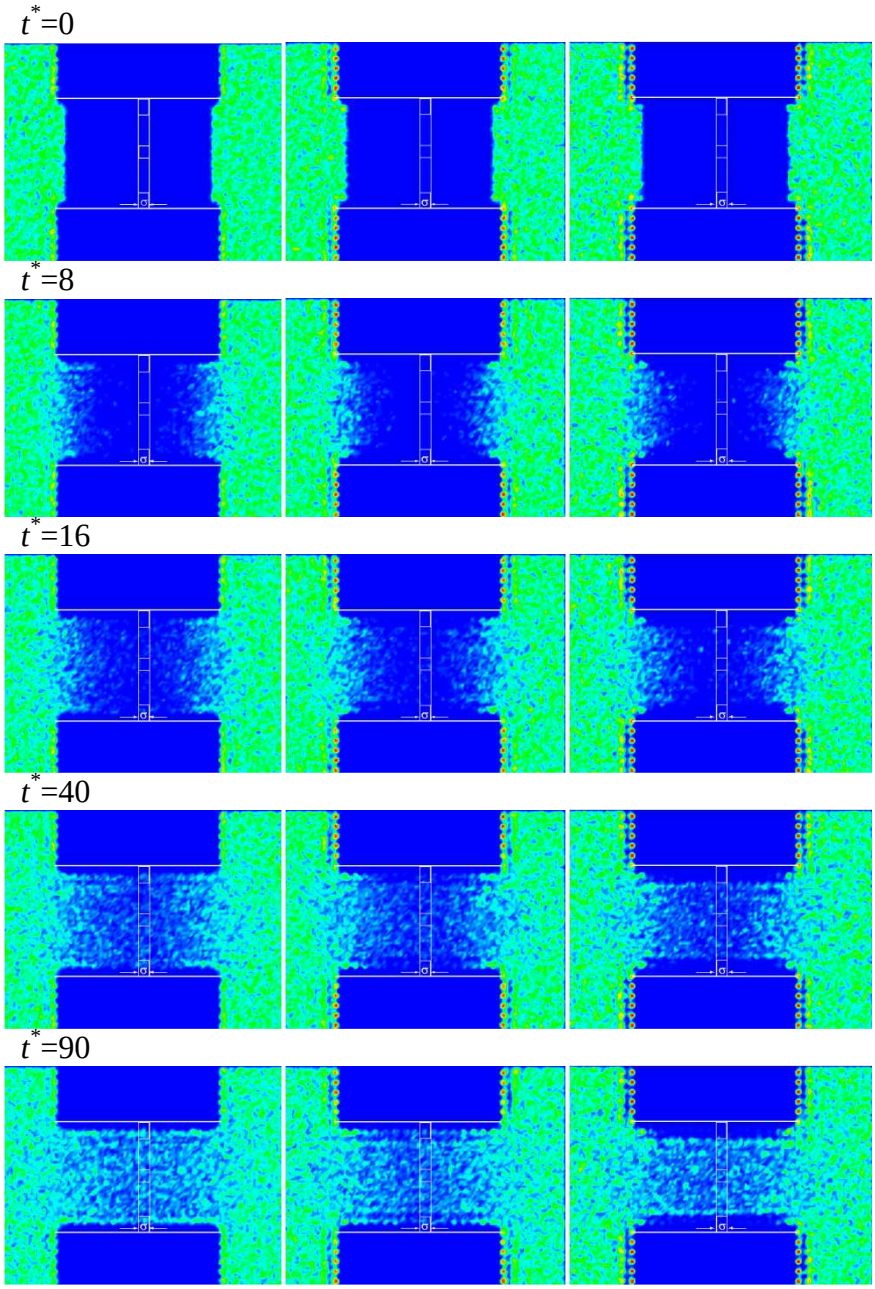

Figure 3.8: Distribution of the relative local density of the fluid 2, ρ_2^*/ρ^*, at various times. Left figures: low adsorption, middle figures: intermediate adsorption, right figure: high adsorption.

3.5.2. Effect of Width of the Gap

To further study the mass diffusion problem in highly confined situation, the effect of the width of the gap on the evolutions of x_2 in the local regions and the global region is presented. To do so, we have measured the evolutions of x_2, keeping $\varepsilon_{fs} = 2.5\varepsilon$ but changing the pore width, W^* using values ranging from 4 to 15. Figure 3.9(a) shows the effect of the width on the density profiles. One interesting feature is that the confinement, in this case, has only a weak effect on the first density peak close to the walls. Thus, we can expect that the local mass diffusion in the boundary regions will be nearly independent of the pore width.

Results provided in Fig. 3.9 indicate that, in all regions, the diffusion of x_2 tends to be faster when the pore width increases, particularly the evolutions in the boundary are unexpectedly different despite the same for density profiles in all the widths in this region. This is due to the 2D effect that there exists the mass flux of the fluid 2 from the centre to the boundaries in the pore, as mentioned above. However, when the pore width is sufficiently large, i.e. when W^* is approximately larger than 10, the x_2 profiles are nearly independent of the pore width. This last trend can be understood by the fact that when the pore width is sufficiently large, the mass flux of species 2 from the center of the pore (parallel to the walls) to the boundary becomes sufficient to yield an apparent diffusion in the boundary region which seems to be independent of the pore width.

Additionally, as shown in Fig. 3.9(d), one can notice that the evolution of x_2 in the global region can be well described by a classical 1D diffusion (Eq. (3.8)) equation for all gap tested with a characteristic time increasing when the pore width decrease as expected for such a solid surface [33]. Thus, if the effective mass diffusion coefficient is made dependent to the pore width and fluid-solid interactions, as in the model of Saugey et al. [33] for instance, it should be possible to reproduce the results obtained in this work using a simple 1D diffusion equation. However, as shown in Sect. 3.5.1, when the fluid-solid interaction increases and the

pore width decreases the mass diffusion process in a slit pore cannot be longer described by a 1D equation and needs a 2D mass diffusion equation with a mass diffusion coefficient varying in space similarly to what done for transverse momentum transfer [46, 50].

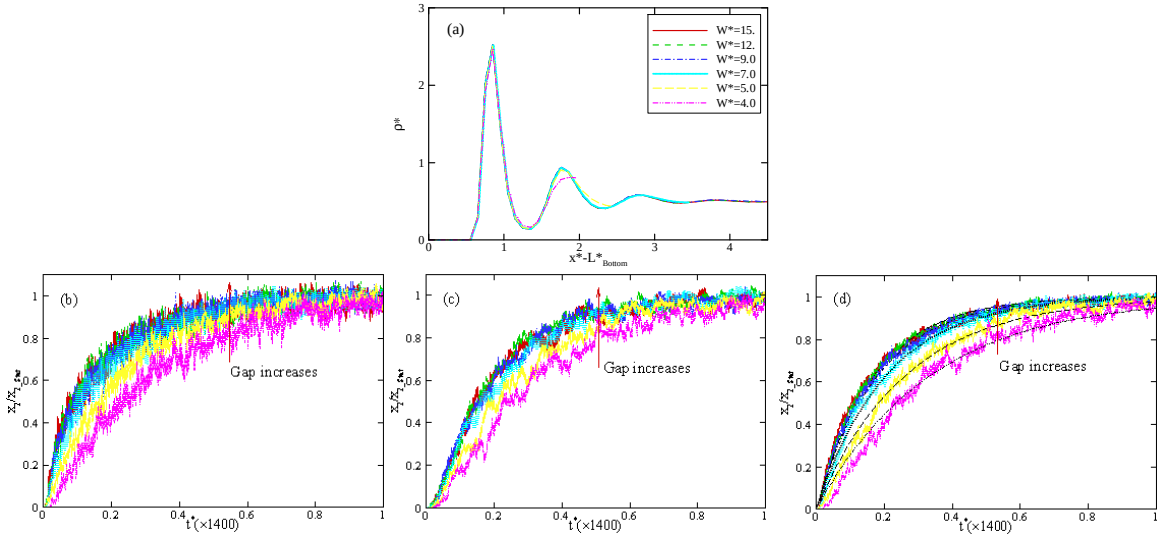

Figure 3.9: (a) Effect of the pore width on the density profiles close to the walls. (b-d) Effect of the pore width on the evolutions of x_2. (b) Central region. (c) Boundary region. (d) Global region. Smooth black curves on (d): fitted curves using Eq. (3.8).

3.6. Conclusions

In this work, we have introduced two Grand Canonical like Molecular Dynamics methods to investigate the properties of Lennard-Jones fluids confined in a slit pore. The basic idea of the two methods is to simulate explicitly the confined fluid directly connected to a reservoir fluid. In order to maintain the reservoir fluid at the target thermodynamic state, we have employed the relaxation schemes of the type of the Berendsen *et al.* [27]. In the first method, the reservoir fluid is coupled with a density bath, so-called the constant density GCMD method, whereas it is with a pressure bath in the second method, named the constant pressure GCMD method.

Results for two different states and different pore widths have shown that both methods provide the same average density and density profiles of the confined fluid and yield consistent results compared with GCMC simulations. In addition, the order of the equilibrium time provided by the two GCMD methods has been found to be very similar. Thus, considering the CPU time and implementation needed by both approaches, the constant density GCMD method proposed in this work is probably the preferable option among the two.

Then, the constant density GCMD method has been employed to investigate the invasion (by mass diffusion) of one LJ fluid into a slit pore filled by another LJ fluid. To do so, the evolution of the molar fraction has been computed in different regions of the center of the pore (perpendicular to the walls) and compared with a 1D diffusion equation. The influence of the fluid-solid interaction (adsorption) and pore width has been investigated.

Results have shown that the evolution of the molar fraction of the invading fluid follows roughly a simple 1D diffusion model when the solid phase is weakly or moderately adsorbent despite the fluid inhomogeneities. In addition, it has been noticed, that the characteristic time of diffusion is increasing when the pore width decreases if the pore width is smaller than 10σ. However, we have found that, when the physical adsorption is strong, the evolution of the molar fraction in the center of the pore (perpendicular to the walls) cannot be described anymore by a one dimension mass diffusion equation. In fact it has been found that the phenomenon becomes a two-dimension diffusion process due to local variations of the effective mass diffusion coefficient perpendicularly to the walls. More precisely, it has been found that, in highly inhomogeneous fluids, the diffusion coefficient close to the walls is smaller than in the central part of the pore (parallel to the walls) and tends to decrease when adsorption increase.

References

[1] G. Karniadakis, A. Beskok and N. Aluru, *Microflows and Nanoflows*, Springer (2004)

[2] L. Bocquet and J.L. Barrat, Soft Matter **3**, 685 (2007)

[3] B.Y. Cao, J. Sun, M. Chen and Z. Y. Guo, Int. J. Mol. Sci. **10**, 4638 (2009)

[4] W. Sparreboom, A. Van Den Berg and J.C.T. Eijkel, New J. Phys. **12**, 015004 (2010)

[5] M. Schoen, *Computer simulation of condensed phases in complex geometries*, New series m: monographs, Lecture note in physics, m17 (1993)

[6] J. Israelachvili, *Intermolecular and Surface Forces*, Academic Press, Third Edition (2010)

[7] J. Klein and E. Kumacheva, Science **269**, 816 (1995)

[8] J. Klein and E. Kumacheva; J. Chem. Phys. **108**, 6996 (1998)

[9] E. Kumacheva and J. Klein, J. Chem. Phys. **108**, 7010 (1998)

[10] S. Granick, Science **253**, 1374 (1991)

[11] A. L. Demirel and S. Granick, Phys. Rev. Lett. **77**, 2261 (1996)

[12] D. J. Adams, Mol. Phys. **29**, 307 (1975)

[13] W. Van Megen and I. Snook J. Chem. Soc., Faraday Trans. **2**, 1095 (1979)

[14] J. J. Magda, M. Tirrell and H. T. Davis, J. Chem. Phys. **83**, 1888 (1985)

[15] Y. Wang, K. Hill and J. G. Harris, J. Chem. Phys. **100**, 3276 (1994)

[16] J. Gao, W. D. Luedtke and U. Landman, Phys. Rev. Let. **79**, 705 (1997)

[17] J. Gao, W. D. Luedtke and U. Landman, J. Chem. Phys., **106**, 4309 (1997)

[18] P. Ungerer, B. Tavitian, A. Boutin, *Applications of Molecular Simulation in the Oil and Gas Industry – Monte Carlo methods*, Technip: Paris (2005)

[19] K. E. Gubbins and J. D. Moore, Ind. Eng. Chem. Res. **49**, 3026 (2010)

[20] L. F. Vega, K. S. Shing and L. F. Rull, Mol. Phys. **82**, 439 (1994)

[21] C. J. Lynch and B. M. Pettitt J. Chem. Phys. **107**, 8594 (1997)

[22] J. C. Wang and K. A. Fichthorn, J. Chem. Phys. **112**, 8252 (2000)

[23] H. Eslami and F. Muller-Plathe, J. Comput. Chem. **28**, 1763 (2007)

[24] H. Eslami, F Mozaffari, J. Moghadasi and F. Muller-Plathe, J. Chem. Phys. **129**, 194702 (2008)

[25] A. Ghoufi, D. Morineau, R. Lefort, I. Hureau, L. Hennous, H. Zhu, A. Szymczyk, P. Malfreyt, and G. Maurin, J. Chem. Phys. **134**, 074104 (2011)

[26] M. Parrinello and A. Rahman, J. Appl. Phys. **52**, 7182 (1981)

[27] H. J. C. Berendsen, J. P. M. Postma, W. F. van Gunsteren, A. Dinola and J. R. Haak, J. Chem. Phys. **81**, 3684 (1984).

[28] N. Quirke, *Adsorption and Transport at the nanoscale*, Taylor and Francis : New York (2006)

[29] D. Ruthven, Molecular Sieves – Science and Technology, **7**, 1 (2008).

[30] S. K. Bhatia, M. R. Bonilla and D. Nicholson, Phys. Chem. Chem. Phys. **13**, 15350 (2011)

[31] R. Krishna, Chemical Society Reviews, **41**, 3099, (2012).

[32] P. Liu, E. Harder, B.J. Berne, J. Phys. Chem. B, **108**, 6595 (2004)

[33] A. Saugey, L. Joly, C. Ybert, J.L. Barrat and L. Bocquet, Journal of Physics: Condensed Matter **17**, S4075 (2005).

[34] J. Mittal, T. M. Truskett, J. R. Errington and G. Hummer, Phys. Rev. Lett. **100**, 145901 (2008).

[35] A. Botan, B. Rotenberg, V. Marry, P. Turq, B. Noetinger, J. Phys. Chem. C, **115**, 16109 (2011).

[36] J. Hansen and I. R. McDonald: *Theory of simple liquid*, Third Edition, Elsevier, (2006)

[37] J. Colombani, G. Galliero, B. Duguay, J.-P. Caltagirone, F. Montel, P.A. Bopp, Phys. Chem. Chem. Phys. **4**, 313-321 (2002).

[38] G. Galliero, J. Colombani, P.A. Bopp, B. Duguay, J.P. Caltagirone, F. Montel, Physica A, **361**, 494 (2006).

[39] Hannaoui, R., Galliero, G., Ameur, D. and Boned, C., Chemical Physics **389**, 53 (2011).

[40] M.P. Allen and D.J. Tildesley, *Computer Simulation of Liquids*, Oxford University Press (1989)

[41] D. Frenkel, B. Smit, *Understanding Molecular Simulation, From Algorithms to Applications*, Academic Press, Second edition (2001)

[42] F. Goujon, P. Malfreyt, J.-M. Simon, A. Boutin, B. Rousseau, A.H. Fuchs, J. Chem. Phys. **121**, 12559-12571 (2004).

[43] E. Cussler, *Diffusion - Mass Transfer in Fluid Systems*, Cambridge Press, Third edition, (2007)

[44] G. Galliero and F. Montel, Phys. Rev. E 78, 041203 (2008).

[45] L. Bocquet and J. L. Barrat, Phys. Rev. E. **49**, 3079 (1994)

[46] L. A. Pohzar and K. E. Gubbins, J. Chem. Phys. **99**, 8970 (1993)

[47] D. Jou, J. Casas-Vasquez, G. Lebon, *Extended Irreversible Thermodynamics*, Springer (1996).

[48] S. Toxvaerd, J. Chem. Phys. **74**, 1998(1981)

[49] H. Hoang, S. Kang and Y. K. Suh, J. Mech. Sci. Tech. **24**, 1401 (2010)

[50] H. Hoang, G. Galliero, J. Chem. Phys, **136**, 124902 (2012).

Chapter 4

Local Viscosity of Inhomogeneous Fluids

In this chapter, using non-equilibrium molecular dynamic simulations, we have explored the local shear viscosity of strongly inhomogeneous fluids. The chapter is divided into three parts. The first part is dedicated to the study of the local shear viscosity of a Lennard-Jones fluid subject to a sinusoidal external field and undergoing a bi-periodical shear flow. It has been found that the viscosity profiles of strongly inhomogeneous fluids can be correctly described if one considers separately translational and configurational contributions to the shear viscosity together with a simple kinetic-like theory for the former and the local average density model combined with an adequate weight function for the latter. Then, using this simple scheme, the local shear viscosity of the Lennard-Jones fluid confined in narrow slit pores and undergoing boundary shear is investigated in the second part. In the last part, we have proposed a more general but tractable scheme that yields quantitatively the configurational viscosity profile of strongly inhomogeneous dense fluids of various types going from the Hard-Sphere to Lennard-Jones fluid.

Part 1

Shear Viscosity of Inhomogeneous Fluids*

* This part was published in J. Chem. Phys. 136, 124902 (2012)

DOI: 10.1063/1.3696898

Abstract:

Using molecular dynamics simulations on inhomogeneous fluids induced by a sinusoidal external field, we have studied the effects of strong density inhomogeneities of varying wavelengths on the shear viscosity computed locally. For dense fluids, the local average density model combined with an adequate weight function yields a good description of the viscosity profiles obtained by simulations. However, for low density inhomogeneous fluids, the local average density model is unable to describe correctly the viscosity profiles obtained by simulations. It is shown that this weakness can be overcome by taking into account the density inhomogeneity in the local translational contribution to the viscosity using a density gradient like approach.

4.1.1. Introduction

With the growing interest on fluids confined in micro/nano-sytems, the modeling of the behavior of inhomogeneous fluid flows has gained considerable attention [1-4]. Due to strong surface effects in such systems, the fluids are generally strongly inhomogeneous in the direction normal to the fluid-solid interfaces (layering of the molecules of the fluid because of adsorption and molecular packing) [5]. To describe these inhomogeneities, classical density function theory (DFT) combined with molecular simulations have shown to be efficient to provide reliable predictions for density profile of simple confined fluids [6]. However, the problem is still open when dealing with the local transport properties of strongly inhomogeneous fluids, even if some attempts exist that are generally based on an Enskog-like kinetic model and Molecular Dynamics (MD) results, see for example Refs [7-19]. This is probably due to the lack of a comprehensive theory to describe the transport properties of dense fluids [20] together with difficulties in assessing the results from an experimental point of view.

Among proposed approaches based on local thermodynamics conditions to predict local viscosity of inhomogeneous fluid, the local average density model (LADM) is one of the most popular [7, 19, 21]. Although, LADM seems to work well to describe velocity profile of Couette flow of inhomogeneous fluids [7, 14], the accuracy of the approach is still questioned [19]. In particular, velocities of fluid flow adjacent to solid surface provided from MD simulations and the model are not always in good agreement [7, 19, 21], mainly because of surface effects. Furthermore, previous studies dealing with the LADM were restricted mainly to dense fluids [19].

So, to improve our understanding of the viscosity of strongly inhomogeneous fluids, we have performed Non-Equilibrium Molecular Dynamics (NEMD) simulations on mono-atomic Lennard-Jones (LJ) fluids in moderately and very dense conditions without

confinement. To do so, we apply an external sinusoidal field on a LJ fluid to generate density inhomogeneities and then shear it bi-periodically as shown on Figure 4.1.1. By doing so, it is possible to study the local shear viscosity of a strongly inhomogeneous pure fluid without geometric confinement and surface effects. Then, using the viscosity profiles provided by NEMD simulations for two different states, we have tested directly the efficiency of some approaches to describe these profiles accurately including a new one.

The outline of the paper is as follows: the details on the methodology used are presented in Sect. 4.1.2. Then the results obtained are provided in Sect. 4.1.3 together with a discussion of the validity of the approaches aiming at describing the local viscosity of strongly inhomogeneous fluids. Finally, the conclusions are drawn in Sect. 4.1.4.

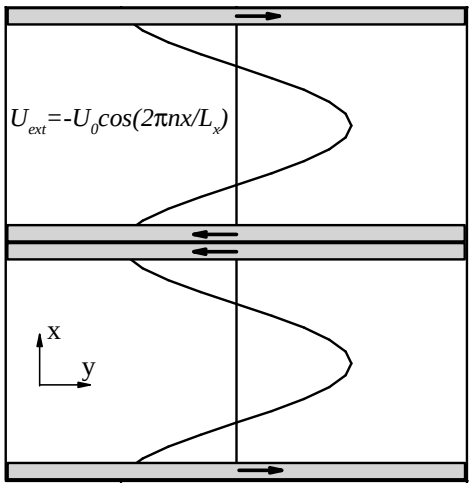

Figure 4.1.1: A 2D sketch of the system simulated in the case n=2.

4.1.2. Model and Theory

4.1.2.1. Inhomogeneous Fluid

In this paper, the interaction between fluid (mono-atomic) particles is described by using the usual truncated Lennard-Jones potential:

$$U_{ij} = \begin{cases} 4\varepsilon\left[\left(\frac{\sigma}{r_{ij}}\right)^{12} - \left(\frac{\sigma}{r_{ij}}\right)^{6}\right] & \text{if } r_{ij} \le r_c \\ 0 & \text{if } r_{ij} > r_c \end{cases} \quad (4.1.1)$$

where r_{ij} is distance between the particles *i* and *j*, ε is the potential depth, σ is the "molecular" diameter and r_c the cut-off radius (taken equal to 3.5σ in this work). In the following the variables have sometimes expressed in usual LJ dimensionless units, noted with a star as superscript.

To induce the density inhomogeneities, see Fig. 4.1.1, we have applied to all particles of the simulation box a Sinusoidally Varying external Potential (SVP), $U_{x,ext}$, in the *x* direction:

$$U_{x,ext} = -U_0 cos\left(2\pi n \frac{x}{L_x}\right) \quad (4.1.2)$$

where L_x is the dimension of the simulation box in the *x* direction, U_0 the amplitude of the SVP and *n* the wavelength parameter. In this study *n* varies from 2 to 12 to test different inhomogeneities wavelength. The amplitudes of the SVP, U_0, have been chosen so that the order of magnitude of the difference between maximal and minimal local density for a given state is roughly the same for all wavelengths and is of the order of 25 % of the average density. More precisely U_0^* varies from 0.25 to 0.48 for the dilute state and from 1.4 to 2.4 for the dense state.

It is worth to emphasize that, when using the SVP to induce the density inhomogeneities, the effects on transport properties resulting from a geometrical confinement and surface effects [9], as in the case of a fluid in a slit pore, are avoided.

4.1.2.2. NEMD Scheme

To shear the inhomogeneous LJ fluid, the NEMD scheme proposed by F. Muller-Plathe has been employed [22]. In this method, the simulation box is divided into N_s slabs (32 in this work) along the *x* direction and the fluid is sheared using a net exchange of the linear

momentum along the *y* direction every N_{swap} time steps. This exchange is performed between the central part of the simulation box, $N_s/2$ and $N_s/2+1$, and the edge slabs, 1 and N_s, to keep the periodic boundary conditions in the *x* direction, see Fig. 4.1.1. At the stationary state, this NEMD scheme induces a bi-periodical velocity profile in the simulation box. Such an approach yields a constant shear stress, τ_{imp}, over nearly the two halves of the simulation box, see Figs. 4.1.2(b) and 4.1.3(b), which simplifies the problem studied. However, in and close to the regions where the exchange is performed the local shear stress is no longer equal to the imposed one, τ_{imp}, [22, 23], see Figs 4.1.2(b) and 4.1.3(b), and so these regions have been discarded to perform the study.

4.1.2.3. Simulation Details

All simulations consist of three steps. In a first step, the fluid subject to a SVP is equilibrated during a run of 10^6 timesteps to induce the density inhomogeneities. Then, in a second step, the NEMD scheme is applied to shear the fluid. In a last step, once the steady state reached, which is ensured by monitoring the evolution of the velocity profile with time, the samplings were performed during at least $0.5\ 10^8$ time steps.

Two different states have been studied in this work, one moderately dense at $T_{ini}^*=2.5$ and $\rho_{ini}^*=0.17$ (that is named “dilute” in the following) and one very dense $T_{ini}^*=0.8$, $\rho_{ini}^*=0.9$ (that is named “dense” in the following). In all simulations, $L_x^* \times L_y^* \times L_z^*$ dimensions of the simulation box have been chosen to be equal to $18 \times 10.5 \times 10.5$ respectively. Classical periodic boundary conditions were applied in all directions. The velocity Verlet algorithm [24] has been applied to integrate the equations of motion with a time-step $\delta t^*=0.002$. A Berendsen thermostat [25] is used on *x* and *z* velocity components during the NEMD simulations, and on all three velocity components (*x*, *y* and *z*) during the equilibrium MD simulations.

To compute the local quantities, the simulation box has been divided into slabs along the *x* direction so that the size of each slab $\Delta x^* = 0.1$. To avoid shear thinning [23] and ensure a good signal to noise ratio in the linear response regime, values chosen for N_{swap} are larger than 150 and 70 respectively for the dilute and dense states. It has been verified that the velocity profiles scaled by the maximal value of velocity are superposing. To reduce statistical uncertainties, results presented in the following correspond to an average over both halves of the bi-periodical simulation box.

4.1.3. Results and Discussions

4.1.3.1. Preliminary Results

At the steady state, the momentum conservation equation for a fluid, in which each particle is subject to an external field F_{ext} in the *x* direction and undergoing a bi-periodical shear flow in the *y* direction, is defined as following [26, 27]:

$$0 = -\nabla\tau - \nabla p - \rho(x) \times \nabla U_{ext} \tag{4.1.3}$$

where **p** is the hydrostatic stress tensor and **τ** the stress deviator tensor. In the Cartesian coordinate system, as used in this work, Eq. (4.1.3) can be rewritten as:

$$0 = -\frac{\partial p_{xx}}{\partial x} - \rho(x) \times \frac{\partial U_{ext}}{\partial x} \quad \text{in the } x \text{ direction} \tag{4.1.4}$$

and

$$0 = \frac{\partial \tau_{yx}}{\partial x} \quad \text{in the } y \text{ direction} \tag{4.1.5}$$

Using the method of plane [27], the local pressure P_{xx} in the *x* direction and the shear stress τ_{xy} in the *x*-*y* plane are defined as functions of the *x* coordinate:

$$P_{xx}(x) = \frac{1}{V_s}\sum_i m v_{i,x}^2\, \delta(x_i - x) - \frac{1}{2A}\left[\sum_{i<j} \frac{x_{ij}^2}{r_{ij}} \dot{U}_{LJ} \frac{1}{|x_{ij}|} \Theta\left(\frac{x-x_i}{x_{ij}}\right) \Theta\left(\frac{x-x_j}{x_{ij}}\right)\right] \tag{4.1.6}$$

$$\tau_{xy}(x) = \frac{1}{V_s}\sum_i m v_{i,x}\left(v_{i,y} - u_y(x)\right) \delta(x_i - x) - \frac{1}{2A}\left[\sum_{i<j} \frac{x_{ij}y_{ij}}{r_{ij}} \dot{U}_{LJ} \frac{1}{|x_{ij}|} \Theta\left(\frac{x-x_i}{x_{ij}}\right) \Theta\left(\frac{x-x_j}{x_{ij}}\right)\right] \tag{4.1.7}$$

where V_s is the volume of a slab, $A = L_y \times L_z$ is the area of the *y*-*z* plane of the simulation box, *m* is the mass of a molecule, $v_{i,\alpha}$ is the α component of the velocity of molecule *i*, $u_y(x)$ is the streaming velocity, x_{ij} is the *x* component of $\mathbf{r}_{ij}$, δ is the Kronecker symbol and $\Theta(x)$ is the Heaviside step function.

Results shown in Figs. 4.1.2 and 4.1.3 confirm that the behavior of the inhomogeneous fluids studied in this work satisfies the previous classical theory, i.e. Eqs. 4.1.4 and 4.1.5 are respected. In particular, the local shear stress is constant over both halves of the simulation box except in regions where the momentum exchange is performed, see Figs. 4.1.2(b) and 4.1.3(b), even if the density is not constant [28]

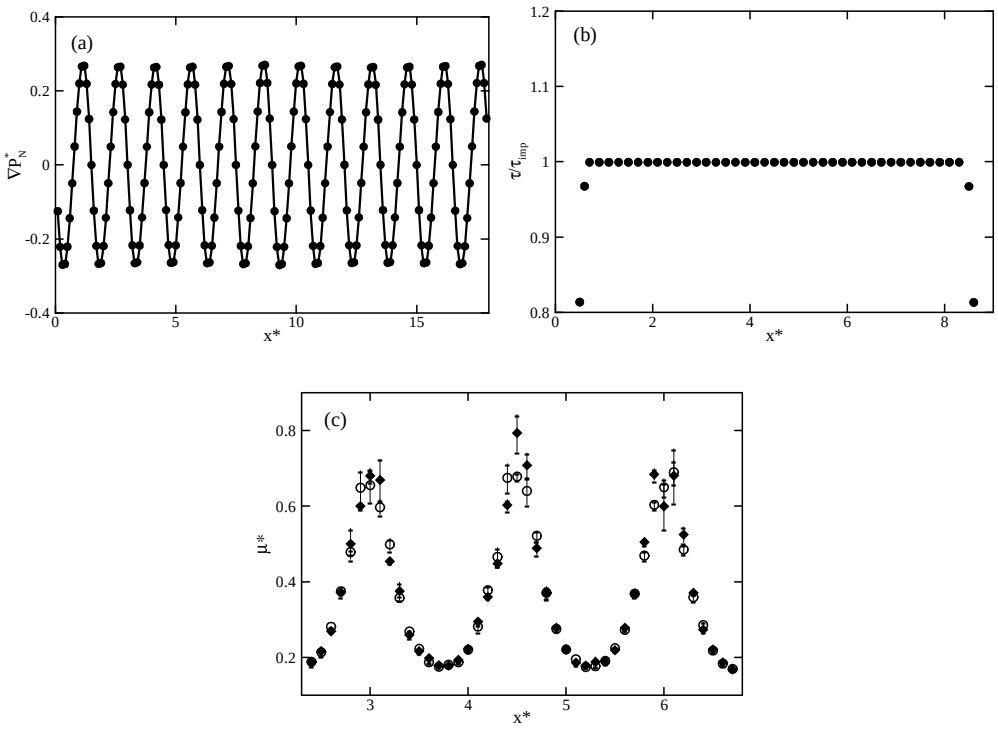

Figure 4.1.2: Local properties of inhomogeneous fluid for ρ*=0.17, *T**=2.5. (a) Gradient of hydrostatic pressure in the *x* direction (symbols) and gradient of external pressure $\rho(x)\frac{\partial U_{ext}}{\partial x}$ (line). (b) Ratio between computational shear stress and imposed one. (c) Viscosity profiles for two different momentum exchange rates: N_{swap} =350 (full symbols) and N_{swap} =150 (open symbols).

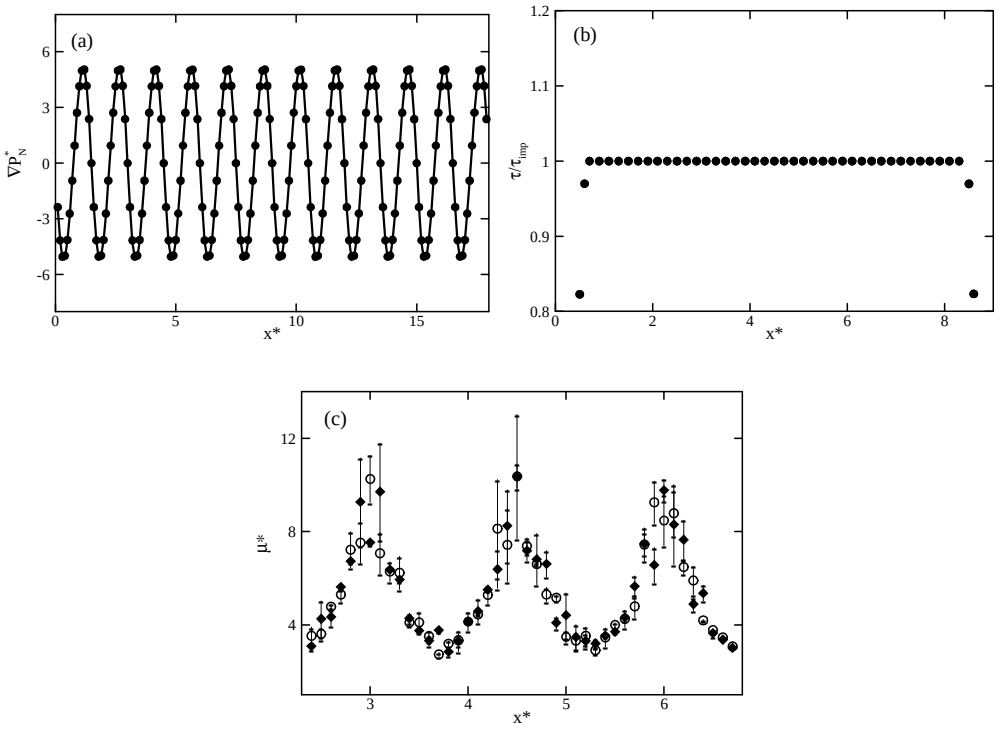

Figure 4.1.3: Local properties of inhomogeneous fluid for ρ^*=0.9, T^*=0.8. Legend is the same as on Fig. 2. (c) N_{swap} =120 (full symbols) and N_{swap} =70 (open symbols)

It is worth to notice that, when the shear rate varies rapidly over a length typical of intermolecular correlations, the classical local Newton's law of viscosity must be generalized by a nonlocal constitutive equation [17, 29], i.e. the classical definition of the local viscosity can be inappropriate [30]. However, in the Couette-like flow simulated in this work, the effect of the variation in strain rate induced from the inhomogeneity of the fluid on the local shear stress remains rather limited in all cases studied here. To confirm this statement, we have performed NEMD simulations with two different momentum exchange rates (i.e. different shear strain) for a given system to compare the results between them. As shown in Fig. 4.1.4, the velocity profiles are superposing (when scaled by the maximum velocity) for the two different momentum exchange rates tested for both states studied here.

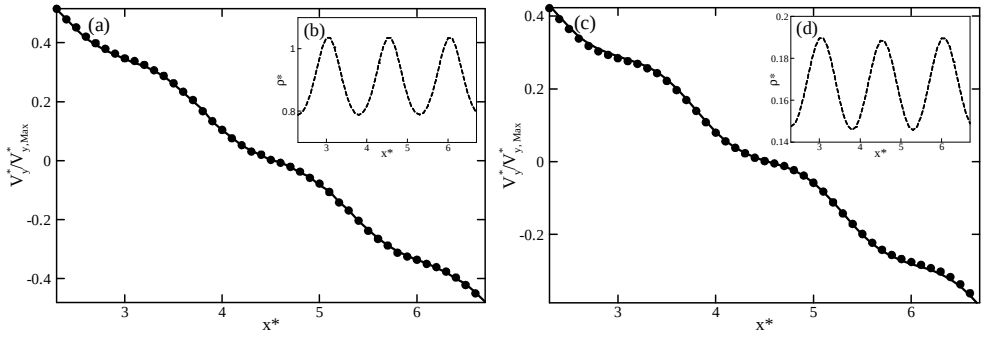

Figure 4.1.4: NEMD velocity profiles (scaled by its maximum value) for two different momentum exchange frequencies and two different states with the corresponding density profiles (long dashed curve in the inserts): (a) and (c) for ρ^*=0.9, T^*=0.8 and n=12 (symbols for N_{swap}=70 and curve for N_{swap} =120). (b) and (d) for ρ^*=0.17, T^*=2.5 and n=12 (symbols for N_{swap} =150 and curve for N_{swap} =350).

In addition, the local viscosity profiles deduced from NEMD simulations combined with the Newton's laws, i.e.

$$\mu(x) = \frac{\tau_{xy}(x)}{\left({du_y(x)}/{dx}\right)}, \tag{4.1.8}$$

indicate that the viscosity profiles of a given system are independent upon the momentum exchange rate, as shown in the Figs. 4.1.2(c) and 4.1.3(c) for two both dilute and dense states. This result confirms that, for the systems studied here, the response is linear.

So, based on these preliminary results, we have considered in the following that the use of the classical Newton's law can be considered as consistent for the cases studied here. Thus, in this work, the local shear viscosity has been deduced from the NEMD simulations using the Newton's laws, Eq. (4.1.8), in which the center finite difference is used to compute the local shear rate.

4.1.3.2. Viscosity Decomposition

When using Eq. (4.1.8) combined with Eq. (4.1.7) it is possible to separate the viscosity in two contributions [11, 23] which is crucial to describe the local viscosity in inhomogeneous fluids as we will see later. The first term on the right hand side of Eq. (4.1.7) represents the translational contribution and the second term the configurational contribution to the local shear stress. Thus, the local shear viscosity estimated from the NEMD simulations can be expressed as the sum of two terms:

$$\mu(x) = \mu_t(x) + \mu_c(x) \tag{4.1.9}$$

where, μ_t is the local translational shear viscosity deduced from :

$$\mu_t(x) = \frac{\frac{1}{V_S}\sum_i m v_{i,x}\left(v_{i,y} - u_y(x)\right)\delta(x_i - x)}{\frac{du_y(x)}{dx}} \tag{4.1.10}$$

and μ_c the local configurational shear viscosity evaluated thanks to:

$$\mu_c(x) = \frac{-\frac{1}{2A}\left[\sum_{i<j}\frac{x_{ij}y_{ij}}{r_{ij}}\dot{U}_{LJ}\frac{1}{|x_{ij}|}\Theta\left(\frac{x-x_i}{x_{ij}}\right)\Theta\left(\frac{x-x_j}{x_{ij}}\right)\right]}{\frac{du_y(x)}{dx}} \tag{4.1.11}$$

In a homogeneous fluid, it has been shown that the translational viscosity of an LJ fluid is, to a very good extent [23], equal to the "zero-density" viscosity, μ_0, deduced from a classical Chapman-Enskog approach for a LJ fluid [31], i.e.:

$$\mu_t^* \approx \mu_0^* = \frac{5}{16\Omega_v}\sqrt{\frac{T^*}{\pi}} \tag{4.1.12}$$

where Ω_v is the collision integral.

To deal with dense fluids for which μ >> μ_0, have been developed an empirical formula [32] that allows, using T^* and ρ^* as inputs, to estimate accurately the residual viscosity μ_r, equal to μ - μ_0, from:

$$\mu_r^* = b_1\left(e^{b_2\rho^*} - 1\right) + b_3\left(e^{b_4\rho^*} - 1\right) + \frac{b_5}{\left(T^*\right)^2}\left(e^{b_6\rho^*} - 1\right) \tag{4.1.13}$$

in which the numerical parameters, b_i, have been adjusted on extensive MD results [32]. When Eqs. 4.1.12 and 4.1.13 are combined, the correlation so defined allows to obtain the viscosity of a homogenous LJ fluid with a maximum absolute deviation below 5 % compared to direct MD results for $0 \leq \rho^* \leq 1.275$ and $0.6 \leq T^* \leq 6$.

It is worth to notice that the above definitions imply that in a homogeneous fluid:

$$\mu_c^* \approx \mu_r^* \tag{4.1.14}$$

4.1.3.3. Local Shear Viscosity Modeling

So, using approach described in section 4.1.2, we have estimated from NEMD simulations the local viscosity of two fluids using Eq. (4.1.8), one in a dilute state at $T_{ini}^*=2.5$ and $\rho_{ini}^*=0.17$ and other one in dense state at $T_{ini}^*=0.8$, $\rho_{ini}^*=0.9$. As can be deduced from the velocity profiles in Fig. 4.1.4 and shown explicitly in Figs. 4.1.5 and 4.1.6, it appears clearly that the local viscosity deduced from NEMD simulations strongly varies with position (i.e. density inhomogeneities) for both states. Moreover, as expected, the viscosity profiles are strongly correlated to the density ones for the two states studied here, see Figs 4.1.4(b), 4.1.4(d), 4.1.5(b) and 4.1.6(b).

A. The van der Waals model

To model the local viscosity profiles obtained by NEMD simulations shown in Figs. 4.1.5 and 4.1.6, we have first tested the simplest approximation, the van der Waals model. This approach consists in considering that the viscosity profile can be deduced directly from the local thermodynamic conditions, (x) and $\rho(x)$, i.e.

$$\mu_{vdW}(x) = \mu_0\big(T(x)\big) + \mu_r\big(T(x),\ \rho(x)\big) \tag{4.1.15}$$

where the two viscosity contributions on the right hand side of the relation (4.1.15) are estimated using Eqs. (4.1.12) and (4.1.13).

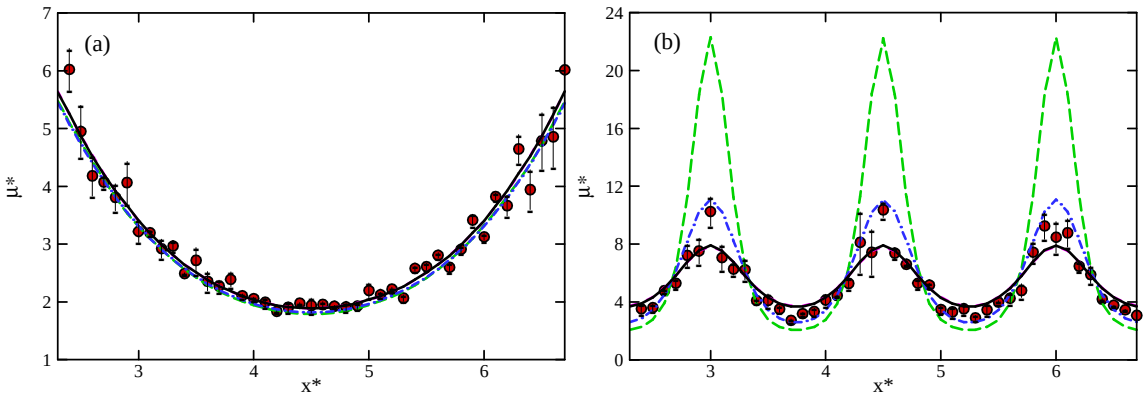

Figure 4.1.5: Local viscosity profiles for the dense state (N_{swap}=70): ρ*=0.9, T*=0.8: (a) n=2, (b) n=12. (Red color) Full circles: the NEMD data, (Green color) long-dashed curve: μ_{vdW} (Eq. 4.1.15), (Blue color) dash-dot curve: μ_{LADM} (Eq. 4.1.18) with the generalized Hard-Rod model (Eq. 4.1.19), (Pink color) dashed curve: μ_{LADM} (Eq. 4.1.18) with the Tarazona (Eq. 4.1.20), (Black color) solid curve: μ_{full} (Eq. 4.1.26) with the Tarazona model.

As shown in Fig. 4.1.5, such an approach is applicable only for a slowly varying density profile, i.e. when the wavelength of density inhomogeneities is large compared to the molecular interaction range. This clearly confirms the limitations of a purely local description based on local thermodynamics properties (to describe local viscosity) which is obviously inadequate for inhomogeneous fluids where the density varies noticeably over a length of the order of one molecular size. Furthermore, a very interesting feature is that for the densest state, Eq. (4.1.8) tends to largely over-predict the variations of the local viscosity, whereas it is the contrary for the dilute state, see Figs. 4.1.5 and 4.1.6.

B. The LADM

A further improvement to model the NEMD viscosity profiles is to use an approach of the type of the Local Average Density Model proposed by Bitsanis *et al.* [7, 21]. For simple fluids, it is well-known that using a coarse-grained local density method can provide a good

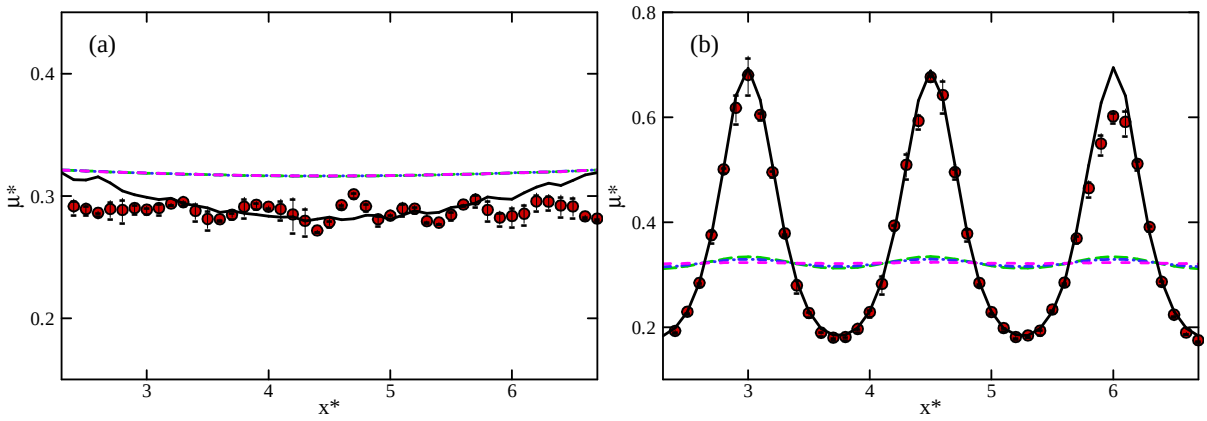

Figure 4.1.6: Local viscosity profiles for the dilute state (N_{swap}=250): ρ*=0.17, T*=2.5: (a) n=2, (b) n=12. Legend is the same as on Fig. 4.1.5.

description of the thermodynamic properties of an inhomogeneous simple fluid [6]. The main idea of these methods is that a local (excess) property $\mathcal{F}(x)$ of an inhomogeneous system can be written as:

$$\mathcal{F}(x) = \mathcal{F}\big(\bar{\rho}(x)\big) \tag{4.1.16}$$

where

$$\bar{\rho}(x) = \int \omega(|\acute{x} - x|)\, \rho(x) d\acute{x} \tag{4.1.17}$$

and $\omega(|\acute{x} - x|)$ is a weight function. Thus, and this is the basic idea of the LADM [7, 14, 21], it is assumed that this approach can be applied to describe local transport property, i.e. $\mathcal{F}$ can represent a transport property.

In this work, and it will become clearer in the following, instead of applying the LADM scheme to the total viscosity as usually done [7, 14, 21], we propose to apply this approach to the local configurational (residual) viscosity only. Thus, the local viscosity based on this modified version of the LADM is assumed to be described by:

$$\mu_{LADM}(x) = \mu_0\big(T(x)\big) + \mu_r\big(T(x), \bar{\rho}(x)\big) \tag{4.1.18}$$

where the two viscosity contributions are estimated using Eqs. (4.1.12) and (4.1.13) and $\bar{\rho}(x)$ is computed from Eq. (4.1.17) combined with a weight function.

There exist various forms of the weight function needed in Eq. (4.1.17) that have been proposed to deal with thermodynamic properties [6, 33]. In this work, we have selected two well known different forms of the weight function:

A first one independent of density, the generalized Hard-Rod model [33] in which

$$\begin{cases} \omega(|x|) = \frac{6}{\sigma^3}\left[\left(\frac{\sigma}{2}\right)^2 - (|x|)^2\right] \text{ when } |x| \leq \frac{\sigma}{2} \\ \omega(|x|) = 0 \text{ elsewhere,} \end{cases} \tag{4.1.19}$$

and a second one density dependent, the Tarazona model, which writes as

$$\omega(|x|) = \omega_0(|x|) + \omega_1(|x|) \times \bar{\rho}(x) + \omega_1(|x|) \times \bar{\rho}(x)^2 \tag{4.1.20}$$

where $\omega_{i=0\div2}(|x|)$ are given in Ref. [33].

When the LADM, Eq. (4.1.18), is combined with both Hard-Rod and Tarazona models, the viscosity profiles obtained are consistent with NEMD ones for the dense state whatever the density inhomogeneity wavelength, see Fig. 4.1.5. More precisely for the dense state at short wavelength, see Fig. 4.1.5(b), the Hard-Rod model tends to slightly overestimate the local viscosity variations whereas it is the contrary for the Tarazona model. In fact, because the configurational viscosity is the dominant term in the dense state, in which μ_c ≈0.98μ, these results indicate that $\mu_r\big(T(x), \bar{\rho}(x)\big)$ yields a reasonable estimate of $\mu_c(x)$ computed by NEMD simulations using Eq. (4.1.11).

C. The full model

Despite the good results for the dense state of the LADM, Eq. (4.1.18) is clearly inappropriate for the dilute state, see Fig. 4.1.6(b). More precisely, because of the good results obtained in dense fluids, we can suspect that the weakness of the approach for the dilute state, in which $\mu_t \approx 0.85\mu$, is due to the fact that $\mu_0\big(T(x)\big)$ is not a good approximation to describe correctly $\mu_t(x)$ of inhomogeneous fluids. In fact, it has been noticed that the local

translational viscosity deduced from Eq. (4.1.10) during the simulation is strongly positively correlated to the local density as can be deduced from Fig. 4.1.4(d).

This correlation between the local translational viscosity and the local density is opposite to what found in homogeneous LJ fluids [23] for which the translational viscosity decreases slightly when the density is increasing. However, this unexpected behavior can be understood by looking to the physical meaning of the translational viscosity. In fact, μ_t represent the contribution to the momentum transfer across a plane by the displacement (diffusion) of molecules, see Eq. (4.1.10). Thus, this quantity is connected to the local number of molecules and the local mobility of each molecule. In other words, μ_t is related to the local density and the local insertion probability. As in an inhomogeneous fluid, the local insertion probability seems to be positively correlated to the local density [16] this can explain that the correlation between the local translational viscosity and the local density should be positive in an inhomogeneous fluid.

To quantify this correlation between the local translational viscosity and the local thermodynamic conditions, the idea is to estimate the ratio between the local translational viscosity computed using Eq. (4.1.10), $\mu_t(x)$, and the translational viscosity of a (homogeneous) fluid in a state corresponding to the local thermodynamic state, $\mu_t\big(\rho(x),T(x)\big)$. To do so, we have assumed that:

$$\frac{\mu_t(x)}{\mu_t\big(\rho(x),T(x)\big)} = \frac{f\Big(exp\big(\beta\vartheta\big(\rho(x),T(x)\big)\big)\Big)}{f\Big(exp\big((\beta\vartheta(x)\big)\Big)} \tag{4.1.21}$$

where ϑ is the chemical potential and *f* is a function of the insertion probability. In addition [23], taking into account the fact that for low enough density $\mu_t\big(\rho(x),T(x)\big) \approx \mu_0\big(T(x)\big)$, and assuming that the function *f* is such that, in a first approximation:

$$\frac{\mu_t(x)}{\mu_0(T(x))} \approx f\left(\frac{exp\big(\beta\vartheta\big(\rho(x),T(x)\big)\big)}{exp\big((\beta\vartheta(x)\big)}\right) \tag{4.1.22}$$

To quantify the local chemical potential, $\upsilon(x)$, appearing in Eq. (4.1.22), we have chosen a very popular approach used in inhomogeneous fluids, the one is called the density gradient theory [34]. In such approach the local chemical potential $\upsilon(x)$ of the inhomogeneous fluid subject to an external field is described by [34]:

$$\vartheta(x) = \vartheta\big(\rho(x), T(x)\big) + U_{ext} + c\,{}^{\partial^2\rho}/_{\partial x^2} \tag{4.1.23}$$

where c is the influence parameter that can be deduced from the direct correlation function accessible by the MD simulations [35]. It should be noticed that the need of the estimation of the influence parameter c is considered to be one of the main shortcoming of the use of the density gradient theory.

Thus, using Eqs. (4.1.22) and (4.1.23), we can deduce that:

$$\frac{\mu_t(x)}{\mu_0(T(x))} \approx f(X) \tag{4.1.24}$$

where $X = exp\left(-\beta\left[U_{ext} + c\,{}^{\partial^2\rho}/_{\partial x^2}\right]\right)$.

To test the relation (4.1.24), first we have computed the influence parameter, c, using the procedure given in Ref. [35]. Using this procedure, the influence parameter is rather sensitive to the determination of the radial distribution function and its long-range part. To reduce uncertainties induced by such sensitivities, we have carried out different independent molecular simulations and performed averages. In the dilute state, we have obtained $c^* = 2 \pm 0.3$. Then, NEMD simulations have been carried out for different SVP wavelengths (n varying from 2 to 12 in Eq. (4.1.2)) in the dilute state and μ_t(x) profiles have been deduced from Eq. (4.1.10) during the simulations.

As clearly shown on Figure 4.1.7(a), the ratio $\frac{\mu_t(x)}{\mu_0(T(x))}$ is independent of the wavelength when expressed in function of X and thus Eq. (4.1.24) is verified which support

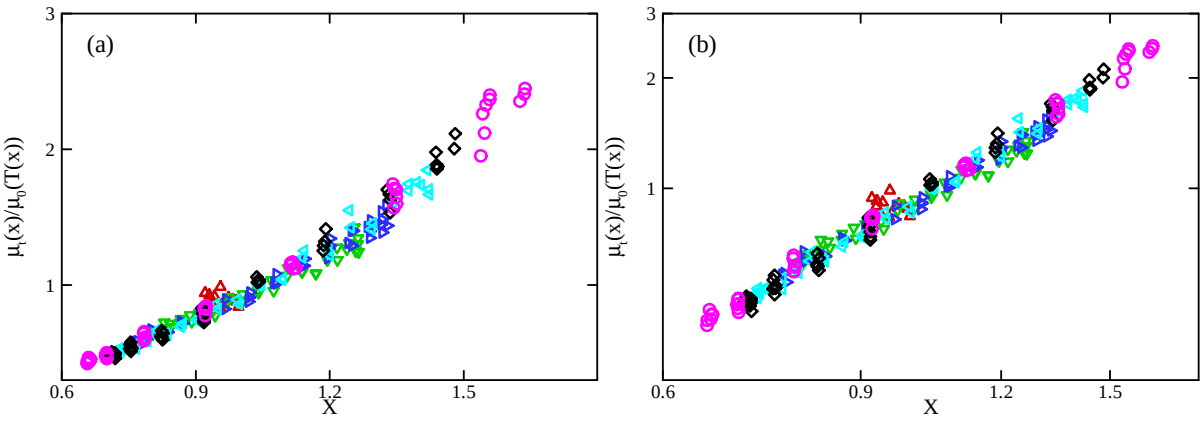

Figure 4.1.7: Correlation between $\mu_t(x)$ and X for the dilute state (using values for n varying from 2 to 12 in Eq. (2)): Deltas n=2, Gradients n=4, Right Triangles n=6, Left Triangles n=8, Diamonds n=10, and Circles n=12. (a) Decimal scaling. (b) Logarithm scaling on the vertical axis.

previous assumptions. Interestingly, see Fig. 4.1.7(b), all data collapse on a power law master curve. From this result, it is possible to deduce that:

$$\mu_t(x) \approx \frac{5}{16\Omega_v}\sqrt{\frac{T^*(x)}{\pi}} \times X^{\alpha}, \tag{4.1.25}$$

where α is an empirical parameter (fitted to 1.75 in this case). It is worth to note that the empirical parameter α is dependent upon the determination of the influence parameter c which is difficult to obtain accurately as mentioned previously.

Thus, to describe accurately the local viscosity of an inhomogeneous fluid for both dilute and dense states, we propose to use:

$$\mu_{full}(x) = \frac{5}{16\Omega_v}\sqrt{\frac{T^*(x)}{\pi}} \times X^{\alpha} + \mu_r\big(T(x), \bar{\rho}(x)\big) \tag{4.1.26}$$

As shown on Figs. 4.1.5 and 4.1.6, the relation (4.1.26) is able to provide a very good estimate of the local viscosity from the local thermodynamic conditions for both dilute and dense states.

4.1.4. Conclusions

Using molecular dynamics, we have studied mono-atomic Lennard-Jones (LJ) fluids (moderately dense and very dense) subject to an external sinusoidal field inducing density inhomogeneities of various wavelengths and undergoing a bi-periodical shear flow. By performing these NEMD simulations, it is possible to study the local shear viscosity of a strongly inhomogeneous pure fluid without geometric confinement and surface effects. For the systems studied and the conditions employed in this work, it has been verified that a nonlocal constitutive equation was not required and that the Newton's laws can be used to define a local viscosity.

As expected, the local shear viscosity has been found to be strongly dependent to the density inhomogeneities of the fluid for both states. To understand how the local viscosity of inhomogeneous fluid is related to the local thermodynamic properties, we have first tested two well known approaches: the van der Waals and the Local Average Density Model combined with two popular weighted functions. NEMD results showed that the vdW model is unable to deal with local shear viscosity of strongly inhomogeneous fluids (for both states) i.e. when the density varies noticeably over a length of the order of one molecular diameter. The LAMD (combined with an adequate weight function) is a simple but efficient approach for all wavelengths when the fluid is sufficiently dense, i.e. when the translational viscosity is small compared to the configurational viscosity.

However, when dealing with low density and moderately dense inhomogeneous fluids, the LADM is unable to describe correctly viscosity profiles. This is due to the fact that the local translational contribution to the viscosity, which is not negligible is such thermodynamic conditions and considered as constant in the usual LADM, is strongly affected by the density inhomogeneities. To take into account this effect, we propose a description of the local translational viscosity in inhomogeneous fluids based on a density gradient like approach.

When this approach is combined with the LADM, we have found that it is possible to describe correctly the local viscosity profiles of strongly inhomogeneous fluids for the two states studied in this work.

References

[1] G. Karniadakis, A. Beskok and N. Aluru, Microflows and Nanoflows, Springer (2004)

[2] L. Bocquet and J.L. Barrat, Soft Matter **3**, 685 (2007)

[3] B.Y. Cao, J. Sun, M. Chen and Z. Y. Guo, Int. J. Mol. Sci. **10**, 4638 (2009)

[4] W. Sparreboom, A. Van Den Berg and J.C.T. Eijkel, New J. Phys. **12**, 015004 (2010)

[5] J. Israelachvili, Intermolecular and Surface Forces, Academic Press (1992)

[6] J. Hansen and I. R. McDonald: Theory of simple liquid, Third Edition, Elsevier, (2006)

[7] I. Bitsanis, T.K Vanderlick, M. Tirell and H.T. Davis, J. Chem. Phys. **87**, 1733 (1987)

[8] L. A. Pohzar and K. E. Gubbins, J. Chem. Phys. **99**, 8970 (1993)

[9] L. Bocquet and J. L. Barrat, Phys. Rev. E. **49**, 3079 (1994)

[10] E. Akhmatskaya, B. D. Todd, P. J. Daivis, D. J. Evans, K. E. Gubbins and L. A. Pozhar, J. Chem. Phys. **106**, 4684 (1997)

[11] X. D. Din and E. E. Michaelides, Phys. Fluids **9**, 3915 (1997)

[12] J. Zhang, B. D. Todd and K. P. Travis, J. Chem. Phys. **121**, 10778 (2004)

[13] O.G. Jepps, S.K. Bhatia and D.J. Searles, J. Chem. Phys. **120**, 5396 (2004)

[14] Z. Guo, T. S. Zhao and Y. Shi, Phys. Rev. E. **71**, 035301 (2005)

[15] G. Galliero, J. Colombani, P.A. Bopp, B. Duguay, J.P. Caltagirone, F. Montel, Physica A **361**, 494 (2006)

[16] J. Mittal, T. M. Truskett, J. R. Errington and G. Hummer, Phys. Rev. Lett. **100**, 145901 (2008)

[17] B. D. Todd, J. S. Hansen and P. J. Daivis, Phys. Rev. Lett. **100**, 195901 (2008)

[18] D.I. Dimitrov, A. Milchev and K. Binder, Macromol. Theory Simul. **17**, 313 (2008)

[19] S. K. Bhatia, M. R. Bonilla and D. Nicholson, Phys. Chem. Chem. Phys. 13, 15350 (2011)

[20] J. Millat, J.H. Dymond, C.A. Nieto de Castro and W.A. Wakeham, Transport Properties of Fluids: Their Correlation, Prediction and Estimation, Cambridge University Press (2005)

[21] I. Bitsanis, S.A. Somers, H.T. Davis and M. Tirrell, J. Chem. Phys. **95**, 3427 (1990)

[22] F. Muller-Plathe, Phys. Rev. E **59**, 4894 (1999)

[23] G. Galliero and C. Boned, Phys. Rev. E **79**, 02120 (2009)

[24] M.P. Allen and D.J. Tildesley, Computer Simulation of Liquids, Oxford University Press (1989)

[25] H. J. C. Berendsen, J. P. M. Postma, W. F. van Gunsteren, A. Dinola and J. R. Haak, J. Chem. Phys. **81**, 3684 (1984)

[26] D. J. Evans and G. P. Morriss, Statistical mechanics of nonequilibrium liquids, The ANU E Press (1990)

[27] B. D. Todd, D. J. Evans and P. J. Daivis, Phys. Rev. E **52**, 1627 (1995)

[28] G. Galliero, Phys. Rev. E **81**, 056306 (2010)

[29] B.D. Todd and J.S. Hansen, Phys. Rev. E **78** (2008)

[30] L. A. Pozhar, Phys. Rev. E **61**, 1432 (2000)

[31] S. Chapman and T. G. Cowling: The mathematical theory of non-unifrom Gases, 3rd ed., Cambridge University Press, Cambridge (1970)

[32] G. Galliero, C. Boned and A. Baylaucq, Ind. Eng. Chem. Res. **44**, 6963 (2005)

[33] T. K. Vanderlick, L. E. Scriven and H. T. Davis, J. Chem. Phys. **90**(4), 2422 (1988)

[34] J.S. Rowlinson, B. Widom, *Molecular Theory of Capillarity* (Dover, New York, 1982).

[35] V. G. Baidakov, S. P. Protsenko, G. G. Chernykh, and G. Sh. Boltachev, Phys. Rev. E **65**, 041601 (2002)

Part 2

Local Viscosity of a Fluid Confined in a Narrow Pore*

* This part was published in Phys. Rev. E 86, 021202 (2012)

DOI: 10.1103/PhysRevE.86.021202

Abstract:

In this paper, molecular dynamics simulations of a simple Lennard-Jones fluid confined in narrow slit pores and undergoing shear have been performed. The aim is to investigate the effects of density inhomogeneities at the fluid-solid interfaces on the shear viscosity profiles. It has been found that the local viscosity was varying strongly with the distance from the solid walls for both dilute and dense fluid states with oscillations correlated to the density ones. To describe the computed viscosity profiles, we propose a scheme that uses the local average density model, combined with an adequate weight function, for the configurational viscosity and a semi-empirical model for the translational viscosity. It is shown that the proposed approach is able to provide viscosity profiles in good agreement with those coming from simulations for different pore widths and for different fluid states (dilute to dense).

4.2.1. Introduction

Fluids confined between solid surfaces are generally strongly inhomogeneous in the direction perpendicular to the fluid-solid interfaces because of surface effects (layering of the molecules of the fluid because of adsorption and molecular packing) [1]. This induces local variations of equilibrium and transport properties of the confined fluids [1-4]. Understanding such variations plays an important role in fundamental and applied researches for nano- and micro-fluidics, which has led to an extensive amount of literature on that topic over the past 30 years [1-6].

Classical density functional theory (DFT) has been shown to be able to provide reliable prediction for strongly inhomogeneous fluids, e.g. density profiles in narrow slit pore [3]. However, the situation is more complex when dealing with the transport properties of inhomogeneous fluids even for simple fluids [6-13]. This is due to the lack of a comprehensive theory to describe the transport properties of non dilute fluids [14] together with difficulties in assessing the results from an experimental point of view. Some attempts exist to deal with that problem. They are mostly based on Enskog-like kinetic model and molecular dynamics (MD) simulations results and can roughly explain the behavior of the viscosity of inhomogeneous fluids [8, 10-11, 15-18]. However, none of them are able to accurately describe the variation in viscosity of very confined fluids [10-11, 15].

Beside the attempts based on the kinetic theory in determining the spatial variation in transport properties of inhomogeneous fluids, there exists another simpler method, which is very easy to implement [6-7]. This method heuristically assumes that a local transport property of an inhomogeneous fluid at a given position is equal to the value of the property at a bulk state corresponding to a locally averaged density around the given position. This approach is called the local average density model (LADM). The LADM reasonably describes the velocity profiles of fluids confined between solid surfaces and undergoing boundary

shears [7, 19]. However, the accuracy of such an approach is still questionable as long as an explicit comparison of the local transport property provided by the LADM with the one directly deduced from the MD simulation data does not always exist. Furthermore, previous papers dealing with the LADM were mainly restricted to dense fluids, and it seems that the model cannot be applied to dilute fluids [6, 20].

So, this paper aims at improving the description of the local transport properties, limited here to shear viscosity, of strongly inhomogeneous fluid confined in a narrow slit pore. To do so, we employ Non-Equilibrium Molecular Dynamics (NEMD) simulations on fluids confined in narrow pore and undergoing boundary shears, as shown in Fig. 4.2.1. Then, we determine the local viscosity (separated into translational and configurational contributions) of the confined fluid, and evaluate the efficiency of some known models, e.g. the van der Waals (vdW) model and the LADM combined with various weight functions. By doing so, we can directly evaluate the limitations of these models in predicting the local viscosity based on the local thermodynamics properties. Finally, using the results from a previous paper on inhomogeneous fluids without confinement [20], we propose a heuristic-like simple method that can overcome the weaknesses of the classical LADM for low density fluids.

The outline of the paper is as follow: Details on the methodology are presented in Sect. 4.2.2. Then, the results are provided in Sect. 4.2.3 together with a discussion on the validity of the models aimed at describing the local viscosity of strongly inhomogeneous fluids. Finally, the conclusions are drawn in Sect. 4.2.4.

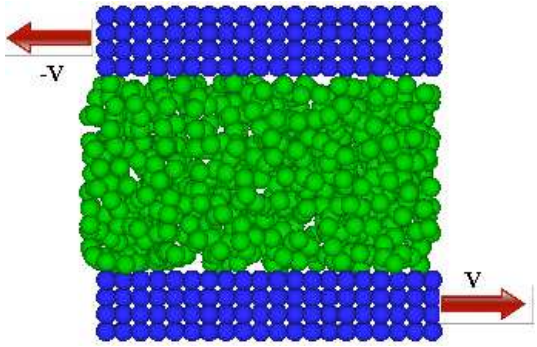

Figure 4.2.1: Scheme of the simulation box used in our paper.

4.2.2. Model and Theory

4.2.2.1. Fluid and Solid Models

In this paper, we study the shear viscosity of simple fluids confined between solid walls. Interaction between fluid particles and fluid-solid particles are described by a usual truncated Lennard-Jones (LJ) potential [21]:

$$U_{ij}(r_{ij}) = \begin{cases} 4\varepsilon_{ij}\left[\left(\frac{\sigma_{ij}}{r_{ij}}\right)^{12} - \left(\frac{\sigma_{ij}}{r_{ij}}\right)^{6}\right] & \text{if } r_{ij} \le r_c \\ 0 & \text{if } r_{ij} > r_c \end{cases} \quad (4.2.1)$$

where r_{ij} is the distance between particles i and j, ε_{ij} is the potential depth, σ_{ij} is the "molecular" diameter and r_c is the cut-off radius (taken equal to $2.5\sigma_{ij}$ in this paper).

The scheme of the simulation box is shown in Fig. 4.2.1, in which each wall is made of four atomic layers distributed on a faced centered cubic lattice with the size of the lattice $a = 1.6\sigma_{ss}$, i.e. a number density of the solid wall $\rho_s \approx 0.98/\sigma_{ss}^3$. The solid particles are fixed at their sites.

Inhomogeneities of the fluid are induced by interactions between fluid and solid particles. To control these inhomogeneities, the fluid-solid interactions are modulated using a classical *k* pre-factor as:

$$\varepsilon_{sf} = k\varepsilon_{ff} = k\varepsilon \tag{4.2.2}$$

$$\sigma_{sf} = \sigma_{ff} = \sigma_{ss} = \sigma \tag{4.2.3}$$

By tuning the amplitude of *k*, one can adapt the magnitude of the first adsorbed fluid layer.

In the following, we express the variables in dimensionless units by using the LJ reduced units. The reduced temperature T^*, density ρ^*, stress P^* and viscosity μ^* are, thus, defined as [21]:

$$T^* = \frac{k_B T}{\varepsilon} \qquad \rho^* = \frac{N_T \sigma^3}{V} \qquad P^* = \frac{P\sigma^3}{\varepsilon} \qquad \mu^* = \mu \frac{\sigma^2}{\sqrt{m\varepsilon}} \tag{4.2.4}$$

where k_B is the Boltzmann constant, N_T is the total number of atoms contained in the volume *V*, and *m* is the mass of the fluid particle.

4.2.2.2. NEMD Scheme

The confined fluid is sheared by moving the walls in opposite parallel directions at a constant velocity, see Fig. 4.2.1. At the stationary state, this scheme yields a constant shear stress in the fluid phase (this point will be checked in the following). It is important to note that the chosen magnitude of the velocity of the walls should be sufficiently large to obtain a high signal-to-noise ratio but must also satisfy that shear thinning is avoided [20].

4.2.2.3. Simulation Details

All simulations consist of three steps. First, the confined fluid is equilibrated during a run of 10^6 time-steps. Then, the NEMD scheme is applied to shear the confined fluid. Finally, once the steady state is reached, which is ensured by monitoring the evolution of the velocity profile with time, the samplings are performed during 3 to 10×10^7 time steps.

The solid walls are composed of a lattice of 10×10 unit cells in the *y* and *z* directions respectively, which corresponds to a number of wall particles $N_w = 1600$ and dimensions of the simulated box $L_y^* = 16$ and $L_z^* = 16$. To provide a high signal-to-noise ratio, the walls are moved with a high velocity on the order of 0.5 in reduced units. However, we have verified that the velocities used in the present paper still lead to a linear response without shear thinning (see Sect. 4.2.3.1).

We have used an in-house code to perform the MD simulations. The equations of motion of the particles are solved by employing the Verlet velocity algorithm with a time step Δt^*=0.002. Classical periodic boundary conditions are applied in all directions [21]. To compute interaction force efficiently, we used the Verlet neighbor list [21]. A Berendsen thermostat [22] is applied to the *x* and *z* velocity components [23] during the NEMD simulations with the time constant, $\tau^* = 0.2$, and to all three velocity components (*x*, *y* and *z*) during the equilibrium MD simulations with $\tau^* = 1$. To compute the local quantities, the simulation box is divided into slabs along the *x* direction using $\Delta x^* \approx 0.11$.

4.2.3. Results and Discussions

4.2.3.1. Preliminary Results

First, to test the proposed methodology, we have carried out MD simulations on a rather dense fluid confined between solid walls separated by $W^* = 10$. To generate the initial configuration we have employed the grand-canonical liked molecular dynamics scheme described in Ref. [24]. In that approach, the pore is simulated in contact with two "bulk" reservoirs maintained at a given state (T_{Bulk} and ρ_{Bulk}). Then, once the equilibrium is reached, the average density in the centre of the pore is extracted and is used to generate the initial configuration of the fluid confined within the slit pore as shown in Fig. 4.2.1. The fluid state employed to perform the preliminary test corresponds to a bulk fluid at $T^* = 2$ and $\rho^* =$

0.625, i.e. a dense supercritical fluid. The *k* pre-factor chosen is equal to 0.387 (moderately adsorbent walls), which provides a maximum of the reduced local density roughly equal to 1, see Fig. 4.2.2(a).

As mentioned previously, during the NEMD simulations the Berendsen thermostat was employed on the *x* and *z* velocity components. So, it is important to check the temperature profile over the *y* direction (not thermostated), as shown in Fig. 4.2.2(b). Two interesting features are observed. First, temperatures in both directions (perpendicular and along the flow) are constant across the entire fluid. Second, the temperature in the *y* direction is equal to the expected one, even if the thermostat was not applied in this direction. This can simply be understood as a consequence of the equi-partition theorem [21, 23].

The momentum conservation equation for a fluid confined in a narrow pore, i.e. at low Reynolds number, and experiencing a boundary shear in the *y* direction (Couette configuration) should lead to constant shear and normal stresses over the *x* coordinate [9, 20]. From the Irving-Kirkwood definition for the pressure tensor, the normal stress P_{xx} and the shear stress τ_{xy} across a plane parallel with the solid surfaces, i.e. the *y*-*z* plane, can be deduced as functions of the *x* coordinate of the plane [9] using

$$P_{xx}(x) = \frac{1}{V_s}\sum_i m v_{i,x}^2\,\delta(x_i - x) - \frac{1}{2A}\left[\sum_{i<j}\frac{x_{ij}^2}{r_{ij}}\frac{\partial U_{LJ}}{\partial r_{ij}}\frac{1}{|x_{ij}|}\Theta\left(\frac{x-x_i}{x_{ij}}\right)\Theta\left(\frac{x-x_j}{x_{ij}}\right)\right] \qquad (4.2.5)$$

$$\tau_{xy}(x) = \frac{1}{V_s}\sum_i m v_{i,x}\left(v_{i,y} - u_y(x)\right)\delta(x_i - x) - \frac{1}{2A}\left[\sum_{i<j}\frac{x_{ij}y_{ij}}{r_{ij}}\frac{\partial U_{LJ}}{\partial r_{ij}}\frac{1}{|x_{ij}|}\Theta\left(\frac{x-x_i}{x_{ij}}\right)\Theta\left(\frac{x-x_j}{x_{ij}}\right)\right] \qquad (4.2.6)$$

where V_s is the volume of a slab, $A = L_y \times L_z$ is the area of the *y*-*z* plane of the simulation box, *m* is the mass of a molecule, $v_{i,\alpha}$ is the α component of the velocity of molecule *i*, $u_y(x)$ is the streaming velocity, x_{ij} is the *x* component of r_{ij}, δ is the Kronecker symbol and $\Theta(x)$ is the Heaviside step function.

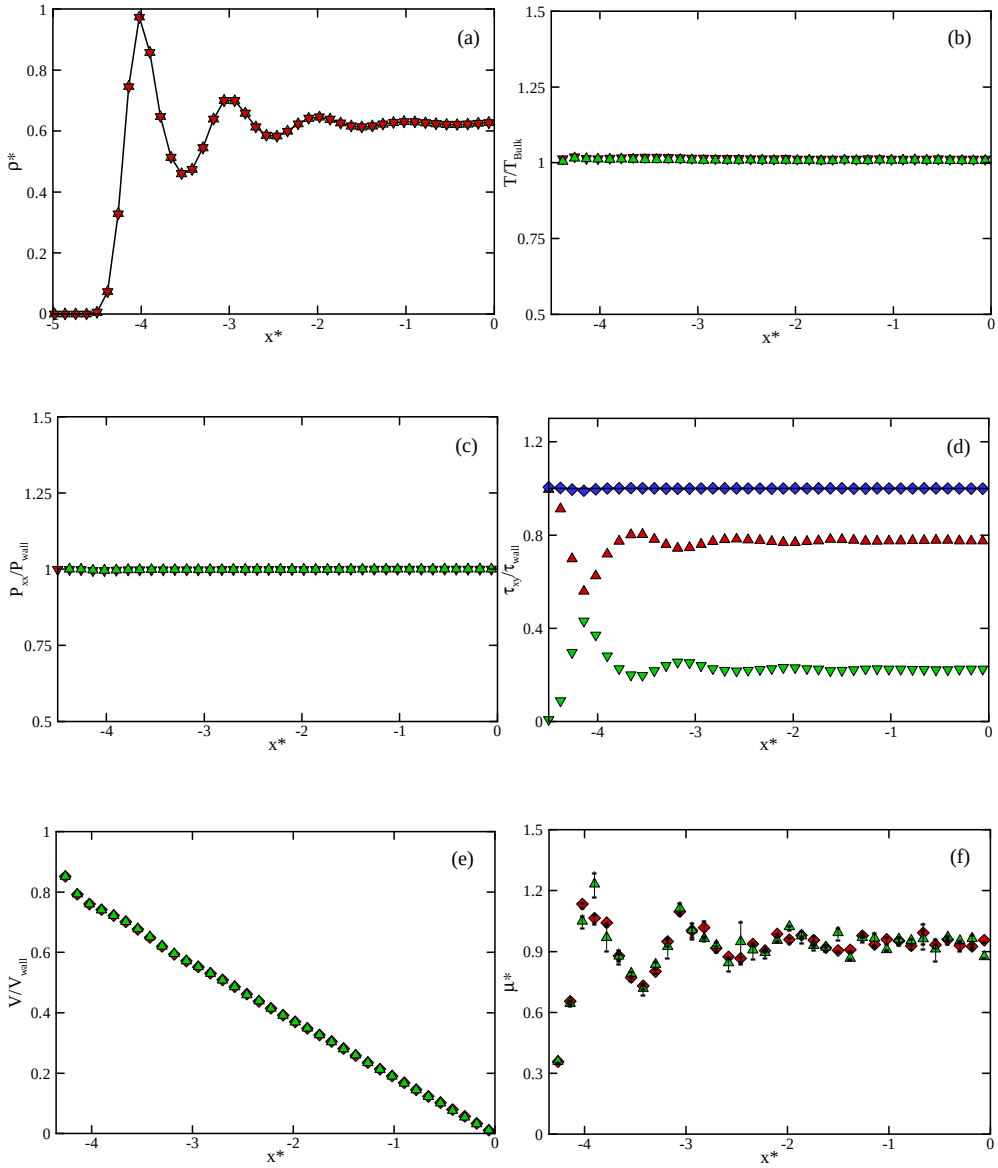

Figure 4.2.2: Preliminary results for the state: ρ^*_{Bulk}=0.625 and T*=2. (a): Density profiles: inverted triangles for equilibrium simulations, triangles for non-equilibrium simulations. (b) Temperature profiles: inverted triangles and triangles for the temperature perpendicular to and along the flow direction. (c) Normal stress profiles: inverted triangles for the normal stress at equilibrium and triangles during non-equilibrium simulations. (d) Shear stress profiles: Diamonds, triangles and inverted triangles for the total, configurational and translational shear stresses, respectively. (e) Velocity profiles: diamonds when $V^*_{wall} = 0.3$, triangles when $V^*_{wall} = 0.6$. (f) Shear viscosity profiles: diamonds when $V^*_{wall} = 0.3$, triangles when $V^*_{wall} = 0.6$.

To compute the local pressure tensor during the MD simulations, we have employed the volume average method which is simply a discretization of Eqs. (4.2.5) and (4.2.6) and is equivalent to the method of planes if a sufficiently fine discretization is employed [25]. So, to divide the simulation box in small slabs perpendicular to the *x* axis, we have used the width of each slab $\Delta x^* \approx 0.11$, which is consistent with what is proposed in Ref. [25] and is sufficient to obtain the normal and shear stress profiles nearly independent of Δx^*. It is worth pointing out that such a formulation of the pressure tensor, Eqs. (4.2.5) and (4.2.6), implies that the kinetic contributions are assigned to the locations where the particles are and the configurational contributions are equally distributed between the particles *i* and *j* considered. Additionally, we have computed P_{wall} and τ_{wall} which are normal and shear stresses acting on the walls due to intermolecular forces between the fluid and the solid molecules.

Results shown in Figs. 4.2.2(c) and 4.2.2(d) confirm that the behavior of the confined fluid studied in this paper satisfies the momentum conservation equation. It is worth noting that even if the density is not constant, see Fig. 4.2.2(a), the local shear stress is constant in the whole fluid and is equal to τ_{wall}.

Equation (4.2.6) is composed of two contributions: the first term on the right hand side is the translational contribution and the second term is the configurational one. Rather surprisingly, the translational contribution increases and the configurational contribution decreases when the local density increases, see Figs. 4.2.2(a) and 4.2.2(d). Such a trend is contradictory with what occurs in a homogeneous fluid where the translational contribution decreases with increasing density [26]. However, this can be explained by the fact that, in an inhomogeneous fluid, the number of particles per volume unit increases with density, but, contrary to what occurs in a homogeneous fluid, the mobility of the particles does not decrease [20, 27]. This can be understood because the momentum transport occurs perpendicular to the dense layer (and the flow) and not parallel to it.

In addition, to test the influence of the shear on the static properties of the confined fluid, we have compared the density and normal pressure profiles at equilibrium with those during non-equilibrium simulations. Results depicted in Figs. 4.2.2(a) and 4.2.2(c) indicate that, for the shear rate used in the present paper, the shear has a negligible effect on the local density and normal pressure.

It is worth pointing out that, when the strain rate varies rapidly over a length typical of intermolecular correlations, the classical local Newton's law of viscosity must be generalized by a nonlocal constitutive equation [28]. However, in the Couette configuration simulated in this paper, the variation in the gradient of the strain rate is small in the region from the pore centre to the first adsorbed layer. This means that the effect of the variation in the strain rate induced from the inhomogeneity of the fluid on the local shear stress can be neglected in this region [29]. It should also be noticed that the remaining region in which the gradient of the strain rate is non-negligible, is rather small, i.e. smaller than $\sigma/2$. So, one can expect that this effect remains rather limited. To confirm this statement, we have performed NEMD simulations with two different velocities of the solid walls, $V^*_{\mathrm{wall}} = 0.3$ and $V^*_{\mathrm{wall}} = 0.6$, to compare the results between them.

As shown in Fig. 4.2.2(e), the velocity profiles are superposing (when scaled by the velocity of the solid walls) for the two different V^*_{wall} 's tested. This is more obvious when looking at the local viscosity profiles deduced from NEMD simulations and using the Newtonian law, i.e. $\mu(x) = \frac{\tau_{xy}(x)}{\left({du_y(x)}/{dx}\right)}$. As shown in Fig. 4.2.2(f), they are independent of the velocity of the solid walls. Thus, in the following, a local shear viscosity has been computed using the Newtonian law in which the center finite difference is used to compute the local shear rate, i.e., $du_y(x)/dx$.

It should be mentioned that we have also performed similar checks for a "dilute" state, i.e. $T^* = 2$ and $\rho^* = 0.291$. All the previous findings on the dense state have been confirmed for the dilute state.

4.2.3.2. Viscosity Decomposition

When using Eq. (4.2.6) combined with the Newtonian equation it is possible to separate the viscosity in two contributions which is crucial to describe the local viscosity of inhomogeneous fluids as we have shown in a previous paper [20]. The first term on the right hand side of Eq. (4.2.6) represents the translational contribution and the second term represents the configurational contribution to the local shear stress [26]. Thus, the local shear viscosity estimated from the NEMD simulations can be expressed as the sum of two terms,

$$\mu(x) = \mu_t(x) + \mu_c(x) \tag{4.2.7}$$

where, μ_t is the local translational shear viscosity computed from :

$$\mu_t(x) = \frac{\frac{1}{V_s}\sum_i m v_{i,x}\left(v_{i,y} - u_y(x)\right)\delta(x_i - x)}{\frac{du_y(x)}{dx}} \tag{4.2.8}$$

and μ_c the local configurational shear viscosity evaluated thanks to:

$$\mu_c(x) = \frac{-\frac{1}{2A}\left[\sum_{i<j} \frac{x_{ij}y_{ij}}{r_{ij}} \frac{\partial U_{LJ}}{\partial r_{ij}} \frac{1}{|x_{ij}|}\theta\left(\frac{x - x_i}{x_{ij}}\right)\theta\left(\frac{x - x_j}{x_{ij}}\right)\right]}{\frac{du_y(x)}{dx}} \tag{4.2.9}$$

From a physical point of view, μ_t correspond to the momentum transfer associated with the displacement (diffusion) of the particles and μ_c corresponds to the contribution due to (interaction) collision between particles. Thus, in a dilute state, μ_t will be the dominant mechanism of momentum transfer whereas it will be μ_c for a dense state.

In a homogeneous fluid, the translational viscosity of an LJ fluid is, to a very good extent [26], equal to the "zero-density" viscosity, μ_0, deduced from a classical Chapman-Enskog approach [30], i.e.,

$$\mu_t^* \approx \mu_0^* = \frac{5}{16\Omega_v}\sqrt{\frac{T^*}{\pi}} \tag{4.2.10}$$

in which Ω_v is the collision integral.

In addition, the configurational viscosity of a LJ homogenous fluid can be described accurately by the correlation developed by Galliero *et al.* [31] using T^* and ρ^* as inputs:

$$\mu_{c,corr}^*(T^*,\rho^*) \approx \left(e^{b_2\rho^*}-1\right) + b_3\left(e^{b_4\rho^*}-1\right) + \frac{b_5}{(T^*)^2}\left(e^{b_6\rho^*}-1\right) \tag{4.2.11}$$

where the numerical parameters, b_i, have been fitted on extensive MD results. When Eqs. (4.2.10) and (4.2.11) are combined, the correlation so built yields an estimate of the shear viscosity of a homogenous LJ fluid with a maximum absolute deviation below 5 % compared to MD results for $0 \leq \rho^* \leq 1.275$ and $0.6 \leq T^* \leq 6$.

4.2.3.3. Local Shear Viscosity Modeling

So, using the approach described previously, we have computed the viscosity profiles of two different fluids using NEMD simulations, one in a dilute state at $T_{Bulk}^*=2.0$ and $\rho_{Bulk}^*=0.291$ and other one in a dense state at $T^*_{\text{Bulk}}=2.0$, $\rho^*_{\text{Bulk}}=0.625$, confined in a pore of a width $W^*=10$. The k pre-factor (related to adsorption) in Eq. (4.2.2) has been taken equal to 0.387 so that the local density remains in the validity range of the LJ shear viscosity correlation, Eq. (4.2.11).

The local viscosity in Fig. 4.2.3 clearly indicates that the local viscosity deduced from NEMD simulations strongly varies with position (i.e. with density inhomogeneities) for both states. Moreover, the viscosity profiles are strongly correlated to the density ones for the two states studied here, a result which is consistent with previous findings on inhomogeneous systems [20]. To better understand the influence of density inhomogeneities on the local shear viscosity, in the following, we separately consider the effects on the two viscosity contributions.

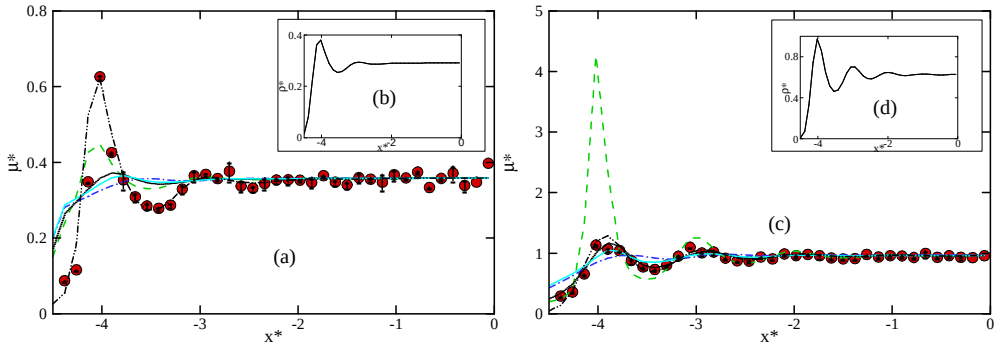

Figure 4.2.3: Shear viscosity profiles (solid curves in the insets: the corresponding density profiles). (a) and (b) T_{Bulk}^{*}=2.0 and ρ_{Bulk}^{*}=0.291, (c) and (d) T_{Bulk}^{*}=2.0 and ρ_{Bulk}^{*}=0.625. Circles for the NEMD simulations results, dashed curve (green color) for the vdW model, solid curve (cyan color) for the LADM + F-M model, dotted curve (black color) for the LADM + H-R model, dashed-dotted curve (blue color) for the LADM + Tarazona model, dashed-dotted-dotted curve (black color) for Eq. (4.2.22).

A. Configurational viscosity

By using Eq. (4.2.9), we have computed the configurational viscosity profiles for both states during the simulations. As shown in Fig. 4.2.4, the configurational viscosity varies with the distance from the solid surface similarly to the density profiles. So, as assumed in the DFT approaches for static properties, we have tested to which extent the NEMD configurational viscosity profiles computed using Eq. (4.2.9), $\mu_c^*(x)$, can be deduced from:

$$\mu_c^*(x) = \mu_{c,corr}^*\left(T^*(x), \rho_{\text{eff}}^*(x)\right) \tag{4.2.12}$$

where $\mu_{c,corr}^*$ is estimated using Eq. (4.2.11) and ρ_{eff}^* is an effective density profile that satisfy the equality in Eq. (4.2.12). Thus, the main question is how $\rho_{\text{eff}}^*(x)$ should be related to the density profiles obtained during MD simulations, i.e., $\rho^*(x)$?

To answer that question, we have first tested the simplest approach, called the van der Waals model [20, 32], that is defined by:

$$\rho_{\text{eff}}(x) = \rho(x) \tag{4.2.13}$$

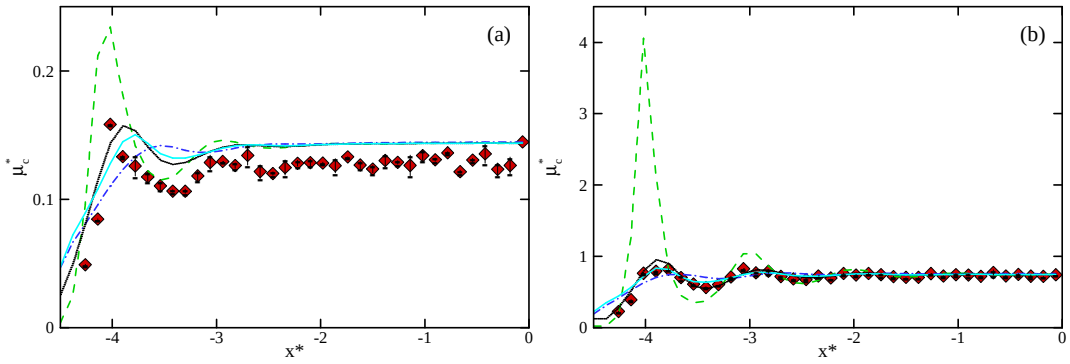

Figure 4.2.4: Configurational viscosity profiles. (a) T^*_{Bulk}=2.0 and ρ^*_{Bulk} =0.291. (b) T^*_{Bulk}=2.0 and ρ^*_{Bulk} =0.625. The legend is the same than in Fig. 4.2.3.

Figure 4.2.4 shows that the vdW model leads to a strong overestimation of the variations in μ_c^* induced by the density inhomogeneities for both states. This result is consistent with the fact that the configurational viscosity is not only affected by the local thermodynamic properties but also is affected by the surrounding density, i.e. non-local effects are expected. Hence, as the vdW model neglects non-local effects, it also fails to yield a good estimate of $\mu_c^*(x)$.

To include non-local effects, we have then used approaches based on the local average density model proposed by Bitsanis *et al.* [7],

$$\rho_{\text{eff}}(x) = \int \omega(|x - \acute{x}|, \{\rho\})\rho(\acute{x})\, d\acute{x} \tag{4.2.14}$$

where $\omega(|x|, \{\rho\})$ is a weight function. There exist various forms of the weight function appearing in Eq. (4.2.14) that have been proposed to deal with static properties [32-33]. In this paper, we have selected among them three well-known different forms. The first one, which is density independent, is the Fischer and Methfessel (F-M) model [33] in which:

$$\omega(|x|) = \begin{cases} \frac{1}{\sigma} & |x| \leq \frac{\sigma}{2} \\ 0 & \text{elsewhere} \end{cases} \tag{4.2.15}$$

The second one, also density independent, the generalized Hard-Rod (H-R) model [33], is defined as:

$$\omega(|x|) = \begin{cases} \frac{6}{\sigma^3}\left[\left(\frac{\sigma}{2}\right)^2 - (|x|)^2\right] & \text{when } |x| \leq \frac{\sigma}{2} \\ 0 & \text{elsewhere} \end{cases} \quad (4.2.16)$$

The last one, which is the most efficient among the three to describe the static properties of confined fluids [33], the Tarazona model, is defined as:

$$\omega\left(|x - \acute{x}|, \rho_{\text{eff}}(x)\right) = \omega_0(|x - \acute{x}|) + \omega_1(|x - \acute{x}|)\rho_{\text{eff}}(x) + \omega_2(|x - \acute{x}|)\rho_{\text{eff}}(x)^2 \quad (4.2.17)$$

where $\omega_{i=0\div2}(|x|)$ are given in Ref. [33]. It is worth to precise that the length over which the non-local effects are taken into account is equal to σ for the first two weight functions, whereas it is equal to 2σ for the last one [32-33].

Figure 4.2.4 shows the results obtained when using Eq. (4.2.12) combined with Eq. (4.2.14) with the three weight functions tested in this paper. From these figures it is clear that, when non-locality is introduced using Eq. (4.2.14), results can be largely improved compared to the simple vdW model. However, rather surprisingly, the two firsts weight functions (that introduce non-locality over a distance equal to σ) yield better results than the Tarazona one (that introduce non-locality over a distance equal to 2σ), see Fig. 4.2.4. This finding is probably related to the fact that thermodynamic quantities are more strongly dependent on long-range interactions than transport properties [34-35]. Such an assumption is supported by the fact that hard-sphere approaches are used to estimate viscosity with a reasonable efficiency [14], whereas, such a fluid model is fundamentally inadequate for thermodynamic properties. Another form of support for that assumption comes from the fact that viscosity is only weakly dependent on the cut-off radius [31, 36-37], whereas, thermodynamic properties are strongly affected by a small cut-off radius value [21, 38].

It should be noted that among the weight functions with the non-locality over a distance equal to σ the generalized H-R function is a more consistent choice because the F-M function, Eq. (4.2.15), is strongly discontinuous at σ/2 whereas the H-R is not. Thus, in the following, the H-R weight function is employed.

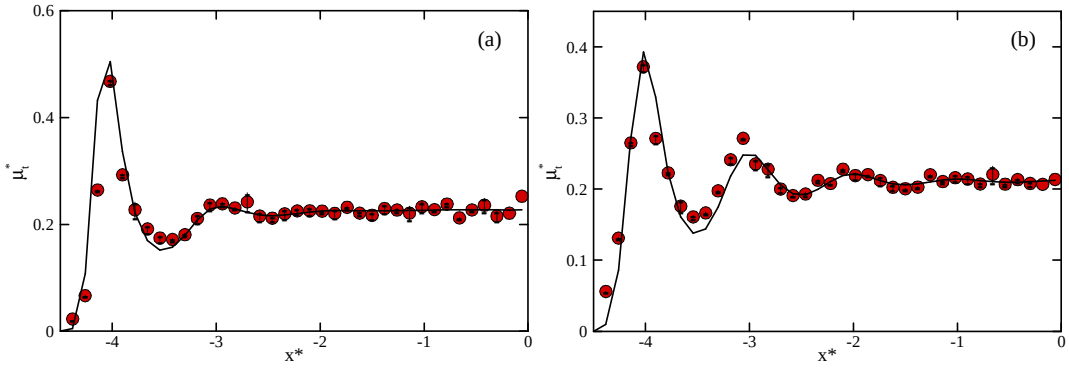

Figure 4.2.5: Translational viscosity profiles. a) T^*_{Bulk}=2.0 and ρ^*_{Bulk} =0.291. (b) T^*_{Bulk} =2.0 and ρ^*_{Bulk} =0.625. Circles for NEMD simulations results, solid curves for Eq. (4.2.21).

B. Translational viscosity

Similar to what was performed for configurational viscosity, the translational viscosity profiles for both states have been computed during the NEMD simulations. As shown in Fig. 4.2.5, the translational viscosity varies appreciably with the distance from the solid surface, i.e. with the densities inhomogeneities. Such a behavior is contradictory with Eq. (4.2.10) which implies a translational viscosity independent of the density. Furthermore, the obvious correlation between the local translational viscosity and the local density is opposite to what found in homogeneous LJ fluids for which the translational viscosity decreases slightly when the density is increasing [26]. This point has already been discussed in Ref. [20] for inhomogeneous fluids without confinement. As explained in this paper, $\mu_t^*(x)$ is connected to the local number of molecules and the local mobility of each molecule, in which the latter is also correlated positively to the local density.

To quantify this correlation between the local translational viscosity and the local thermodynamic conditions, the idea is to quantify the ratio between $\mu_t^*(x)$ and the translational viscosity of the bulk fluid, $\mu_{t,\mathrm{Bulk}}^*$, i.e. the translational viscosity of the fluid in the bulk reservoir in contact with the porous medium (at the same chemical potential than the

one of the confined fluid). For that purpose, we assume that the translational viscosity is a function of the density and of the insertion probability [20], which leads to:

$$\frac{\mu_t(x)}{\mu_{t,Bulk}} = \frac{g(\rho(x))\times f\left(\rho(x),exp\left(\beta\vartheta(\rho(x),T(x))\right)\right)}{g(\rho_{\text{Bulk}})\times f\left(\rho_{\text{Bulk}},exp(\beta\vartheta(\rho_{\text{Bulk}},T_{\text{Bulk}}))\right)} \tag{4.2.18}$$

where ϑ is the chemical potential, g a function of the density and f is a function of the insertion probability. From the thermodynamic equilibrium condition we can write that:

$$\vartheta\big(\rho(x),T(x)\big) = \vartheta(\rho_{\text{Bulk}},T_{\text{Bulk}}) \tag{4.2.19}$$

Then, from Eqs. (4.2.18) and (4.2.19), we can deduce, as a first order approximation, that $\frac{\mu_t(x)}{\mu_t(\rho_{\text{Bulk}},T_{\text{Bulk}})}$ is a function of $\frac{\rho(x)}{\rho_{\text{Bulk}}}$ only. It should be mentioned that such an approximation is valid only when the variations of $\frac{\rho(x)}{\rho_{\text{Bulk}}}$ are not too large, i.e. when the fluid-solid interactions are not too strong. Starting from that assumption, using the NEMD results obtained, we have found that a simple power law is sufficient to provide reasonable results, see Fig. 4.2.6, i.e., the local translational viscosity can be well described by:

$$\mu_t(x) = \mu_{t,Bulk} \times \left(\frac{\rho(x)}{\rho_{\text{Bulk}}}\right)^{\gamma} \tag{4.2.20}$$

where γ is a parameter function of the bulk state ($\gamma \approx 3$ for the dilute state and $\gamma \approx 1.4$ for the dense state). Again, it should be pointed that this relation will remain valid only when the variations in $\frac{\rho(x)}{\rho_{\text{Bulk}}}$ are not too large, i.e., $\frac{\rho(x)}{\rho_{\text{Bulk}}}$ between 2/3 and 3/2.

To estimate the relation between γ and ρ_{Bulk} and T_{Bulk}, we have performed NEMD simulations for 30 different systems, keeping $k = 0.387$, on a large range of bulk states (T^*_{Bulk} varies from 1.5 to 4 and ρ^*_{Bulk} varies from 0.2 to 0.7) and various pore widths (W^*varies from 5 to 10). Results indicate that γ increases with decreasing bulk density and increasing bulk temperature. In other words, the local viscosity is more strongly correlated to $\left(\frac{\rho(x)}{\rho_{\text{Bulk}}}\right)$ at higher bulk temperature and lower bulk density. Based on these results, we propose a correlation for γ,

$$\gamma = 0.8 \times \frac{\exp\left(0.022 \times T^{2}_{\mathrm{Bulk}}\right)}{\rho_{\mathrm{Bulk}}} \tag{4.2.21}$$

As shown in Fig. 4.2.5, Eqs. (4.2.20) and (4.2.21) are able to yield a reasonable $\mu_t(x)$ profiles based on the local thermodynamic properties.

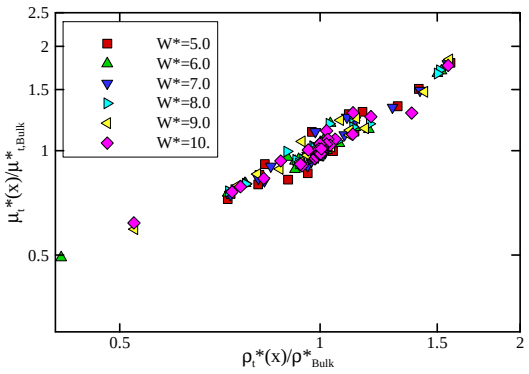

Figure 4.2.6: Correlation between $\mu_t^*(x)/\mu_{\mathrm{t,Bulk}}^*$ and $\rho^*(x)/\rho_{\mathrm{Bulk}}^*$ in the dense state using different pore widths from 5σ to 10σ.

C. Local viscosity

Thus, to quantitatively describe the local viscosity of pure fluids confined in not too adsorbent narrow pores over a large range of thermodynamic conditions, we propose to use:

$$\mu(x) \approx \frac{5}{16\Omega_v}\sqrt{\frac{\overline{T(x)}}{\pi}} \times \left(\frac{\rho(x)}{\rho_{\mathrm{Bulk}}}\right)^{\gamma} + \mu_{c,corr}\left(T(x), \rho_{\mathrm{eff}}(x)\right) \tag{4.2.22}$$

in which, ρ_{eff} is deduced using Eq. (4.2.14) with the H-R weight function defined by Eq. (4.2.16) and γ is obtained by Eq. (4.2.21).

As shown in Figs. 4.2.3, 4.2.7 and 4.2.8, the local viscosities predicted from the local thermodynamic condition using Eq. (4.2.22) are consistent with the ones provided by NEMD simulations for different thermodynamic conditions (two temperatures and two densities) and various pore widths.

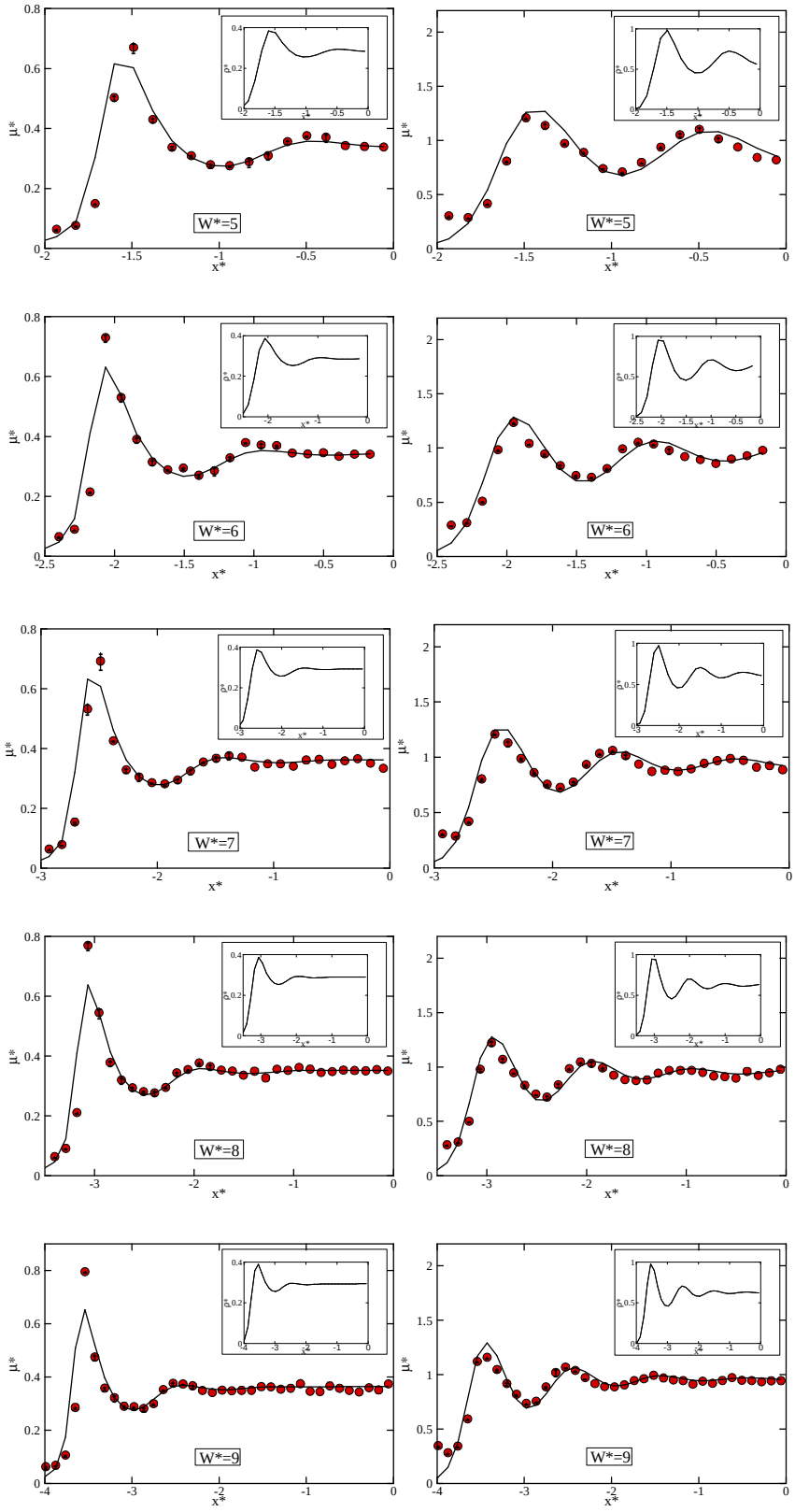

Figure 4.2.7: Viscosity profiles for various pore widths (with corresponding density profiles in the insets). Left: dilute state. Right: dense state. Circles for NEMD simulations and curves for Eq. (4.2.22).

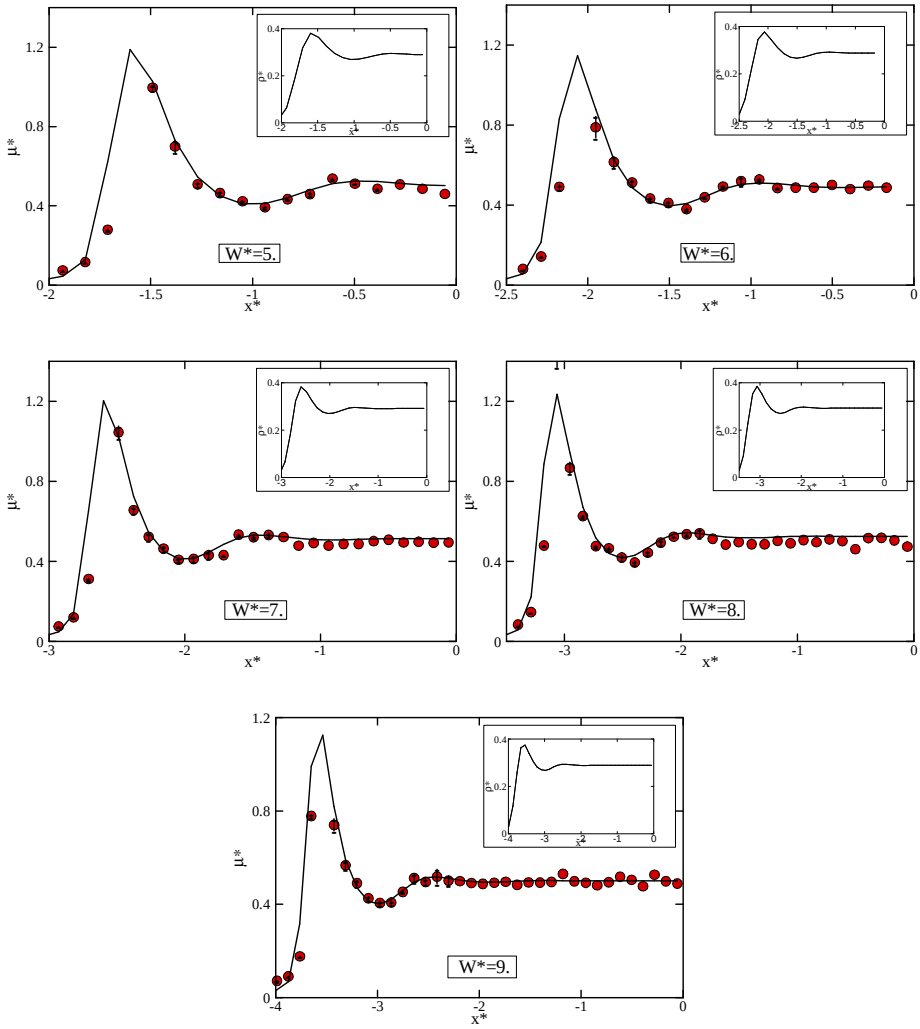

Figure 4.2.8: Viscosity profiles for various pore widths for T^*_{Bulk}=4.0 and ρ^*_{Bulk} =0.291. The legend is the same than on Fig. 4.2.7.

4.2.4. Conclusions

In the present paper, we have investigated the local shear viscosity of Lennard-Jones fluids confined in narrow slit pores by using molecular dynamics simulations of a Couette like configuration. It is shown that, when using such configuration with the appropriate parameters, the variation of the gradient of the strain rate is small in the region from the pore centre to the first adsorbed layer. The remaining region, in which this variation is non-negligible, is limited to regions close to the walls that are smaller than σ/2. So, it is consistent

to define a local viscosity from the classical Newton's equation and a non local constitutive equation is not required in this case.

The local shear viscosity has been found to vary strongly with the distance to the walls and to be dependent on the density inhomogeneities of the fluid. To quantitatively understand this behavior, we have decomposed the local viscosity into configurational and translational contributions. Interestingly, it has been found that both contributions vary with the distance to the walls.

NEMD results showed that the local average density model provides a reasonable estimate of the local configurational viscosity when combined with the appropriate weight function which seems to be the Hard-Rod one for the systems studied here. However, it has been found that this approach is insufficient to yield good results of the viscosity profiles in the dilute state, i.e. when the configurational viscosity is small compared to the translational viscosity.

Based on extensive simulations, we have proposed a simple relation to describe the translational viscosity profiles starting only from the density profiles. Thus, when this relation is combined with the LADM + H-R model for the configurational viscosity, we have found that it is possible to quantitatively determine the shear viscosity profiles of a confined LJ fluid for different pore widths (five to ten molecule sizes) and for different fluid states (dilute to dense) when the solid walls are not too adsorbent.

References

[1] J. Israelachvili, *Intermolecular and Surface Forces*, Academic Press, Third Edition (2010)

[2] G. Karniadakis, A. Beskok and N. Aluru, *Microflows and Nanoflows*, Springer (2004)

[3] J. Hansen and I. R. McDonald: Theory of simple liquid, Third Edition, Elsevier

[4] M. Schoen, *Computer simulation of condensed phases in complex geometries*, New series m: monographs, Lecture note in physics, m17 (Springer-Verlag, Berlin–Heidelberg, 1993).

[5] K. E. Gubbins and J. D. Moore, Ind. Eng. Chem. Res. **49**, 3026 (2010)

[6] S. K. Bhatia, M. R. Bonilla and D. Nicholson, Phys. Chem. Chem. Phys. 13, 15350 (2011)

[7] I. Bitsanis, T.K Vanderlick, M. Tirell and H.T. Davis, J. Chem. Phys. **87**, 1733 (1987)

[8] L. A. Pohzar and K. E. Gubbins, J. Chem. Phys. **99**, 8970 (1993)

[9] B. D. Todd, D. J. Evans and P. J. Daivis, Phys. Rev. E **52**, 1627 (1995)

[10] E. Akhmatskaya, B. D. Todd, P. J. Daivis, D. J. Evans, K. E. Gubbins and L. A. Pozhar, J. Chem. Phys. **106**, 4684 (1997)

[11] X. D. Din and E. E. Michaelides, Phys. Fluids **9**, 3915 (1997)

[12] J. Zhang, B. D. Todd and K. P. Travis, J. Chem. Phys. **121**, 10778 (2004)

[13] J. S. Hansen, P. J. Daivis and B. D. Todd, J. Chem. Phys. **126**, 144706

[14] J. Millat, J.H. Dymond, C.A. Nieto de Castro and W.A. Wakeham, Transport Properties of Fluids: Their Correlation, Prediction and Estimation, Cambridge University Press (2005)

[15] L. A. Pozhar, Phys. Rev. E **61**, 1432 (2000)

[16] U. M. B. Marconi and S. Melchionna, J. Chem. Phys. **131**, 014105 (2009).

[17] U. M. B. Marconi and S. Melchionna, J. Phys.: Condens. Matt. **22**, 364110 (2010)

[18] J. Grant Hill, J. Chem. Phys. **135**, 044104 (2011)

[19] Z. Guo, T. S. Zhao and Y. Shi, Phys. Rev. E **71**, 035301 (2005)

[20] H. Hoang, G. Galliero, J. Chem. Phys. **136**, 124902 (2012)

[21] M.P. Allen and D.J. Tildesley, Computer Simulation of Liquids, Oxford University Press (1989)

[22] H. J. C. Berendsen, J. P. M. Postma, W. F. van Gunsteren, A. Dinola and J. R. Haak, J. Chem. Phys. **81**, 3684 (1984)

[23] D. J. Evans and G. P. Morriss, Statistical mechanics of nonequilibrium liquids, The ANU E Press (1990)

[24] H. Hoang and G. Galliero, J. Chem. Phys. **136,** 184702 (2012)

[25] D. M. Heyes, E. R. Smith, D. Dini, and T. A. Zaki, J. Chem. Phys. 135, 024512 (2011)

[26] G. Galliero and C. Boned, Phys. Rev. E **79**, 02120 (2009)

[27] J. Mittal, T. M. Truskett, J. R. Errington and G. Hummer, Phys. Rev. Lett. **100**, 145901 (2008)

[28] B. D. Todd, J. S. Hansen and P. J. Daivis, Phys. Rev. Lett. 100, 195901 (2008)

[29] B. D. Todd and J. S. Hansen, Phys. Rev. E 78, 051202

[30] S. Chapman and T. G. Cowling: The mathematical theory of non-unifrom Gases, 3rd ed., Cambridge University Press, Cambridge (1970)

[31] G. Galliero, C. Boned and A. Baylaucq, Ind. Eng. Chem. Res. **44**, 6963 (2005)

[32] P. Tarazona, J. A. Cuesta and Y. Martínez-Ratón, Density functional theories of hard particle systems, Lecture note in physics, **753**, (Springer-Verlag, Berlin–Heidelberg, 2008).

[33] T. K. Vanderlick, L. E. Scriven and H. T. Davis, J. Chem. Phys. **90**(4), 2422 (1988)

[34] T. Young and H.C. Andersen, J. Phys. Chem. B **109**, 2985 (2005)

[35] T. Young and H. C. Andersen, J. Chem. Phys. **118**, 3447 (2003)

[36] O.C. Nwobi, L.N. Lon, Micci M.M., J. of Thermophysics and Heat Transfer **12**, 322 (1998)

[37] K. Meier, A. Laesecke, S. Kabelac, J. Chem. Phys. **121**, 3671 (2004).

[38] G. Galliero, M.M. Pineiro, B. Mendiboure, C. Miqueu, T. Lafitte, D. Bessières, J. Chem. Phys. **130**, 104704 (2009).

Part 3

From the Hard-Sphere to the Lennard-Jones Viscosity of Strongly Inhomogeneous Fluids*

Hai Hoang, Guillaume Galliero

* Most of this part was published in J. Phys.: Condens. Matter 25 485001 (2013)

DOI: 10.1088/0953-8984/25/48/485001

Abstract:

The way to model adequately the non-local contributions due to the interactions of particles separated by a given distance into the local shear viscosity of dense strongly inhomogeneous fluids composed of spheres is explored in this work using Non Equilibrium Molecular Dynamics simulations. It is shown that a simple local average density model with state independent weight functions is able to yield good results for a fluid composed of quasi-hard spheres. However, when going to smoothly repulsive potential, such an approach must be completed by taking into account that the distributions of the normalized contributions depend on their interaction potential and on the temperature but not on the density. Finally, using a simple perturbation scheme, it is shown how to extend the approach to model the local shear viscosity of dense strongly inhomogeneous Lennard-Jones fluids starting from the density profile.

4.3.1. Introduction

An accurate description of fluid flows through nano-, micro-materials and the design optimization of nano-, micro-devices rely on the precise knowledge of the transport properties of strongly confined fluids [1-2]. In such systems the fluids are generally strongly inhomogeneous because of surface effects and geometric confinement [3]. To deal with such systems, most works have been dedicated to Enskog-like kinetic models combined with molecular dynamics (MD) simulations [4-7] as a test. However, such approaches are rather difficult to employ compared to what exists to deal with static properties [3] and exhibit deficiencies in some cases because of the intrinsic limitations of an Enskog like approach to deal with dense fluids.

A longstanding question is how to construct an approach similar to what has been successfully developed for the static properties of inhomogeneous fluids, the density functional theory (DFT), to deal with transport properties [3, 8]. This domain was pioneered by Bitsanis et al. [9] who proposed the local average density model (LADM). In this method it is heuristically assumed that a local transport property of an inhomogeneous fluid at a given position is equal to the value of the property in a bulk state corresponding to a locally averaged density around the given position. However, this approach, combined with usual DFT weight functions [3, 13], does not always lead to a good estimate of the local viscosity [8, 10-12].

Thus, this paper aims at providing a general tractable scheme able to yield quantitatively the viscosity profile of strongly inhomogeneous dense fluids of various types starting from the density profile. To do so, employing Non-Equilibrium Molecular Dynamics (NEMD) simulations, we propose to study the local viscosity of three types of fluids, the quasi-Hard Sphere (HS), the Weeks-Chandler-Andersen (WCA) and the Lennard-Jones (LJ)

fluids, subject to an external sinusoidal field to induce density inhomogeneities as shown in Fig. 4.3.1.

The outline of the paper is as follows: the details on the methodology used are presented in Sect. 4.3.2. Then, the results obtained are provided in Sect. 4.3.3 together with a discussion of the validity of the approaches aiming at describing the local viscosity of strongly inhomogeneous fluids. Finally, the conclusions are drawn in Sect. 4.3.4.

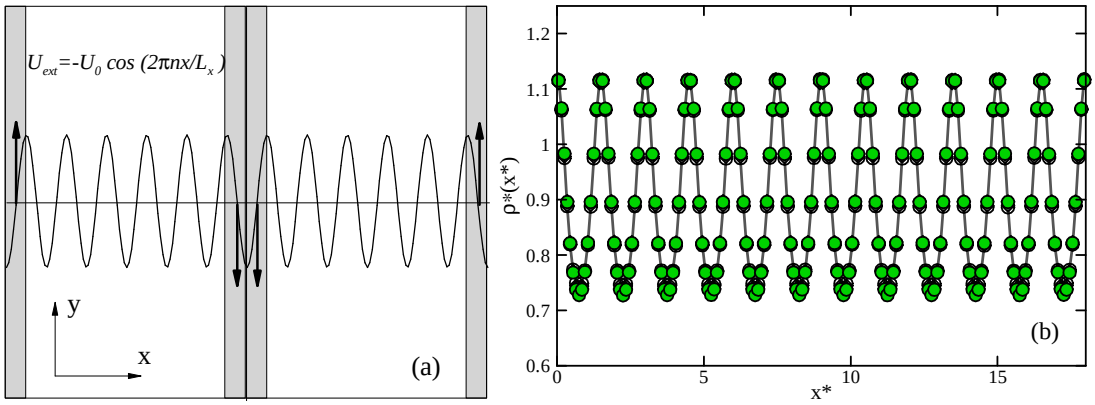

Figure 4.3.1: (a) A 2D sketch of the simulated system. (b) Density profiles of the inhomogeneous fluids for $\rho^*_{\mathrm{Ini}} = 0.9$. Line : quasi-HS fluid, diamonds : LJ fluids and circles : WCA fluids. Open symbols : $T^* = 0.8$ and full symbols : $T^* = 2.0$.

4.3.2. Molecular Simulations

4.3.2.1. Fluid Models

As mentioned in the introduction, we study in this work the local viscosity of three types of simple inhomogeneous fluids composed of spheres interacting through different potential. The quasi-HS fluid is described by an interaction potential such as:

$$U_{\mathrm{quasi-HS}}(r_{ij}) = \varepsilon \left(\frac{r_{ij}}{\sigma}\right)^{144} \tag{4.3.1}$$

where r_{ij} is distance between the particles *i* and *j*, ε are σ are the energy and the "molecular" diameter respectively. The choice of a repulsive exponent equal to 144 ensures that the simulated fluid possesses characteristics similar to that of a hard sphere fluid with a diameter equal to σ [14-15] while keeping the potential continuous.

The LJ fluid interactions are described by:

$$U_{LJ}(r_{ij}) = \begin{cases} 4\varepsilon\left[\left(\frac{\sigma}{r_{ij}}\right)^{12} - \left(\frac{\sigma}{r_{ij}}\right)^{6}\right] & \text{if } r_{ij} \le r_c \\ 0 & \text{if } r_{ij} > r_c \end{cases} \tag{4.3.2}$$

where r_c the cut-off radius (taken equal to 2.5σ in this paper).

The WCA fluid interactions are described by:

$$U_{WCA}(r_{ij}) = \begin{cases} 4\varepsilon\left[\left(\frac{\sigma}{r_{ij}}\right)^{12} - \left(\frac{\sigma}{r_{ij}}\right)^{6}\right] + \varepsilon & \text{if } r_{ij} \le 2^{1/6}\sigma \\ 0 & \text{if } r_{ij} > 2^{1/6}\sigma \end{cases} \tag{4.3.3}$$

In the following, variables noted with a star as superscript correspond to classical reduced quantities.

4.3.2.2. Inhomogeneous Fluid

To induce the density inhomogeneities [11], see Fig. 4.3.1(a), we have applied to the simulation box a Sinusoidally Varying external Potential (SVP), U_{ext}, in the *x* direction:

$$U_{ext} = -U_0 cos\left(2\pi n \frac{x}{L_x}\right) \tag{4.3.4}$$

where L_x is the dimension of the simulation box in the *x* direction, U_0 the amplitude of the SVP and *n* the wavelength parameter. In this work, L_x is chosen to be equal to 18σ, and n equals to 2 and 12 to test different inhomogeneity wavelengths. It should be noted that the set of $L_x = 18\sigma$ and $n = 12$ leads to variations of the density profiles over a distance typical to what occur in confined fluids. Thus, starting from the same initial density, $\rho^*_{\text{ini}} = 0.9$, for $n = 12$ we have generated density profiles that are superposing by tuning U_0: one for the

quasi-HS ($T^* = 1$), two for the WCA ($T^* = 0.8$ and 2) and two for the LJ fluid ($T^* = 0.8$ and 2), see Fig. 4.3.1(b); for $n = 2$, the amplitudes of the SVP, U_0, have been chosen so that the order of magnitude of minimal local density is roughly the same for $n = 12$. In addition, another initial density has been considered for the quasi-HS fluid at $\rho^*_{\mathrm{Ini}} = 0.75$ (and $T^* = 1$).

4.3.2.3. NEMD Scheme

To shear the inhomogeneous fluids so obtained, the NEMD scheme proposed by F. Muller-Plathe has been employed [16]. In this method, the simulation box is divided into N_s slabs (32 in this work) along the *x* direction and the fluid is sheared using a net exchange of the linear momentum along the *y* direction every N_{swap} time steps. This exchange is performed between the central part of the simulation box, $N_s/2$ and $N_s/2+1$, and the edge slabs, 1 and N_s, to keep the periodic boundary conditions in the *x* direction, see Fig. 4.3.1(a). N_{swap} is chosen such as the effect of the variations in the strain rate induced from the inhomogeneity of the fluid on the local shear stress can be neglected [11] to avoid the need of a non-local constitutive equation to quantify the local shear viscosity [17]. It is then possible to compute locally the translational (kinetic) and configurational (collisional) contributions to the shear viscosity [11]. Thus, a local configurational shear viscosity, $\mu^c(x)$, has been computed using the classical Newtonian law, i.e.

$$\mu^c(x) = \frac{\tau^C_{xy}(x)}{\left({du_y(x)}/{dx}\right)} \tag{4.3.5}$$

where $u_y(x)$ the streaming velocity at x and $\tau^C_{xy}(x)$ is the configurational shear stress:

$$\tau^c_{xy}(x) = -\frac{1}{2A}\left[\sum_{i<j} \frac{x_{ij}y_{ij}}{r_{ij}} \frac{\partial U}{\partial r_{ij}} \frac{1}{|x_{ij}|} \Theta\left(\frac{x-x_i}{x_{ij}}\right) \Theta\left(\frac{x-x_j}{x_{ij}}\right)\right] \tag{4.3.6}$$

where $A = L_y \times L_z$ is the area of the *y*-*z* plane of the simulation box. The volume average method is employed to compute the local configurational shear stress in which the width of

each slab is $\Delta x^* = 0.1$ [18], and the center finite difference is used to approximate the local shear rate $du_y(x)/dx$. To reduce the statistical uncertainties, the computed viscosity profiles shown in Fig. 4.3.2 correspond to an average over 12 independent runs and the error bars represents the standard deviation. In addition, as only dense fluid will be dealt with in this paper, we will not consider the translational contribution to the viscosity which is negligible for such states [11].

4.3.3. Results and Discussions

4.3.3.1. Classical LADM

To model the viscosity profiles shown on Figs. 4.3.2 and 4.3.3, as a starting point, we retain the main idea of the LADM approach, i.e. the viscosity profiles of strongly inhomogeneous fluid are related to non-local contributions and a simple weighted average of the local density over a given distance can be sufficient to take into account these effects. In the original work, Bitsanis *et al.* suggested the use of the HR weight function [9], and in subsequent works Guo *et al.* employed the Tarazona weight function [19-20]. They showed that the use of such functions can lead to a good prediction for the velocity profiles of inhomogeneous fluid. However, such weight functions were originally developed for equilibrium properties [21] and their applications to the shear viscosity have not rigorously been justified. In particular, in DFT approaches the basic idea is similar to the LADM but is applied to a quantity (the excess free energy) per molecule [3]. Thus, we have considered that the non-local contributions should be taken into account through the kinematic configurational viscosity ($\eta^c = \mu^c / \rho$), a quantity per molecule, leading to a local

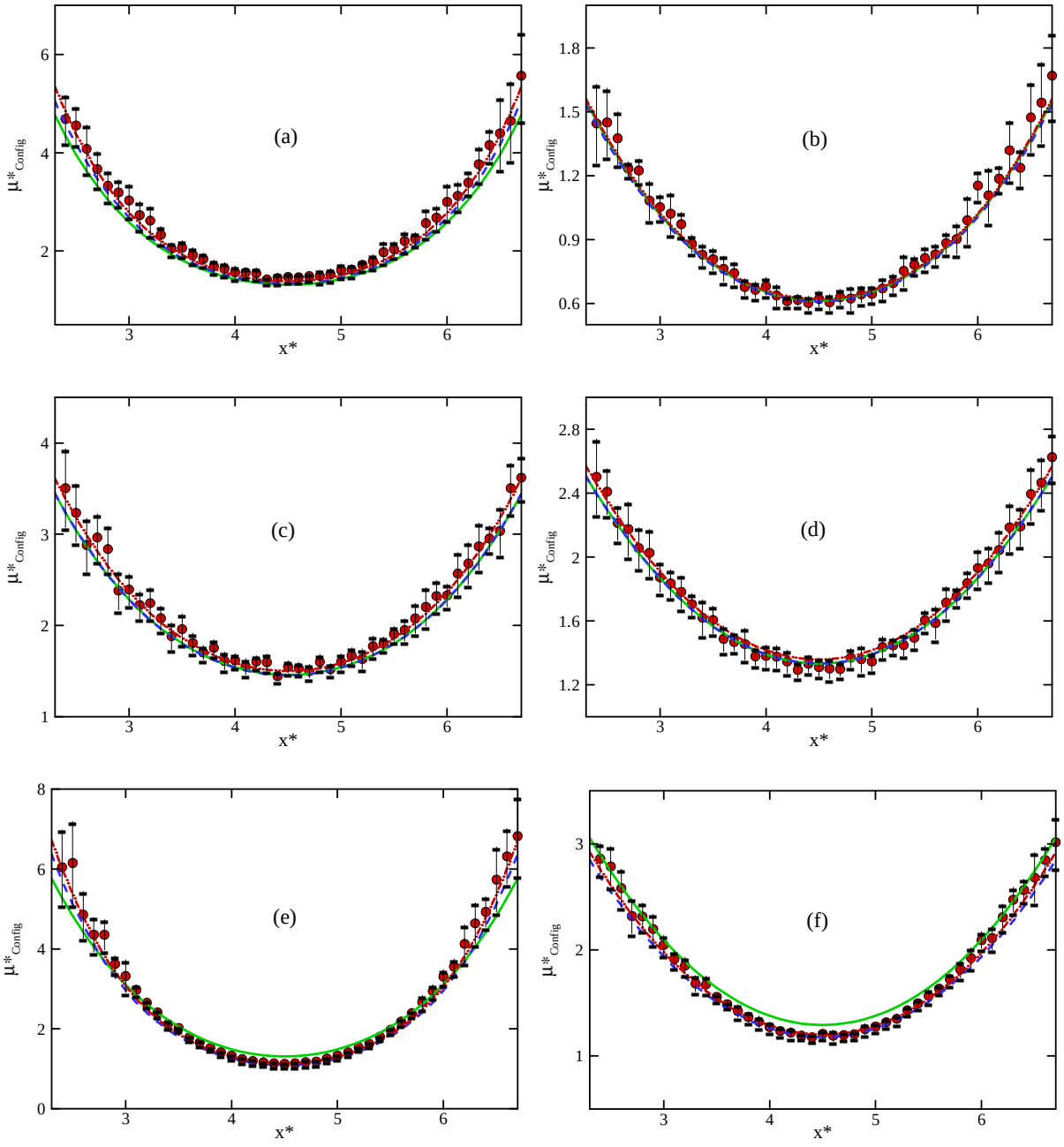

Figure 4.3.2: Viscosity profiles of the inhomogeneous fluids for the slowly varying density, i.e. $n = 2$. (a) Quasi-HS fluid with $\rho^*_{\mathrm{Ini}} = 0.9$ and $T^* = 1$. (b) Quasi-HS fluid with $\rho^*_{\mathrm{Ini}} = 0.75$ and $T^* = 1$. (c) WCA fluid with $\rho^*_{\mathrm{Ini}} = 0.9$ and $T^* = 0.8$. (d) WCA fluid with $\rho^*_{\mathrm{Ini}} = 0.9$ and $T^* = 2$. (e) LJ fluid with $\rho^*_{\mathrm{Ini}} = 0.9$ and $T^* = 0.8$. (f) LJ fluid with $\rho^*_{\mathrm{Ini}} = 0.9$ and $T^* = 2$. Circles: NEMD simulations. Dashed (blue) and dashed-dotted-dotted lines (red): LADM combined with the HR and Tarazona models, respectively. Solid (green) lines: proposed scheme, Eqs. (4.3.7), (4.3.9), (4.3.13) and (4.3.15).

configurational viscosity given by:

$$\mu^c(x) = \rho^\tau(x)\eta^c(\bar{\rho}) \tag{4.3.7}$$

where $\eta^c(\bar{\rho})$ is the kinematic viscosity of a bulk fluid at a density $\bar{\rho}$ and :

$$\rho^\tau(x) = \int \psi(x - \acute{x}, \rho)\rho(\acute{x})\, d\acute{x} \tag{4.3.8a}$$

$$\bar{\rho}(x) = \int \omega(x - \acute{x}, \rho)\rho(\acute{x}) d\acute{x} \tag{4.3.8b}$$

where, $\psi(x, \rho)$ and $\omega(x, \rho)$ are weight functions of the position and the density similarly to what used in classical DFT generalized approaches [19].

To estimate the "bulk" η^c for the different densities in Eq. (4.3.7), we have used the Sigurgeirsson and Heyes [22] relation for the quasi-HS, direct MD simulations for the WCA fluid and the Galliero et al. [23] correlation for the LJ fluid. In homogeneous fluids, these viscosity correlations are able to provide data within 5% of the direct MD simulations results.

As shown in Fig. 4.3.2, for a slowly varying density profile, i.e., $n = 2$, the viscosity profiles provided from both models are in very good agreement with those obtained from the NEMD simulations whatever the type of fluid, the initial density and the temperature. This clearly indicates that the approaches developed for the equilibrium thermodynamics of the strongly inhomogeneous fluids are applicable to prediction for the local viscosity when the density profile is slowly varying. Otherwise, for a strongly varying density profile, i.e., $n = 12$, the H-R model yields good result for the quasi-HS fluid at $\rho^*_{\mathrm{Ini}} = 0.75$ and for the WCA and LJ fluids when $T^* = 2$, but the viscosity variations are overestimated for the other systems, as shown in Fig. 4.3.3. The Tarazona model provides reasonable results for the quasi-HS fluid at $\rho^*_{\mathrm{Ini}} = 0.9$ and for the WCA and LJ fluids when $T^* = 0.8$ but tends to noticeably underestimate the variations for other states. This confirms [8, 10-12] that usual weight functions combined with Eq. (4.3.7) are unable to provide a quantitative estimation of the viscosity profiles for different types of fluid and different states.

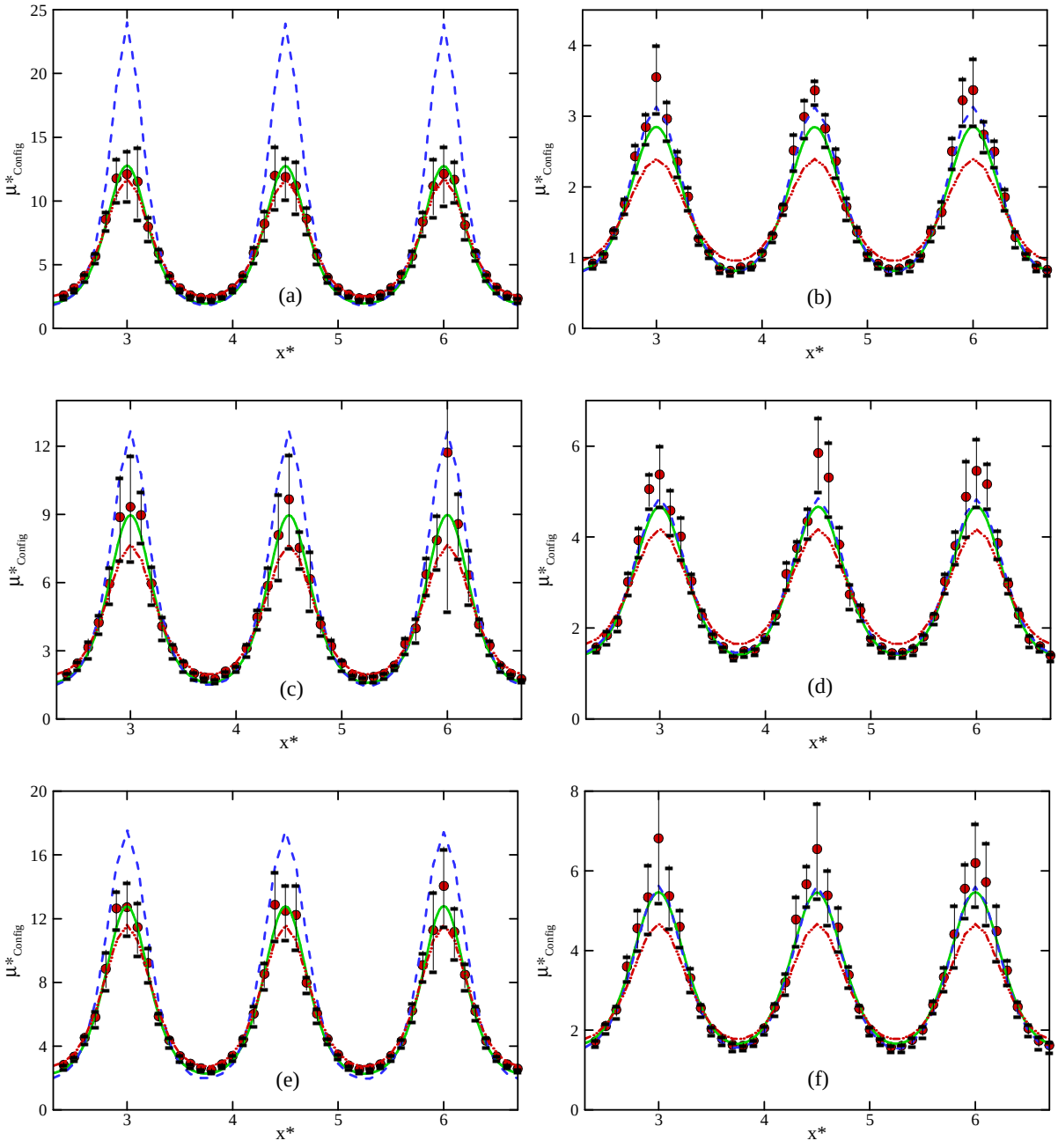

Figure 4.3.3: Viscosity profiles of the inhomogeneous fluids for the strongly varying density, i.e., $n = 12$. (a) Quasi-HS fluid with $\rho^*_{\mathrm{Ini}} = 0.9$ and $T^* = 1$. (b) Quasi-HS fluid with $\rho^*_{\mathrm{Ini}} = 0.75$ and $T^* = 1$. (c) WCA fluid with $\rho^*_{\mathrm{Ini}} = 0.9$ and $T^* = 0.8$. (d) WCA fluid with $\rho^*_{\mathrm{Ini}} = 0.9$ and $T^* = 2$. (e) LJ fluid with $\rho^*_{\mathrm{Ini}} = 0.9$ and $T^* = 0.8$. (f) LJ fluid with $\rho^*_{\mathrm{Ini}} = 0.9$ and $T^* = 2$. Legend is the same than in Fig. 4.3.2.

4.3.3.2. Towards a More General Scheme

To develop the general scheme proposed in this work, we will first show that is possible to obtain good results for the quasi-HS fluid taking into account a peculiarity of the momentum exchange compared to what used to deal with free energy. In a second step, we will describe how it is possible to approximate what occurs in a smoothly repulsive WCA fluid by taking into account the influence of the normalized contribution to the shear viscosity induced by the interactions of particles separated by a given distance. Finally, using a simple perturbation scheme, we will show how it is possible to obtain results for the LJ fluid starting from the WCA fluid.

A. The quasi-HS fluid

To deal with the quasi-HS fluid, we start from the fact that in some DFT approaches it is assumed that the local properties should be defined at the center of the colliding molecule, e.g. the generalized van der Waals and Tarazona models, or at the position of contact, e.g. the HR model [21]. As the former approach, i.e. $\psi(x) = \delta(x)$, leads generally to better results than the latter, we have retained it:

$$\rho^{\tau}(x) = \rho(x) \tag{4.3.9a}$$

In addition, the configurational viscosity is induced by collisions between molecules which occurs only at contact, i.e. when $x = \sigma/2$, in a quasi-HS fluid. However, contrary to what is needed to deal with free energy as in usual DFT, the exchange of momentum (i.e., the configurational shear stress) depends on the angle that is formed between the colliding molecules relatively to the direction of the flow as taken into account in kinetic theories developed to deal with that problem [4-7]. Hence, we propose to model the average density by:

$$\bar{\rho}(\sigma, x) = \int_0^{\sigma/2} \bar{\rho}_{HR}(\sigma, x)\, d\left(\frac{\sigma/2 - x}{\sigma/2}\right) \tag{4.3.9b}$$

where $\bar{\rho}_{HR}(\sigma, x)$ is the local average density obtained by using the HR model which relies on the Fischer and Methfessel assumption [24]. As shown in Figs. 4.3.3(a) and 4.3.3(b), using this simple approach, the configurational viscosity profiles obtained for the quasi-HS fluids are in very good agreement with NEMD results for both states and provides better results than those coming from the "usual" approaches. In addition, as shown in Figs. 4.3.2(a) and 4.3.2(b) the proposed approach predicts quantitatively the viscosity profiles obtained from the NEMD simulations for slowly varying density profiles.

B. The WCA fluid

When going to smoothly repulsive potentials (WCA fluid) one has to take into account that the exchange of momentum between particles is not restricted to the contact position (i.e. a distance equal to σ) as for the quasi-HS fluid. Thus, to analyze and quantify the differences between quasi-HS and WCA fluids, we have computed the following relative quantity using NEMD simulations on homogeneous (bulk) WCA fluids for different thermodynamic states ($\rho^*_{\text{Bulk}} = 0.5$ to 1 and $T^* = 0.8$ to 3):

$$f_{\eta,WCA}(r,\rho,T) = \frac{1}{\eta^C_{WCA}(\rho,T)} \frac{\partial\left(\eta^C_{r,WCA}(r,\rho,T)\right)}{\partial r} \tag{4.3.10}$$

where, $\eta^C_{r,WCA}(r,\rho,T)$ is the contribution to the kinematic configurational viscosity induced by interactions between molecules separated by r or less from each others. This allows quantifying the distribution of the intermolecular distances that contribute to the configurational viscosity. It should be noticed that f_η reduces to a Dirac located at a distance *d* = σ for a quasi-HS fluid.

As shown in Fig. 4.3.4(a), $f_{\eta,WCA}$ is strongly peaked, with a position of the maximum that decreases when temperature increases. A very interesting feature of $f_{\eta,WCA}$ of the WCA fluid is that it is not dependent on the density, see Fig. 4.3.4(a). Furthermore, as expected, the distance range over which $f_{\eta,WCA}$ is non-negligible increases when temperature increases.

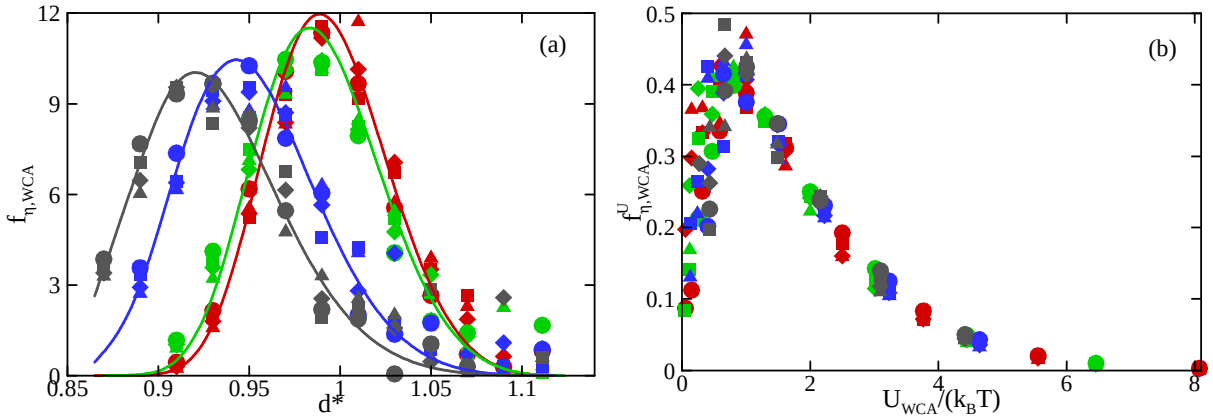

Figure 4.3.4: Dependence of f_η with: (a) Distance d^* and (b) Interaction potential βU_{WCA}, for different homogeneous states. Symbols: NEMD simulations (deltas for $\rho^*_{\text{Bulk}} = 0.5$, diamonds for $\rho^*_{\text{Bulk}} = 0.75$, squares for $\rho^*_{\text{Bulk}} = 0.9$ and circles for $\rho^*_{\text{Bulk}} = 1.$). Lines: Eq. (4.3.12b). Red color: $T^* = 0.8$. Green color: $T^* = 1$. Blue color: $T^* = 2$. Dark color: $T^* = 3$.

This clearly indicates that the non-local contributions associated to the kinematic configurational viscosity of a WCA fluid cannot be properly handled by a weight function independent of temperature as usually assumed in the LADM approach [9].

To model $f_{\eta,WCA}$, which is so independent on density but dependent on temperature, we start from the assumption that the region over which $f_{\eta,WCA}$ is not negligible is related to the way the molecule explore the potential for a given temperature. So, $f_{\eta,WCA}$ should be related to βU_{WCA} where $\beta = \frac{1}{k_B T}$. We have then estimated in homogeneous WCA fluid for different states the following quantity:

$$f^U_{\eta,WCA}(\beta U_{WCA}(r),T) = \frac{1}{\eta^C_{WCA}(\rho,T)} \frac{\partial\left(\eta^C_{r,WCA}(r,\rho,T)\right)}{\partial\left(\beta U_{WCA}(r)\right)} = \frac{f_{\eta,WCA}(r,T)}{\beta U'_{WCA}(r)} \qquad (4.3.11)$$

Very interestingly, as shown on Fig. 4.3.4(b), $f^U_{\eta,WCA}$ is a unique function of βU_{WCA} for all states studied which strongly support the previous assumptions.

To describe $f_{\eta,WCA}^{U}$, we start from the fact that it quantifies which parts of a continuous potential between two particles contribute the most to the momentum exchange between the particles. So $f_{\eta,WCA}^{U}$ must be related to the way the particles are distributed relatively to each others, i.e. the radial distribution function *g(r)*. Thus, if we assume that $f_{\eta,WCA}^{U}$ is simply proportional to $g(r)$, we can deduce that $f_{\eta,WCA}^{U}$ should be proportional to $exp(-\beta U_{WCA})$ as long as $f_{\eta,WCA}^{U}$ is independent of density. Finally, as by definition $\int f_{\eta,WCA}^{U}\, d(\beta U_{WCA}) = 1$, we can deduce that:

$$f_{\eta,WCA}^{U}(\beta U_{WCA}) = \beta U_{WCA} e^{-\beta U_{WCA}} \tag{4.3.12a}$$

and so:

$$f_{\eta,WCA}(r,T) = \beta^2 U_{WCA} U'_{WCA} e^{-\beta U_{WCA}} \tag{4.3.12b}$$

As clearly shown on Fig. 4.3.4(a), Eq. (4.3.12b) is able to describe very well the NEMD results of homogeneous WCA fluids for all thermodynamic states.

To quantify the local configurational viscosity of an inhomogeneous WCA fluid, it is rational to hypothesize that the contribution induced by the interactions of molecules separated by a distance d can be determined analytically by $\rho^{\tau}(r)\eta_{WCA}^{C}\big(\bar{\rho}(d,r)\big)f_{\eta,WCA}(d)$, where $\rho^{\tau}(r)$ and $\bar{\rho}(d,r)$ are described using Eqs. (4.3.9a) and (4.3.9b) respectively. However, the use of the molecular simulations to directly test this hypothesis is difficult due to the associated statistical uncertainties. In terms of integral this hypothesis can be re-stated as that the contributions induced by the interactions of molecules separated by a distance less than d, can be evaluated by $\rho^{\tau}(x)\int_0^d \eta_{WCA}^{C}\big(\bar{\rho}(x',x)\big)f_{\eta,WCA}(x')dx'$. Using the NEMD simulations, we have checked such hypothesis for several values of d. Results shown in Fig. 4.3.5 indicate that the hypothesis make sense. Thus, we can deduce that the local configurational viscosity of a WCA fluid is simply described by:

$$\mu_{WCA}^{C}(x) = \rho^{\tau}(x)\int \eta_{WCA}^{C}\big(\bar{\rho}(x',x)\big)f_{\eta,WCA}(x')\,dx' \tag{4.3.13}$$

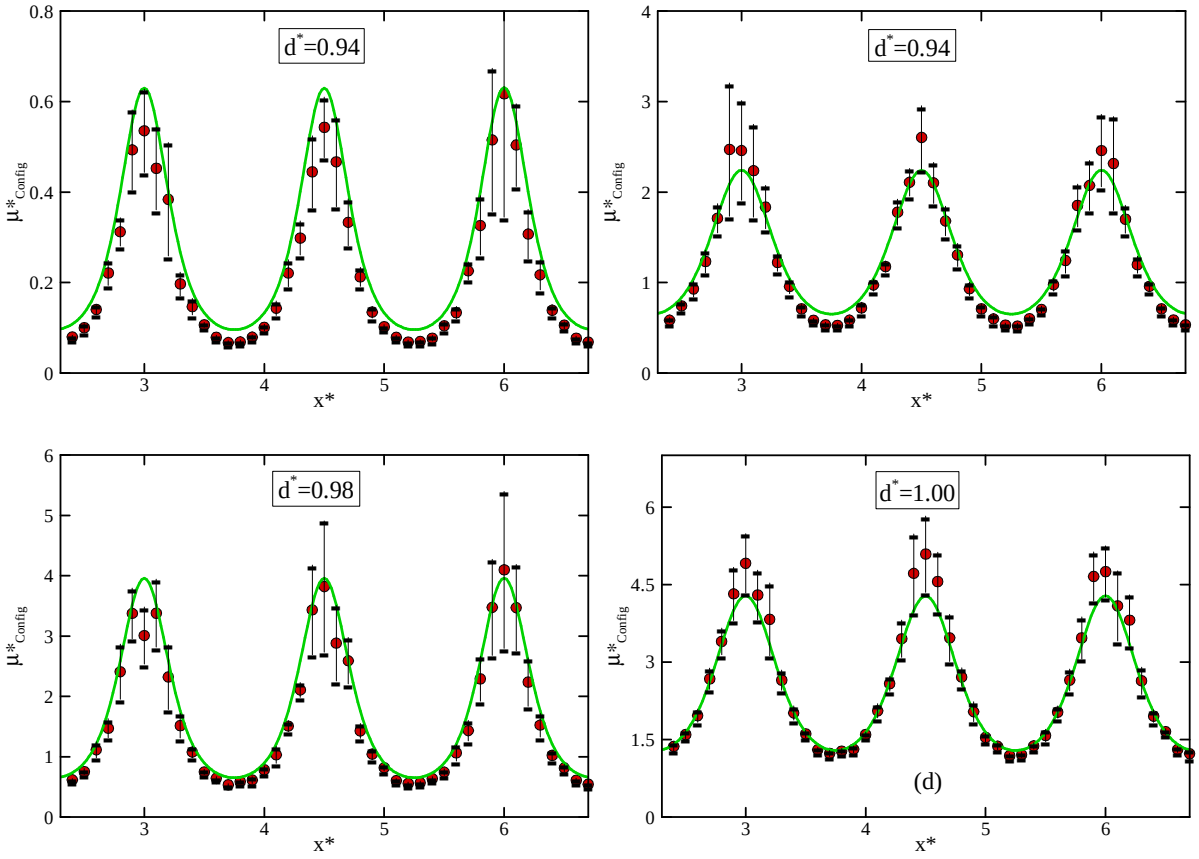

Figure 4.3.5: The contributions induced by the interactions of molecules separated by a distance less than d into the local viscosity for the WCA fluid. Left figure: $\rho^*_{\mathrm{Ini}} = 0.9$ and $T^* = 0.8$. Right figure: $\rho^*_{\mathrm{Ini}} = 0.9$ and $T^* = 2.0$. Symbols: NEMD simulations. Curves: $\rho^{\tau}(x) \int_0^d \eta^c_{WCA}\big(\bar{\rho}(x', x)\big) f_{\eta,WCA}(x') dx'$.

As shown on Figs. 4.3.2(c), 4.3.2(d), 4.3.3(c) and 4.3.3(d), it appears that such a scheme is able to describe very well the NEMD results for the two studied initial states with slowly and strongly varying densities. One should notice that such an approach should be, *a priori*, valid for other repulsive potentials than the WCA one.

C. The LJ fluid

To take into account the attractive contribution of the LJ potential, compared to the WCA potential, we use a perturbation scheme in which the reference chosen is the WCA fluid

[3]. Thus, for a given bulk state, the ratio between the configurational viscosities of the LJ fluid and the WCA fluid can be expressed as a function of the temperature only [25]:

$$\alpha = \frac{\mu_{LJ}^{C}(\rho^*,T^*)}{\mu_{WCA}^{C}(\rho^*,T^*)} = 1 + \frac{\theta}{T^*} \tag{4.3.14}$$

where θ is a constant. To test Eq. (4.3.14), we have performed NEMD simulations of the WCA homogeneous fluid for various thermodynamics conditions. As shown on Fig. 4.3.6(a), the relation (4.3.14) yields very good result in homogeneous fluids if one takes θ = 0.34. To test further this relation in inhomogeneous conditions, we have computed the ratio $\frac{\mu_{LJ}^{C}(x)}{\mu_{WCA}^{C}(x)}$ for the two inhomogeneous states studied in this work, $\rho_{\mathrm{Ini}}^{*} = 0.90$ and $T^* = 0.8$ and $\rho_{\mathrm{Ini}}^{*} = 0.90$ and $T^* = 2$. As shown in Fig. 4.3.6(b), Eq. (4.3.14) seems to hold very well locally even in strongly inhomogeneous fluids. Thus, when Eq. (4.3.14) is combined with Eq. (4.3.13), one obtains for a LJ inhomogeneous fluid:

$$\mu_{LJ}^{C}(x) = \alpha\rho^{\tau}(x) \int \eta_{WCA}^{C}\big(\bar{\rho}(x',x)\big) f_{\eta,WCA}(x')\, dx' \tag{4.3.15}$$

As shown on Figs. 4.3.3(e) and 4.3.3(f), it is then possible to get a very good estimate of the local configurational LJ viscosity profiles of a strongly inhomogeneous fluid using Eq. (4.3.15). It is worth to notice that the use of Eq. (4.3.15) also yields very good prediction for the viscosity profiles for slowly varying densities, see Figs. 4.3.2(e) and 4.3.2(f). The small differences that appear mainly come from the intrinsic limitations of the simple perturbation scheme employed, Eq. (4.3.14).

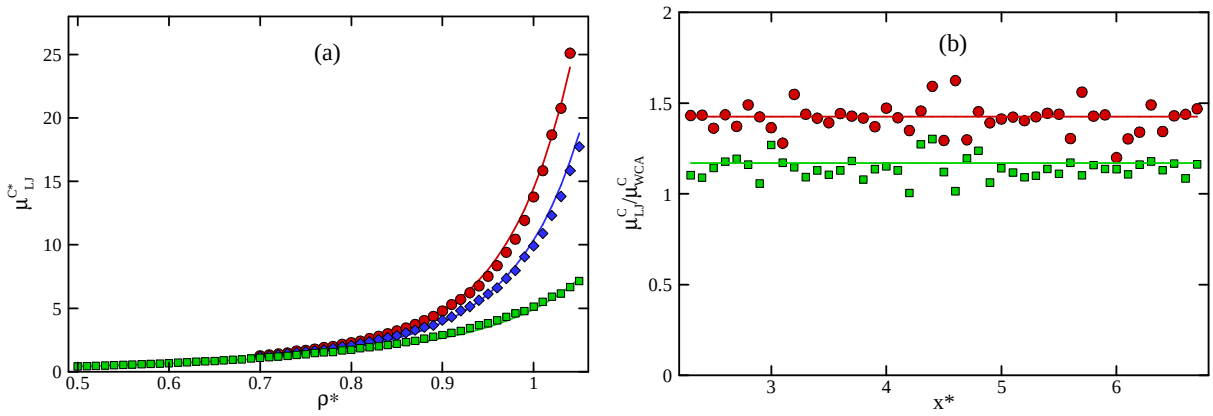

Figure 4.3.6: (a) Configurational viscosity of the LJ homogeneous fluid. Lines: correlation proposed by Galliero et al. [21]. Symbols: NEMD results of the WCA fluids multiplied by α. Circles : $T^* = 0.8$. Diamonds : $T^* = 1$. Squares : $T^* = 2$. (b) $\frac{\mu_{LJ}(x)}{\mu_{WCA}(x)}$ in inhomogeneous fluids for the two studied states (n = 12). Straight lines: Eq. (4.3.14). Symbols: NEMD results. Red circles: $\rho^*_{\mathrm{Ini}} = 0.90$ and $T^* = 0.8$ .Green squares: $\rho^*_{\mathrm{Ini}} = 0.90$ and $T^* = 2$.

4.3.4. Conclusions

In this work, we have studied how to predict quantitatively the local viscosity of a dense inhomogeneous fluid starting from the density profile. To do so, Non Equilibrium Molecular Dynamics simulations have been performed on three types of fluids, the quasi-HS, WCA and LJ fluids, subject to a Sinusoidally Varying external Potential inducing the density inhomogeneities.

It has been found that for a slowly varying density profile the local viscosity obtained from the simulations can be well described by using the Local Average Density Model combined with weight functions developed for the equilibrium thermodynamics of strongly inhomogeneous fluids for all type of fluid, initial density and temperature considered in this work. However, for strongly inhomogeneous fluids (i.e. important density variations over one molecular distance) such schemes cannot provide a good estimation of the viscosity profiles for different types of fluid and different states.

To develop a general scheme able to tackle all systems studied in this work, we have first dealt with the semi-HS fluid. By taking into account the effect of the angle formed between the colliding molecules relatively the direction of the flow on the collisional viscosity, a simple weight function has been proposed which combined with the LADM is able to provide a good prediction of the local viscosity of the semi-HS fluid whatever the states and the inhomogeneities used in this work. Then, by analyzing the distributions of the normalized contribution induced by the interactions of particles separated by a given distance into the shear viscosity, we have developed a scheme that yields the WCA viscosity profiles in good agreement with those obtained from the simulations. It should be noticed that such a scheme for predicting the shear viscosity of the WCA fluid should be valid for other smoothly repulsive potentials. Finally, it is shown that the local viscosity of a strongly inhomogeneous LJ fluid can quantitatively be deduced from the one of the WCA fluid by using a simple perturbation scheme.

References

[1] J. Israelachvili, *Intermolecular and Surface Forces*, Academic Press, Third Edition (2010)

[2] G. Karniadakis, A. Beskok and N. Aluru, *Microflows and Nanoflows*, Springer (2004)

[3] J. Hansen and I. R. McDonald: Theory of simple liquid, Third Edition, Elsevier

[4] E. Akhmatskaya, B. D. Todd, P. J. Daivis, D. J. Evans, K. E. Gubbins and L. A. Pozhar, J. Chem. Phys. **106**, 4684 (1997)

[5] X. D. Din and E. E. Michaelides, Phys. Fluids **9**, 3915 (1997)

[6] L. A. Pozhar, Phys. Rev. E **61**, 1432 (2000)

[7] U. M. B. Marconi and S. Melchionna, J. Phys.: Condens.Matter **22**, 364110 (2010)

[8] S. K. Bhatia, M. R. Bonilla and D. Nicholson, Phys. Chem. Chem. Phys. **13**, 15350 (2011)

[9] I. Bitsanis, T.K Vanderlick, M. Tirell and H.T. Davis, J. Chem. Phys. **87**, 1733 (1987)

[10] J. S. Hansen, P. J. Daivis and B. D. Todd, J. Chem. Phys. **126**, 144706

[11] H. Hoang, G. Galliero, J. Chem. Phys. **136**, 124902 (2012)

[12] H. Hoang, G. Galliero, Phys. Rev. E **86**, 021202 (2012)

[13] P. Tarazona, J. A. Cuesta, and Y. Martinez-Raton, Density Functional Theories of Hard Particle Systems, Lecture Notes in Physics Vol. 753 (Springer-Verlag, Berlin/Heidelberg, 2008).

[14] D. M. Heyes and A. C. Branka, J. Chem. Phys. **122**, 234504 (2005)

[15] K. M. Dyer, B. M. Pettitt and G. Stell, J. Chem. Phys. **126**, 034502 (2007)

[16] F. Muller-Plathe, Phys. Rev. E **59**, 4894 (1999)

[17] B. D. Todd and J. S. Hansen, Phys. Rev. E **78**, 051202

[18] D. M. Heyes, E. R. Smith, D. Dini, and T. A. Zaki, J. Chem. Phys. **135**, 024512 (2011)

[19] Z. Guo, T. S. Zhao and Y. Shi, Phys. Rev. E. **71**, 035301 (2005)

[20] Z. Guo, T. S. Zhao and Y. Shi, Phys. Fluids **18**, 067107 (2006)

[21] T. K. Vanderlick, L. E. Scriven and H. T. Davis, J. Chem. Phys. **90**(4), 2422 (1988)

[22] H. Sigurgeirsson and D. M. Heyes, Mol. Phys. **101**, 469 (2003)

[23] G. Galliero, C. Boned and A. Baylaucq, Ind. Eng. Chem. Res. **44**, 6963 (2005)

[24] J. Fischer and M. Methfessel, Phys. Rev. A **22**, 2836 (1980)

[25] F. D. C. Silva, L. A. F. Coelho, F. W. Tavares and M. J. E. Cardoso, J. Quant. Chem. **95**, 79 (2003)

Chapter 5

Shear Behavior of a Confined Thin Film: Influence of the Molecular Dynamics Scheme Employed*

* This chapter has been published in J. Chem. Phys. 138, 054707 (2013)

DOI: 10.1063/1.4789582

Abstract:

In this work, we have considered and compared two molecular dynamics schemes widely used when studying a thin fluid film confined between solid surfaces and undergoing boundary shear. In the first approach, the non-equilibrium simulations are performed on a confined fluid explicitly connected to bulk reservoirs. In the second one, non-equilibrium simulations are carried out on the confined fluid only, in which the average density is deduced from a prior simulation in the grand canonical ensemble. We have found that the apparent properties (average density and effective viscosity) of a strongly confined Lennard-Jones liquid are significantly different using one scheme or the other when the solid surfaces induce a strong structure in the whole fluid, i.e. for small separations between the solid surfaces. Furthermore, the shear velocity dependence of the friction force has been found to be as well very sensitive to the approach chosen and can be well understood in terms of the fluid structure which can even lead to a visco-plastic behavior of the fluid in some cases. Finally, it is shown that the first scheme is the only one usable to explore the history-dependence of the friction force as observed in experiments.

5.1. Introduction

Solid surfaces separated by a thin fluid film and sliding from each other play an important role in a variety of contexts both from the fundamental and the industrial point of views: friction, lubrication, wear, etc.[1-4]. Many studies demonstrated that the thin fluid film is the main origin of unusual experimental behaviors in such systems, for examples the stick-slip slide and the static friction [3-5]. So, the mechanical and rheological properties of the thin fluid film undergoing the shear have gained increasing attention recently. In fact, due to adsorption and molecular packing, the fluid molecules have a general tendency to organize themselves into layered structures parallel to the solid surfaces. Such local structure in the thin fluid film yields apparent physical properties that are often different from those of the bulk [6]. Experimental, theoretical and simulation works have shown that the properties in such systems depend on the nature of the fluid, the fluid-solid interaction, the operational conditions (e.g. sliding velocity and temperature), and the separation (e.g. distance between the solid surfaces or the load) [3-4].

In such highly confined systems where the typical length is the nanometer or even less, some dedicated apparatus have been developed to analyze experimentally their physical properties [1]. However, they cannot provide directly all the properties of the thin fluid film. To complement the experiments in such extreme conditions and to better understand the various phenomena occurring in very thin film, molecular simulations [7] have shown to be a valuable tool on idealized systems [2-6]. More precisely using molecular simulations, the dependence of the properties of a simple thin fluid film confined between two walls undergoing boundary shears has extensively been explored during the last two decades [2-4]. It has been found that the effective viscosity increases with the width decreasing and are always higher than that in the bulk [8], consistently with experiments [1]. In addition, it has been noticed that an increase in the strength of the fluid-solid interaction tends to decrease the

slipping length of the fluid [9-10]. In particular, Glosli et al. [11] observed from molecular simulations that the energy dissipation occurs by a discontinuous or continuous mechanism depending on the fluid-solid interaction strength. The effect of the sliding velocity of the walls confining the film has also been explored by using molecular simulations. It has been found that the dependence of the friction force on the velocity follows a simple thermal activation model, i.e. the friction coefficient in the Amontons law is a function of the velocity [3-4, 11-13].

A very important point concerning all these simulations is related to the choice of the technique employed as there exit a lot of different molecular simulations types. The Monte-Carlo (MC) simulation in the grand canonical (GC) ensemble has shown to be the most suitable simulation type to provide the equilibrium properties of thin fluid films [2]. However, in the cases of sheared thin fluid films one needs to employ Molecular Dynamics (MD) simulations, more precisely Non-Equilibrium MD (NEMD) simulations, instead of Monte-Carlo ones [14]. The implementation of the MD simulation in the GC ensemble is usually not easy and requires much CPU time than GC-MC. There exist nevertheless a non negligible number of algorithms proposed in literature [15-19] to deal with equilibrium and Non-Equilibrium MD simulations in a GC-like ensemble (i.e. a part of the simulation box, the reservoir, is maintained at a given state), that we will name GCMD in the following.

However, to study the properties of the thin fluid film undergoing boundary shear most of the MD simulations have been performed in the following way: first, averaged properties (often density) of the thin fluid film at equilibrium state are estimated from the MC or MD simulations in the GC ensemble and then these averaged properties are used as an input (initial configuration) to NEMD simulations in the NXT ensemble, where X=V if the volume is kept constant and X=P if the pressure is kept constant, so-called the GC-NXT scheme [2-3, 8, 20-24]. This two steps procedure implicitly implies, among others, that the

number of the molecules of the thin fluid film is assumed to be the same in and out of equilibrium, which is a strong assumption in some cases. However, it is clear that the implementation of the MD simulations using a GC-NXT scheme is simpler and requires less CPU time than that of GCMD approaches. Furthermore, in some cases, results provided from such GC-NXT schemes can be consistent with those obtained from experiments [3, 8]. It is thus interesting to better quantify what the limitations of the GC-NXT scheme are as long as most of the studies have been performed using such an approach [3, 8, 20-24].

Thus, in this paper we have performed MD simulations using the two approaches, GCMD and GC-NVT, on a very thin fluid film composed of Lennard-Jones spheres and undergoing boundary shear. Then, we have compared the results of the simulations together. By doing so we will show that the choice of the approach, GCMD or GC-NVT, may have an explainable big impact on the estimated properties of a very thin simple fluid undergoing a boundary shear.

This article is organized as follows. In Sect. 5.2 some details on the MD simulations are described. Then, results obtained from the two schemes are presented, compared and analyzed in Sect. 5.3. Finally, we summarize some highlighting results in Sect. 5.4.

5.2. Molecular Dynamics Simulations

5.2.1. Particle Modeling

For simplicity all solid and fluid molecules have been modeled as spherical ones. All interactions are described by a classical truncated Lennard-Jones (LJ) 12-6 potential between pairs of particle:

$$U_{LJ}(r) = \begin{cases} 4\epsilon\left[\left(\frac{\sigma}{r}\right)^{12} - \left(\frac{\sigma}{r}\right)^{6}\right] & \text{if } r \le r_c \\ 0 & \text{if } r > r_c \end{cases} \tag{5.1}$$

where r is the distance between the two particles, ε is the potential depth, σ is the particle diameter, and r_c is the cut-off diameter (=3.5σ in this work). The potential depth and the diameter of the solid-fluid interaction are defined in term of the fluid-fluid interactions respectively as follows:

$$\sigma_{\mathrm{f-s}} = \sigma_{\mathrm{f-f}} = \sigma \text{ and } \varepsilon_{\mathrm{f-s}} = 2\varepsilon_{\mathrm{f-f}} = 2\varepsilon \tag{5.2}$$

Such parameters correspond to a rather adsorbent wall type.

In the following, we express the variables in dimensionless units by using the LJ reduced units. The reduced time t^*, temperature T^*, density ρ^*, stress P^* and viscosity μ^* are thus defined as [7]:

$$t^* = \frac{t}{\sigma\sqrt{m/\varepsilon}},\ T^* = \frac{k_B T}{\varepsilon},\ \rho^* = \frac{N_T \sigma^3}{V},\ P^* = \frac{P\sigma^3}{\varepsilon},\ \mu^* = \mu\frac{\sigma^2}{\sqrt{m\varepsilon}} \tag{5.3}$$

where t is the time, m the mass of the fluid particle, k_B is the Boltzmann constant and N_T the total number of atoms contained in the volume V.

5.2.2. Simulation Schemes

In this paper, we have employed the constant density Grand Canonical like Molecular Dynamics method proposed by Hoang and Galliero [15] to carry out all the molecular simulations in the GC ensemble. It consists in simulating explicitly the confined systems in contact with reservoirs maintained at the desired density and temperature (which is equivalent to maintain a constant chemical potential for a pure fluid). Figure 5.1 shows a sketch of the simulation box that contains both fluid and solid particles. Periodic boundary conditions (PBC) have been applied on all three directions. The solid molecules are arranged in a faced centered cubic (FCC) to form two solid walls. In the x direction, the solid walls are separated by a distance (W^*) that defines the width of the gap confining the fluid. The solid walls are of finite size in the x and y directions, whereas, they are extended through the whole cell in the z direction.

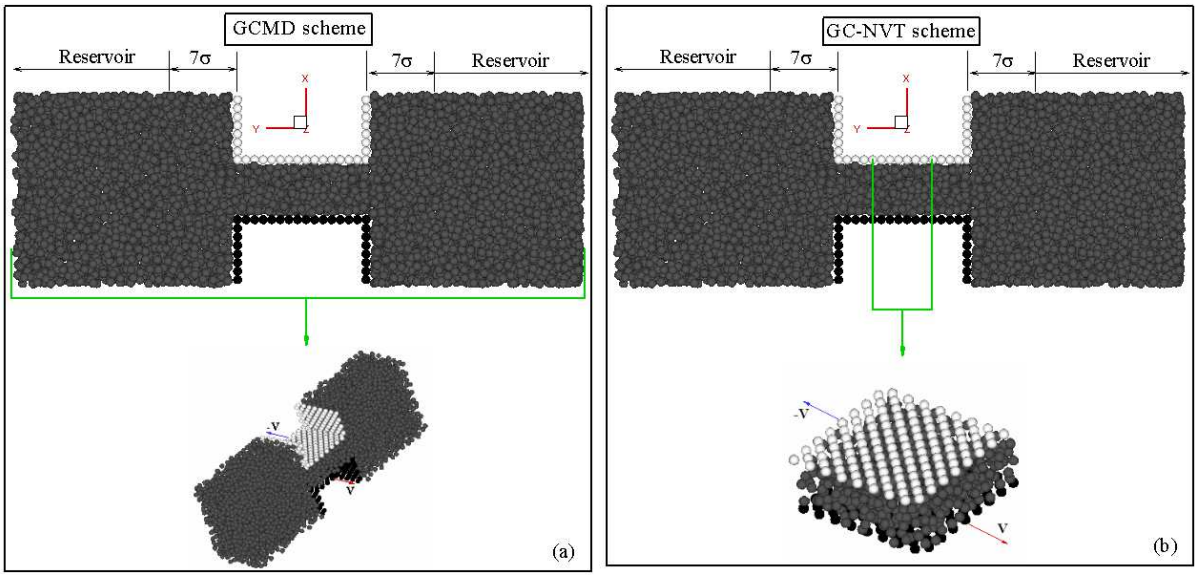

Figure 5.1: Sketch of the GCMD and GC-NVT schemes: Above figures correspond to the simulation system used to equilibrate the confined system. Bottom figures correspond to the NEMD simulations.

To maintain the density of the fluid in the reservoir at the desired value, the *y* coordinates of the molecules in the reservoir region and the *y* size of this region are scaled at each time step by the quantity [15]:

$$\lambda_\rho = 1 - \frac{\Delta t}{\tau_\rho}\left(\frac{\rho_0}{\rho_{res}} - 1\right) \tag{5.4}$$

where, ρ_{res} is the instantaneous density in reservoir regions, ρ_0 is the target density, Δt is the time step and τ_ρ is the density time constant. To control the temperature, we have employed the partial Berendsen thermostat, i.e. the temperatures of fluid in and out of the confined space are independently maintained at the same desired value [25-26]. According to this method, at each time step the velocities are scaled by a quantity:

$$\lambda_T = 1 + \frac{\Delta t}{2\tau_T}\left(\frac{T_0}{T} - 1\right) \tag{5.5}$$

where, τ_T is the temperature time constant, T_0 is the target temperature and T is the instantaneous temperature.

As mentioned in the introduction, the NEMD simulations on the properties of the confined fluid undergoing the boundary shear can be performed by using GC-NVT or GCMD schemes. For both approaches first the system is equilibrated at a given temperature and density in the reservoirs, see Fig. 5.1, then:

- For the GCMD approach, the two horizontal walls are moved at the desired velocity to induce the shear in the confined fluid while maintaining the reservoirs at the desired temperature and density, see Fig. 5.1(a).
- For the GC-NVT approach, the averaged density in the central part of the pore is evaluated and is used as an input to construct a new simulation box (with periodic boundary conditions on *y* and *z* directions) composed of the confined fluid and the two horizontal walls only without the reservoirs, see Fig. 5.1(b). Then, this new confined system is sheared by moving the two walls in opposite directions.

5.2.3. Numerical Details

We have used an in-house code to perform the MD simulations [15, 24]. The motion equations of the fluid particles are solved by employing the Verlet velocity algorithm [7] with a time step Δt^*=0.002, whereas the solid particles are fixed at their sites on a CFC lattice with a size of the lattice $a = 1.6\sigma$. In all simulations the state of the fluid in the reservoir is maintained at $\rho^* = 0.7$ and $T^* = 1$, which correspond to a liquid state in bulk conditions for the cutoff employed in this work [27]. Periodic boundary conditions and neighbor list have been applied [7].

The confined fluid in contact with the reservoir is equilibrated during 2×10^6 time steps followed by a simulation period of 2×10^6 time steps during which the sampling is carried out to determine the equilibrium properties. Once the system has been equilibrated, the NEMD simulations are carried out during 4×10^6 time steps, discarding the first 2×10^6

time steps to reach the steady state and sample data. To reduce the statistical uncertainties, the results provided in the following correspond to an average over 6 different independent runs, exceptions noted, and the error bars represents the standard deviation.

5.3. Results and Discussions

5.3.1. Width Dependence of Density and Apparent Viscosity.

In this section, we present some properties, density and effective/apparent viscosity of a confined fluid at the steady state obtained from the two schemes described above, i.e. GCMD and GC-NVT schemes. The density is an averaged quantity over the full pore width (i.e. over W^*). Shear stress has been estimated using the intermolecular forces between the confined fluid and the solid molecules [24]:

$$\tau_{xz} = \frac{1}{A}\sum_{i=1}^{N_F}\sum_{j=1}^{N_S} -\frac{\partial U_{LJ}(r_{ij})}{\partial r_{ij}}\frac{z_{ij}}{r_{ij}} \tag{5.6}$$

where N_F and N_S are the numbers of fluid and solid particles respectively, A is the area of the y-z plane of the solid surface and z_{ij} is the z component of $\mathbf{r}_{ij}$. Such a formulation yields results which are the same than those obtained using the Irving-Kirkwood formula averaged over the space considered [24]. Then, from the knowledge of the shear stress, the effective/apparent viscosity of a confined fluid can be defined as:

$$\mu^*_{\mathrm{Eff}} = \frac{\tau^*_{xz}}{\dot{\gamma}^*} = \frac{\tau^*_{xz}}{2V^*_{\mathrm{W}}/_{W^*}} \tag{5.7}$$

where $\dot{\gamma}^*$ is the shear rate, V^*_{W} is the velocity of the solid wall and W^* is distance between the two walls.

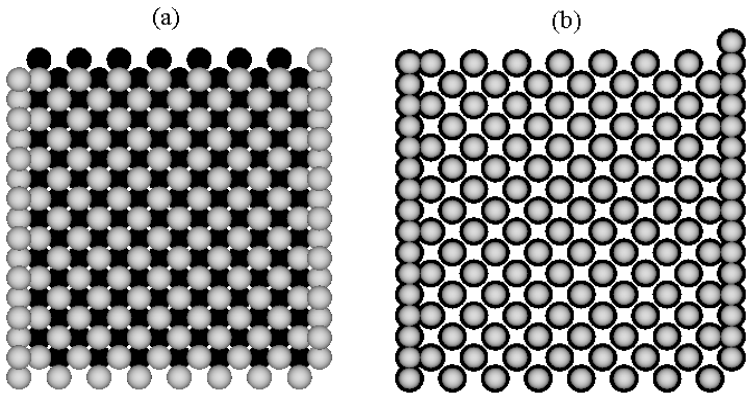

Figure 2: Relative structural order between the solid surfaces. (a) Out-of-registry. (b) In-registry.

Density

When the two walls are moved at a constant velocity, the two solid surfaces alternate (continuously) between an out-registry configuration, see Fig. 5.2(a), and an in-registry configuration, see Fig. 5.2(b). So, we have first computed the equilibrium density for different pore widths, ranging from W^*=1.9 and W^*=10, for the two types of configurations. Averaged densities are shown in Fig. 5.3.

As expected, results shown in Fig. 5.3 indicate that the average density appreciably varies (between 0.38 and 0.82 in reduced unit) with the width for $W^* < 7$, and is nearly constant for larger widths. This reflects the strong inhomogeneity of the confined fluid due to physical adsorption and molecular packing [2, 6]. Furthermore, as well known [2], both configurations (out of registry and in-registry) exhibit important differences in terms of density dependence on the pore width, when $W^* < 6$, see Fig. 5.3, because of the differences in structural order they induce in the confined fluid. The out of registry configuration undergoes first-order transitions at $W^* \approx 2.1$ and 3.8 and second-order ones at $W^* \approx 3.3$ and 5.1, while the in registry configuration undergoes first-order transitions at $W^* \approx 2.9$ and 4.8 and second-order ones at $W^* \approx 2.5$ and 4.2, see Fig. 5.3. It should be noted that,

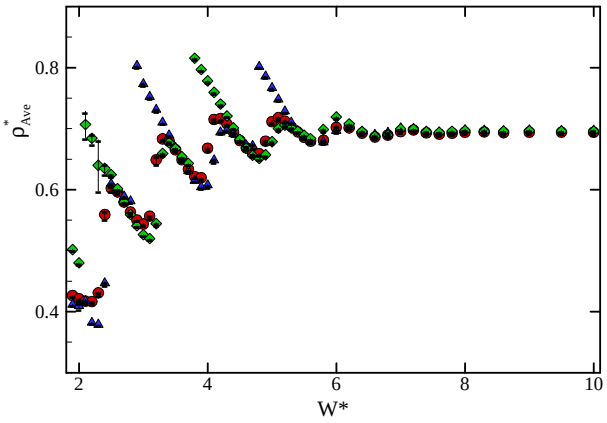

Figure 5.3: Variation in the average density with the width. Diamonds and deltas correspond to the densities obtained at equilibrium out-of-registry and in-registry configurations, respectively. Circles are the densities from the GCMD simulation at the steady non-equilibrium state.

for a width just above the first order transition, the fluid behaves more like a solid phase than a fluid one [2]; we will come on that point later.

These different density behaviors at equilibrium can be simply understood in terms of the fluid structure in the confined space, see Fig. 5.4. The molecules in the first adsorbed layer (boundary layer) of the confined fluid will preferably form a commensurate layer being out-of-registry with the solid surface. Then, this fluid layer induces other one that is also out-of-registry with it and so on. For example, in the in-registry configuration of the solid walls, the formation of a third layer is facilitated by constructive interference of the two boundary layers, whereas it is not the case for the formation of fourth layer, and so on [2]. Thus, the confined fluid in the in-registry configuration undergoes a first-order transition for the widths which corresponds to a change of the number of layers from even to odd and a second-order one for the situations from odd to even, whereas it is the opposite in the out-of-registry. These different transitions are clearly exhibited by the evolution of the density profiles in the pore versus width for both solid surface configurations as shown in Figs. 5.4(a) and 5.4(b). More

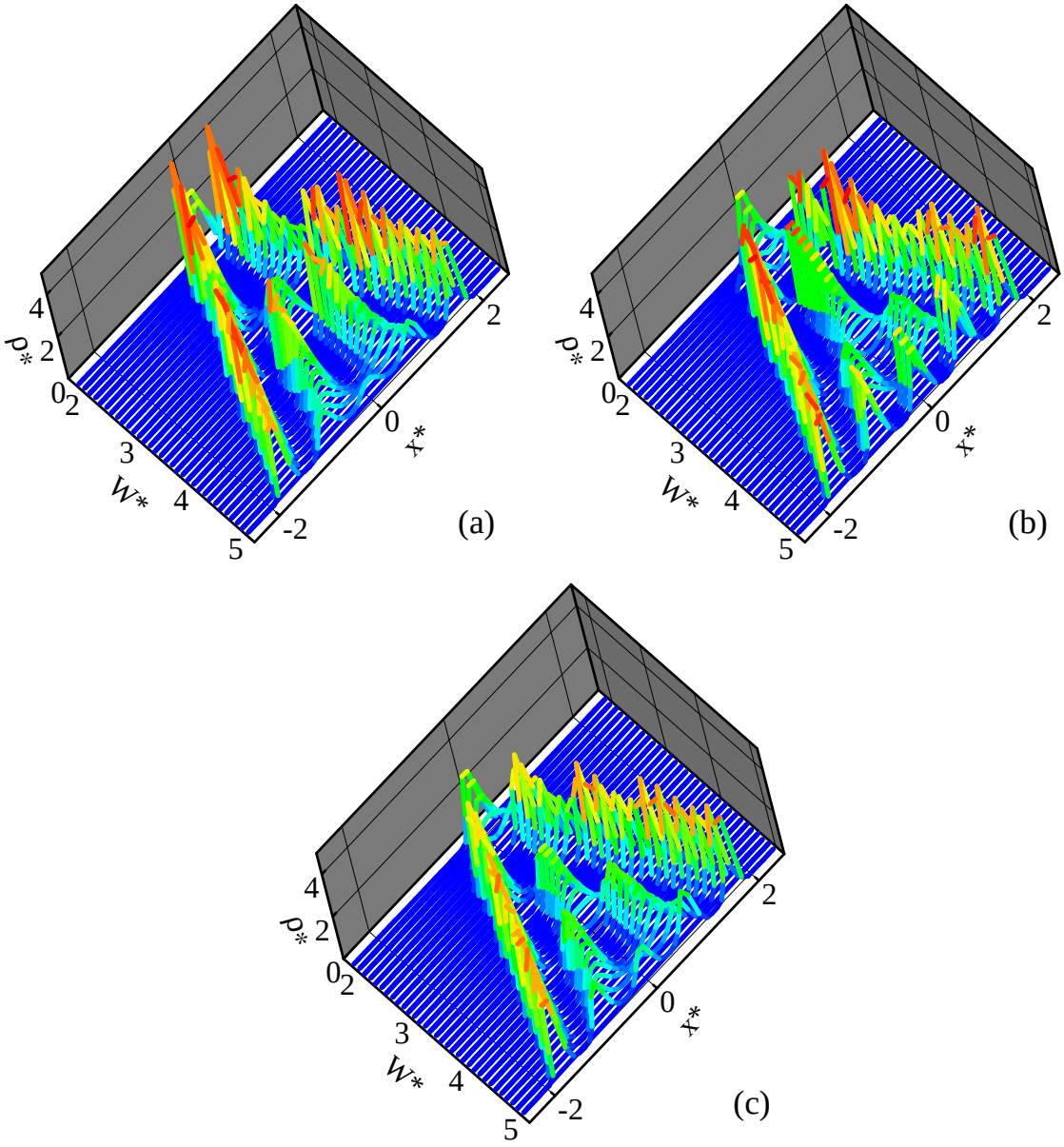

Figure 5.4: Density profiles for different pore widths. (a) The out-of-registry configuration at the equilibrium state. (b) The in-registry configuration at the equilibrium state. (c) GCMD simulations at the steady non-equilibrium state.

precisely, a first order transition corresponds to a sudden appearance of one new central layer (of large amplitude) when increasing the width while a second order correspond to a continuous appearance of a new central layer (of smaller amplitude).

To investigate how the boundary shear influences the density of the confined fluid, it is important to verify that the shearing velocity is sufficiently small such that the assumption that the state of the system is completely re-equilibrated at each time is satisfied. In other words, the "non-equilibrium" average density computed during GCMD has to be independent of the velocity of the walls. It should be noted that the out of registry initial condition has been chosen to initialize non-equilibrium GCMD.

Several wall velocities have been tested, see next section, but it has been found that for a wall velocity corresponding to an effective shear rate $\dot{\gamma}^* = {2V_w^*}/{W^*} = 0.01$ the average density obtained was found to be the same as for $\dot{\gamma}^* = 0.0025$, except for some widths corresponding to first-order transition where a relative difference smaller than 3% was noticed. Thus, the non-equilibrium results presented in this section (both for GCMD and GC-NVT) correspond to $\dot{\gamma}^* = 0.01$. It should be noted that such a shear rate is one order of magnitude lower than the shear rate associated to the shear thinning threshold of a bulk LJ liquid [28-29].

As shown in Fig. 5.3, the average density during GCMD simulations, ρ^*_{GCMD}, lies always between the equilibrium densities of the out-of-registry and in-registry configurations. This can be understood because, during GCMD simulations, the density is limited by the relative structural ordering induced by the in-registry and out of registry configurations. In addition, it is interesting to note that the GCMD results in Fig. 5.3 indicate that the confined fluid does not undergo any first-order transition and only second-order transitions occur at $W^* \approx 2.5, 3.3, 4.1$ and 5.1. This behavior is seen from the nearly continuous evolution of the density profiles (appearance of new central layer when increasing width see above) in the pore versus width during GCMD simulations, Fig. 5.4(c), compared to the equilibrium ones, Figs. 5.4(a) and 5.4(b).

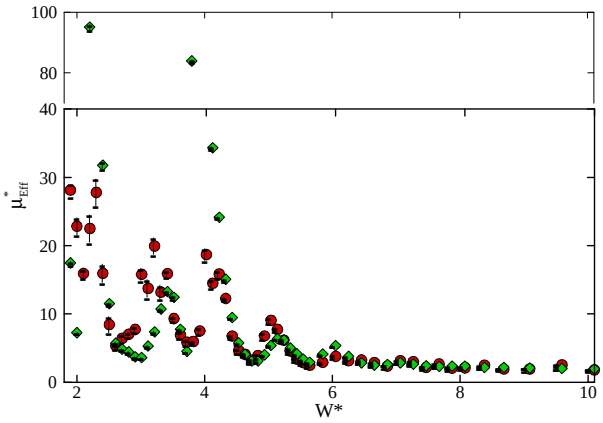

Figure 5.5: Variation in the effective viscosity with the width. Diamonds and circles correspond to the effective viscosities obtained by GC-NVT and GCMD schemes, respectively.

Shear Viscosity

For the same systems than for density, the apparent shear viscosity has been computed using both GCMD and GC-NVT approaches using $\dot{\gamma}^* = 0.01$. Both approaches have been employed using an equilibration step made using an out-of-registry configuration of the solid walls.

As clearly shown in Fig. 5.5, the two schemes provide the same values for the apparent shear viscosity only when the width is sufficiently large when $W^* > 6$ similarly to what found for density. Furthermore, as well known [1], shear viscosity in such confined situation can be a lot larger than in bulk. More precisely, for the shear rate used, the apparent viscosity reaches a value 25 times larger than the bulk one ($\mu^*_{Bulk} = 1.23$ [30]) using the GCMD approach and is found to be nearly two orders of magnitude larger than the bulk value using the GC-NVT scheme. In addition, shear viscosities can be noticeably different using GCMD and GC-NVT schemes when the width between the two surfaces decreases. In fact, it appears from Figs. 5.3 and 5.5 that the shear viscosities so obtained follow more or less the evolution of the average density. This is not so surprising as long as in dense fluids the shear

viscosity is positively correlated with density [8, 30] and tends to diverge when a solid like phase appears. In fact, it appears clearly from Fig. 5.5 that the first- and second-order transitions found during equilibrium simulations are noticeable on the viscosity as well. There exist a "jump" in the viscosity at $W^* \approx 2.1$ and 3.8, and a continuous increase at $W^* \approx 3.3$ and 5.1 when employing GC-NVT approach while there is only a continuous increase at $W^* \approx 2.1, 3.2, 4$ and 5 when the GCMD scheme is used.

Thus, it appears clearly that both density and apparent viscosity computed using the two different approaches do not always lead to the same results when the systems are very confined (i.e. a thin fluid of a few molecular diameters). These differences are particularly large when corresponding to a situation where a strong structural order is induced in the confined fluid by the relative configuration of the solid walls.

5.3.2. Sliding Velocity Dependence of the Average Friction Force

As exhibited by various study [3, 11-13], the average friction force, i.e. the shear stress, is strongly dependent on the wall velocities, i.e. the shear rate. So, the average friction force has been computed for different wall velocity using both GCMD and GC-NVT schemes starting from an equilibrium situation corresponding to an out-of registry configuration of the walls. In addition, different widths $W^* = 3.3,\ 3.9$ and 4.5 have been explored. These values have been chosen to correspond to different situations from the structural order point of view, see Figs. 5.4 and 5.6. $W^* = 3.3$ and 3.9 correspond to second-order and just above first-order transitions at the equilibrium state (out of registry), respectively. $W^* = 4.5$ corresponds to a state for which equilibrium densities for both out-of-registry and in-registry configurations of the solid surfaces are similar, see Fig. 5.6. Such situations also correspond to equilibrium average densities (out of registry) at $W^* = 3.3$ and 3.9 being smaller and larger than the non-

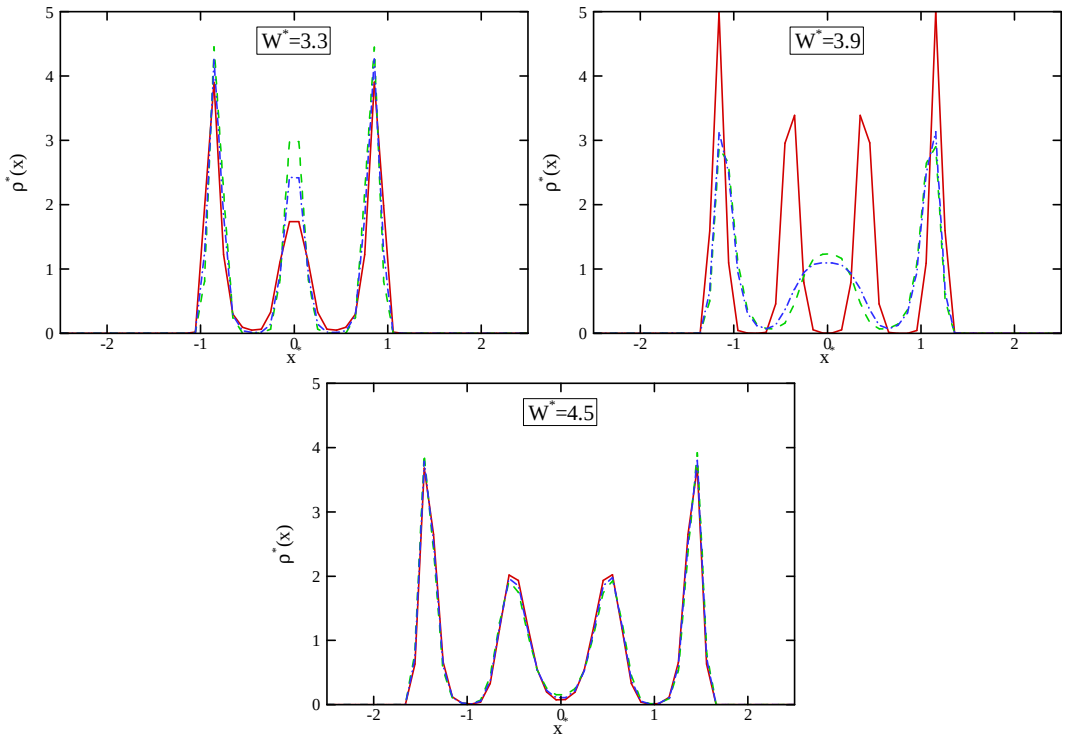

Figure 5.6: Density profiles for various pore widths (W*=3.3, 3.9 and 4.5). Solid curves (red color) correspond to the out-of-registry configuration at equilibrium, dashed curves (green color) to the in-registry configuration at equilibrium and dashed-dotted curves (Blue color) correspond to the GCMD results.

equilibrium GCMD densities at low shearing velocity respectively, and similar densities at $W^* = 4.5$, see Fig. 5.3.

Figure 5.7 shows the variation in the average friction force with the wall velocity for different widths. It is clear from this figure that the two schemes may lead to different behaviors of the dependence of the average friction force on the wall velocity. In particular, results provided by the GC-NVT scheme indicate that the average friction force increases monotonously when the wall velocity increases for all cases considered here, whereas the average friction force obtained from the GCMD scheme can initially decreases (and then increases when $\dot{\gamma}^* > 0.02$) when the wall velocity increases in the $W^* = 3.9$ case. Furthermore, the amplitude of the average friction force can be completely different using one

scheme or another as shown when $W^* = 3.9$. As in the previous section, these differences can be rather well understood as we will show in the following.

Usually, to relate the average friction force with the wall velocity in the configuration simulated in this work, a simple thermal activation model is employed [3, 11-13, 31]. In previous studies, it was shown that the variation in the average friction force with the wall velocity given by NEMD simulations is well described by such model [11-13], i.e. the dependence of the average friction force on the velocity follows an equation defined as:

$$\langle v_z \rangle = A\left(e^{\left(\frac{B\langle \tau_{zx} \rangle}{k_B T}\right)} - e^{-\left(\frac{B\langle \tau_{zx} \rangle}{k_B T}\right)}\right) \tag{5.8}$$

where, $\langle v_z \rangle$ is the average velocity, A and B are parameters that characterize the state of the confined system. It is important to notice that it is assumed that these parameters are independent on the velocity in such studies [11, 13]. For the system we study, we have $\langle v_z \rangle \sim V_{\text{Wall}}$, so:

$$V_{\text{Wall}} = A\left(e^{\left(\frac{B\langle \tau_{zx} \rangle}{k_B T}\right)} - e^{-\left(\frac{B\langle \tau_{zx} \rangle}{k_B T}\right)}\right) \tag{5.9}$$

Results shown in Fig. 5.7 indicate that the average friction force computed during GC-NVT simulations are well described using Eq. (5.9) (with A and B taken constant) for $W^* = 3.3$ and 4.5, whereas it is not the case for $W^* = 3.9$. Concerning GCMD simulations, such a modeling holds very well for $W^* = 4.5$ but is inadequate for $W^* = 3.3$ and 3.9.

When $W^* = 4.5$, it should be recalled that such a wall gap corresponds to a state in which in-registry, out-of-registry and non equilibrium GCMD densities are similar, see Figs. 5.3 and 5.6. Thus, when the fluid structure is not too largely affected by the walls configuration, this result confirms that Eq. (5.9), with A and B taken constant, gives good results compared to NEMD simulations for all shear rate explored.

It should be noticed however that when the shearing velocity increases the GCMD scheme leads to a slightly reduced friction force compared to the GC-NVT scheme. This is

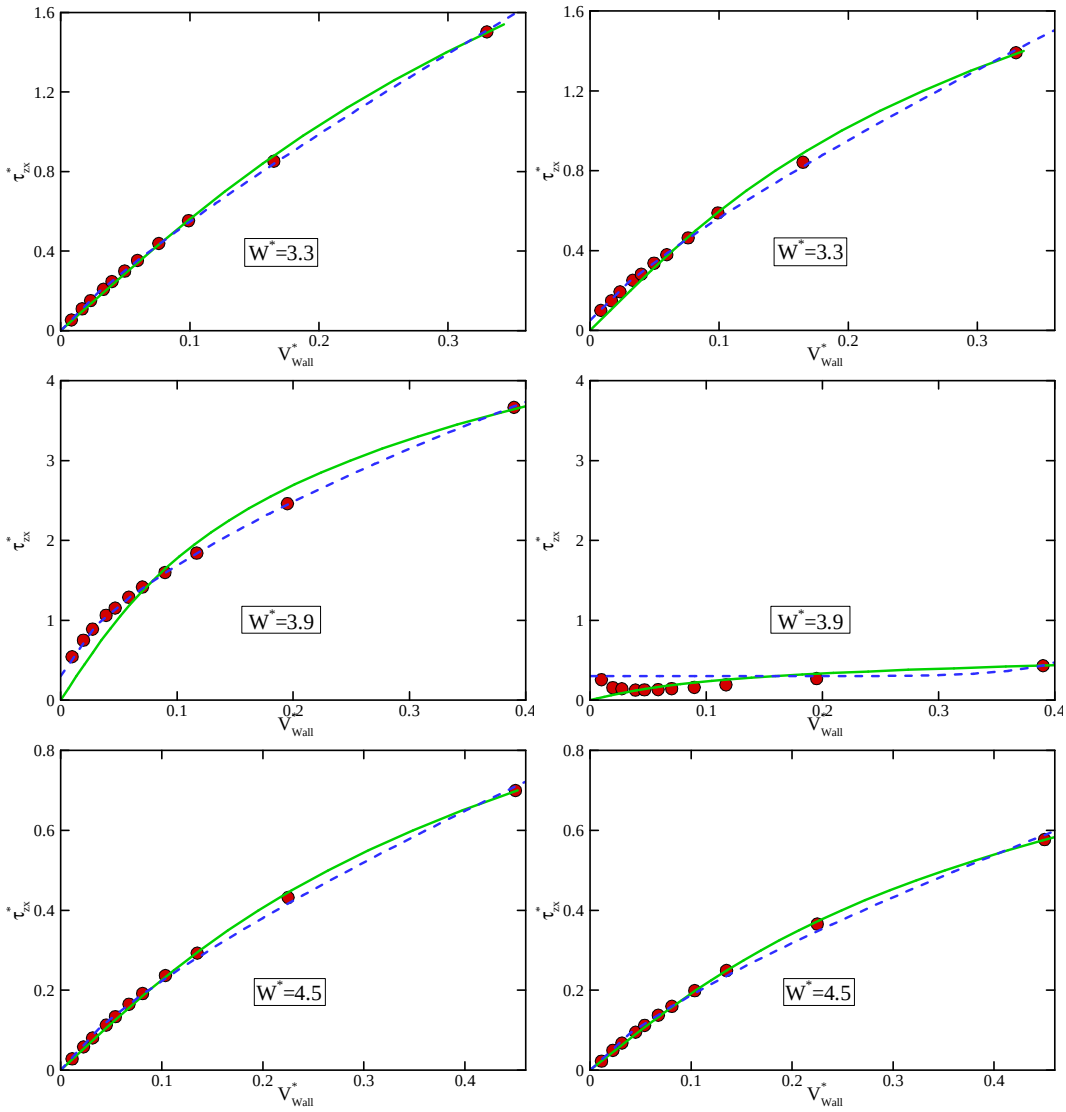

Figure 5.7: Variation in the average friction force with the sliding velocity. Left figures: GC-NVT scheme. Right figures: GCMD scheme. Symbols correspond to the results obtained from the molecular simulations. Solid curves (Green color) are obtained using Eq. (5.9), and dashed curves (Blue color) are obtained using Eq. (5.10).

probably related to the slight decrease of the average density with the shearing velocity in the GCMD case, as shown in Fig. 5.8. In fact, the average density of the confined fluid during GCMD simulations generally decreases with the shear velocity increase. This is mainly due to the fact that the pressure of a fluid usually increases when the shearing velocity increases [32], which induces a squeezing out of the confined fluid from the pore space.

For $W^* = 3.9$, a width just above a first order transition (out of registry), the behavior using the GC-NVT scheme resembles to an activated process but with a non null yield stress, as τ_{zx} is not vanishing when V_{Wall} tends to zero, see Fig. 5.7. This means that the confined fluid behaves as a visco-plastic fluid [33] that cannot be modeled simply by using Eq. (5.9). To model a visco-plastic fluid, the Herschel-Bulkley equation is widely used as [33]:

$$\tau_{zx} = \tau_0 + k\dot{\gamma}^n \tag{5.10}$$

where τ_0 is the yield stress, k and n are model parameters. As shown in Fig. 5.7, it is clear that Eq. (5.10) (with k and n taken constant, and $n < 1$ indicating a shear thinning behavior) describes better the shearing velocity dependence of the friction force than Eq. (5.9) for this situation.

The results obtained using the GCMD approach for $W^* = 3.9$, see Fig. 5.7 are even more surprising. As for GC-NVT simulations there is a non null yield stress. However, when the shear rate increases there is a noticeable decreases of the shear stress followed by a more classical activation type behavior when $\dot{\gamma}^* > 0.025$. Furthermore, the friction force at high shear rate is nearly one order of magnitude smaller than during the GC-NVT simulations. Hence, such a complex behavior cannot be described by Eq. (5.9) or Eq. (5.10), but can be understood qualitatively. The decrease of the shear stress with the wall velocity increase at low shear rates in GCMD simulations is induced by the fact that the central layers of the confined fluid reorganize themselves when the shear is applied (and the density profile becomes similar to that of the in-registry configuration, see Fig. 5.6, with a big decrease in the average density, see Fig. 5.8), whereas it is not the case when employing the GC-NVT simulations, see Fig. 5.9. This explains these two different behaviors in the GCMD and GC-NVT schemes at low shear velocities. At higher shear rates, the fluid changes insignificantly with the shear increase (apart from a small decreases in the average density, see Fig. 5.8)

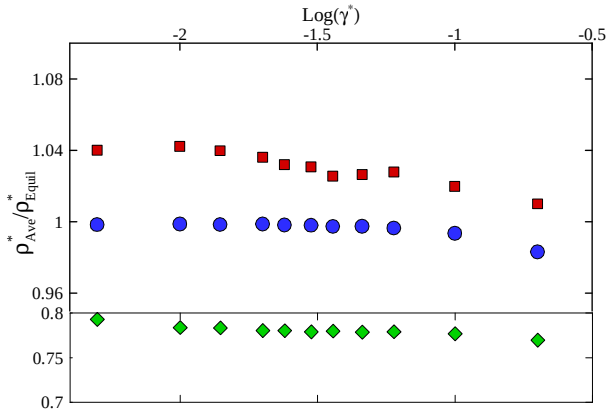

Figure 5.8: Variation in $\rho^*_{\mathrm{Ave}}/\rho^*_{\mathrm{Equi}}$ with the shear rate during GCMD simulations. Squares (Red color) correspond to $W^* = 3.3$, diamonds (Green color) to $W^* = 3.9$ and circles (Blue color) to $W^* = 4.5$.

while keeping a density profile very similar to the equilibrium in registry configuration one and so behave as a simple fluid-like system well described by a thermally activated model.

In the case of $W^* = 3.3$, the shear velocity dependence of the average friction force obtained by the GC-NVT scheme is well described by the simple thermal activation model, see Fig. 5.7. This is simply due to a central fluid layer at the initial out of registry configuration of the solid surfaces which is not strongly structured (corresponding to a second order transition, cf. Sect. 5.3.1.). In addition, the density is kept constant during the GC-NVT simulations and so the central fluid layer remains not too strongly structured while being sheared. It should be noted that in this situation, the use of the Herschel-Bulkley equation also yields a good description for the shearing velocity dependence of the friction force using a zero yield stress, see Fig. 5.7.

When employing the GCMD scheme in the case of $W^* = 3.3$, there is one main difference with the GC-NVT results, see Fig. 5.7, which is the appearance of a small yield stress (a weak visco-plastic behavior). This is due to the fact that this width is not so far from the first order transition (at $W^* = 2.9$) for an in registry configuration. Therefore during

GCMD simulations the confined fluid gain matter from the reservoirs which leads to a slight increase the average density compared to equilibrium value for low shear, see Figs. 5.6 and 5.8. Thus, in this case the variation in the friction force with the shearing velocity is better modeled by the Herschel-Bulkley equation, Eq. (5.10) than by a simple activation model Eq. (5.9), see Fig. 5.7.

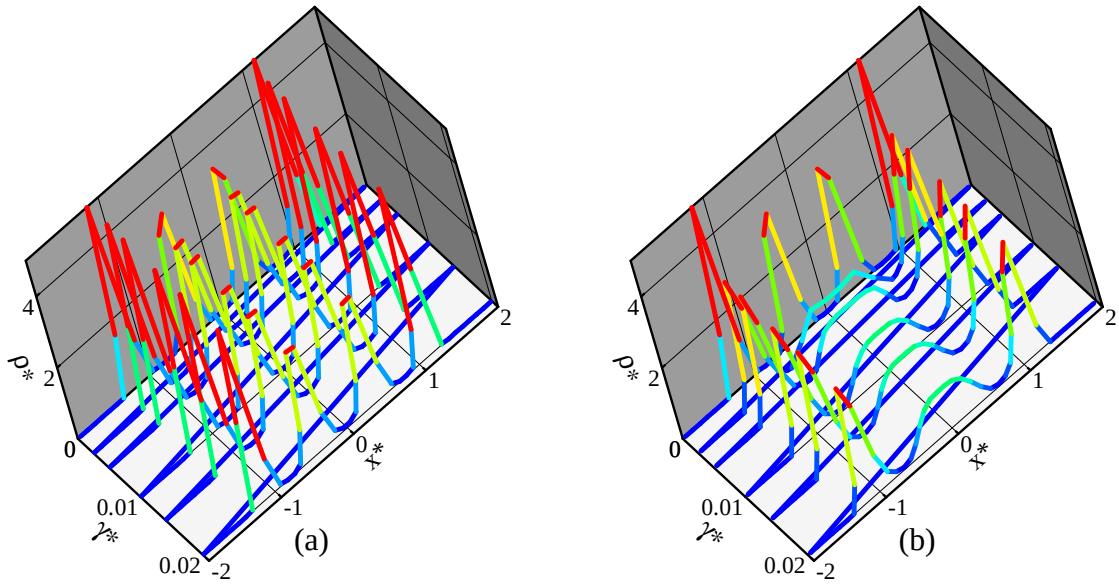

Figure 5.9: Density profiles at $W^* = 3.9$ for different shear rates. (a) GC-NVT scheme. (b) GCMD scheme.

5.3.3. Time Dependence of Friction Force

The results presented in the previous section were corresponding to stationary state conditions. However, it is clear from the previous results that the (re-)organization of the confined fluid under shear is what drives the friction force. It is so interesting to look at the transient behavior for the different systems studied in this work. In order to reduce the statistical uncertainties, the results provided in this section correspond to an average over 20 different independent runs. Figure 5.10 shows the dependence of the friction force with time

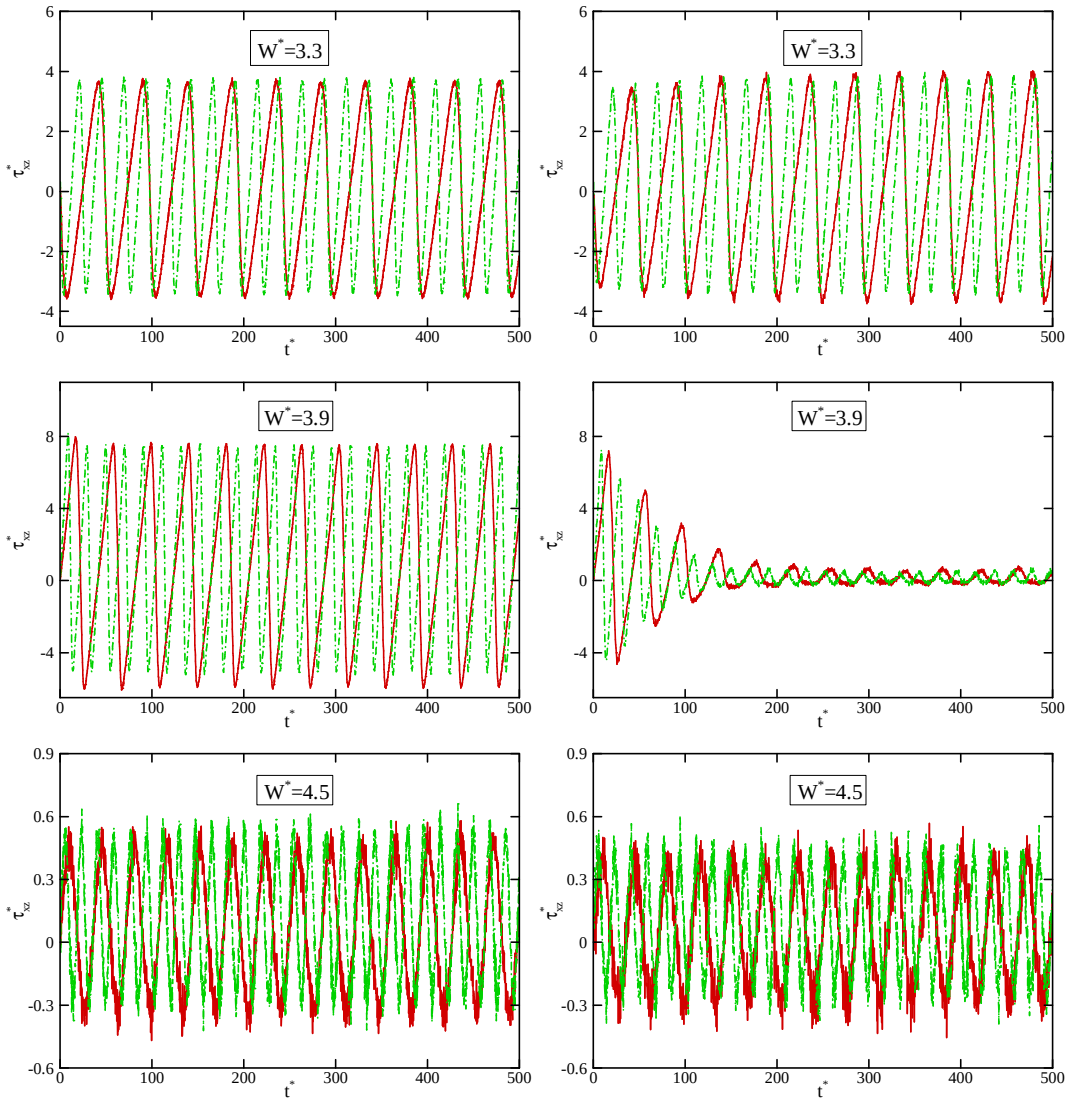

Figure 5.10: Variation of the friction force with time. Left figures: GC-NVT scheme. Right figures: GCMD scheme. Solid curves correspond to $\gamma^* = 0.01$, dashed-dotted curves correspond to $\gamma^* = 0.02$.

for $W^* = 3.3,\ 3.9$ and 4.5 and sliding velocities corresponding to $\gamma^* = 0.01$ and 0.02. It is important to recall that for both type of simulations, GCMD and GC-NVT, the initial system is equilibrated in an out-of registry configuration.

As expected, all cases exhibit an oscillatory behavior of the friction force with a period $\theta^* = \frac{L^*_{\mathrm{Lat}}}{2V^*_{\mathrm{Wall}}}$ [3-4], where L^*_{Lat} is the lattice size, see Fig. 5.10. This behavior is simply due to

the periodic structure of the solid surfaces. Interestingly, all results obtained using the GC-NVT scheme exhibit this oscillatory behavior with constant amplitude after starting sliding the solid surfaces. However, the amplitude of the oscillation is constant only for $W^* = 4.5$ when employing the GCMD approach. More precisely, the amplitude of the oscillation increases slightly with time for $W^* = 3.3$ and decreases noticeably when $W^* = 3.9$.

The behaviors shown in Fig. 5.10 are consistent with previous results. During GC-NVT simulations the average density is constant and the density profiles are not affected by the shear, see Fig. 5.9. Thus, the confined fluid does not reorganize itself noticeably when shearing and so the amplitude of the friction force oscillations is not time dependent. When the GCMD scheme is employed the average density changes, see Fig. 5.8, and the density profiles can be strongly modified as shown on Figs. 5.6 and 5.9. The slight increase of the oscillation amplitude for $W^* = 3.3$ is so simply due to a slight increase in the average density see Fig. 8 and more precisely to an increase of the central layer density, see Fig. 5.6. The large decreases of the oscillation amplitude of the friction force with time found for $W^* = 3.9$ is related to the strong reorganization of the central layers of the confined fluids, see Figs. 5.6 and 5.9, as already discussed.

It is interesting to note that experiments show that the friction force is history-dependent [3]. Results shown in Fig. 5.10 clearly indicate that such characteristic of a system can be observed using the GCMD scheme, whereas it is not the case during GC-NVT simulations. For the systems simulated in this work, such behavior is induced only by modifications (on the density profiles) in the confined fluid which can lead to an increase or a decrease of the average density of confined fluid and not by any change in the structure of the solid walls. The use of the GCMD scheme should so be preferred to the GC-NVT scheme to look after such phenomena.

Concerning the shape of these oscillations, Glosli et al. [11] estimated the dependence of the friction force with time by performing GC-NVT simulations to explore the mechanisms of energy dissipation of confined systems undergoing a boundary shear. They observed that, in a confined system, for a given width the energy dissipation can occur by a discontinuous "plucking" mechanism, i.e. the friction force rapidly varies from the maximum to the minimum value, or a continuous "viscous" mechanism, i.e. the friction force smoothly varies. They have shown that the type of energy dissipation regime depends on the interaction strength between the fluid and solid. It is clear from the results shown in Fig. 5.10 that the regime can be modified as well by changing the width of the confined system. More precisely, results obtained for both schemes indicate that the internal energy is dissipated by the plucking-like mechanism when the width is sufficiently small, when $W^* = 3.3$ and 3.9 (at short time for the GCMD case when $W^* = 3.9$), see Fig. 5.10. In contrast, it is the viscosity-like mechanism that is occurring for $W^* = 4.5$. In fact the mechanism of energy dissipation is strongly related to the magnitude of the peaks of the friction force, i.e. energy barrier [3], as shown by the GCMD results for $W^* = 3.9$. For high energy barrier the plucking-like regime occurs while it is the viscous-like one that takes place when the energy barrier is low.

5.4. Conclusions

To deal with static properties of highly confined fluids between surfaces, the situation is rather clear and molecular simulations in the Grand-Canonical ensemble are well adapted. However, when the system is put out of equilibrium through a boundary shear to deal with dynamic properties, there are two general molecular simulation schemes used in the literature to tackle such a problem. In the first approach, the NEMD simulations are performed directly in a GC-like ensemble (i.e. by connecting the out of equilibrium studied system to "bulk" reservoirs), so-called the GCMD scheme. In the second one, NEMD simulations are

performed in the NVT ensemble in which the state (number of molecules) is an input coming from a prior GC simulation at equilibrium, named the GC-NVT scheme. The latter scheme relies on a hypothesis that the number of molecules (the average density) is unchanged by the boundary shear, which is questionable in some cases. However, in terms of CPU time and implementation needs, the GC-NVT approach is clearly preferable as long as the hypothesis is valid. So, in this work, we have applied these two schemes to a simple Lennard-Jones liquid confined between two solid flat walls and undergoing boundary shear to quantify the differences between what they are providing as physical properties.

First, we have explored the average density of the confined fluid at a low shearing velocity. Results have indicated that both schemes provide nearly the same average density only when the separation between the solid surfaces is sufficiently large enough, i.e. $W^* > 6$ for the system studied in this work. The differences noted for smaller widths are due to significant effects of the relative structural ordering induced on the fluid by the solid surfaces configuration at small separation which can lead to first-order and second-order transitions. The main difference between the two schemes comes from the fact that the variation in the average density of the GCMD scheme does not exhibit first-order transitions but only second-order transitions. Concerning the apparent shear viscosity computed for the same conditions, the results have been found to be as well strongly dependent on the scheme used for a small separation between the surfaces with a behavior consistent to what found for density.

Second, the shear velocity dependence of the friction force has been studied at three different widths, $W^* = 3.3, 3.9$ and 4.5 corresponding to three different cases from the fluid structure point of view. Both schemes have shown that for a width corresponding to an equal average density, $W^* = 4.5$ the friction force is generally monotonously increasing with the increase in the wall velocity, which can be well described by a simple thermal activation model. However, for the smaller widths corresponding to a stronger fluid structure, results

may strongly differ between the GC-NVT and GCMD schemes. In particular when using the GCMD scheme for $W^* = 3.9$ the friction force can initially decrease with the velocity increase because of the possible exchange of matter with the reservoirs. Interestingly, both schemes have shown that the friction force is not always vanishing when the shear velocity tends to zero if the confined fluid is strongly structured. Thus, in some peculiar conditions, the Lennard-Jones fluid studied in this work can behave as a visco-plastic one.

Finally, we have studied the time dependence of the friction force for the three different widths mentioned above. It has been found that all cases exhibit an oscillatory behaviour of the friction force, which is simply due to the periodic structure of the solid surfaces. Furthermore, it has been confirmed that the shape of the oscillations are of two types, plucking or viscous, and is strongly related to the magnitude of the peaks in the friction force (the energy barrier). For the larger width, both schemes provide nearly the same constant oscillations in the friction force. However, for small widths, while the amplitude of the oscillations is nearly constant after starting sliding the solid surfaces when using the GC-NVT scheme, it can change in some cases (decrease or increase) when the GCMD scheme is used. This means that the use of the GCMD scheme is preferable to explore the history-dependence of the friction force as observed in experiments.

References

[1] J. Israelachvili, *Intermolecular and Surface Forces*, Academic Press, Third Edition (2010)

[2] M. Schoen, *Computer simulation of condensed phases in complex geometries*, New series m: monographs, Lecture note in physics, m17 (1993)

[3] M. H. Muser, M. Urbakh and M. O. Robbins, Adv. Chem. Phys. 126, 188 (2003)

[4] J. Gao, W. D. Luedtke, D. Gourdon, M. Ruths, J. N. Israelachvili and U. Landman, J. Phys. Chem. B 108, 3410 (2004)

[5] G. He, M. H. Muser and Mark O. Robbins, Science 284, 1650 (1999)

[6] J. Hansen and I. R. McDonald: Theory of simple liquid, Third Edition, Elsevier

[7] M.P. Allen and D.J. Tildesley, *Computer Simulation of Liquids*, Oxford University Press (1989)

[8] I. Bitsanis, S. A. Somers, H. T. Davis and M. Tirrell, J. Chem. Phys. 93, 3427 (1990)

[9] J. L. Barrat and L. Bocquet, Phys. Rev. Lett. 82, 4671 (1999)

[10] M. J. Stevens, M. Mondello, G. S. Grest, S. T. Cui, H. D. Cochran and P. T. Cummings, J. Chem. Phys. 106, 7303 (1997)

[11] J. N. Glosli and G. M. McClelland, Phys. Rev. Lett. 70, 1960 (1993)

[12] G. He and M. O. Robbins, Tribol. Lett. 10, 7 (2001)

[13] M. R. Farrow, A. Chremos, P. J. Camp, S. G. Harris and R. F. Watts, Tribol. Lett. 42, 325 (2010)

[14] K. E. Gubbins and J. D. Moore, Ind. Eng. Chem. Res. 49, 3026 (2010)

[15] H. Hoang and G. Galliero, J. Chem. Phys. 136**,** 184702 (2012)

[16] M. Lupkowskia and F. van Swol, J. Chem. Phys. 95, 1995 (1991)

[17] J. Gao, W. D. Luedtke and U. Landman, Phys. Rev. Lett. 79, 705 (1997)

[18] J. Gao, W. D. Luedtke and U. Landman, J. Phys. Chem. B 102, 5033 (1998)

[19] L. Zhang, R. Balasundaram and S. H. Gehrke, J. Chem. Phys. 114, 6869 (2001)

[20] J. J. Magda, M. Tirrell and H. T. Davis, J. Chem. Phys. 83, 1888 (1985)

[21] Z. Guo, T. S. Zhao and Y. Shi, Phys. Rev. E. 71, 035301 (2005)

[22] Z. Guo, T. S. Zhao and Y. Shi, Phys. Fluids 18, 067107 (2006)

[23] A. Botan, B. Rotenberg, V. Marry, P. Turq , and B. Noetinger, J. Phys. Chem. C 115, 16109 (2011)

[24] H. Hoang and G. Galliero, Phys. Rev. E 86, 021202 (2012)

[25] H. J. C. Berendsen, J. P. M. Postma, W. F. van Gunsteren, A. Dinola and J. R. Haak, J. Chem. Phys. 81, 3684 (1984).

[26] Q. Cai, A. Buts, N.A. Seaton, M.J. Biggs, Chem. Eng. Sci. 63, 3319 (2008)

[27] G. Galliero and C. Boned, J. Chem. Phys. 129, 074506 (2008).

[28] M. Kröger and S. Hess, Phys. Rev. Lett. 85, 1128-1131 (2000).

[29] G. Galliero, C. Boned, Phys. Rev. E 79, 021201 (2009).

[30] G. Galliero, C. Boned, A. Baylaucq, Ind. Eng. Chem. Res. 44, 6963-6972 (2005).

[31] H. Eyring, J. Chem. Phys. 4, 283 (1936)

[32] D. M. Heyes, J. Chem. SOC., Faraday Trans. 2, 82, 1365 (1986)

[33] H. A. Barnes, *A handbook of elementary rheology*, Published by University of Wales Institute of Non-Newtonian Fluid Mechanics, Aberystwyth (2000)

Chapter 6

Shear-Induced Swelling/Shrinkage in Narrow Slit Pores*

* This chapter is being prepared to be submitted for publication

Abstract:

In this work, using molecular simulations, we have explored the swelling/shrinkage induced by shear of a simple slit pore immerged in a Lennard-Jones liquid reservoir. First, at equilibrium, it has been verified that the average relative position of the two walls is the one corresponding to a (stable) normal pressure in the confined fluid equal to that in the bulk reservoir. Then, we have noticed that the pore can swell or shrink when the solid walls are displaced in parallel with the fluid-solid interface. This is due to the fact that the normal pressure of the confined fluid appreciably varies with the relative structural ordering between the solid (crystalline) surfaces for a given size. Thus, when the solid walls are moved parallelly at a constant velocity, the instantaneous pore size oscillates with time and yields, on average, a shear-induced swelling/shrinkage.

6.1. Introduction

Understanding the mechanical response of a tight porous medium in which pores are filled partially or completely by a fluid and subject to an external action, e.g. external stress or change of the surrounding environment, plays an important role in many engineering problems: low permeability reservoirs (Shale, Coal Bed Methane, etc.) in petroleum engineering, activated carbons/zeolites in chemical engineering processes, cement paste in civil engineering, etc. [1-4]. In such situations where the pore sizes are of the order of one to ten molecular sizes, the main problem is how to take into account the solid-fluid interaction in the mechanical response of the whole porous medium composed of the fluid and the solid matrix [4-9].

For porous medium in which the pores are sufficiently large, typically macropores (> 50 nm), which are well described by the classical continuum theories, the local mechanical response of an isotropic porous medium is governed by the conventional constitutive equations which are written as [10-11]:

$$\bar{\sigma} = K\bar{\epsilon} - b\bar{p} \tag{6.1a}$$

$$\bar{\varphi} = b\bar{\epsilon} + \bar{p}/N \tag{6.1b}$$

$$\bar{s}_{ij} = 2G\bar{e}_{ij} \tag{6.1c}$$

where $\bar{\sigma}$ is a confining stress, $\bar{\epsilon}$ is a volumetric strain, $\bar{p}$ is a fluid pore pressure, $\bar{\varphi}$ is a porosity, $\bar{s}_{ij}$ is a deviatoric stress, $\bar{e}_{ij}$ is a deviatoric strain, and K, b, N and G are the bulk modulus, Biot coefficient, Biot modulus and shear modulus, respectively.

The problem becomes more complex, when the size of the pores decreases below 50nm (i.e. when micropores and mesopores are involved). In such porous medium, the surface effects due to the fluid adsorbed on the solid surface and the molecular packing due to

confinement can be dominant over the volume effects [2-3, 12-13] and can induce for instance swelling in clays [4-9]. In other words, the effect of the solid-fluid interaction, in particular the adsorption, cannot be neglected [1] and characterized by simply introducing a modified fluid pore pressure $\bar{p}$ into the constitutive equations, i.e., in Eqs. (6.1a) and (6.1b) [6-7, 9]. It should be noticed that the effects due to the molecular parking becomes significant as the size of pores decreases to values of the order of the distance of molecular interactions (i.e. micropores < 2 nm) [2].

To take into account the surface effect due to the adsorption in the volumetric deformation of mesoporous solids, i.e. pores sizes from 2nm to 50 nm, during adsorption-desorption hysteretic cycles, Gor and Neimark [14] introduced the definition of the adsorption stress $\bar{\sigma}_S$ instead of the fluid pore pressure $\bar{p}$, in which $\bar{\sigma}_S$ is determined from the vapor pressure using the Derjaguin theory. Such definition implies that the Biot coefficient is equal to one. In a recent study on the CO_2 swelling of coal and carbon adsorbents in which porous medium are at the mesoscale, Vandamme et al. [6] extended the conventional constitutive equations to additionally involve the effect of the adsorption that is determined by using the Langmuir adsorption isotherm. However, it is clear that such approaches are insufficient when a microporous medium is involved, i.e. pore size below 2nm, as long as in such highly confined systems the structure in the whole fluid (and not only in the vicinity of the walls) can be strongly affected by the confinement itself [2]. This confinement may lead for instance to a structural order in the fluid which strongly affects all its physical properties [13, 15-18] and may even lead even to phase transitions [12].

To deal with a microporous medium, one has to take into account both the surface effects due to the adsorption and the molecular packing. Pijaudier-Cabot et al. [7] used molecular simulations on simple pores to demonstrate that such effects are responsible for the volumetric deformation of the material. Then they revisited poromechanics in the context of

microporous materials with a continuous pore size distribution. To account for the surface effects, the constitutive equations were re-formulated by introducing an apparent porosity and an interaction free energy that are related to the Gibbs adsorption isotherm. In a recent study, Brochard et al. [9] derived poroelastic constitutive equations for a generic porous medium, in which the surface effects are characterized by the amount of fluid adsorbed that was shown to depend on both the fluid bulk and pressure and the strain of the medium.

It should be noticed that the derived constitutive equations for microporous medium have assumed that the adsorption stress, i.e. the normal pressure in the pore (sometimes called solvation pressure), and the density of the fluid in the pore are independent on the deviatoric strain. The volume of a pore is so assumed to be unchanged when the part of the solid phase forming the pore is displaced in the direction parallel to the solid-fluid interface. This can be inadequate when dealing with microporous medium in which the solid phase is highly structured and the solid-fluid interactions are strong. This is simply due to the fact that for a given pore size, the relative ordering between the solid surfaces has a significant effect on the properties of the fluid in the pore [12, 18].

Thus, in this work using extensive molecular dynamics (MD) simulations we explore the volumetric deformation of a simple saturated (by a liquid) slit pore induced by the solid displacement in the direction parallel with the solid-fluid interface. To do so, we analyze the swelling/shrinkage (i.e. the gap between the two walls) due to a relative displacement of the solid walls, see Fig. 6.1.

This article is organized as follows. In Sect. 6.2, some details on the MD simulations technique employed are provided. Then, results obtained from the molecular simulations are presented and discussed in Sect. 6.3. Finally, we summarize the highlighting results in Sect. 6.4 which forms the conclusion.

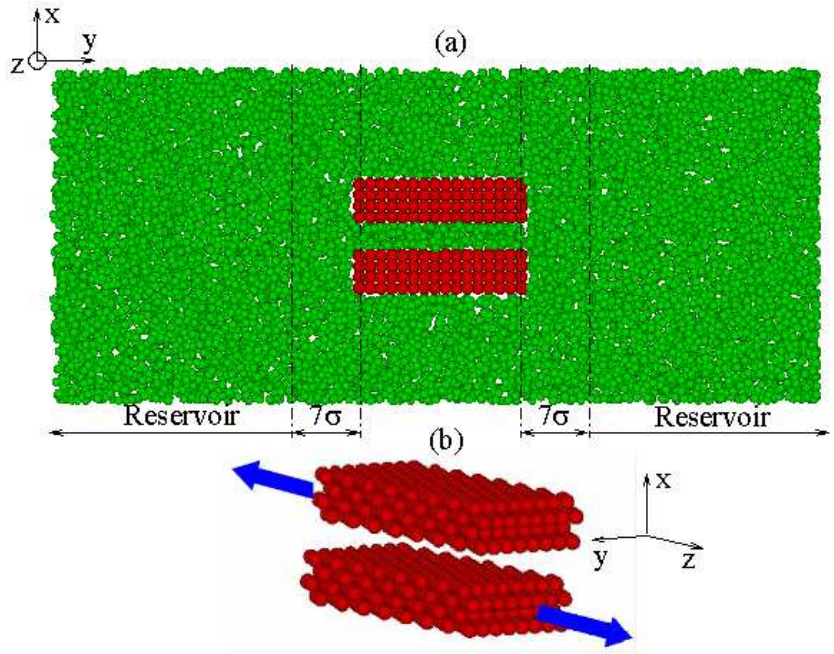

Figure 6.1: (a): Side view of the simulation cell used in the Grand Canonical like Molecular Dynamics. (b): A schematic representation of the solid displacement in the direction parallel to the solid-fluid interface.

6.2. Model and Simulations

6.2.1. Pore and Fluid Models

All fluid and solid molecules have been modeled as spherical ones. All interactions are described by a classical truncated Lennard-Jones (LJ) 12-6 potential between pairs of particle:

$$U_{LJ}(r) = \begin{cases} 4\epsilon \left[\left(\frac{\sigma}{r}\right)^{12} - \left(\frac{\sigma}{r}\right)^{6} \right] & \text{if } r \le r_c \\ 0 & \text{if } r > r_c \end{cases} \quad (6.2)$$

where r is the distance between the two particles, ε is the potential depth, σ is the particle diameter, and r_c is the cut-off diameter (=3.5σ in this work).

The potential depth and the diameter of the solid-fluid interaction are defined in term of the fluid-fluid interactions respectively as follows:

$$\sigma_{\mathrm{f-s}} = \sigma_{\mathrm{f-f}} = \sigma \text{ and } \varepsilon_{\mathrm{f-s}} = \varepsilon_{\mathrm{f-f}} = \varepsilon \quad (6.3)$$

The solid walls are formed by molecules arranged on a faced centered cubic (FCC) lattice and it is assumed that their structures are unchanged during the swelling/shrinkage, i.e. the Biot coefficient in Eq. (6.1) is equal to one [10-11]. The walls are separated by a distance L^*_{Gap}.

In the following, variables noted with a star as superscript correspond to classical LJ reduced quantities, i.e. [19]:

$$t^* = \frac{t}{\sigma\sqrt{m/\varepsilon}},\ T^* = \frac{k_B T}{\varepsilon},\ \rho^* = \frac{N_T \sigma^3}{V},\ p^* = \frac{p\sigma^3}{\varepsilon} \tag{6.4}$$

where t is the time, m the mass of the fluid particle, k_B is the Boltzmann constant and N_T the total number of atoms contained in the volume V.

6.2.2. Simulation Schemes

The fluid in a porous medium is such that its full chemical potential is the same in different pores which is as well the same chemical potential than the one of the fluid reservoir (bulk) to which the system is connected. Therefore, molecular simulations in the grand canonical (GC) ensemble on fluids confined in narrow pores are well adapted to study the swelling/shrinkage [12, 16, 18].

Thus, to perform the MD simulations, we have employed the constant density Grand Canonical like Molecular Dynamics method proposed by Hoang and Galliero [16] which is similar to the one proposed by Gao et al. [20]. It consists in simulating explicitly the fluid in the pore in direct contact with reservoirs maintained at the desired density and temperature (which is equivalent to maintain a constant chemical potential for a pure fluid). Figure 6.1 shows a sketch of the simulation box that contains both fluid and solid particles. Periodic boundary conditions (PBC) have been applied on all three directions. The configuration has been chosen so that the fluid out of the pore space is inappreciably influenced by a small change in the pore studied.

To maintain the density of the fluid in the reservoirs at the desired value, the *y* coordinates of the molecules in the reservoir region and the *y* size of this region are scaled at each time step by the quantity [16]:

$$\lambda_\rho = 1 - \frac{\Delta t}{\tau_\rho}\left(\frac{\rho_0}{\rho_{res}} - 1\right) \tag{6.5}$$

where, ρ_{res} is the instantaneous density in reservoir regions, ρ_0 is the target density, Δt is the time step and τ_ρ is the density time constant. To control the temperature of fluid, we have employed the Berendsen thermostat [19], i.e. at each time step the velocities of the fluid molecules are scaled by a quantity:

$$\lambda_T = 1 + \frac{\Delta t}{2\tau_T}\left(\frac{T_0}{T} - 1\right) \tag{6.6}$$

where, τ_T is the temperature time constant, T_0 is the target temperature and T is the instantaneous temperature.

To study the swelling/shrinkage of the pore, the solid walls forming the pore are not allowed to move in the *y* direction but only in the *x* direction during the simulations, exceptions noted. To model the solid displacement in the direction parallel to the solid-fluid interface, the walls are prescriptively moved in the *z* direction, see Fig. 6.1. The equation of motion of the centers of mass of the solid walls in the x direction is governed by the classical equation of motion as:

$$N_S m_S \ddot{x}_S = \sum_{i=1}^{N_F} \sum_{j=1}^{N_S} -\frac{\partial U_{LJ}(r_{ij})}{\partial r_{ij}} \frac{x_{ij}}{r_{ij}} \tag{6.7}$$

where N_S, m_S and x_S are the number of solid molecules, the mass of a solid molecule and the coordinate of the center of mass in the *x* direction for each solid wall respectively. To avoid as much as possible the effects due to the finite size of the two solid walls in the *y* direction, Eq. (6.7) is only applied to the solid molecules in the sampling region as described in Ref. [16].

6.2.3. Numerical Details

We have used an in-house code to perform the MD simulations, in which the calculation of force on each molecule is parallelized by using the functional decomposition algorithm [21-22]. The motion equations of the fluid particles are solved using the Verlet velocity algorithm with a time step Δt^*=0.002 [19], whereas the solid molecules are fixed at their sites on a CFC lattice with a size of the lattice $a = 1.6\sigma$. In all simulations the state of the fluid in the reservoir is maintained at $\rho^* = 0.7$ and $T^* = 1$, which correspond to a liquid state in bulk conditions for the cutoff employed in this work [23]. To compute the force on each fluid molecules effectively, we have combined the minimum-image criterion and the neighbor list [19]. As mentioned previously PBC have been applied on all directions.

Before the moving the two walls, the systems are equilibrated in an out-of registry configuration, which is done in two steps:

- First, the simulations are performed with the solid walls fixed in space for 10^6 time steps.
- Second, the walls are let free to move over the *x* direction using Eq. (7) for 10^6 time steps.

Once the system has been equilibrated, the solid walls displacement is done by moving the solid walls in the *z* direction. Then the simulations are continuously carried out during $2 \times 10^6 - 3 \times 10^6$ time steps, discarding the first $1 \times 10^6 - 2 \times 10^6$ time steps to reach the steady state or re-equilibrate and sample data.

6.3. Results and Discussions

6.3.1. Preliminary Results

6.3.1.1. Normal Pressure

At equilibrium, for the systems studied, i.e. a Biot coefficient equal to one [10-11], the constitutive equations, Eq. (6.1), implies that the pore size is equal to a value for which the normal pressure exerted on the solid wall due to the confined fluid is equal to the one due to the fluid outside the pore. Hence, the pore width at equilibrium can be estimated a priori, if the dependence of the normal pressure (of the confined fluid) with the pore size is determined [24]. It should be noticed that, at the molecular scale, because of the fluctuations, the size of pore will in fact fluctuate around this average equilibrium distance.

So, using MD simulations, we have first determined the variation in the normal pressure of the confined fluid with its size for the out-of registry configuration. As well known [2], results shown in Fig. 6.2 indicate that the normal pressure noticeably oscillates for the smallest pore for small wall gap, i.e. $L^*_{Gap} < 7$ for the system studied in this work. The amplitude is increasing when the pore decreases and is nearly constant and equal to the pressure of the fluid in the reservoir for the larger widths. Such behavior simply reflects the strong inhomogeneity of the fluid in the pore in the direction perpendicular to the solid-fluid interface due to physical adsorption and molecular packing [12-13]. It is important to notice that, for such configuration with a fixed distance between the walls, the variations in the normal pressure with the size of the pore exhibits “unstable” regions in which the normal pressure increases with the size increasing.

As mentioned previously, to avoid possible disturbance induced by the surrounding fluids, a sufficiently large fluid system should be employed. As shown in Fig. 6.2, the normal pressure in a pore is nearly constant when the size of the pore is large, i.e. $L^*_{Gap} > 7$ for the

system explored in this work. Hence, in the following, the distance between the slit pore and its replica over the *x* direction (because of PBC) is initially chosen to be equal to 16σ.

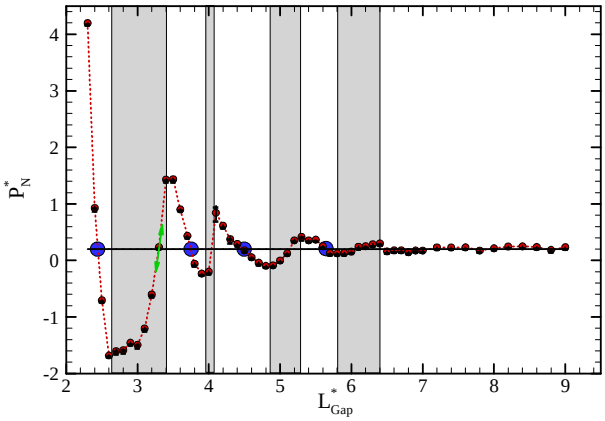

Figure 6.2: Variation in the normal pressure with gap size. The shadowed regions represent the "unstable" regions in which the normal pressure increases when the gap is increasing. Large circles (Blue color) correspond to the "average" pore size at equilibrium. Small circles (Black color) correspond to the simulation results. Solid line represents the pressure in the reservoir. Dashed curve serves as guide for the eye.

6.3.1.2. Swelling/Shrinkage

According to the constitutive equations, the "average" size of pore at the equilibrium state can easily be determined from Fig. 6.2 by finding abscissa of intersections of the normal pressure curve and the line of the reservoir pressure, i.e., when $P_N^* = P_{\text{Reservoir}}^*$, but only in the stable region of the normal pressure curve versus width. To confirm this statement, we have performed MD simulations letting the walls free to move over the *x* direction (the pore can so shrink or swell) as described in Sect. 6.2.3 starting from various initial sizes of pore.

As expected, results displayed in Fig. 6.3(a) indicate that the average sizes of the pore at equilibrium obtained from such simulations are exactly the same as those deduced from Fig. 6.2. Thus, the value of the average equilibrium gap depends on the initial size as shown in Fig. 6.4. For instance, when $L_{\text{Gap}-\text{Init}}^* = 2.90$ at the initial state the normal pressure in the

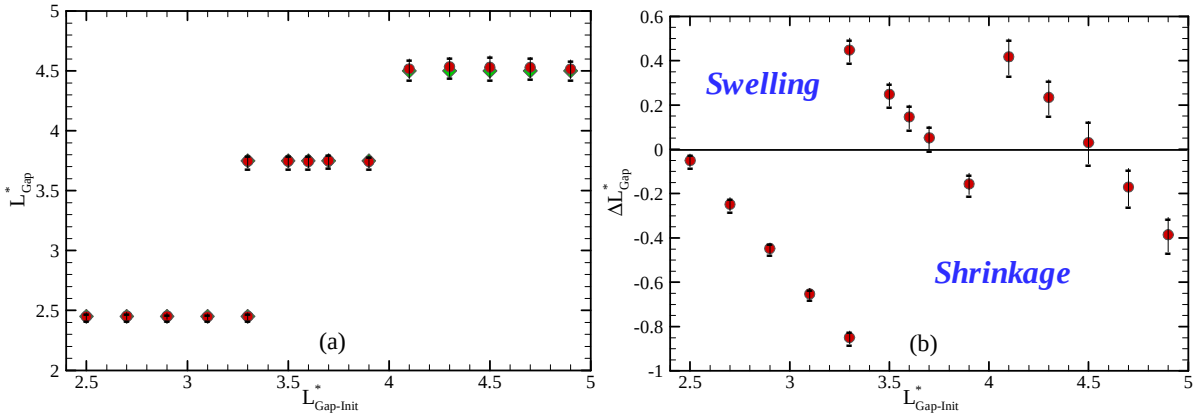

Figure 6.3: (a) Pore size at equilibrium. Circles (Red color) correspond to the simulation results, diamonds (Green color) to the constitutive equations. (b) Deformation of the pore induced by the presence of a fluid in it.

pore is less than the one outside the pore and so the pore width decreases ($L^*_{\mathrm{Gap}} = 2.45$) until P^*_N in the pore is equal to $P^*_{\mathrm{Reservoir}}$ as shown in Fig. 6.4.

It is important to emphasize that the pore width at equilibrium never reaches a value corresponding to an unstable region of the "unstable" P^*_N in which the normal pressure increases with the increase of the gap increasing, see Figs. 6.2 and 6.3. This can be understood as a consequence of the fluctuation in the thermodynamics of the fluid. Because of this, a pore with an initial gap for which P^*_N is nearly equal to $P^*_{\mathrm{Reservoir}}$ and which corresponds to an unstable region, i.e. $L^*_{\mathrm{Gap-Init}} = 3.30$ for the system studied, can swell or shrink, see Figs. 6.3 and 6.4.

Additionally, it is interesting to point out that, as expected, the pore width at equilibrium fluctuates around $L^*_{\mathrm{Gap-Equi}}$ over a non negligible range especially when $L^*_{\mathrm{Gap-Equi}}$ is large, see Fig. 6.4. This can be explained by considering the derivative of the normal pressure with the pore size around the equilibrium values which tends to decrease (in absolute value) when the pore size increases, as shown in Fig. 6.2.

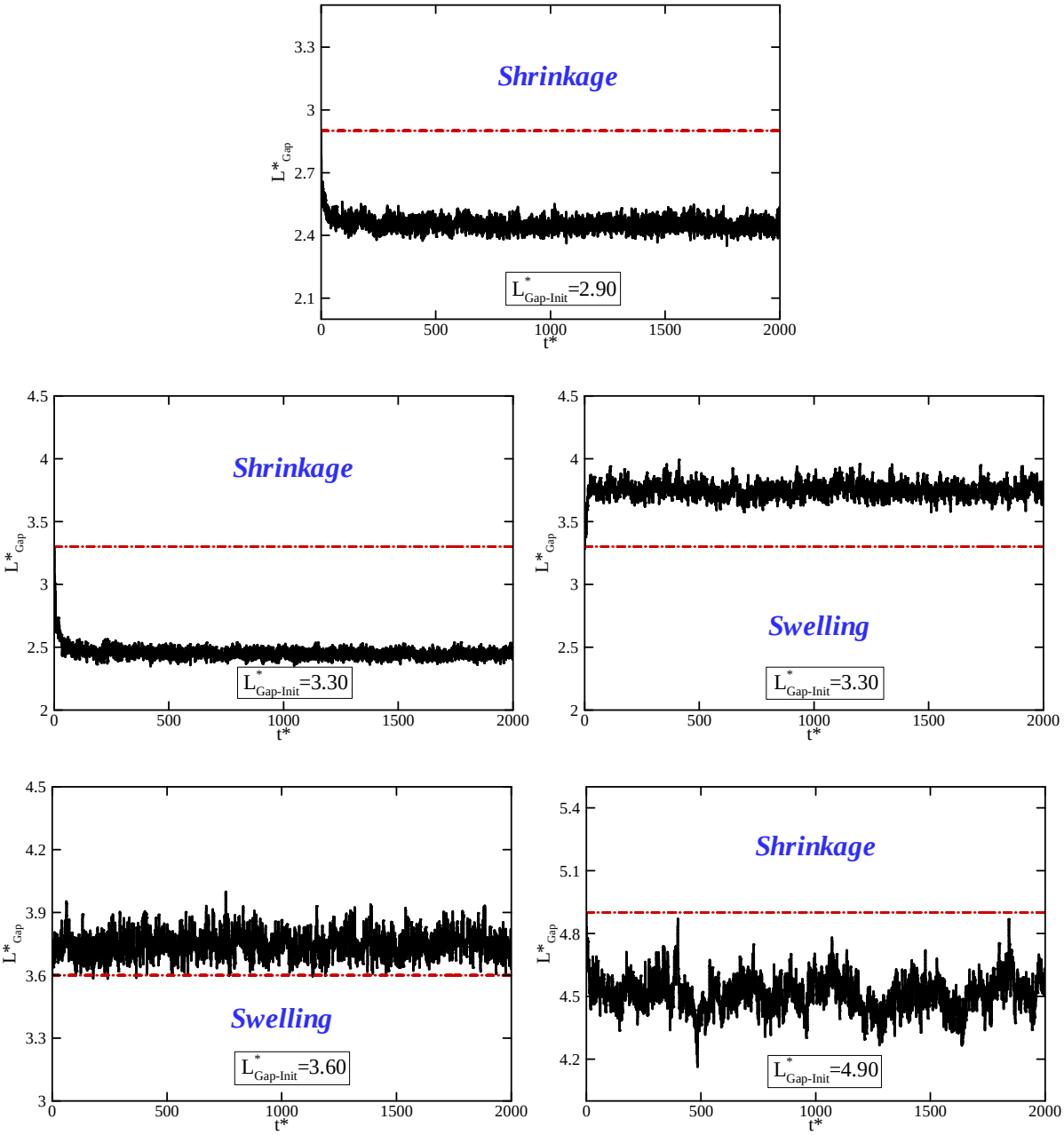

Figure 6.4: Variation in the pore size with the time without shear. Solid curves correspond to the simulation results, Dashed-Dotted curves to the initial pore size.

6.3.2. Swelling/Shrinkage Induced by Walls Displacement

As mentioned previously, the use of the conventional and recently modified constitutive equations leads to an unchanged pore width when the solid walls are moved in the direction parallel to the solid-fluid interfaces, i.e. the shear is not assumed to influence the

normal pressure. However, in a narrow pore for which its size is comparable to the typical distance of interaction between molecules, the relative structural ordering between the solid walls has a significant effect on the fluid in the pore [12, 18], in particular on the normal pressure of the confined fluid. This means that a relative displacement of the two solid walls can modify the normal pressure of the fluid. Hence, a pore can swell or shrink if the solid walls are translated of a given distance in the direction parallel to the solid-fluid interface. We will called that effect "static" swelling/shrinkage in the following.

To explore such static swelling/shrinkage of a pore, we have computed the variation in the pore width with the amplitude of the solid walls displacement Δz. To do so, we have performed MD simulations in which, once the system has reached the equilibrium, the solid walls are moved in opposite direction of a distance $\Delta z/2$, see Fig. 6.1(b). It should be noticed that the change from the initial out-of-registry configuration to an in-registry configuration of the two solid walls, corresponds to $\Delta z_{\mathrm{Max}} = a/2$.

Figure 6.5 depicts the variation in the pore size with the solid displacement Δz^* for three different initial equilibrium pore widths. Results clearly indicate that the pore can swell or shrink because of a solid displacement in the direction parallel to the solid-fluid interface. The pore swells when $L^*_{\mathrm{Gap-Equi}} = 2.45$, whereas it shrinks when $L^*_{\mathrm{Gap-Equi}} = 3.75$. Such behaviors are a consequence of the change in the normal pressure induced from the variation of the relative structural ordering between the solid walls when the solid walls are moved [18]. The effects of the relative structural ordering are more significant in narrower pores and so the swelling/shrinkage in a narrower pore is more appreciable than that in a larger pore, see Fig. 6.5.

It is interesting to note that for a narrow pore in which the number of layers of the fluid is even, starting from the initial out-of-registry configuration the pore swells when the walls are moved. Whereas the pore shrinks for an odd number of layers, see Figs. 6.5 and 6.6.

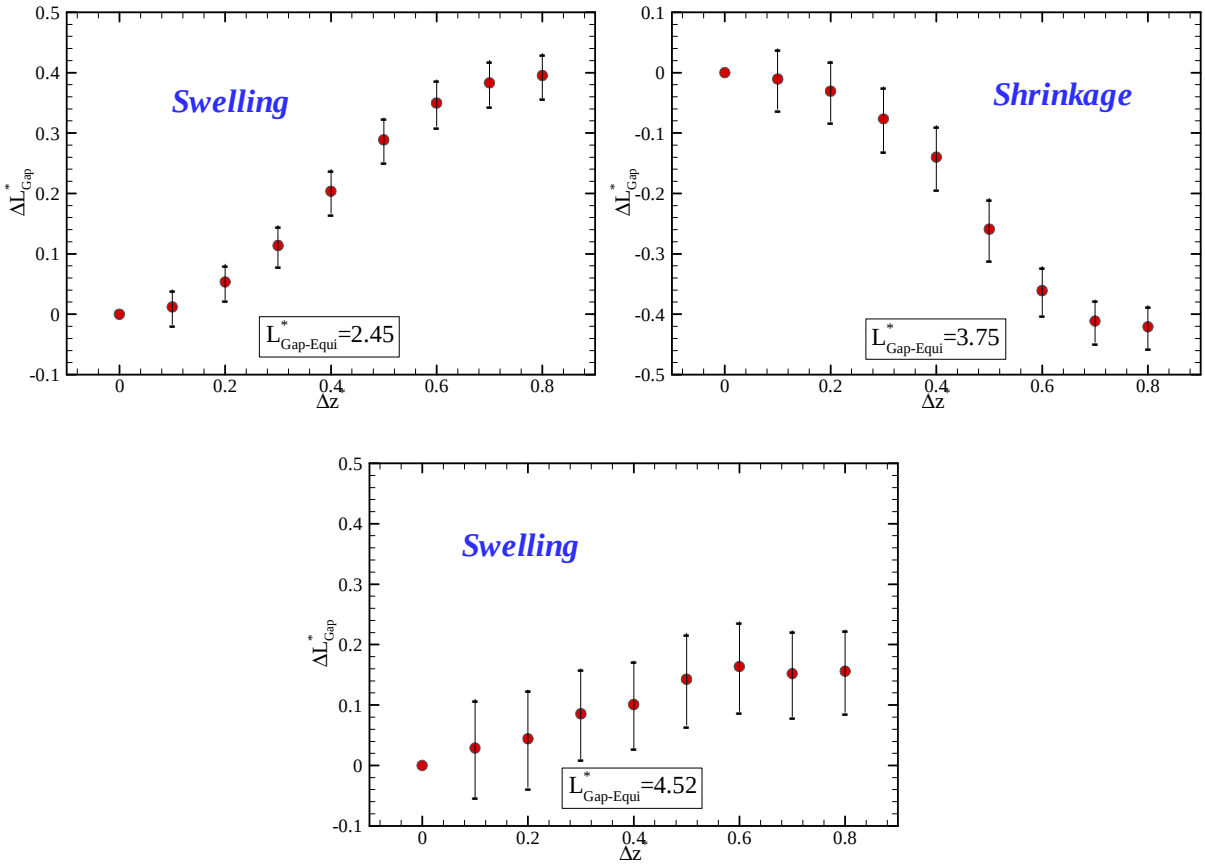

Figure 6.5: Variation of the pore size for a given solid displacement Δz^*.

This can be simply understood from the fact that, for a given pore size, the fluid in the out-of-registry configuration is more strongly structured when the number of layers is even, whereas it is opposite for the odd number of layers [12, 18].

6.3.3. Dynamic Swelling/Shrinkage

In the previous section, we have investigated the swelling/shrinkage of narrow pores induced by solid walls displacement in the direction parallel to the solid-fluid interface. It seems so interesting to explore the swelling/shrinkage of a pore when the solid walls are moved at a constant velocity, i.e. to induce a dynamic swelling/shrinkage. To do so, we have performed MD simulations in which, once the system has reached the equilibrium, the solid

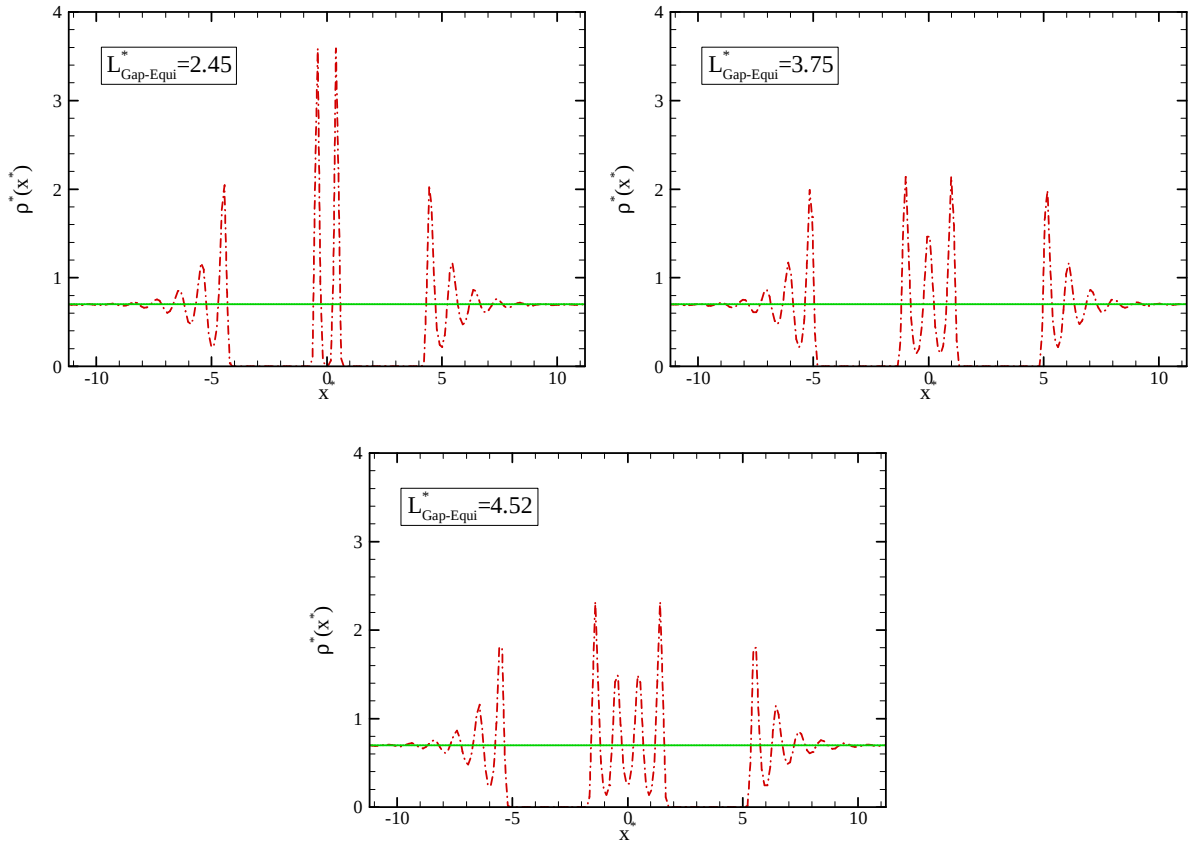

Figure 6.6: Density profiles. Dashed-Dotted curves correspond to the simulation results. Solid lines are the density in the reservoir.

walls are moved at a constant velocity in the direction parallel to the solid-surface interface, see Fig. 6.1.

When the velocity is sufficiently small, it is consistent to assume that the state of the system is completely re-equilibrated at each time. In other words, the pore size at any time should depend only on the instantaneous relative structural ordering between the solid surfaces. The instantaneous pore size while moving slowly the solid walls should so vary between the values corresponding to the in-registry and out-of-registry configurations. Thus, we have carried MD simulations as mentioned for different wall velocities were employed to check this assumption and to explore the behavior of the dynamic swelling/shrinkage for large moving velocities.

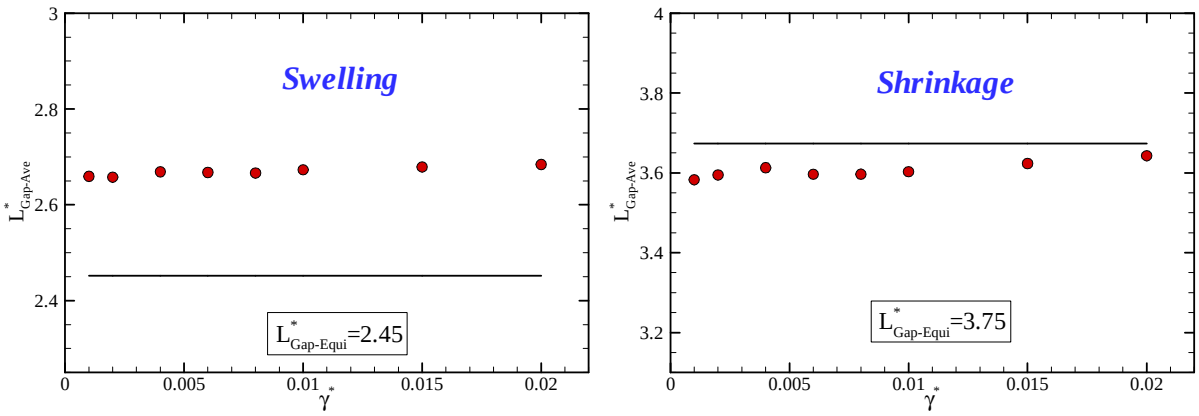

Figure 6.7: Variation in the average size of the pore with the shear rate $\gamma^* = V^*_{\mathrm{Wall}}/2L^*_{\mathrm{Gap-Equi}}$ during dynamic swelling/shrinkage. Symbols correspond to the simulation results. Lines are the size of the pore at equilibrium.

Figure 6.7 shows the dependence of the average pore size for different shear rates $\gamma^* = V^*_{\mathrm{Wall}}/2L^*_{\mathrm{Gap-Equi}}$. Results indicate that the average size is slightly dependent on the shear rate for the range used in this work. More precisely, the pore size is nearly constant, when $\gamma^*_0 < 0.01$, and slightly increases with the shear rate when $\gamma^*_0 > 0.01$. The latter trend is mainly due to the fact that the pressure of a fluid usually increases when the wall velocity increases [18, 25]. It should be noticed that γ^*_0 is one order of magnitude lower than the shear rate associated to the shear thinning threshold of a bulk LJ liquid [26-27].

Figure 6.8 displays the variation of the pore size with time for different walls velocities. As expected, all cases exhibit an oscillatory behavior with a period $\theta^* = a^*/2V^*_{\mathrm{Wall}}$. This behavior is simply due to the periodic structure of the solid surfaces. It is interesting to notice that the values of peaks and valleys are nearly equal to the equilibrium ones corresponding to the in-registry or out-of-registry configurations for low walls velocities, whereas it is not the case for high velocities, see Figs. 6.5 and 6.8. In other words, the walls velocity has a noticeable effect on the instantaneous size of a pore, which is not so obvious when looking only to the average size, see Figs. 6.7 and 6.8. In particular, the amplitude of the

oscillations is reduced when the walls velocity increases. Such behaviors can be understood in terms of re-equilibration of the fluid in the pore undergoing shear. For low enough shear rate the pore size is governed only by the effect of the relative structural ordering between the solid surfaces, not by the wall velocity. When the shear rate is sufficiently large, the fluid in the pore does not have enough time to re-equilibrate and so the effect of the relative structural ordering is reduced.

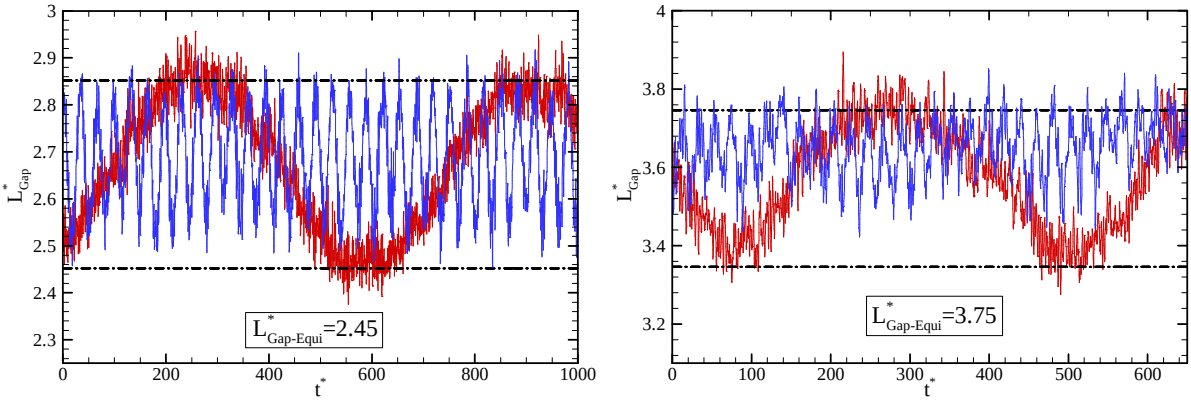

Figure 6.8: Variation in the pore size with the time when the solid walls are moved at a constant velocity. Red curves correspond to $V^*_{\mathrm{Wall}}/2L^*_{\mathrm{Gap-Equi}} = 0.001$, blue curves to $V^*_{\mathrm{Wall}}/2L^*_{\mathrm{Gap-Equi}} = 0.02$. Dashed-Dotted lines represent the pore size corresponding to the in-registry and out-of-registry configurations at equilibrium.

6.4. Conclusions

The pore-mechanics approach have shown to be a valuable tool to study the deformation of a porous media partially or fully saturated by a fluid. In its present form, such theory assumes that a deformation of the solid phase in the direction parallel to the solid-fluid interface (at the pore scale) does not affect the fluid pressure. However, this seems to be incorrect for systems in which the fluid is highly structured due to a strong solid-fluid interaction. So, in this work, using molecular simulations we have explored the volumetric deformation of a simple slit pore induced by shear.

First, we have estimated at equilibrium the normal/solvation pressure of a confined Lennard-Jones liquid for fixed pore width. As expected, it has been found that the normal pressure varies appreciably (damped oscillations) with the pore size for narrow pores, i.e.when $L_{Gap}^{*} < 7$ for the system studied in this work. Then, using simulations in which the slit pore was immerged in a fluid reservoir and allowed to swell/shrink, it has been verified that the relative equilibrium position of the two walls is the one corresponding to a normal pressure in the confined fluid equal to that in the bulk reservoir. However, even if that last condition is respected, the system should be in the stable part of the normal pressure dependence to the pore width (i.e. a pressure that decreases when the width increases). Thus, whatever the initial state, the equilibrium pore size never reaches a value corresponding to an unstable region.

Second, the swelling/shrinkage of a pore induced by a displacement of the solid walls (immerged in a fluid reservoir) of a given distance in the direction parallel to the solid-fluid interface has been investigated. Results have shown that, in narrow pores, the average pore size is changed by such solid displacement, i.e. there is a shear-induced swelling/shrinkage. This effect is simply due to the fact that the normal pressure of the simulated fluid appreciably varies with the relative structural ordering between solid surfaces (going from out of registry to in registry configurations).

Finally, we have explored the situation in which solid walls are moved at a constant velocity. It has been found that the velocity employed has only a slight effect on the average pore size, whereas it implies a noticeable effect on the instantaneous pore size. More precisely, while all cases exhibit an oscillatory behavior of the instantaneous pore size, which is simply due to the periodic structure of the solid surfaces, the amplitude of the oscillations is reduced when the walls velocity increases. Such behaviors can be understood in terms of re-equilibration of the fluid in the pore undergoing shear.

References

[1] O. Coussy, Mechanics and Physics of Porous Solids, John Wiley & Sons, Chichester (2010)

[2] J. Israelachvili, *Intermolecular and Surface Forces,* Academic Press, Third Edition (2010)

[3] G. Karniadakis, A. Beskok and N. Aluru, Microflows and Nanoflows, Springer (2004)

[4] R. L. Anderson, I. Ratcliffe, H. C. Greenwell, P. A. Williams, S. Cliffe and P. V. Coveney, Earth-Science Reviews 98, 201 (2010).

[5] E. J. M. Hensen and B. Smit, J. Phys. Chem. B 106, 12664 (2002)

[6] M. Vandamme, L. Brochard, B. Lecampion and O. Coussy, J. Mech. Phys. Solids 58, 1489 (2010)

[7] G. Pijaudier-Cabot, R. Vermorel, C. Miqueu and B. Mendiboure, C. R. Mecanique 339, 770 (2010)

[8] N. Malikova, E. Dubois, V.e Marry, B. Rotenberg und P. Turq, Zeitschrift für Physikalische Chemie 224, 153 (2010)

[9] L. Brochard, M. Vandamme and R. J. M. Pellenq, J. Mech. Phys. Solids 60, 606 (2012)

[10] M. A. Biot, "General Theory of Three Dimensional Consolidation", J. Appl. Phys. 12, 155 (1941)

[11] O. Coussy, Poromechanics, John Wiley & Sons, Chichester (2004)

[12] M. Schoen, Computer simulation of condensed phases in complex geometries, New series m: monographs, Lecture note in physics, m17 (1993)

[13] J. Hansen and I. R. McDonald: Theory of simple liquid, Third Edition, Elsevier

[14] G. Y. Gor and A. V. Neimark, Langmuir 26, 13027 (2010)

[15] I. Bitsanis, S. A. Somers, H. T. Davis and M. Tirrell, J. Chem. Phys. 93, 3427 (1990)

[16] H. Hoang and G. Galliero, J. Chem. Phys. 136**,** 184702 (2012)

[17] H. Hoang and G. Galliero, Phys. Rev. E 86, 021202 (2012)

[18] H. Hoang and G. Galliero (Accepted for publication in J. Chem. Phys.)

[19] M.P. Allen and D.J. Tildesley, Computer Simulation of Liquids, Oxford University Press (1989)

[20] J. Gao, W. D. Luedtke, and U. Landman “Structure and solvation forces in confined films: Linear and branched alkanes” J. Chem. Phys. 106, 4309 (1997)

[21] G. Galliero "Thermodiffusion dans les fluides de Lennard-Jones par dynamique moleculaire" Phd Thesis, Univesité Bordeaux I (2003)

[22] Y. Aoyama and J. Nakano "RS/6000 SP: Practical MPI Programming" International Technical Support Organization, IBM (1999)

[23] G. Galliero and C. Boned, J. Chem. Phys. 129, 074506 (2008)

[24] J. J. Magda, M. Tirrell and H. T. Davis, J. Chem. Phys. 83, 1888 (1985)

[25] D. M. Heyes, J. Chem. SOC., Faraday Trans. 2, 82, 1365 (1986)

[26] M. Kröger and S. Hess, Phys. Rev. Lett. 85, 1128-1131 (2000).

[27] G. Galliero, C. Boned, Phys. Rev. E 79, 021201 (2009).

Chapter 7

Conclusion and Perspective

7.1. Conclusions

To better understand and to improve the modeling of the physical characteristics of a fluid confined in a micro-porous medium, it is crucial to estimate its properties (static and dynamic) at the pore-scale. Thus, using extensive molecular dynamics (in adequate ensembles) on simple fluids confined in slit nanopores, we have tried to provide a fundamental information/model on some points of such a problematic. It is important to emphasize that even if the simulations were carried out on very simple system, the general methodology described in this work is applicable (in most cases in a straightforward manner) to realistic systems at the pore scale using appropriate molecular models while keeping in mind the limitations in terms of CPU.

The MD simulations in the grand canonical (GC) ensemble are probably the most suitable to deal with the confined systems and to extract an information comparable to what could be measured experimentally. Although there have been a non negligible number of algorithms proposed in the literature to deal with such ensemble using MD simulations, none seems to possess all possible advantages. Hence, we have proposed a slightly modified version of the algorithm proposed by Gao et al. It consists in simulating explicitly the fluid in the pore in direct contact with reservoirs maintained at the desired thermodynamics state through a relaxation scheme of the type proposed by Berendsen et al. Using this algorithm, the transient behavior of the mass diffusion process associated with the migration of one fluid into another one confined between parallel atomistic solid walls has been studied. Results on isotopic Lennard-Jones mixtures have shown that for a confined system in which the local density varies very strongly with the position, i.e. highly adsorbent walls, the mass diffusion

process is noticeably slowed down as expected and, more important, is a 2D phenomenon because the diffusion coefficient is no longer constant perpendicular to the walls. Otherwise, for weakly or moderately adsorbent it still follows roughly a 1D diffusion model with a characteristic time that is reduced compare to the bulk situation.

As the local estimation of the mass diffusion coefficient is not easy to handle, we have then studied the effect of fluid density inhomogeneities on the local viscosity. More precisely, using non-equilibrium MD simulations in a Couette like configuration, we have computed the local viscosity of strongly inhomogeneous fluids induced by a sinusoidal external field or by confinement in a slit pore for different states and for different fluid types going from the Hard-sphere one to the Lennard-Jones one. Simulations results have shown that the local viscosity appreciably varies with the position whatever the state and cannot be described by a simple van der Waals approach, i.e. non locals effects should be taken into account. To quantitatively predict the viscosity profiles from the local thermodynamics conditions (the density profile), we have proposed a simple scheme that is based on separating the local viscosity into the translational (kinetic) and configurational (collisional) contributions. The former can quantitatively be determined by using a simple kinetic-like theory, whereas a local average density model (LADM) combined with an adequate weight function has been employed for the latter. More precisely a generalized LADM has been developed that seems to be efficient for all types of spherical fluids assuming the density inhomogeneities are known.

Then, to analyze the apparent/effective properties that are deduced from such simulations on a sheared thin liquid confined in a slit pore, we have performed simulations using the two molecular dynamics schemes that are the most widely used in the literature. In the first approach, the non-equilibrium simulations are performed on a confined fluid directly connected to bulk reservoirs. In the second one, non-equilibrium simulations are carried out

on the confined fluid only, in which the average density is deduced from a prior simulation in the grand canonical ensemble. Using these schemes, the apparent properties (average density, effective viscosity and friction force) of a Lennard-Jones liquid confined in narrow slit pore (of a fixed width) and undergoing boundary shear have been determined. It has been found that the apparent properties can be significantly different using one scheme or the other when the (crystalline) solid surfaces induce a strong structure in the whole fluid, i.e. for small separations between the solid surfaces. In particular, it is shown that the first scheme is the only one usable to explore the history-dependence of the friction force as observed in experiments. Furthermore, because of this strong fluid structure, for precise walls distance corresponding to a first order phase transition a visco-plastic (and shear thinning) behavior of the confined thin liquid can appear.

The last part of this work was devoted to investigate through MD simulations the swelling/shrinkage of such slit pore (i.e. the walls are allowed to move from each other). In particular, we have studied the swelling/shrinkage induced by shear of a simple slit pore immerged in a Lennard-Jones liquid reservoir. Results have shown that, on average, the pore can swell or shrink when the solid walls are displaced in parallel with the fluid-solid interface, i.e. a shear-induced swell/shrink can exist which is not yet taken into account in usual poromechanics theories. This effect is simply due to the fact that the normal pressure of the confined fluid appreciably varies with the relative structural ordering between the solid (crystalline) surfaces for a given pore size. So, when the solid walls are moved parallelly at a constant velocity, the instantaneous pore size oscillates with time. It has been noticed that the walls velocity has a slight effect on the average pore size, but induces a significant modification of the magnitude of the oscillation. This is related to the time needed to re-equilibrate the fluid in the pore.

7.2. Perspectives

A large part of the work done during this thesis was dedicated to noticeably enhance the possibilities of an already existing in house MD code called *Transpore* and to design efficient algorithms to quantify various properties of a fluid confined in a (micro-) porous medium. Thus, one of the main perspective of this work is to apply the developed schemes to more realistic fluid and solid systems (in particular related to geosciences and civil engineering problems) to provide data that could be eventually compared to experimental results directly or used as inputs to a macroscopic simulator. In addition, depending on the findings on such realistic systems it would be a step forward to propose experiments in order to assess the numerical findings. In the following, only the short terms perspective are presented.

Concerning mass diffusion in low permeability situations, we have already developed a slightly modified (in collaboration with Dr. Benazzouz) technique that allows studying the transient behavior of gas diffusion into a confined liquid. Such a method may allow estimating effective diffusion coefficients of various gases (methane, longer alkanes, carbon dioxide) into water confined in clay for example which would be useful as inputs (through homogenization) for a large variety of problems (cap-rock leakage, CO2 storage, etc.). At equilibrium, it allows as well quantifying the solubility of such gases in the confined fluid which may be an additional useful information concerning the storage capabilities of such systems. Another interesting topic would be to compare the results obtained in the strongly adsorbent situation with what can yield a 2D diffusion equation (using finite volume for instance) with mass diffusion coefficient variable in space. If such simplification is possible this would ease the finding an adequate homogenization approach.

A formulation was proposed to describe the local shear viscosity of strongly inhomogeneous fluids starting from the density profile. It would be interesting to check that

the proposed formulation is suitable for other soft sphere fluids and to which extent it can be applied to mixtures. Additionally, the situation in which long range interaction occurs (i.e. Coulombic ones) would be interesting to analyze as long as it may lead to similar non local effects on the local viscosity but over much longer distances than when only van der Waals interaction occurs. In addition, at low density the proposed formulation is not fully satisfying and we expect that a simple kinetic like scheme (including the external field induced by the fluid-solid potential and the fluid structure) could be designed.

When dealing with apparent properties of confined thin film it would be interesting to look after the influence on the load dependence of the shear fiction. In particular, we are planning to study why the relation between the dynamic friction force and the load is following the Amonton's law for high load. It would be enriching as well to explore the swelling/shrinkage and the evolution of composition in the pore in mixtures when the bulk pressure evolves (e.g. discontinuous pore size like in pure fluids or not ?). In addition, it is compulsory, in collaboration with Dr. Vermorel and Pr. Pijaudier-Cabot, to envisage including these effects in an enhanced poromechanics approach to extend the benefit of the work done at the pore scale to the porous medium scale.

Modélisation de Fluides Simples Confinés dans des Nanopores Lamellaires: Transport et Poromécanique

Résumé:

Ce travail vise à étudier les propriétés de transport et le comportement poromécanique de fluides simples confinés dans des nanopores lamellaires par le biais de simulations moléculaires. Pour ce faire, nous avons proposé différents schémas de simulations de la dynamique moléculaire dans des ensembles adaptés aux propriétés étudiées (diffusion de masse, viscosité, force de friction, gonflement …). Il a été note que les propriétés de transport de fluides fortement inhomogènes variaient fortement dans la direction perpendiculaire aux murs solides. Nous avons alors proposé une approche non-locale permettant de déterminer quantitativement la viscosité locale de fluides inhomogènes à partir du profil de densité et applicable pour des sphères dures, molles et le fluide de Lennard-Jones. Il a été également montré qu'un fluide de Lennard-Jones fortement confiné pouvait avoir un comportement viscoplastique (et rhéofluidifiant) si un ordre structurel était induit dans le fluide par la position relative des murs solides. Enfin, nous avons montré qu'une modification importante de la pression de solvatation du fluide confiné peut être induite par cisaillement ce qui peut induire un gonflement « dynamique » d'un nanopore lamellaire.

Mots clés: simulation de dynamique moléculaire, poromécanique, nanopores, fluide inhomogène, propriétés de transport, force de friction, gonflement, théorie fonctionnelle de la densité.

Modeling of Simple Fluids Confined in Slit Nanopores: Transport and Poromechanics

Abstract:

This work aims at investigating the transport properties and the poromechanics of simple spherical fluids confined in slit nanopores through molecular simulations. To do so, we have proposed different schemes to perform molecular dynamics simulations in ensembles adequate to deal with the properties we were looking after (mass diffusion, shear viscosity, friction force, swelling …). The transport properties of strongly inhomogeneous fluids were found to be varying with space perpendicularly to the solid walls. We have then proposed a non-local approach to determine quantitatively the local shear viscosity of such inhomogeneous fluids from the density profile applicable from the Hard-Sphere to the Lennard-Jones fluids. In addition, it has been shown that highly confined Lennard-Jones fluid may exhibit a visco-plastic (+ shear thinning) behavior when a strong structural order is induced in the whole confined fluid because of the relative position of the solid walls. Finally, it was demonstrated that shear induced modifications of the solvation pressure of a confined fluid may exist that leads to a "dynamic" swelling when a slit micropore is sheared.

Keywords: molecular dynamics simulation, poromechanics, nanopores, inhomogeneous fluids, transport properties, friction force, swelling, density functional theory.